Sound from Rough Wall Boundary Layers

William Nathan Alexander

Dissertation submitted to the faculty of the Virginia Polytechnic Institute
and State University in partial fulfillment of the requirements for the degree of
Doctor of Philosophy In Aerospace Engineering

William J. Devenport
Stewart Glegg
Roger L. Simpson
Joseph A. Schetz

September 29, 2011
Blacksburg, Virginia

Keywords: roughness noise, wall-jet, microphone array

Sound from Rough Wall Boundary Layers

William Nathan Alexander

ABSTRACT

Turbulent flow over a rough surface produces sound that radiates outside the near wall region. This noise source is often at a lower level than the noise created by edges and bluff body flows, but for applications with large surface area to perimeter ratios at low Mach number, this noise source can have considerable levels. In the first part of this dissertation, a detailed study is made of the ability of the Glegg & Devenport (2009) scattering theory to predict roughness noise. To this end, comparisons are made with measurements from cuboidal and hemispherical roughness with roughness Reynolds numbers, hu_τ/v, ranging from 24 to 197 and roughness height to boundary layer thickness ratios of 5 to 18. Their theory is shown to work very accurately to predict the noise from surfaces with large roughness Reynolds numbers, but for cases with highly inhomogeneous wall pressure fields, differences grow between estimation and measurement. For these surfaces, the absolute levels were underpredicted but the spectral shape of the measurement was correctly determined indicating that the relationship of the radiated noise with the wavenumber wall pressure spectrum and roughness geometry appears to remain relatively unchanged. In the second part of this dissertation, delay and sum beamforming and least-squares analyses were used to examine roughness noise recorded by a 36-sensor linear microphone array. These methods were employed to estimate the variation of source strengths through short fetches of large hemispherical and cuboidal element roughness. The analyses show that the lead rows of the fetches produced the greatest streamwise and spanwise noise radiation. The least-squares analysis confirmed the presence of streamwise and spanwise aligned dipoles emanating from each roughness element as suggested by the LES of Yang & Wang (2011). The least-squares calculated source strengths show that the streamwise aligned dipole is always stronger than that of the spanwise dipole, but the relative magnitude of the difference varies with frequency.

Acknowledgements

I would like to thank my wife, Ashley, who was been supportive and encouraging throughout my educational pursuits. She has helped me during the most stressful times and has given me one of the greatest joys in my life, my son. She always kept me focused on the big picture beyond school and daily routine to our life together as a family. My world has changed rapidly in the past few years and it has only been for the better. I owe Ashley a great debt for her love. I look forward to the future with Ashley and Brady as our family expands and as we travel through life's experiences together.

I would also like to thank my family. My mother, Suzanne, and my father, Chris, have always encouraged me to excel in my academics and reinforced the importance of education. My siblings, Sarah and Ryan, have been great friends and have been there when I needed to talk. My in-laws have also helped by babysitting and bringing some of their wonderful farm goods to the house.

I would like to thank my advisor Dr. William Devenport. It has been an honor to study under his tutelage. The knowledge I have gained during my graduate studies is invaluable and I attribute it to his great leadership and direction. He has a passion for research that is contagious. He has also helped guide and advise me as friend, and I look forward to continuing our professional and personal relationship.

My graduate education has also been assisted by Dr. Stewart Glegg. He is a brilliant mind and I have been lucky to have worked with him. I hope to continue our collaborations in the future. I would also like to thank the other members of my committee, Dr. Roger Simpson and Dr. Joseph Schetz, for their academic counseling. I would also like to thank the Office of Naval Research and Dr. Ki-Han Kim for their support through grant N00014-08-1-0934.

The members of the Lab 7 research group have all contributed in some way to my project through their direct assistance in measurements or through their creation of a wonderful work environment. I would specifically like to thank Dr. Aurelien Borgoltz, Dr. Dustin Grissom, Dr. Ben Smith, and Dr. Joshua Staubs for introducing me to graduate life and imparting to me much of their learned knowledge from their research experiences. Other people I would like to recognize who have worked directly on the roughness noise project include Matt Rasnick, Ryan Catlett, and Mike Morton. The remaining members of Lab 7 that have made my experience so great include Jon Forest, Ben Worrall, and Manuj Awasthi.

Lastly, I would also like to thank the members of the Aerospace and Ocean Engineering Department in particular Mark Montgomery, James Lambert, Bill Oetjens, and Rachel Hall Smith. My experiences in graduate school have been a blessing and I appreciate the contributions of everyone involved including all those I have not specifically named here but which have contributed to my graduate education. I truly am grateful for my graduate experience.

Thank you,

Nathan Alexander

All photos by author, 2011

Table of Contents

Nomenclature

Roman

c_∞	Speed of sound
C_f	Skin friction coefficient
f	Frequency
h	Roughness height
k_o	Acoustic wavenumber
Re_θ	Momentum thickness Reynolds number
U_c	Convection velocity
U_o	Nozzle exit velocity
U_m	Maximum local velocity
U_e	Edge velocity (equivalent to U_m)
u_τ	Friction velocity
$\boldsymbol{x}$	Observer position
$\boldsymbol{y}$	Source position

Greek

Γ	Wavenumber filter function defined by the roughness geometry
δ	Boundary layer thickness
δ (-)	Uncertainty
δ^*	Displacement thickness
θ	Momentum thickness
κ	Wavenumber
ν	Kinematic viscosity
$\Phi_{PP}(\boldsymbol{x}, \omega)$	Far field pressure spectrum
$\Phi_{pp}(\boldsymbol{\kappa}, \omega)$	Wavenumber wall pressure spectrum
$\Phi_{pp}(\omega)$	Near field pressure spectrum
ρ	Density
τ_W	Wall shear stress
ω	Angular frequency

List of Figures

List of Tables

Chapter 1 Introduction

1.1 Motivation

Roughness noise is a low-level noise source that is often overshadowed by the noise created by turbulent flow over edges or by jets. However, for applications at low Mach number and high Reynolds number with small perimeter to surface area ratios, roughness noise can become a significant contributor to the total noise produced. This is a typical scenario for marine vehicles. As other noise sources have been studied and diminished, interest in roughness noise has been increased, but little knowledge has been ascertained about the generation mechanism until very recently. Research on the subject has been hampered by inadequate facilities as measurements of roughness noise eluded researchers even in laboratory settings because of contaminating background noise.

The development of the anechoic wall-jet facility at Virginia Tech has led to significant advancements in roughness noise research. The design, construction, and iterations of this facility are detailed in Grissom (2007). The final product was a wall-jet that allowed for far field measurement of radiating roughness noise without having to immerse microphones in regions of flow. This facility has extremely low background noise operating levels that allow for straightforward measurement of roughness noise from even hydrodynamically smooth surfaces.

Recent theoretical progress and experimental studies in this wall-jet tunnel, such as those presented in Glegg & Devenport (2009), Devenport *et al*. (2010), and Devenport *et al*. (2011) have shown that the roughness noise may be a predictable function of the surface geometry and the wavenumber wall pressure spectrum. This study details the analysis of noise from discrete element cuboidal and hemispheral roughness in a turbulent wall-jet flow. Measurements of the radiated far field and surface pressure spectrum inside these surfaces are used to compare with theoretical predictions of the roughness noise using the theory of Glegg & Devenport (2009) assuming a homogeneous wall pressure field. The noise from short fetches of large, discrete cuboidal and hemispherical roughness are also analyzed using a linear microphone array to determine the source strength variation through fetches of roughness and to analyze the directivity of individual sources.

1.2 Previous Roughness Noise Research

Lighthill (1952) first made a theoretical link between turbulent fluid motion and the acoustic field it generates. Lighthill's acoustic analogy is a rearrangement of the Navier-Stokes equation into a form resembling the wave equation as shown in Equation 1-1.

$$\frac{\partial^2(\rho')}{\partial t^2} - c_\infty^2 \frac{\partial(\rho')}{\partial x_i^2} = \frac{\partial T_{ij}}{\partial x_i \partial x_j}$$

Eq. 1-1

$$\text{where} \quad T_{ij} = \rho u_i u_j + p_{ij} - \rho' c_\infty^2 \delta_{ij}$$

T_{ij} is the Lighthill stress tensor, $\rho u_i u_j$ is the Reynolds stress, and c_∞ is the speed of sound.

This formulation requires no assumptions or approximations and gives the exact solution to the radiated sound outside of the flow where the acoustic propagation would be equal to c_∞. In this analysis, Lighthill found that the turbulent noise produced from a free field flow radiates as a quadrupole scaling on the eighth power of velocity.

Curle (1955) reformulated Lighthill's solution using a Greens function for a bounded region. This resulted in a dipole source field generated on the surface of the boundary. These dipoles vary with velocity to the sixth power and are therefore more efficient producers of noise than quadrupole sources at low Mach number. Curle's extended version of Lighthill is shown in Equation 1-2. This is an exact formulation, like Lighthill's equation, except that it assumes a solid, impenetrable boundary.

Eq. 1-2

$$\rho'(\boldsymbol{x},t)c_\infty^2 = \frac{\partial}{\partial x_i}\int_S \left[p_{ij} + \rho u_i u_j\right]_{\tau=\tau^*} \frac{n_j dS(y)}{4\pi|\boldsymbol{x}-\boldsymbol{y}|} + \frac{\partial^2}{\partial x_i \partial x_j}\int_V \left[T_{ij}(\boldsymbol{y},\tau)\right]_{\boldsymbol{\tau}=\boldsymbol{\tau}^*} \frac{dV(\boldsymbol{y})}{4\pi|\boldsymbol{x}-\boldsymbol{y}|}$$

where τ^* is the retarded time that corrects for the time delay for the acoustic wave to propogate from source to observer, $\boldsymbol{x}$ is the observer position, and $\boldsymbol{y}$ is the source location. Powell (1960) extended Curle's analysis for a rigid, planar, infinite boundary case and found that using an image method the dipole source field on the surface is cancelled leaving only the quadrupole term.

Skyurdzyk & Haddle (1960) present some of the earliest experimental work on roughness noise. They studied the noise from a rotating cylinder with different surface roughness applied submerged in the Garfield Thomas Water Tunnel at Pennsylvania State University. Skyurdzyk & Haddle (1960) suggest that flow noise is directly related to the surface drag, and therefore, hydrodynamically smooth roughness contained within the laminar sublayer will not produce increased far field noise. They argue that the noise is created by the increased turbulence generated by the roughness. Therefore, the onset of roughness noise generation can be determined by a critical velocity below which roughness noise will not be produced. They studied four different rough surfaces including 180grit and 60grit sandpaper roughness coating the outside of the spinning cylinder and measured the radiated noise using hydrophones mounted on the inside of the tank. They found that the boundary layer noise was enhanced by the presence of roughness confirming the existence of roughness noise and that the total noise levels increased with velocity at a slope steeper than that produced by the smooth wall flow. Although, for the different rough walls, they observed that the slope of the velocity dependence changed and did not indicate a specific source mechanism typical of a dipole or quadrupole source. They also found a dependency on the density of the roughness.

Chanaud (1969) measured the radiated far field noise of a spinning disk with circumferential rings of roughness placed around the center of the disk on the top and bottom and with roughness placed on the ¼" wide edge of the disk. His experiment was conducted in the Herrick Laboratories' anechoic room. The roughness had a maximum height of 0.032" and measurements were made at disk tip speeds of 158ft/s to 315ft/s. The disk had a diameter of 24". Chanaud concluded that the directivity of the roughness noise source was indeed a dipole, but his measurements were contaminated with edge noise due to flow over the periphery of the disk. There was a clear increase of noise due to the surface roughness above 3150Hz. He also concludes through time-delay correlation measurements that the increase in noise is produced at the location of the roughness elements.

Cole (1980) presents results from one of the first roughness noise experiments conducted in a conventional turbulent boundary layer flow. His research was performed at the David W. Taylor Naval Ship Research and Development Center's Anechoic Flow Facility using a flat plate covered in 80 and 40grit sandpaper roughness. The far field noise of the roughness was measured using a parabolic-reflector microphone system. Both dipole and quadrupole scalings were examined to normalize the data, but the results were inconclusive both collapsing the data within a few decibels. Cole suggests that the source may be an admixture of the two types, and therefore, both scaling laws apply to some degree. He also notes that the presented data may be influenced by the background noise of the tunnel contaminating the far field noise recorded by the reflector.

The first conclusive characterization of the roughness noise source came from Hersh (1983). He measured the sound radiated from roughened pipe flow with exit speeds up to 120m/s using 36 to 180 grit sandpaper surfaces. He found the roughness noise scaled as a dipole source to the sixth power of velocity. Care was taken to ensure that the measured noise was not created by an enhanced lip dipole source from the pipe exit due to the presence of the roughness. Examination of the lip dipole showed its power levels well below that of the jet noise and roughness noise. Hersh also observed that the roughness noise was dependent on the size of the roughness. Larger roughness produced greater noise, but also shifted the maximum noise levels to lower frequencies. Hersh attempted to scale the data using two methods: first using the friction velocity and the equivalent sand roughness height and second with the friction velocity and momentum thickness. A better collapse was produced using the equivalent sand roughness height as the length scale.

Howe (1984) developed a scattering theory of roughness noise generation which details the process of converting the near field pressure fluctuations to radiating acoustic waves. He states that the assumption of surface dipoles cancelling each other as described by Powell (1960) is invalid with the introduction of surface irregularities. Therefore, roughness noise will behave as a distribution of dipole sources over the rough surface. Howe theoretically models a rough surface as an arrangement of hemispherical bosses on a planar wall and compares his far field results with the noise recorded by Hersh (1983). Absolute comparisons were not possible because of unknowns in Hersh's experiment, but the data show similar trends. Howe agreed with the sixth power of velocity scaling indicating a dipole source and the spectral shapes of his far field spectra were also similar to that of Hersh.

The analysis of Howe (1984) assumed inviscid flow over the rough surface and was therefore only applicable for large roughness Reynolds numbers, hu_τ/ν. Therefore, in 1986, Howe continued his analysis of the rough wall flow and introduced viscous effects into the analysis specifically including the no-slip condition on the wall. This analysis particularly regarded roughness completely contained within the viscous sublayer having $hu_\tau/\nu < 5$. It was found that the inclusion of viscous effects raised the predicted far field by up to 2-3dB. Howe (1988) uses Chase's (1987) wavenumber wall pressure spectrum to make roughness noise predictions, but empirically modifies his formulation to include the effects of the interstitial flows on the rough wall. He adds the effects produced by diffraction of the enhanced Reynolds stresses due to the roughness with Chase's spectrum for a smooth wall. Again, Howe uses Hersh's data for spectral shape comparison and to adjust the constants in his empirical formula but cannot evaluate the accuracy of the absolute predicted values. The shape of the produced spectrum was very similar to experimental data. Overall, the greatest contribution of Howe's work was to relate the radiated far field noise to the wavenumber wall pressure spectrum and the rough surfaces characteristics including roughness density and size.

The scattering mechanism was theoretically investigated by Howe, but cannot be applied to very large roughness as it does not account for self-generated drag induced dipoles from local vortex shedding. More recently, Glegg *et al.* (2007) investigated the scattering and drag dipole mechanisms for roughness of varying size to determine their relative strengths. For roughness that does not extend beyond the log layer, they find that the far field is dominated by the scattering of the wall pressure fluctuations and effects of vortex shedding can be ignored. Also, the two source mechanisms are suggested to scale differently. Glegg *et al.* (2007) suggest scaling the scattered pressure fluctuations using a frequency scaling based on the roughness lengthscale. The suggested frequency scaling for vortex shedding is based on the roughness height. Therefore, the two source mechanisms should be easily separated, and for most roughness noise cases, the dominant source will be the scattering of turbulent pressure fluctuations.

Citing the findings of Howe (1988) and noting the importance of the wavenumber wall pressure spectrum on the radiated acoustics, Farabee & Geib (1991) experimentally analyzed the wavenumber wall pressure spectrum of rough wall flows. Their study was conducted in the Anechoic Flow Facility at David Taylor Research Center. They applied three types of surface roughness to the wall of the tunnel, two in the fully rough regime and one that was transitionally rough. The roughness fetches were 2m long in the streamwise direction and a six sensor wall pressure microphone array was positioned immediately downstream of the rough surface. Rough wall boundary layers recover slowly back to smooth wall conditions according to the study of Antonia & Luxton (1972). Therefore, although this array was placed in a smooth wall condition, effects of the wall roughness extended over the microphone array. Their measurements show that wall roughness increases the intensity of the pressure fluctuations on the convective ridge of the wavenumber wall pressure spectrum and tend to shift it to lower frequencies. This indicates that the roughness creates larger turbulence Reynolds stresses and slows the convected eddies traveling over the surface. They also recorded increases in the sonic component of the wavenumber wall pressure spectrum and conclude that the increased levels in this region are due to scattering of the convective region by the rough surface. They note that their findings in the subconvective and supersonic regions may be corrupted by convective pressures and facility background noise, respectively, but that their findings in the convective and supersonic regions qualitatively agree with Howe (1988).

Liu & Dowling (2007) investigated the diffraction theory of Howe (1988) using several smooth wall wavenumber pressure spectra models that were adapted to the higher friction velocities and boundary layer thicknesses of rough wall flows. They compared predictions of Hersh's (1983) experiment using these modified models with Howe's (1988) estimation and found that the Howe model fit the data best, but that all of the models produced similar results. This validated Howe's theory of a scattering mechanism. Liu & Dowling (2007) applied Howe's theory to open-jet wind tunnel measurements of roughness noise from hemispherical roughness. Again, they found that the wavenumber pressure spectrum model used in the theoretical predictions made an insignificant difference and that the theoretical predictions were better at low frequency than higher frequencies. They attribute this to the assumption in the scattering theory that the boundary layer thickness to acoustic wavelength ratio is much less than 1. The estimations begin to deviate from the measurements at the same frequencies this assumption becomes invalid.

Anderson *et al.* (2007) completed wall pressure spectrum measurements using methods similar to the measurements of Farabee & Geib (1991), but also measured the radiated far field noise using a 63-sensor far field microphone array. Measurements of the wavenumber wall pressure spectrum agree with the results of Farabee & Geib (1991) showing increases in the convective and sonic regions with increasing roughness height. The far field microphone array produced measurements of the variation in

source strength along the length of the examined rough surfaces. They found that the front of the roughness fetch produced the greatest noise with the strength diminishing in the streamwise direction. They applied several recommended scalings to the recorded far field spectra from the rough surfaces. These included Cole's (1980) inner and outer variable dipole and quadrupole suggested normalizations. None of the suggested scalings worked to collapse the spectral data completely and neither the dipole nor quadrupole velocity scaling was confirmed. Their data appear to suggest a combination of the two source types.

Liu *et al.* (2008) conducted another roughness noise experiment using phased microphone array technology. They studied the noise from two rough surfaces made of discrete hemispherical elements having different roughness heights and densities using both a high and low frequency microphone array. They analyzed their beamformed data using standard techniques that assume monopole sources. They then compared their measured source maps to a beamformed source map of a theoretical field of dipole sources with a source strength distribution as calculated using the method of Liu & Dowling (2007). The simulated and measured roughness noise produced similar beamformed solutions confirming the dipole nature of the source and the approximate source strength solution of Liu & Dowling (2007). The highest frequencies of their measurement were overestimated by 3dB and the streamwise decline in source strengths was underpredicted.

Coinciding with the theoretical and experimental work on roughness noise, Yang & Wang (2009, 2010, 2011) have been developing computational predictions of roughness noise from cuboidal, hemispherical, and cylindrical fetches of discrete elements using high resolution LES. The flow field is solved using the LES, and the acoustics are calculated with the Curle (1955)-Powell (1960) integral solution to Lighthill's (1952) acoustic analogy. In Yang & Wang (2009), specific attention is brought to the noise produced by an individual hemispherical element and the results of interaction between two hemispherical elements. The studied roughness elements have roughness Reynolds numbers, hu_τ/ν, equal to 95. They found that local vortex shedding is not a significant contributor to the total noise produced by the shedding element but the trailing element's noise is enhanced by the vortices impinging on its surface. They also describe the presence of streamwise and spanwise aligned dipoles emanating from each roughness element.

Yang & Wang (2010, 2011) concern the noise from 40 element fetches of roughness arranged in 4 spanwise by 10 streamwise grid patterns with hu_τ/ν = 168. They compare the differences in sound produced by hemispherical, cuboidal, and cylindrical roughness and find the cuboidal roughness produces the greatest noise. The source strength variation throughout each fetch also varies for the differing roughness geometries. The lead row is the weakest producer of noise for both the cylindrical and hemispherical surfaces while it is the strongest for the cuboidal. One of the advantages of a computational simulation is that quantitative results are available for all locations in the domain. Therefore, they were able to calculate local RMS surface pressure and surface pressure spectra around and on the surface of roughness elements and correlate the results with the streamwise and spanwise dipole fluctuations. They found that the roughness noise sources are confined within the very near region of the roughness elements so that there is little coherence of the noise produced by adjacent elements. The majority of sound produced by the individual elements was created by the impinging vortices and the edges on the lead side of the cuboidal and cylindrical elements. Very little sound was produced by the downstream portions of the roughness elements.

1.3 Recent studies at Virginia Tech

An anechoic wall-jet facility was constructed at Virginia Tech in 2005 specifically for the study of roughness noise. The design of this facility is discussed in detail by Grissom (2007) along with presentations of the noise from stochastic and wavy wall surfaces. The aerodynamic characteristics of smooth and rough wall flows in the facility were examined in Smith (2008). This wall-jet tunnel was designed to negotiate around the problems encountered by previous studies of roughness noise, mainly the contaminating background noise. Grissom (2007) recorded noise from hydrodynamically smooth surfaces confirming the existence of a scattering mechanism as suggested by Howe (1988) for small roughness. Also, he noticed that the shape of the radiated far field noise varied between measurements from the wavy wall surfaces and the stochastic surfaces. Therefore, he concluded that inner or outer variable scalings would be unable to collapse the data from these differing roughness geometries. Grissom also found that the wavy wall surface exhibited specific directionality. It was tested with ribs aligned at several angles to the flow direction thereby rotating the wavenumber vector of the surface. The surface generated the most far field noise with the ribs aligned perpendicular to the flow producing a signal-to-noise ratio of approximately 25dB. When the ribs were aligned parallel to the flow direction very little far field noise was recorded. None of the previously proposed simple scaling models (Cole, 1980, Howe, 1988, Farabee & Geib, 1991, Glegg *et al*., 2007) would account for such a directional effect because they do not contain a physical explanation of the roughness noise generation mechanism. Grissom's (2007) study suggests that future studies need to focus on capturing the interaction and behavior of the wavenumber wall pressure spectrum with specific roughness geometries.

The theory proposed in Glegg & Devenport (2009), which was the result of experimental and theoretical collaboration between researchers at Virginia Tech and Florida Atlantic University, is the first to provide a clear relationship between non-specific roughness geometry, the wavenumber wall pressure spectrum and the radiated far field noise. Therefore, unlike the theory of Howe (1988), which was derived for a distribution of hemispherical surface roughness, their theory could be applied to any surface geometry to estimate the far field noise. Their "*Unified Theory of Roughness Noise*" is shown in Equation 1-3.

Eq. 1-3

$$\rho'(\boldsymbol{x},\omega)c_\infty^2 \approx \frac{-\mathbf{i}k_o e^{\mathbf{i}k_o|\boldsymbol{x}|}}{2\pi|\boldsymbol{x}|}\int p_s(\kappa_1,\kappa_3,\omega)\left\{\frac{x_1\zeta^{(1)}}{|\boldsymbol{x}|}+\frac{x_3\zeta^{(3)}}{|\boldsymbol{x}|}-\mathbf{i}k_o h\zeta^{(2)}\right\}(2\pi)^2 d\kappa_1 d\kappa_3$$

where k_o is the acoustic wavenumber, p_s is the wavenumber surface pressure spectrum, h is the roughness height, $\zeta^{(1)}$ and $\zeta^{(3)}$ are the wavenumber transforms of the surface slope in the longitudinal and lateral directions, and $\zeta^{(2)}$ is the wavenumber transform of the surface. They show if a distribution of hemispherical bosses is assumed, that the result yields the same solution as presented in Howe (1998). They also develop their theory for two other example surface geometries: a wavy wall and a piecewise continuous surface. Their analysis of the wavy wall surface shows that a sinusoidal surface will radiate the near field pressure spectrum corresponding to the wavenumber vector of this surface thus providing an indirect measure of the wavenumber wall pressure spectrum. This explains the directional phenomenon observed in Grissom's (2007) measurements of a wavy wall surface. The convective ridge of the theoretical wavenumber wall pressure spectrum peaks at spanwise wavenumbers of zero. Therefore, the wavy wall surface will produce a maximum sound when the ribs are aligned perpendicular to the flow creating a wavenumber vector without a spanwise component.

The noise from wavy wall surfaces was investigated further in Devenport *et al*. (2010). In this study, they used Glegg & Devenport's (2009) theory to make measurements of the wavenumber wall pressure spectrum of the wall-jet flow and compared their results to the model of Chase (1980, 1987). By rotating the ribbed surface, which alters the wavenumber vector of the surface, they were able to make measurements corresponding to an arc passing through the wavenumber wall pressure spectrum as shown in Figure 1-1. Their measurements showed that the convection velocity of the wall-jet (~$0.41U_e$) was considerably slower than that for conventional turbulent boundary layers (~$0.60U_e$) and that the peak of the convective ridge may also be broader.

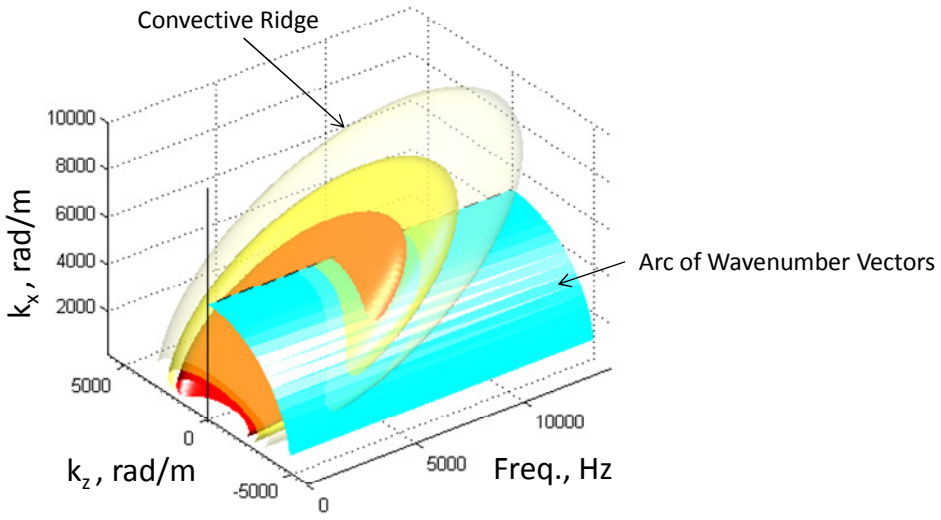

Figure 1-1. Diagram of measurement of wavenumber wall pressure spectrum on an arc of wavenumber vectors

The theoretical piecewise surface discussed in Glegg & Devenport (2009) was analyzed as a representation of stochastic surfaces that have vertical sides. The results show that this configuration is wavenumber white assuming $\omega h/U_c < 1$ so that the specific geometry of the surface is not needed. The far field sound can be approximated with only general information about the observer location and wall pressure spectrum. The resulting predicted far field spectrum when normalized on the wall pressure spectrum should produce a slope of ω^2. The theory of Glegg & Devenport (2009) for surfaces with vertical sides shows that the far field noise would be related to a homogeneous wall pressure spectrum as shown in Equation 1-4.

$$\Phi_{PP}(\boldsymbol{x},\omega) \approx C\left(\frac{x_1}{|\boldsymbol{x}|}\right)^2 \frac{(k_o h)^2 \Sigma \Phi_{pp}(\omega)}{|\boldsymbol{x}|^2} \qquad \text{Eq. 1-4}$$

$$\text{where} \quad C = \frac{\alpha^2}{4\pi^2}$$

$\Phi_{PP}(\boldsymbol{x},\omega)$ is the radiated far field, Σ is the roughness area, and $\Phi_{pp}(\omega)$ is the single point wall pressure spectrum. Therefore, if the far field noise is normalized on the single point wall pressure spectrum, the resulting curve should only be a function of $(k_o h)^2$. This relationship was partially confirmed in Alexander (2009) and Devenport *et al*. (2011). These studies show the measured noise from stochastic

roughness ranging from hydrodynamically smooth to fully rough conditions using 20grit to 180grit sandpaper. The results as reported in Alexander (2009) are shown in Figure 1-2. The studies find the $(k_o h)^2$ relation as expected at lower frequencies, below 5kHz. Above this, the data fan out deviating from the ω^2 slope in order of roughness height. The smallest roughness retains the ω^2 slope to higher frequencies than the larger roughness sizes. They term this frequency where the expected result appears to differ from the observed behavior the "break frequency". They attribute this "break frequency" to a dependency on the roughness grain sizes because the relationship shown in Equation 1-4 is only valid for homogeneous wall pressure fields. Therefore, the hypothesized relation is void when the turbulence scales become smaller than the individual roughness grains.

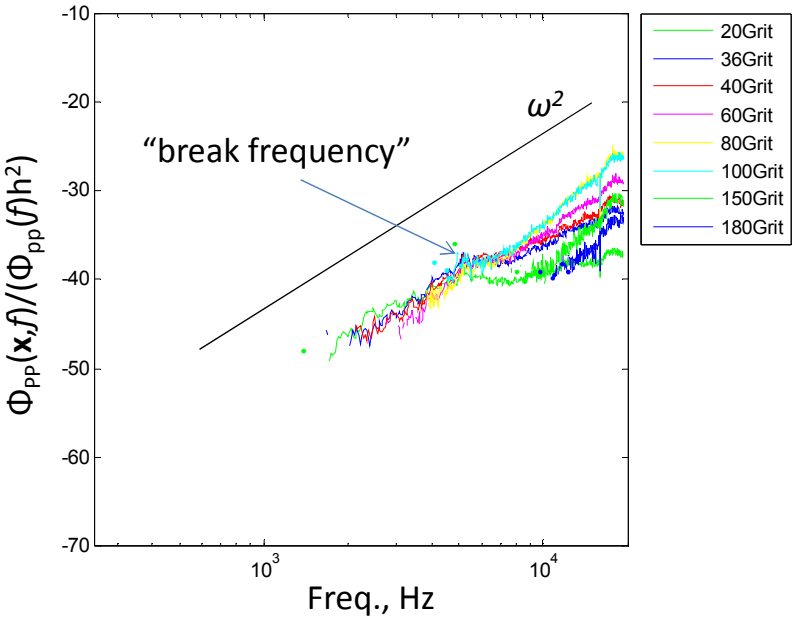

Figure 1-2. Normalization of noise from stochastic roughness presented in Alexander (2009)

The roughness noise problem is speculated to change when the roughness elements are large compared to the boundary layer thickness. The wall pressure field over such a surface would be highly inhomogeneous. The noise from rough surfaces with large roughness height to boundary layer thickness ratios was studied in Rasnick (2010). He calculated the per-element average non-dimensional drag dipole spectra for turbulent wall-jet flow over multi-element gravel, cuboidal, and hemispherical roughness fetches using the theory of Glegg *et al*. (2007). These elements were as large as 55% of the boundary layer thickness. His experiment involved only a single microphone placed in the far field to record the radiated noise, and therefore, he was unable to separate the contributions from individual elements.

1.4 The Wavenumber Wall Pressure Spectrum

The theoretical descriptions of roughness noise as given by Howe (1988) and Glegg & Devenport (2009) relate the radiated far field sound to the wavenumber wall pressure spectrum. Therefore, it is important to understand the development and form of a few of the current and most used models. The wavenumber wall pressure spectrum decomposes the wall pressure frequency spectrum into the contributing lengthscales at each frequency so that the intensity of pressure fluctuations from various size

flow structures can be observed. One of the first models of this spectrum was presented by Corcos in 1964 using curve-fits to measured spatial correlations in turbulent boundary layers. The Corcos model as given by Howe (1998) is shown in Equation 1-5.

$$\frac{\Phi_{pp}(\boldsymbol{\kappa},\omega)}{\Phi_{pp}(\omega)} = \frac{l_1}{\pi[1+l_1^2(\kappa_1-\omega/U_c)^2]}\frac{l_3}{\pi[1+l_3^2\kappa_3^2]}$$

Eq. 1-5

$$\text{Where } l_1 \approx 9\,U_c/\omega \text{ and } l_3 \approx 1.4\,U_c/\omega$$

$\Phi_{pp}(\boldsymbol{\kappa},\omega)$ is the wavenumber wall pressure spectrum, $\Phi_{pp}(\omega)$ is the wall pressure frequency spectrum, κ_1 and κ_3 are the longitudinal and lateral wavenumbers, and U_c is the convection velocity. This model provides good estimations of the convective ridge, the most intense region of turbulent pressure scales, but overpredicts wavenumbers below this peak in the subconvective region.

There were a few attempts to improve the modeled spectrum of Corcos. Efimtsov (1982), using the same empirical method as Corcos (1964), incorporated the effects of boundary layer thickness on the spatial correlations. His result was similar to the model shown in Equation 1-5, but replaces the definitions of the correlation lengths $l_1$and l_3 with Equation 1-6 as reported in Graham (1997).

$$l_1 = \delta\left[\left(\frac{a_1\left(\frac{\omega\delta}{u_\tau}\right)}{U_c/u_\tau}\right)^2 + \frac{a_2^2}{\left(\frac{\omega\delta}{u_\tau}\right)^2 + (a_2/a_3)^2}\right]^{-1/2}$$

Eq. 1-6

$$l_3 = \delta\left[\left(\frac{a_4\left(\frac{\omega\delta}{u_\tau}\right)}{U_c/u_\tau}\right)^2 + \frac{a_5^2}{\left(\frac{\omega\delta}{u_\tau}\right)^2 + (a_5/a_6)^2}\right]^{-1/2} \quad for\ M_\infty < 0.75$$

$$l_3 = \delta\left[\left(\frac{a_4\left(\frac{\omega\delta}{u_\tau}\right)}{U_c/u_\tau}\right)^2 + a_7^2\right]^{-1/2} \quad for\ M_\infty > 0.9$$

where δ is the boundary layer thickness, u_τ is the friction velocity, and a_1 through a_7 are constants with values 0.1, 72.8, 1.54, 0.77, 548, 13.5, and 5.66, respectively. This model was an improvement, but still overpredicted the low wavenumber region.

Smol'yakov & Tkachenko (1991) give a model of the wavenumber wall pressure spectrum empirically fitting measured spatial correlations similar to Corcos (1964) and Efimtsov (1982). In Smol'yakov & Tkachenko, rather than accounting for the longitudinal and lateral correlation lengths separately, as done in the previous models, they calculated the Fourier transform using the combined root sum of squares correlation length. Their suggested model is given in Equation 1-7. This model has a narrower convective peak than previous versions and also diminishes the levels at low wavenumbers while retaining the supposed wavenumber white shape observed in experiment in this region.

$$\frac{\Phi_{pp}(\boldsymbol{\kappa},\omega)}{\Phi_{pp}(\omega)} = 0.02467A(\omega)h_{ST}(\omega)[F(\boldsymbol{\kappa},\omega) - \Delta F(\boldsymbol{\kappa},\omega)]$$

$$A(\omega) = 0.124\left(\frac{U_c}{\omega}\right)^2\left[1 - \frac{U_c}{4\omega\delta^*} + \left(\frac{U_c}{4\omega\delta^*}\right)^2\right]^{1/2} \qquad h_{ST}(\omega) = \left[1 - \frac{m_1 A}{6.515\sqrt{G}}\right]^{-1}$$

$$m_1 = \frac{1+A^2}{1.025+A^2} \qquad G = 1 + A^2 - 1.005m_1 \qquad \text{Eq. 1-7}$$

$$F(\boldsymbol{\kappa},\omega) = \left[A^2 + \left(1 - \frac{\kappa_1 U_c}{\omega}\right)^2 + \left(\frac{\kappa_3 U_c}{6.45\omega}\right)^2\right]^{-3/2}$$

$$\Delta F(\boldsymbol{\kappa},\omega) = 0.995\left[1 + A^2 + \frac{1.005}{m_1}\left\{\left(m_1 - \frac{\kappa_1 U_c}{\omega}\right)^2 + \left(\frac{\kappa_3 U_c}{\omega}\right)^2 - m_1^2\right\}\right]^{-3/2}$$

Ffowcs Williams (1982) derived a model from Lighthill's acoustic analogy with constants left to be determined from experiment. A simplified version of their formulation was given by Hwang & Geib (1984) assuming incompressible flow, but this model is divergent in high wavenumber. Its high wavenumber region does not satisfy the requirement that the integral of the normalized wavenumber wall pressure spectrum equal one as given in Equation 1-8. Therefore, this model is not considered further but is worthy of note since it was a theoretical attempt to model the wavenumber pressure spectrum and not simply an empirical fit of experimental data.

$$\int_{-\infty}^{\infty}\int_{-\infty}^{\infty}\frac{\Phi_{pp}(\boldsymbol{\kappa},\omega)}{\Phi_{pp}(\omega)}\,d\kappa_3\,d\kappa_1 = 1 \qquad \text{Eq. 1-8}$$

Chase's (1980, 1987) models, similar to Ffowcs Williams, are built on theoretical and experimental analysis and therefore include a number of adjustable constants to fit observations. His recommended model, assuming incompressibility, is given in Equation 1-9 as reported in Chase (1987). This is an update of his 1980 version to better model the subconvective wavenumber region. His estimated spectrum is lower in this region than the greatly overpredicted values of Corcos (1964), but Chase (1987) does not produce a wavenumber white shape. The convective regions of both the 1980 and 1987 models are nearly the same. Chase (1987) attempts to address the compressibility issues relating to the sonic and supersonic wavenumbers, but unknown parameters in his model, as encountered by the evaluation of Ffowcs Williams (1982), limit reliable application of his incompressible model in the acoustic and subconvective domains.

$$\frac{\Phi_{pp}(\boldsymbol{\kappa},\omega)}{\Phi_{pp}(\omega)} = \frac{\rho^2 u_\tau^3}{\Phi_{pp}(\omega)[k_+^2 + (b\delta)^{-2}]^{5/2}}\left\{C_T|\boldsymbol{\kappa}|^2\left[\frac{k_+^2 + (b\delta)^{-2}}{|\boldsymbol{\kappa}|^2 + (b\delta)^{-2}}\right] + C_M\kappa_1^2\right\}$$

$$\text{Where} \quad h_C = 3 \quad C_T h_C = 0.014 \quad C_M h_C = 0.466 \quad b = 0.75 \qquad \text{Eq. 1-9}$$

$$\text{And} \qquad k_+^2 = \frac{\left(\frac{\omega}{U_C} - \kappa_1\right)^2}{h_C^2\left(\frac{u_\tau}{U_C}\right)^2} + \boldsymbol{\kappa}^2$$

The single point spectrum of Chase was given in two parts in 1980 and 1987. The resultant formulation is given as:

$$\Phi_{pp}(\omega) = \Phi_T(\omega) + \Phi_M(\omega)$$

$$\text{Where } \Phi_T(\omega) = \pi C_T h_C \rho^2 u_\tau^4 \omega^{-1} \alpha^{-1}(1+\alpha^{-2}) \text{ and}$$
$$\Phi_M(\omega) = r_M a_+ \rho^2 u_\tau^4 \omega^{-1} \alpha^{-3}(1+\mu^2\alpha^2)$$

Eq. 1-10

$$\alpha = [1 + (U_c/\omega b\delta)^2]^{-1/2} \qquad r_M = 1 - C_T h_C/(C_T h_C + C_M h_C)$$

$$a_+ = (2\pi h_C/3)(C_T + C_M) \qquad \mu = h_C u_\tau / U_c$$

The previously discussed models, excluding Ffowcs Williams (1982), are compared in Figure 1-3. The models of Corcos (1964) and Efimtsov (1982) are similarly shaped with the values of Efimtsov falling slightly below that of Corcos. Smol'yakov & Tkachenko (1991) and Chase (1987) have much narrower peaks at these conditions with much lower subconvective and viscous regions. The wavenumber white subconvective regions, as observed in experiment, are apparent in the Corcos, Efimtsov, and the Smol'yakov & Tkachenko spectra where as the Chase spectrum continues to decline with decreasing wavenumber. There is little conclusive evidence as to which specific model of the wavenumber wall pressure spectrum is the best as reported in a review of each model by Graham (1997). Therefore, several models should be examined in reference to a particular issue. Both the Chase and Corcos spectra are analyzed further in this report through the theory of Glegg & Devenport (2009) that relates the wavenumber wall pressure spectrum to roughness noise.

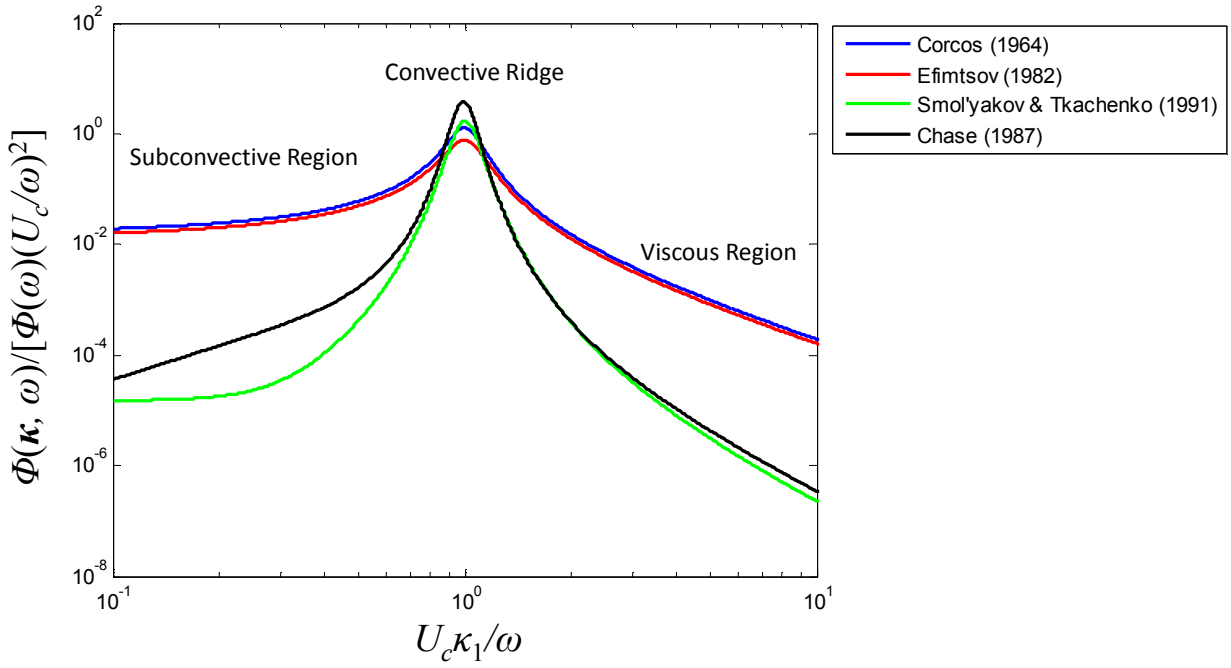

Figure 1-3. Comparison of wavenumber wall pressure spectrum models with inputs U_c=30m/s and ω=10000 rad/m

1.5 Microphone Array Data Processing

Phased microphone arrays have been used in previous roughness noise studies (Anderson *et al.*, 2007, Liu *et al.*, 2008) to determine source directivity and strength distributions. This study also details microphone array measurements of roughness noise, and the data are analyzed using beamforming and least-squares analysis techniques. Therefore, a brief background and discussion of processing methods for phased microphone arrays is needed to understand current applications and practices.

An early study of phased microphone arrays was conducted by Billingsley & Kinns (1976) to locate noise sources on jet engines. They used a linear array of fourteen ¼" Bruel & Kjaer microphones. By weighting the components of the measured cross-spectral matrix to account for various sensor to source distances and summing the results, they were able to focus their array on different locations over a defined region. This type of analysis is termed delay and sum beamforming. A similar form of their analysis which does not assume uncorrelated sources is given by Tester & Glegg (2008) shown in Equation 1-11.

$$\boldsymbol{B} = \boldsymbol{G}_{inv}\boldsymbol{C}\boldsymbol{G}_{inv}^{H} = \boldsymbol{W}\,\boldsymbol{Q}\,\boldsymbol{W}^{H} \qquad \text{Eq. 1-11}$$

where $\boldsymbol{B}$ is the beamformed solution of windowed source strengths, $\boldsymbol{G}_{inv}$ is the inverse monopole steering matrix, $\boldsymbol{C}$ is the cross-spectral matrix, $\boldsymbol{W}$ is the windowing function, and $\boldsymbol{Q}$ is the cross-spectral density of the source strength. The Billingsley & Kinns (1976) analysis assumes monopole sources which have arbitrary directionality. They found that the resolution of the array in accurately pinpointing the source locations was affected by its aperture, which is the angle drawn from the array's extremities to the source, and the frequency. The resolution becomes finer with increasing microphone spacing and frequency. Therefore, in the design of a microphone array, the source locations and frequencies of interest should be taken into consideration when determining the sensor spacing. More recently, deconvolution methods (Brooks & Humphreys (2006), Brooks (2006)) have been developed that improve the resolution of the beamformed source maps but are more complicated and time consuming.

This beamforming method works well but the steering vectors generally assume monopole sources. This is typically not the case encountered in aeroacoustic applications. Many noise sources are dipoles which have a specific directionality. Jordan *et al.* (2002) investigated the effects of monopole beamforming techniques on measurements of dipole sources. They found that measurement of a dipole source using a linear array perpendicular to its axis produced a void in the beamformed map at the location of the source when using the conventional monopole technique. This is due to the lobes of the dipole, which are 180° out of phase, cancelling each other when the steering vector is focused at its origin. They correct for this by observing the focal location where the phase of the microphones passes through 180°. This is the location of the dipole source. The phase of the microphone signals on either side of the dipole source can then be adjusted accordingly so that the summation is constructive instead of the out of phase signals cancelling each other. Jordan *et al*. (2002) find the beamforming method incorporating the modified cross-spectral matrix correctly identifies the source location and suppresses other sound sources. The drawback of their experiment is that it involved only a single dipole with known orientation. The problem becomes much more complicated if multiple dipoles are included with various orientations.

Beamforming methods often work well to identify source locations, but determining source strengths can be difficult, especially if multiple sources contained within a single lobe of a source map need to be independently analyzed. If the source location and type is known, an accurate source strength

solution can be determined using inverse methods like that presented in Nelson & Yoon (2000). Nelson & Yoon (2000) use the inverse of a transformation matrix altering the source strength to the measured noise, to solve for the source strength using a least-squares method. The first step to their method is modeling the noise source into a discrete distribution of sources so that the frequency response function of the source measurement can be determined as shown in Equation 1-12.

$$\vec{P} = \boldsymbol{G}\vec{q} \qquad \text{Eq. 1-12}$$

where $\vec{P}$ is a complex vector of the measured acoustic response, $\vec{q}$ is a vector of the models source strengths, and $\boldsymbol{G}$ is the transformation matrix dependent on the source model. If this representation is extended to solve for the cross-spectral density of source strengths, $\boldsymbol{Q}$, using the measured cross-spectral matrix of acoustic pressures, $\boldsymbol{G}_{pp}$, Equation 1-12 can be rearranged into Equation 1-13.

$$\boldsymbol{Q} = \boldsymbol{G}^{+}\boldsymbol{G}_{pp}\boldsymbol{G}^{+H} \qquad \text{Eq. 1-13}$$

where H is the Hermitian transpose and the plus sign indicates a pseudo-inverse. The pseudo-inverse has to be used when the source to sensor ratio is not one creating a matrix $\boldsymbol{G}$ with a differing number of rows and columns. In this case, the exact inverse cannot be determined. The solution to this matrix equation is then solved using a least-squares analysis to minimize the error between the determined matrix of source strengths and the measured cross-spectra.

Nelson & Yoon (2000) find that the accuracy of their solution using this least-squares method is dependent upon the condition number, σ, of the matrix $\boldsymbol{G}$ defined by:

$$\sigma(\boldsymbol{G}) = \|\boldsymbol{G}\| \, \|\boldsymbol{G}^{+}\| \qquad \text{Eq. 1-14}$$

A large condition number increases the sensitivity of the solution to perturbations in the measured cross-spectral matrix, $\boldsymbol{G}_{pp}$, and the transformation matrix, $\boldsymbol{G}$. They find that there are several geometrical factors that influence the condition number. The condition number is negatively impacted by low source spacing to wavelength ratios, increasing distance between source and sensor locations, differing source and sensor geometrical configurations, and asymmetry of the source and sensor positions.

Yoon & Nelson (2000) discuss two different methods of increasing the accuracy of the least-squares solutions affected by ill-conditioned transformation matrices: Tikhonov regularization and singular value discarding. Tikhonov regularization is used to improve the conditioning of the calculation by weighting various parts of the matrix $\boldsymbol{G}$ to reduce its norm. Singular value discarding involves the removal of the smallest values in the matrix $\boldsymbol{G}$ that are responsible for the poor conditioning of the inverted matrix. These are the values corresponding to the ratio of largest to smallest singular values that determine the condition number. They compare their least-squares source strength solutions to experimental measurements of a randomly vibrating plate and vary the condition number of the measurements by changing the assumed source model and microphone configuration. They find their method works well when the condition number is made sufficiently small either by experimental set-up or the discussed matrix conditioning techniques.

1.6 Objectives

A reliable method to predict roughness noise is needed. The extent to which the scattering theory of Glegg & Devenport (2009) applies, especially for surfaces with large roughness Reynolds numbers or roughness height to boundary layer thickness ratios, has not been examined. Previous studies show that their theory works well to collapse the noise produced by stochastic roughness up to a "break frequency", but the origin of this "break frequency" is not well understood. Also, for surfaces with very large roughness elements which have local vortex shedding, the relationship of the radiated noise with the wavenumber wall pressure spectrum may change. These surfaces produce inhomogeneous wall pressure fields. Therefore, the radiated noise may vary locally over the surface. This study attempts to address these issues by focusing on the noise generated by fetches of discrete cuboidal and hemispherical roughness. The noise from these surfaces is analyzed using far field and surface pressure measurements and is compared to results from current roughness noise theory. A linear microphone array was designed to measure the generated roughness noise produced by the fetches and a novel least-squares source strength analysis method was developed to decompose the contributions from individual sources to the radiated far field. The explicit objectives of this study are:

- To analyze the relationship of roughness noise with boundary layer, wall pressure, and rough wall characteristics by measuring the far field noise and wall pressure fluctuations in fetches of discrete cuboidal and hemispherical roughness elements.
- To assess the theory of Glegg & Devenport (2009) by estimating the produced far field noise for fetches of discrete cuboidal and hemispherical surface roughness and comparing with experimental measurements.
- To determine the effect of multiple discrete roughness elements and their relative locations on the produced far field noise from each source location.
- To support or refute the discrete element roughness noise model composed of a pair of uncorrelated dipole sources aligned streamwise and spanwise to the flow direction.
- To provide the information needed to validate computational predictions of roughness noise.

Chapter 2 Experiment Description, Instrumentation, and Analysis Techniques

2.1 Anechoic Wall-Jet Facility

All data were taken in the Virginia Tech Anechoic Wall-Jet Facility shown in Figure 2-1. This tunnel was purpose-built in 2005 to study roughness noise. A wall-jet style tunnel was chosen because far field microphones could be easily placed outside of the flow to record radiated roughness noise. The tunnels aerodynamic and acoustic characteristics have been analyzed in several papers including Grissom (2007), Smith (2008), Alexander (2009), and Devenport *et al*. (2011).

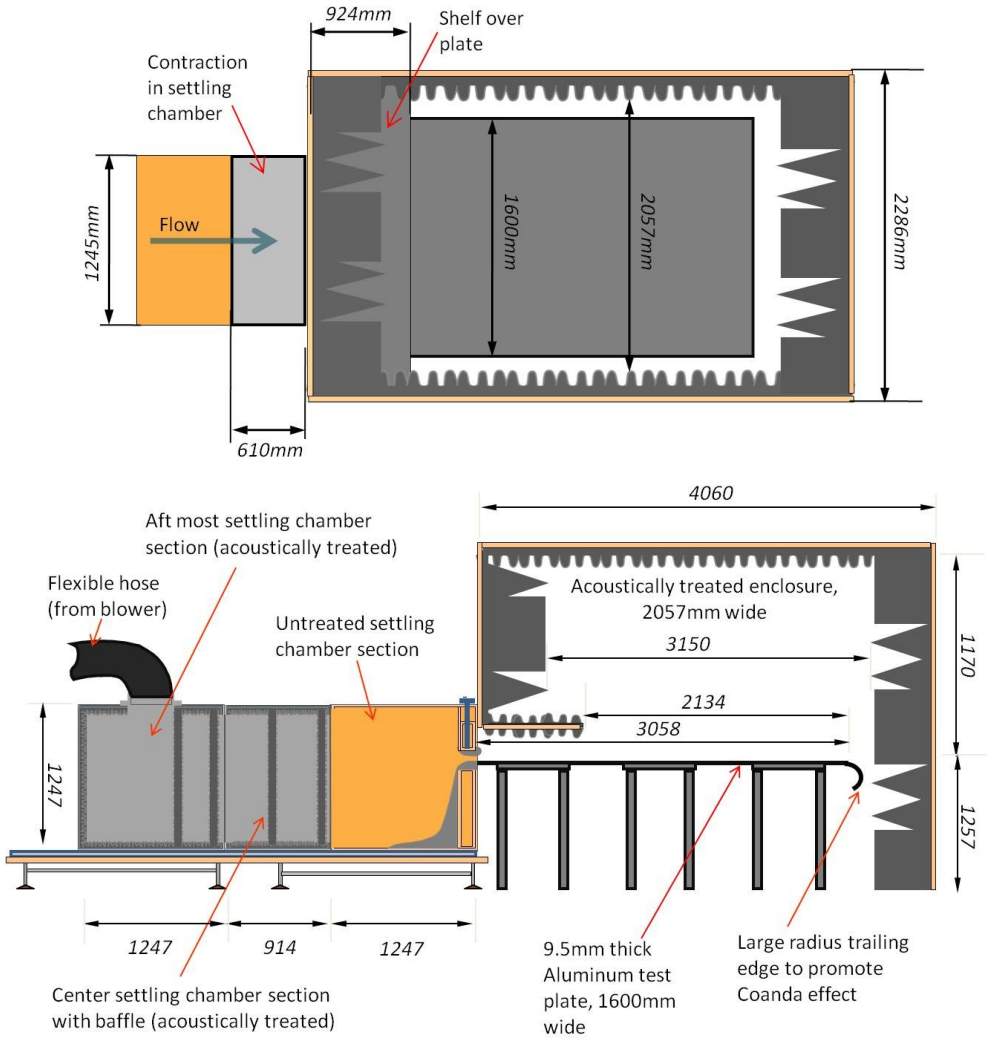

Figure 2-1. Schematic of Virginia Tech Anechoic Wall-Jet Facility (dimensions in mm)

The tunnel structure is made of MDF reinforced with 2" steel box beam. A Cincinnati Fan model HP-8D20 centrifugal blower powers the tunnel and is separated from the settling chamber by a flexible rubber hose. A SSA-8 discharge silencer is attached to the blower outlet to dampen acoustic vibrations through the hose. The settling chamber has several acoustic baffles that block direct noise radiation from the hose inlet through to the nozzle. The initial two thirds of the settling chamber are acoustically treated leading up to the nozzle section. The acoustic baffles are lined with fiberglass blankets to absorb acoustic energy.

A detailed view of the nozzle section can be seen in Figure 2-2. The bottom half of the nozzle is stationary and was designed using the relation in Fang *et al*. (2001) shown in Equation 2-1.

$$y = (h_1 - h_2)\left[1 - \frac{1}{X_m^2}\left(\frac{x}{L}\right)^3\right] + h_2 \qquad x < X_m$$

$$y = \frac{(h_1 - h_2)}{(1 - X_m)^2}\left(1 - \frac{x}{L}\right)^3 + h_2 \qquad x > X_m$$

Eq. 2-1

where h_1 is the nozzle exit height, h_2 is the initial height from the reference plane, X_m is the matched point, x is the distance from the nozzle, and L is the nozzle length. The values used for this contraction were h_1=0.681m, h_2=0, X_m=0.254m, and L=0.610m. The top half of the nozzle can be adjusted to vary the outlet opening height and therefore has no ramp leading to the nozzle exit. The nozzle height was kept at a constant 12.7mm for all reported data and was set by lowering the upper half of the nozzle down onto a set of gauge blocks. The top half of the nozzle was milled from two pieces of PVC joined at the center line of the plate. Its shape is a fusion of a quarter ellipse having a 3:1 ratio inside of the settling chamber spliced with a 38.1mm radius circular profile exit. The nozzle is 1206mm wide in the spanwise direction.

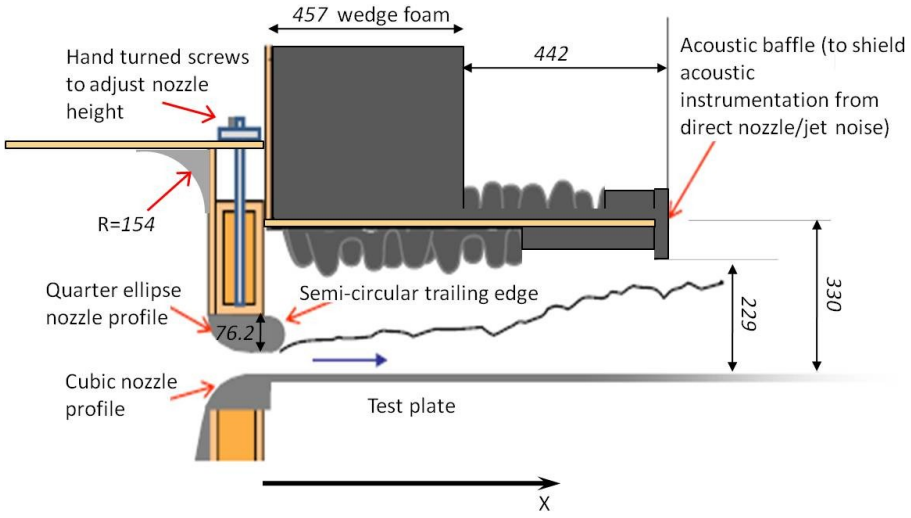

Figure 2-2. Detailed view of nozzle and shelf of acoustic enclosure (dimensions in mm)

Flow is accelerated through the nozzle exit and is exhausted over a flat aluminum plate 3058mm long and 1600mm wide enclosed in a removable acoustically treated chamber. As the flow travels along the plate the edge velocity reduces. All edges are kept far away from any regions of significant flow to

avoid the production of edge noise. The flow travels off of the end of the plate which is rounded to promote a Coanda effect where it diffuses out through the bottom of the acoustic enclosure.

The anechoic chamber has 457mm wedges on the fore and aft walls. The sidewalls and ceiling are covered in 89mm egg crate foam with a total thickness of 203mm. The bottom of the chamber is open and is approximately 70mm off of the floor allowing the flow to exhaust into the lab atmosphere. The acoustic enclosure has a shelf over the nozzle exit to block direct noise radiation from the nozzle to microphones placed above it. The shelf is made of MDF and is covered in the egg crate foam and 25.4mm thick flat foam. The wall-jet's maximum velocity occurs well below the bottom of the shelf which is 330mm above the plate.

Measurements presented in Grissom (2007) show that the operating background noise of the wall-jet is dominated by turbulence noise that scales with the eighth power of velocity. Further analysis of the background levels of the wall-jet are included in Section 2.5.1.3. Measurements in Grissom (2007) and Alexander (2009) show the tunnel is sufficiently quiet to measure roughness noise even from hydrodynamically smooth surfaces. A study of the acoustic response of the anechoic chamber in Alexander (2009) concluded that the chamber did not significantly influence far field measurements of a source emanating from the flat plate.

A schematic of a wall jet profile is shown in Figure 2-3. U_m is the profiles maximum velocity, $y_{1/2}$ is the height above the boundary layer where the velocity is half of its maximum value, δ is the boundary layer thickness, and δ_{90} is the height inside the boundary layer at which the velocity is 90% of its maximum value. Aerodynamic characteristics of the Virginia Tech Anechoic Wall-Jet can be approximated by relations similar to those found in Wygnanski *et al*. (1992) and Narasimha *et al.* (1973) shown in Equation 2-2.

$$\frac{U_m}{U_o} = 4.97\mathrm{Re}_j^{n+1}\mathrm{Re}_x^n$$

$$\frac{y_{1/2}}{b} = 0.0335 Re_j^{m-2} Re_x^m \qquad \text{Eq. 2-2}$$

$$\frac{\delta^*}{b} = 0.0156\mathrm{Re}_j^{p-2}\mathrm{Re}_x^p$$

where U_o is the nozzle exit velocity, Re_j is the Reynolds number based on nozzle exit height, Re_x is the Reynolds number based on the streamwise distance from the nozzle, δ^* is the boundary layer displacement height, and b is the nozzle exit height. These relations have been customized for this tunnel by curve fitting data from measured profiles at various locations downstream of the nozzle exit to determine the values of n, m, and p which are -0.512, 1.0451, and 0.888, respectively. These relations have been updated from Smith (2008) after taking aerodynamic measurements with the acoustic enclosure in place over the flat plate. The aerodynamic measurements in Smith (2008) were recorded with the acoustic enclosure removed. The updated results are reported in Devenport *et al*. (2011). The wall-jet profile is self-similar and therefore the boundary layer thickness and momentum thickness can be determined from the simple approximations given in Equation 2-3.

$$\delta \approx 15.4\delta^*$$

Eq. 2-3

$$\theta \approx 0.74\delta^*$$

Spanwise measurements in Smith (2008) show that the center 810mm of the flow remains two-dimensional as far as 1867mm downstream of the nozzle exit. All rough surfaces were placed well within the limits of this two-dimensional region. Rough surfaces were typically placed 1257mm downstream of the nozzle exit where U_m varies from 7-22m/s and δ varies from 21-16mm for nozzle exit velocities of 20-60m/s.

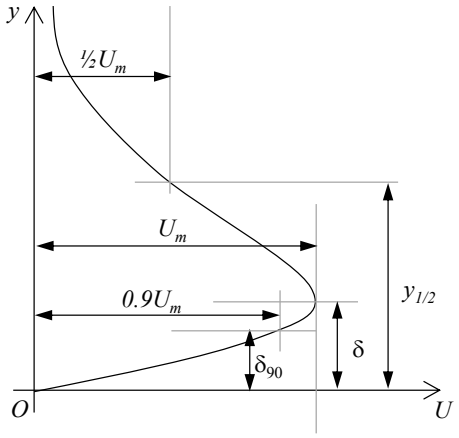

Figure 2-3. Wall-jet profile and definition of parameters

The coordinate system used to describe microphone and roughness locations is shown in Figure 2-4. The origin is located at the spanwise center of the nozzle exit plane. The *y*-axis is perpendicular from the plane of the plate, the *x*-axis is measured in the streamwise direction, and the *z*-axis completes the right-hand rule.

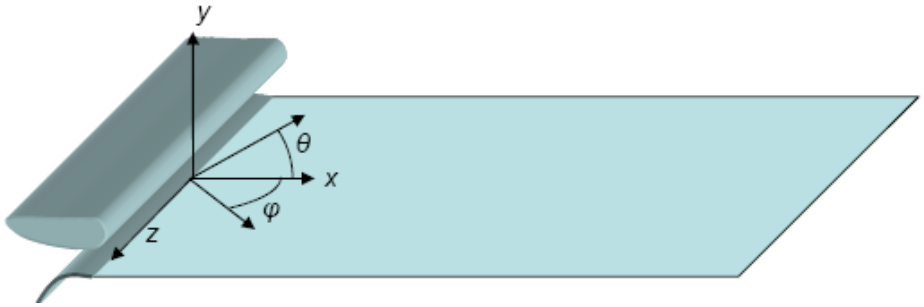

Figure 2-4. Coordinate system

2.2 Far Field Microphone Instrumentation

The following is a description of the single point far field measurement instrumentation. Discussion of the linear microphone array is in Section 2.4. Bruel & Kjaer's ½" free-field microphones type 4190 were used to record the far field noise produced by the rough surfaces. These microphones were used because of their high sensitivity and low noise floors and have a flat frequency response up to

20kHz. The microphones were used with a B&K Nexus 2690 A0S4 signal conditioning amplifier. The signals were then high-pass filtered at 250Hz using a Krohn-Hite model 3364 filter to improve the digitized resolution of the frequency range where roughness noise was perceptible. An Agilent E1432 16-bit digitizer was used with Agilent Vee Pro data acquisition software. Data were recorded at 51200Hz with a digital anti-aliasing filter. Frequency spectra are the result of 1000 averages of 2048 samples each. Microphone calibrations were completed frequently using a Bruel & Kjaer type 4228 pistonphone.

Microphones were placed in various positions around the acoustic chamber using microphone holders with small cross sectional areas that were attached to acoustically treated scaffolding described in detail in Alexander (2009) and Rasnick (2010). A typical arrangement is shown in Figure 2-5. The scaffolding is made from 80/20 beams and is securely attached to the legs that support the flat plate of the wall-jet. The scaffolding stands vertically on either side of the plate and then has two horizontal bars that extend over the plate. Microphones were attached to the 80/20 bar and therefore could be easily positioned anywhere in the chamber free from any vibrations that may be present in the structure of the acoustic enclosure. Since many microphone locations were used during the experiment, the exact location of the microphones will be presented with the corresponding data.

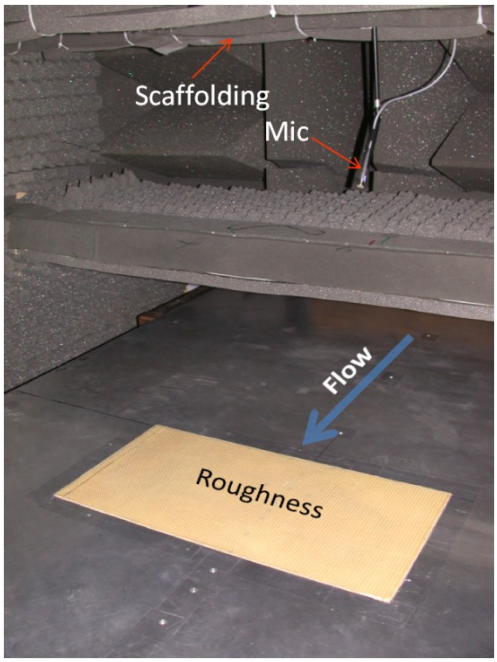

Figure 2-5. Typical far-field microphone arrangement

2.3 Wall Pressure Microphone Instrumentation

Sennheiser type KE-4-211-2 electret microphones were used to record wall pressure fluctuations. These microphones have a 1mm diameter sensing area and have a flat frequency response out to 10kHz within 1dBm. Their nominal factory sensitivity is 10mV/Pa. The microphones were used with 5V DC power supplies and 2.5 gain amplifiers designed in-house and described in Mish (2003). The microphone pinhole size was reduced to 1/4mm using 5.1mm diameter circular cut-outs of 0.26mm thick brass shim stock with 1/4mm holes drilled through the centers. These pieces were then super glued to the tops of the Sennheiser microphones. A modified Sennheiser microphone is shown in Figure 2-6. The

modified pinhole allowed for higher frequency measurements without contamination due to spatial averaging over the original larger diameter sensing area.

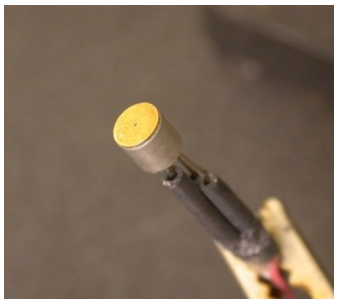

Figure 2-6. Sennheiser KE-4-211-2 microphone with a brass 1/4mm pinhole

The Sennheiser microphones were calibrated in the anechoic chamber of the wall-jet tunnel. The calibration set-up is shown in Figure 2-7. The flat plate was covered with 25.4mm thick melamine foam that dampened acoustic reflections from the large flat surface. A University Sound model ID60C8 speaker was positioned on the shelf of the chamber and was driven with a Carver power amplifier model TFM-6CB which was provided a white noise signal by an Agilent VXI data acquisition system. Microphones were placed on a short speaker stand with a small cross-sectional area approximately 2m across the chamber on the end of the plate. A 1/8" Bruel & Kjaer type 4138 microphone was first used to record the white noise signal for reference. The Bruel & Kjaer microphone was calibrated itself before each measurement using a B&K type 4228 pistonphone. The 1/8" microphone has a flat frequency response up to 140kHz and was used with a Nexus 2690-A-OS2 signal conditioning amplifier. The modified Sennheiser microphone was then placed in the same position as the reference microphone and the white noise recorded again. Data for both microphones was recorded at 51200Hz by an Agilent E1432 16-bit digitizer and are the result of 1000 averages of 2048 samples. The calibration is the result of dividing the measured voltage response of the Sennheiser by the measured pressure values recorded by the calibrated 1/8" B&K microphone. To reduce uncertainty, a frequency averaging scheme like that employed in Smith (2008) and Alexander (2009) was used to smooth the Sennheiser calibration. The calibration below 800Hz was assumed to be the average value between 500Hz and 800Hz. From 800-2000Hz, $1/24^{th}$ octave bands were averaged centered on each frequency. Above 2kHz, the calibration was averaged on $1/12^{th}$ octave bands.

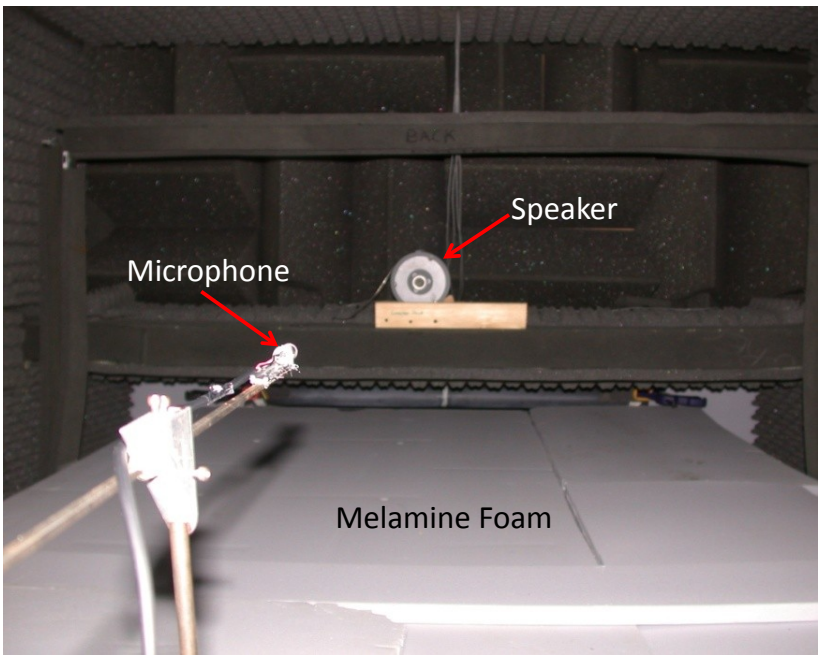

Figure 2-7. Wall pressure microphone calibration arrangement

Figure 2-8 shows the effect of the smaller pinhole size on the response of the Sennheiser microphone. The smaller pinhole reduces the sensitivity of the microphone at higher frequencies but is a necessary adjustment for the wall pressure measurements since the pressure fluctuations travel across the face of the microphone and not perpendicular to it. There is also a resonant frequency range 2-5.5kHz where the microphone actually becomes more sensitive to pressure fluctuations just before the steep polynomial decline in sensitivity.

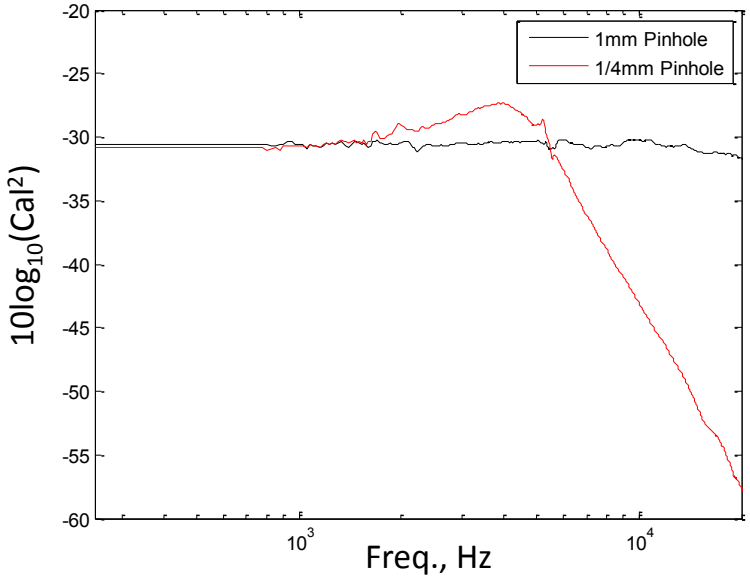

Figure 2-8. Sennheiser calibration with a 1mm and 1/4mm pinhole

Figure 2-9 shows a diagram of the wall pressure microphones installed in the plate of the wall-jet. During measurements the microphones were placed through nylon bushings that increased the outer diameter of the microphone in order to securely fit into 9.5mm holes drilled through the flat plate of the wall-jet. The microphones were pushed up through the bottom of the plate with the face of the nylon bushing flush with the wall. The microphones were adjusted so that the brass microphone face was either flush with the wall or, if roughness was present, with the substrate of the rough surface.

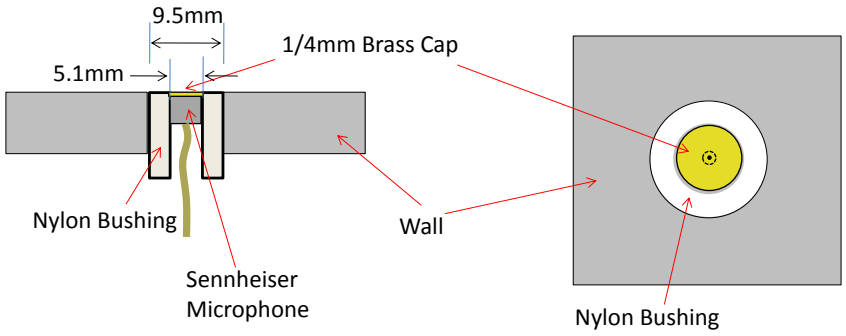

Figure 2-9. Diagram of Wall Pressure microphone installation

Wall pressure measurements were recorded using an Agilent Vee Pro data acquisition system along with a 16-bit E1432 digitizer. Data were collected at 51200Hz and spectra are the average of 1000 records of 2048 samples each.

2.4 Microphone Array Instrumentation

Figure 2-10 and Figure 2-11 show a 36-sensor linear microphone array designed specifically for this study. The same high sensitivity ½" B&K 4190 microphones used for single point far field measurements were used for the microphone array. The microphones were placed as close together as possible with a spacing 15.1mm center to center. This kept the aperture of the array small so that the array could be placed in various regions of influence of the produced roughness noise. In particular was the desire to place the array in regions dominated by the spanwise or streamwise aligned dipoles produced by the roughness. The linear array allowed for measurements on axes that would entirely isolate either the spanwise or streamwise dipoles.

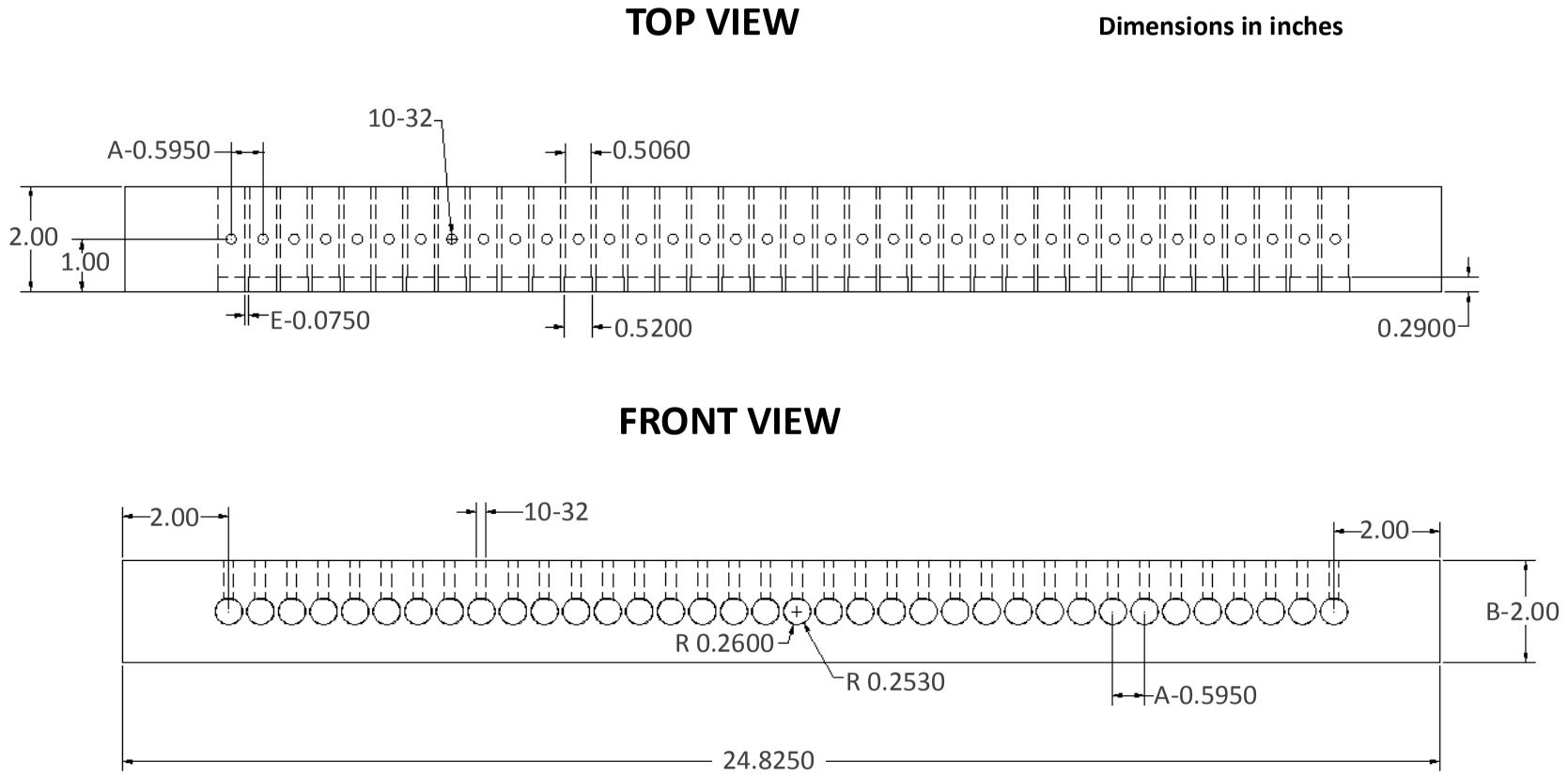

Figure 2-10. Diagram of linear microphone array

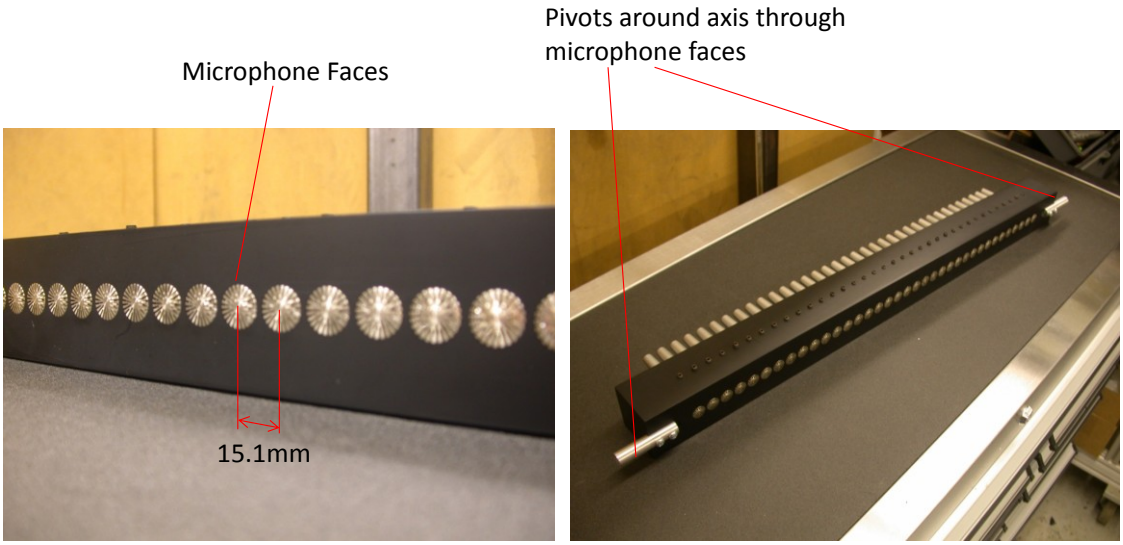

Figure 2-11. Linear Microphone Array

The array structure was assembled from a single Delrin block with aluminum pins inset into the face on either side. The microphones fit through precisely drilled holes in the Delrin and were held snug with Nylon set screws. The microphone faces were flush with the face of the Delrin. The array was suspended by the end pins using two aluminum mounts that attached to the 80/20 scaffolding in the tunnel. The array would then hang 220mm below the scaffolding. The receiving angle of the array could be adjusted to point directly at the noise source on the plate.

Figure 2-12 shows several arrangements of the microphone array in the anechoic chamber. The array was positioned in four separate locations which will be referred to as Array Positions 1-4 as labeled. The first location was on the edge of the plate outside of the flow. The array was resting on the aluminum plate with the middle of the array centered on the leading edge of where the roughness elements were placed, x=1257mm, so that the position of individual sensors only varied in the x-dimension. This location should be dominated by noise from the theoretical spanwise dipole of a roughness source. The second location was above the shelf of the anechoic chamber suspended from the 80/20 scaffolding. This position evenly distributed the microphones on either side of the roughness element so that the microphone positions varied in the z-dimension only. This array position would record noise dominated by the streamwise dipole. The last two locations were also suspended from the 80/20 frame directly above the spanwise center of the plate at x=1257mm with the axis of the array aligned spanwise and then streamwise. Measurements of the sensor locations at each array position were recorded using a FaroArm Fusion coordinate measuring machine. The locations of the array center for the four positions are given in Table 2-1.

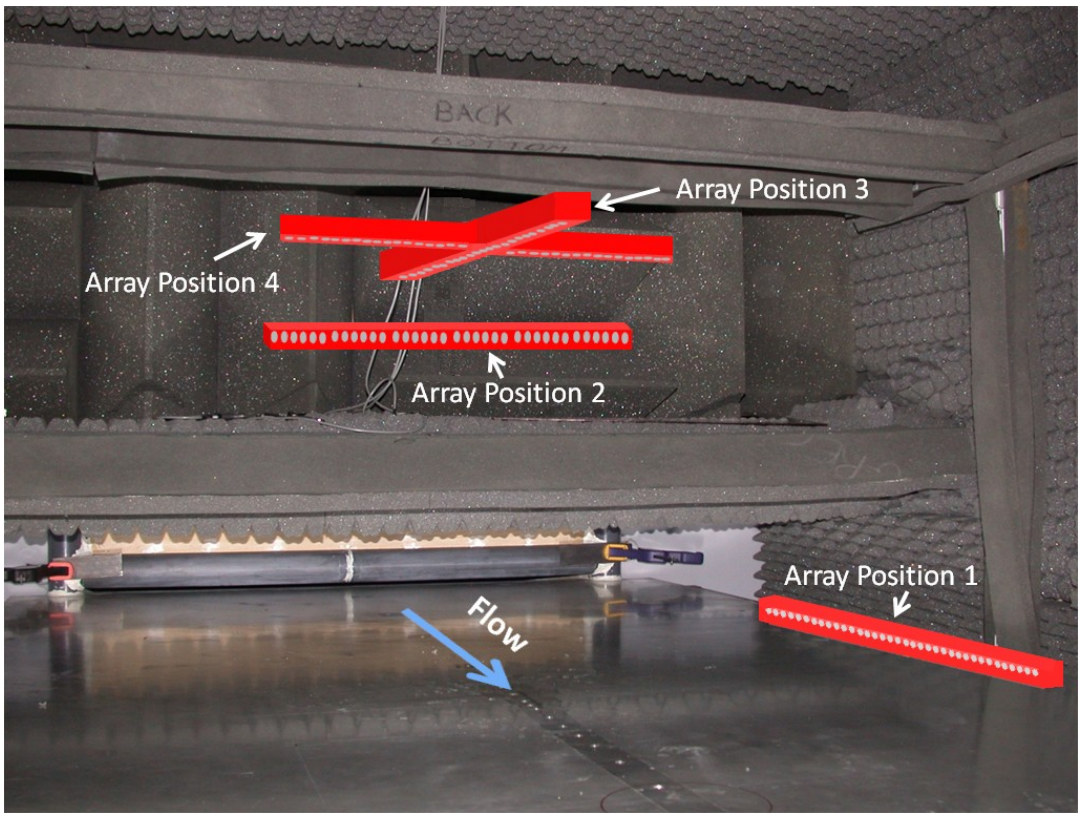

Figure 2-12. Microphone Array Positions

	x, mm	y, mm	z, mm	Θ	φ
Array Position 1	1258	25.4	-715	0°	90°
Array Position 2	915	585	0	-56°	0°
Array Position 3	1366	626	0	-90°	-90°
Array Position 4	1257	597	-1	-90°	0°

Table 2-1. Locations of array center for the four measured positions

Data were collected from the array using the Bruel & Kjaer Pulse 14 Time Recorder platform along with six B&K 3050-A LXI six-channel modules with 24-bit A/D conversion. The modules were tied together with a NetGear ethernet switch. Data were sampled over 40s at 65536Hz. The final spectra are the average Fourier transform of 2560 to 5119 records of 1024 samples each. Before analysis, these narrow band spectra were frequency averaged over $1/10^{th}$ octave bands to reduce uncertainty and the recorded tunnel background noise was subtracted. Data from the microphone array were calibrated using single microphone measurements of roughness noise recorded from the same central point of the microphone array in Array Position 2. The procedure was used to eliminate a large scalloping effect due to the presence of the Delrin block surrounding the microphones. The calibration procedure involved multiplying the array measured cross-spectral matrix by the ratio of the single microphone autospectrum and array measured autospectrum of the roughness noise.

2.5 Array Data Processing Methods

Data from the array were analyzed using two main methods. A conventional beamforming method which assumes monopole sources was used to visualize the data while a least-squares method was used to separate and estimate the source strengths of the individual dipole noise sources.

2.5.1 Beamforming

2.5.1.1 Beamforming Algorithm

A conventional delay and sum beamforming method was used to visualize the data recorded at each microphone array position separately. Delay and sum beamforming uses the cross-spectral matrix of the recorded array data and the known locations of the microphone sensors. The phase and magnitude of the measurements are adjusted to account for the change in distance from each microphone to a focal point. The cross-spectral matrix is then summed. This procedure is then repeated for many locations over a defined focus area and the summations can be plotted producing a source map. Peaks occur in the source map when the cross-spectral matrix adds constructively indicating the location of a source. The summation and phase adjustment were completed using the matrix calculation from Tester & Glegg (2008) shown in Equation 2-4.

$$\vec{\mathbf{b}} = diag\left(\boldsymbol{G}_{inv}\boldsymbol{C}\boldsymbol{G}_{inv}^{H}\right) \qquad \text{Eq. 2-4}$$

where $\boldsymbol{C}$ is the background-subtracted cross-spectral matrix and $\boldsymbol{G}_{inv}$ is the inverse monopole transformation matrix or steering matrix which applies a magnitude and phase adjustment to the individual elements of the cross-spectral matrix for multiple focal points. The superscript H denotes the Hermitian transpose. The resultant $\mathbf{b}$ vector is the phase delayed and summed solution for all focal points.

The Green's function for the acoustic propagation of a monopole source at $\mathbf{y}_j$ to a sensor at $\mathbf{x}_m$ is shown in Equation 2-5.

$$G_{j,m} = \frac{e^{ikr_{j,m}}}{4\pi r_{j,m}} \qquad r_{j,m} = \left|\mathbf{x}_m - \mathbf{y}_j\right| \qquad \text{Eq. 2-5}$$

where k is the acoustic wavenumber and $r_{j,m}$ is the absolute distance between the microphone and source location. Therefore, the elements of $\boldsymbol{G}_{inv}$ are defined as in Equation 2-6.

$$G_{inv\ j,m} = r_{j,m}e^{-ikr_{j,m}}/r_c\sqrt{M} \qquad \text{Eq. 2-6}$$

where r_c is a reference distance and M is the number of microphones. A reference distance of 1m was used for all presented source maps.

2.5.1.2 Qualities of the Linear Array's Source Maps

Figure 2-13 shows a simulated measurement of a 10368Hz noise source located 1m away from the microphone array. The sensors of the linear microphone array only vary in the z-direction. Three point source images are shown in Figure 2-14 produced by steering the array over the highlighted areas. Plane A is contained in the x-z plane, Plane B is in the y-z plane, and Plane C is in the x-y plane. These source maps demonstrate the inability of the linear array to accurately locate sources outside of its orientation

axis. As the focal point moves along the array's axis there is a clear peak at the source location, but when the focal point moves closer and further away or perpendicular to the array's axis, the point source's location becomes uncertain. Further, to determine the source strength, the source maps must be integrated over a selected area of which the choice is often unclear. Therefore, sweeps through the two dimensional source maps along the array's axis, as shown in Figure 2-15, will often be used to compare results from several roughness types or flow conditions and only qualitative observations and comparisons will be made from the results.

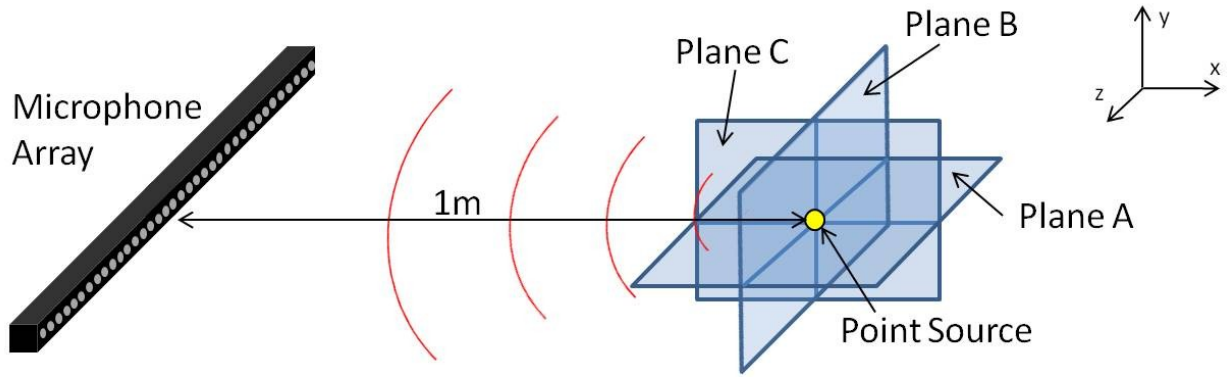

Figure 2-13. Point source simulation

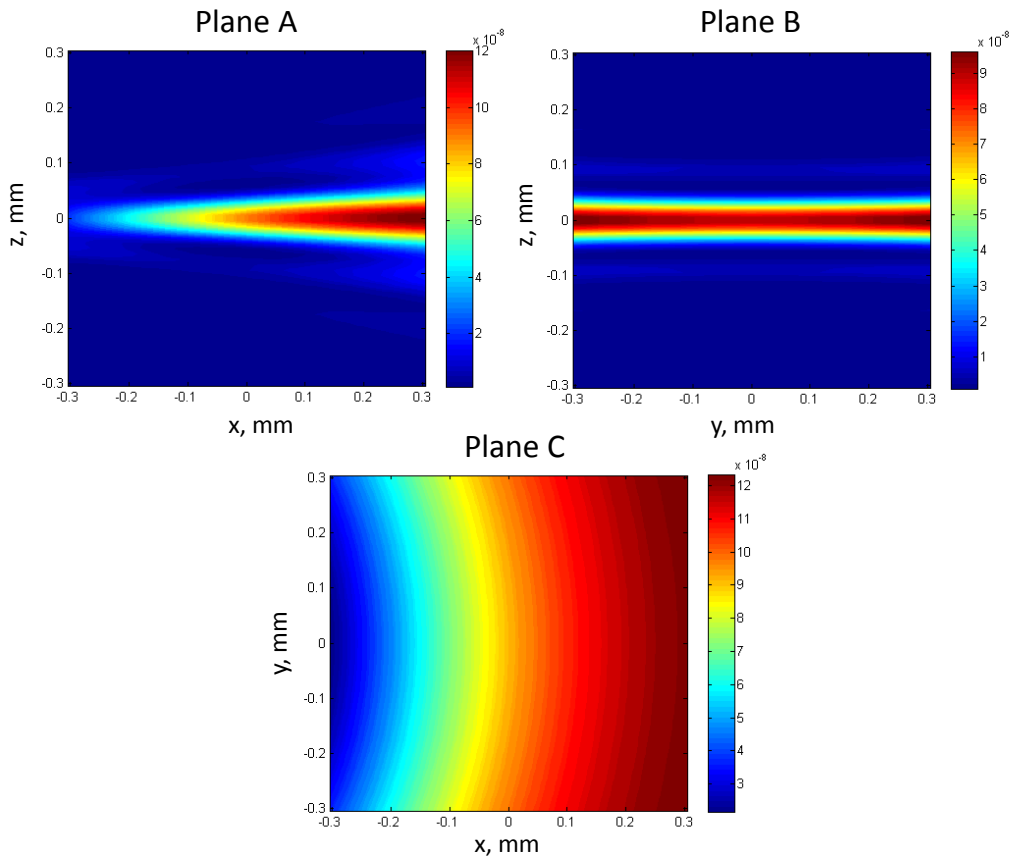

Figure 2-14. Source maps in Pa^2/Hz for 10368Hz point source located at (0, 0, 0)

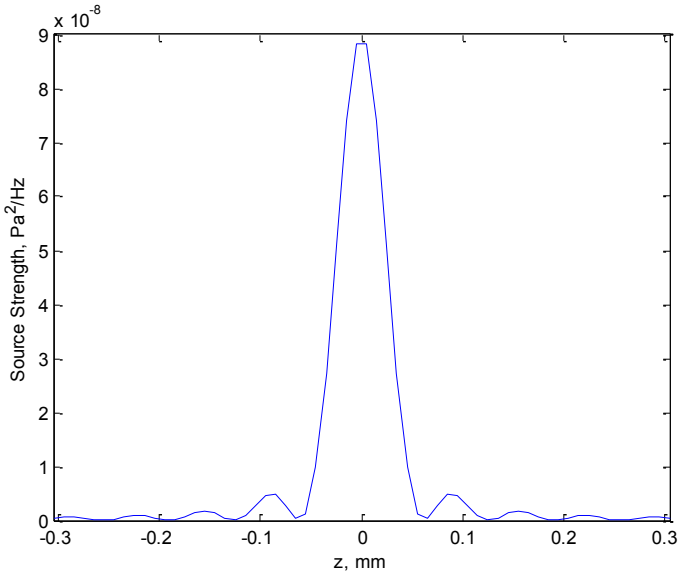

Figure 2-15. Sweep through source map of Plane A at x=0

Although the small aperture of the array allows it to be easily placed in a narrow region of noise dominated by a single lobe of the directionality field, it limits the array's ability to distinguish between multiple sources especially at lower frequencies where the main lobe peak of a beamformed source becomes wider. Figure 2-16 displays simulated source maps at two different frequencies, 3008Hz and 10368Hz, generated by focusing on Plane A of Figure 2-13 again this time with two sources centered around (0,0,0) separated by 0.1m on the *z*-axis. At the lower frequency the two sources appear as one and at the higher frequency dual peaks are visible. The array's application in this study required measurements of deterministic surfaces with elements as close as 5.5-16.5mm. Therefore, individual sources produced by roughness elements will not be distinguishable from one another within the measured frequency range, but general trends can be observed over the entire roughness fetch areas.

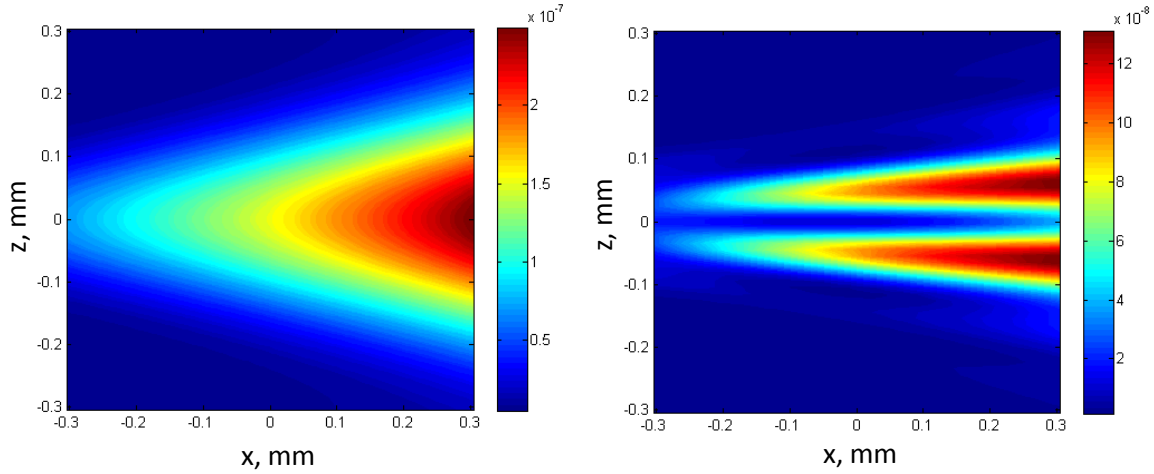

a) **b)**

Figure 2-16. Source maps of two sources located at (0.05, 0) and (-0.05, 0) at a) 3008Hz and b) 10368Hz

2.5.1.3 Background Subtraction Method

Background noise measurements of the tunnel were made at each array position and subtracted from the recorded roughness noise data. The background and roughness noise were both averaged over 1/10th octave bands before subtraction to reduce uncertainty. The background noise as recorded from each array position at 10368Hz with a nozzle exit velocity of 60m/s is shown in Figure 2-17. These source maps are focused at the location rough surfaces were placed on the plate. Array Position 1 shows the background noise predominantly coming from the direction of the nozzle exit. This is the only microphone array position that has a direct line of sight to the nozzle. Array Position 2 which is shielded by the shelf of the wall jet has the lowest recorded background noise levels. The background noise from this position is dominated by turbulence noise and shows the spanwise variation of the noise. Due to the positioning of the array's sensors, the array does not have sufficient resolution to conclude the location of the peak source strength in the *x*-direction. There is an asymmetry in this source map showing the negative *z*-direction to be slightly louder. The same result is viewed in the spanwise variation from Array Position 4. A similar asymmetry was recorded in the aerodynamic properties by Morton (2011) using a quadwire probe and is due to the slight spanwise variation of the wall-jet flow. The effect of this flow variation on the recorded noise is discussed in Chapter 5 along with the presentation of the beamformed

data. Array Position 3 shows the background noise coming from the direction of the nozzle exit at this position. The peak of the noise occurs around x=1220mm, but the general trend of the source map is an increase in the direction of the nozzle. This peak may be an effect of the shelf, which was shown to increase the growth of the mixing layer by 25% in Devenport *et al.* (2011), and the noise from the nozzle exit.

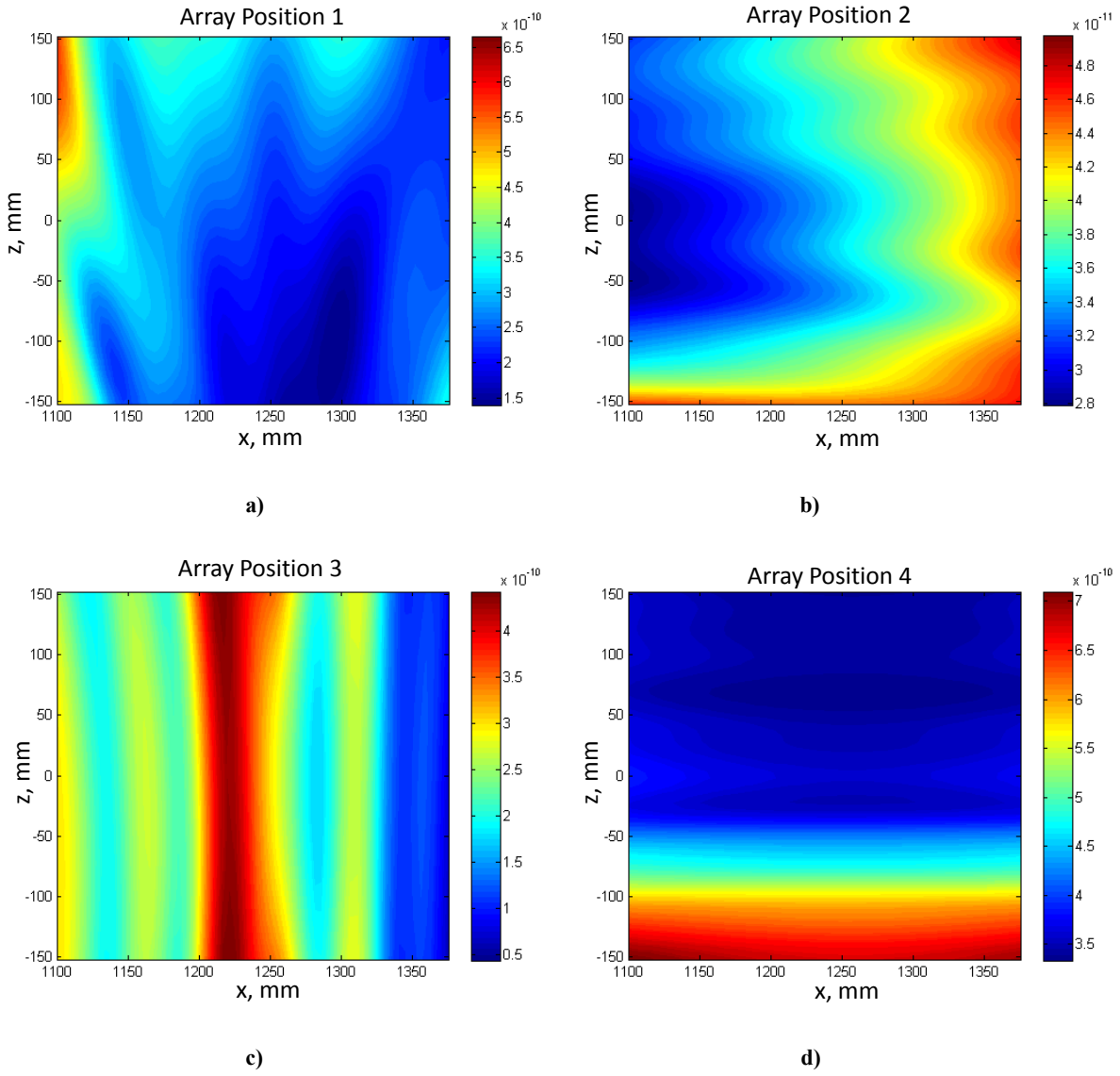

Figure 2-17. Background noise as recorded from each array position at 10368Hz and U_o=60m/s

Figure 2-18 shows a measurement of a single 3mm cubic element with and without the background noise subtracted as recorded from Array Position 4 at 10368Hz. This displays the clear improvement of the measurement and isolation of the noise produced by the roughness element alone. This also shows the need for the microphone array to isolate the noise produced by the roughness element from that of the background of the tunnel. The background noise is significantly stronger than that produced by the cube as recorded from this array position, but after subtraction the source map clearly identifies the roughness noise source. Using the background-subtracted microphone array data, the source

strengths of individual roughness elements can be determined. This source strength analysis will be discussed in Section 2.5.2.

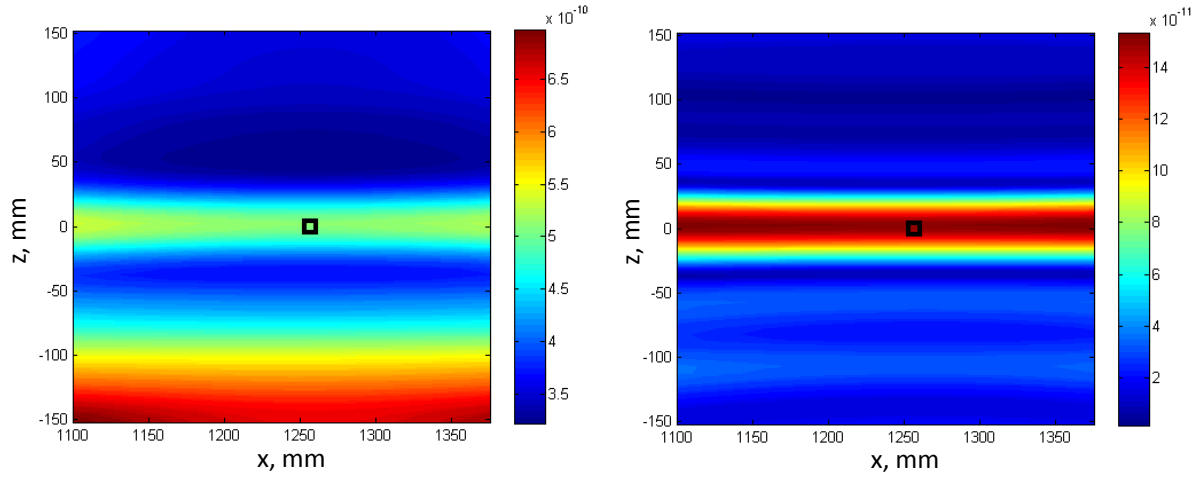

Figure 2-18. Measurement of single cubic element from Array Position 4 a) without b) and with the background noise subtracted

2.5.1.4 Acoustic Source Convection Correction

Preliminary array measurements of roughness noise recorded in the wall jet tunnel at Array Position 1 showed peak source locations downstream of the physical location of the roughness. To study this phenomenon, array measurements were made of white noise radiating from four locations on the flat plate which bound the region where rough surfaces were placed. The white noise was created using an Agilent VXI data acquisition system which provided a white noise signal to a Koss SparkPlug SP3 earbud speaker. This speaker was positioned from the bottom of the plate through each one of four 9.5mm diameter holes separately so that the noise was projected away from the flat surface and recorded by the microphone array in the far field. Data were recorded at all four array positions and nozzle exit velocities ranging from 20-60m/s. Figure 2-19 shows a sweep through the beamformed source map with the array at Array Position 1 measuring a source at x=1259mm, z=40mm for nozzle exit velocities 20-60m/s. The source appears to convect as far as 30.1mm downstream at the highest velocity. To accurately determine the convection distances for each experimental condition, the measured cross-spectral phase was compared with the ideal phase distribution for a source at the known location. The RMS error between the measured and ideal phase were adjusted to a minimum by manipulating the ideal phase via numerically shifting the x-location of the simulated ideal source. This method worked well for Array Position 1. Convection estimates could not be determined for Array Positions 2 and 4 because the array was oriented spanwise. Therefore, the array's x-dimension resolution was poor and the error never produced a clear minimum. For Array Position 3, the acoustic propagation vector from source to array occurred in only a short region of significant flow velocity. Therefore, the estimated source convection distances are not as large as the Position 1 results. The tabulated convection results for Array Position 1 and 3 are given in Table 2-2 and Table 2-3, respectively.

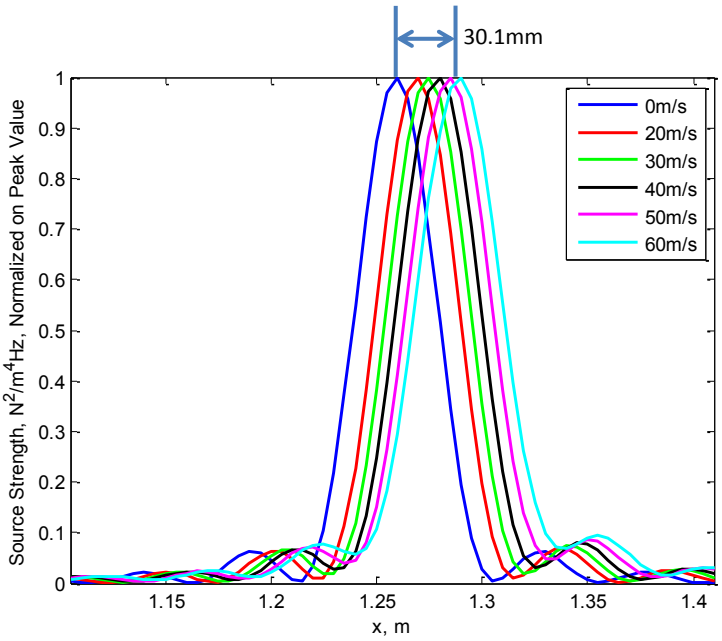

Figure 2-19. Sweep through 10368Hz source map at z=37.5mm showing convection effect

Source Position, mm		U_o, m/s				
		60	50	40	30	20
x=1259 z=-43	Convection Distances, mm	25	21.4	17.2	13.3	9.1
x=1259 z=40		30.1	25.2	20.2	15.4	10.2
x=1358 z=40		27.1	22.4	17.7	12.5	7.5
x=1357 z=-42		23.5	19.9	16	12	7.8

Table 2-2. Source convection results for Array Position 1

Source Position, mm		U_o, m/s				
		60	50	40	30	20
x=1259 z=-43	Convection Distances, mm	14.1	12	10.4	8.3	6.4
x=1259 z=40		15.1	12.2	10.3	7.9	6
x=1358 z=40		11.6	9.6	7.9	5.9	3.9
x=1357 z=-42		12.8	10.8	8.7	6.7	4.8

Table 2-3. Source convection results for Array Position 3

These convection results were consistent with simple estimates due to the local velocity shown in Equation 2-7.

$$d = \frac{r}{c_\infty} U_m \qquad \text{Eq. 2-7}$$

where r is the distance the source vector is immersed in significant flow velocity, c_∞ is the speed of sound, and U_m is the local maximum velocity. Referring to the aerodynamic results of Smith (2008) and Devenport *et al.* (2010), at Array Position 1operating conditions for the 60m/s case were approximately r=440mm and U_m=22m/s, yielding a convection distance of 28mm, within a few millimeters of the observed distances.

To correct for the convection effect, the source maps produced from measurements at Array Position 1and Array Position 3 were skewed using the measured convection distances calculated from the white noise calibrations. Convective distances were determined for every point in the source maps by interpolating and extrapolating the results over the entire focus area. The calculated convective distances were subtracted from the *x*-locations of the source map to realign the figures as if no flow was present. Since there was no observed source convection for Array Positions 2 and 4 these maps were not altered. An original and modified source map are shown in Figure 2-20 for the measurement of roughness noise from a single 3mm cubic element located at *x*=1257, *z*=0 with a nozzle exit velocity of 60m/s. The original map displays the source downstream of the physical location while the modified picture correctly identifies the source location in the *x* direction.

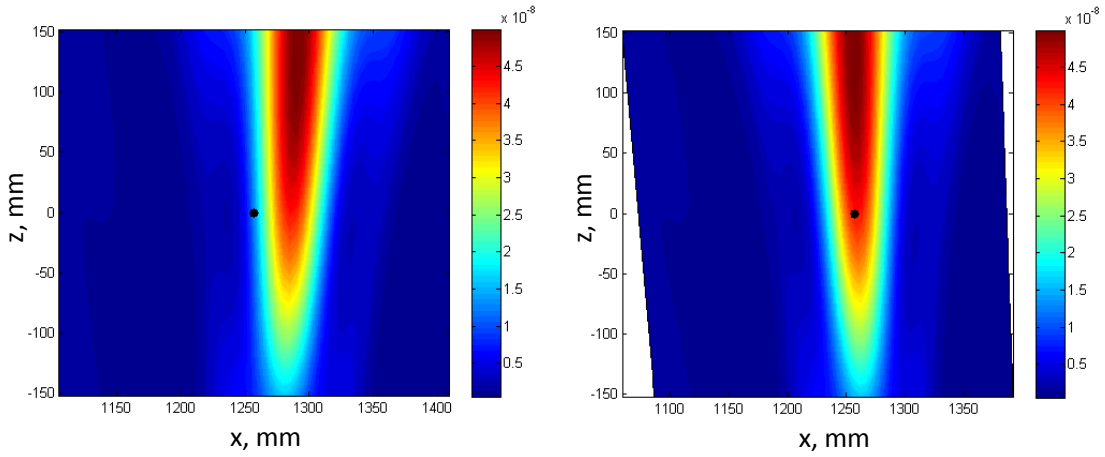

Figure 2-20. Source maps from Array Position 1 for a single 3mm cube located at x=1257, z=0 (black dot) at a nozzle exit velocity of 60m/s a) unaltered b) and corrected (Pa^2/Hz)

2.5.2 Least-Squares Source Strength Analysis

2.5.2.1 Least-Squares Source Strength Calculation

Figure 2-16 shows that the linear microphone array's resolution limits its potential to distinguish the strength of multiple sources spaced closely together. This was the motivation to investigate a least-squares approach of source strength estimation. A novel least-squares method was developed to separate and estimate the source strengths of individual elements in multi-element fetches of discrete roughness.

Derivation of the least-squares method begins by writing the recorded pressures at a single sensor as the summation of the response due to individual sources in Equation 2-8.

$$P_m = q_1 G_{m,1} + q_2 G_{m,2} + \cdots q_j G_{m,j} \quad \text{Eq. 2-8}$$

where P_m is the acoustic pressure recorded at microphone m, q_j is the source strength of source j, and $G_{m,j}$ is the Green's function for the acoustic propagation of source j to sensor m.

For this analysis, each roughness element was assumed to radiate uncorrelated spanwise and streamwise aligned dipoles with half-space Green's functions defined by Equation 2-9.

$$G_{m,j} = \frac{ikcos\theta_{m,j} e^{ikr_{m,j}}(1+i/kr_{m,j})}{2\pi r_{m,j}} \qquad cos\theta_{m,j} = \hat{\mathbf{x}} \cdot (\mathbf{x}_m - \mathbf{y}_j)/r_{m,j} \quad \text{Eq. 2-9}$$

where $\hat{\mathbf{x}}$ is the dipole directionality unit vector. The cross-spectrum between two microphones, m and n, can be calculated using Equation 2-8 multiplying P_m by the conjugate of P_n. As the signals from the uncorrelated sources are averaged, the cross source terms disappear leaving only a linear combination of the source components as in Equation 2-10.

$$\overline{P_m P_n^*} = \overline{q_1^2} G_{m,1} G_{n,1}^* + \overline{q_2^2} G_{m,2} G_{n,2}^* + \cdots \overline{q_j^2} G_{m,j} G_{n,j}^* \quad \text{Eq. 2-10}$$

This equation can be rewritten for all terms in the cross-spectral matrix as:

$$\overrightarrow{\boldsymbol{G}_{pp}} = \boldsymbol{G}_{GG} \vec{\boldsymbol{Q}} \quad \text{Eq. 2-11}$$

where $\vec{\boldsymbol{Q}}$ is a vector of mean squared source strengths, $\boldsymbol{G}_{GG}$ is a transform matrix of cross-spectral Green's functions, and $\overrightarrow{\boldsymbol{G}_{pp}}$ is the measured cross-spectral matrix put into vector form. The source strengths can then be calculated using a least-squares algorithm with a non-negative solution constraint.

2.5.2.2 Comparison with Nelson & Yoon (2000)

This method differs from previous least-squares methods in that it assumes the sources are uncorrelated. Nelson & Yoon (2000) developed a least-squares method for solving for the cross-spectral source strength matrix as shown in Equation 2-12.

$$\boldsymbol{Q} = \boldsymbol{G}^{+} \boldsymbol{G}_{pp} \boldsymbol{G}^{+H} \quad \text{Eq. 2-12}$$

where $\boldsymbol{Q}$ is a matrix of source strengths, $\boldsymbol{G}$ is a transfer function matrix with dimensions mxj, and $\boldsymbol{G}_{pp}$ is the cross-spectral matrix. This method leads to solutions in the off-diagonal terms of the matrix $\boldsymbol{Q}$ which are known to be zero for uncorrelated sources.

A simple comparison between methods displays the weaknesses of a more general least-squares approach such as Nelson & Yoon (2000) to correctly determine the acoustic source strengths given conditions consistent for measurements of roughness noise sources. A simulated measurement is shown in Figure 2-21. Five sensors spaced 10mm apart are located 1m away from five white noise monopole sources in a similar arrangement in free-space. This simulation's dimensions are approximate to the roughness noise measurements that were taken in the anechoic wall-jet. The sources produce an

uncorrelated white noise that is measured by each sensor. Using the proposed method which assumes uncorrelated sources, the exact source strength solution is calculated for all sources and frequencies.

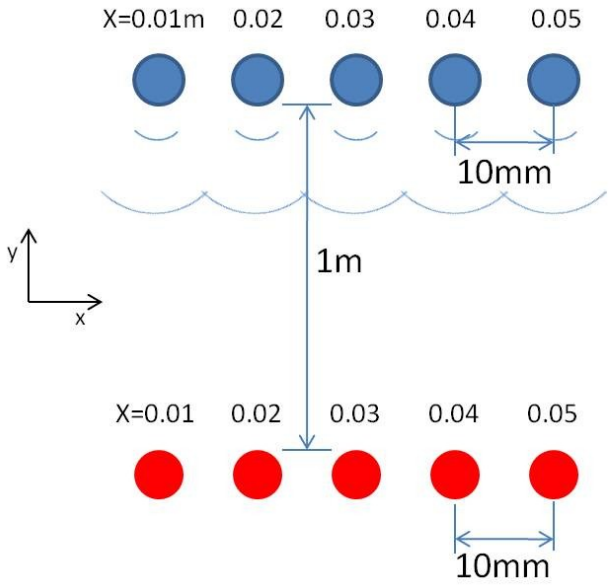

Figure 2-21. Simulated measurement of acoustic sources

Figure 2-22 shows the total percent RMS error in the source strength matrix calculation using Nelson & Yoon's (2000) formulation. The error increases towards lower frequencies giving values that are 100% off at 7kHz and steadily decreases with a slope of f^{-8}. If the simulation measurement and calculation is completed again for an increased source spacing of 100mm, the produced errors are over a million times smaller. This displays the dependence of the source spacing to wavelength ratio. These findings agree with Nelson & Yoon who also state some other geometric conditions that can adversely affect the solution. They conclude that their method works best with a geometrically similar arrangement of sensors and sources and with low sensor to source spacing. Unfortunately, these stipulations make use of their least-squares method impractical for this study.

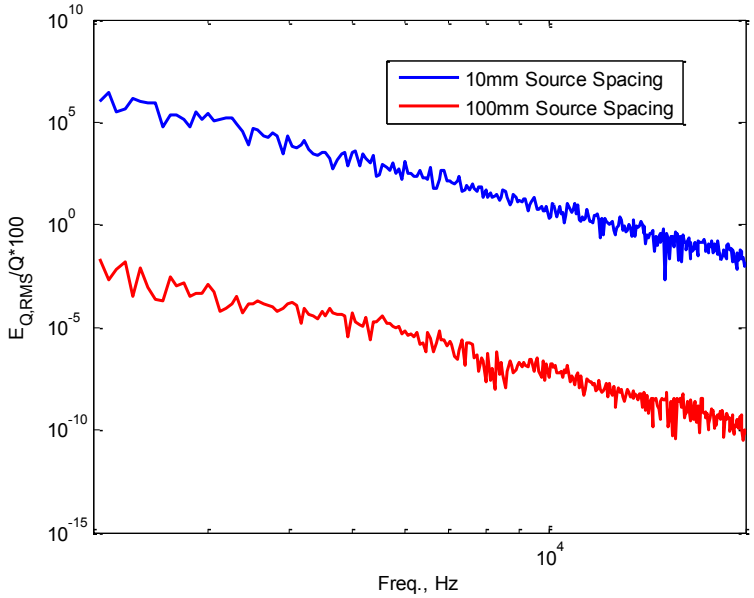

Figure 2-22. Percent RMS error of the calculated source strengths using Nelson & Yoon (2000)

The uncorrelated source method preferred in this study also enables the data taken from multiple array positions to be used in the same calculation. The transform matrix and vector of cross-spectral terms can be appended to include any number of independent equations because this least-squares method does not require cross-spectral terms between all of its components. The Nelson & Yoon (2000) method requires a full cross-spectral matrix of all input data. These data are unknown between measurements at different array positions restricting the calculation to only one array position at a time. Therefore, Nelson & Yoon's method was not considered during the analysis of the roughness noise data.

2.6 Rough Surfaces

Fetches of deterministic roughness were studied to analyze the produced far field noise dependence on surface geometry including element size, shape, and configuration. Fetches of 3mm hemispherical and cubic elements were used as well as fetches of 1mm hemispheres. All rough surfaces were placed starting at approximately 1257mm downstream of the nozzle exit where incoming aerodynamic conditions were as shown in Table 2-4 giving roughness height to boundary layer ratios of 5-18%.

U_o, m/s	δ, mm	δ^*, mm	θ, mm	U_m, m/s
20	20.9	1.36	1.01	7.5
30	19.1	1.24	0.92	11.1
40	17.9	1.16	0.86	14.8
50	17.1	1.11	0.82	18.4
60	16.4	1.06	0.79	21.9

Table 2-4. Aerodynamic characteristics at lead of roughness fetch

The rough surfaces were made of molded epoxy with a combination backing including a sheet of Kevlar for strength topped with a sheet of sketch paper that sealed the porous surface. The two-layer backing made the substrate, and therefore the outer perimeter step of the roughness sheet, 0.30mm thick. Far field noise and wall pressure measurements made with a molded smooth surface showed no increased pressure fluctuations due to the step perimeter. This is an improvement from the earlier study of Alexander (2009) whose noise and wall pressure results may have been influenced by the larger 1.2-1.6mm step perimeter around the tested deterministic roughness. Figure 2-23 shows the 3mm cubic and hemispherical elements molded on the Kevlar/paper backing.

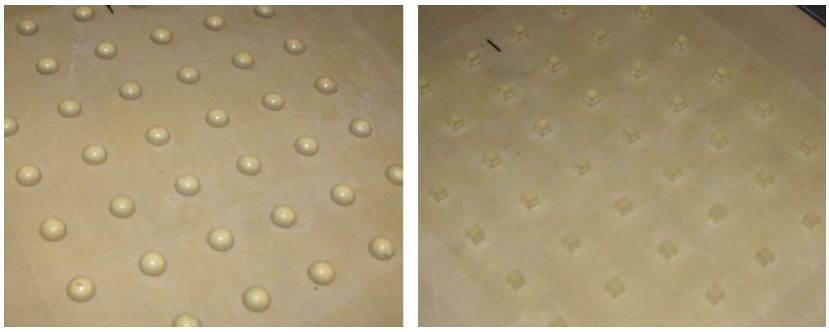

Figure 2-23. Molded 3mm hemispherical and cubic elements

The perimeters of the rough surfaces were taped to the plate using 0.08mm thick packing tape. This kept the flow from lifting the surface and filled the sharp corner of the step created by the boundary. Double sided tape was used on the underside of the 610x305mm fetches to keep the surfaces lying flat. For the wall pressure measurements, the area surrounding each microphone location was fixed using double sided tape to prevent the surface from fluttering. Many different combinations of fetch size and element size and shape were studied using various analysis techniques. Each will be described below along with the type of analysis conducted.

2.6.1 Single Element to 42 Element Fetches

Microphone array data were taken for fetches of 3mm cubic and hemispherical elements. The fetch sizes ranged from a single element to 42 element sheets arranged in six spanwise rows and seven streamwise columns. The microphone array measured cubic surfaces are shown in Figure 2-24. Similar measurements were made from hemispherical elements arranged in the 6x7, 6x5, 6x2, 6x1, and 1x1 configurations. The elements in these fetches were spaced 16.5mm center-to-center in a grid pattern. Each measurement was completed with the desired rough surface attached to the plate. The front center of the roughness fetches were placed in the same starting location of the plate (x=1257mm, z=0) for all measurements.

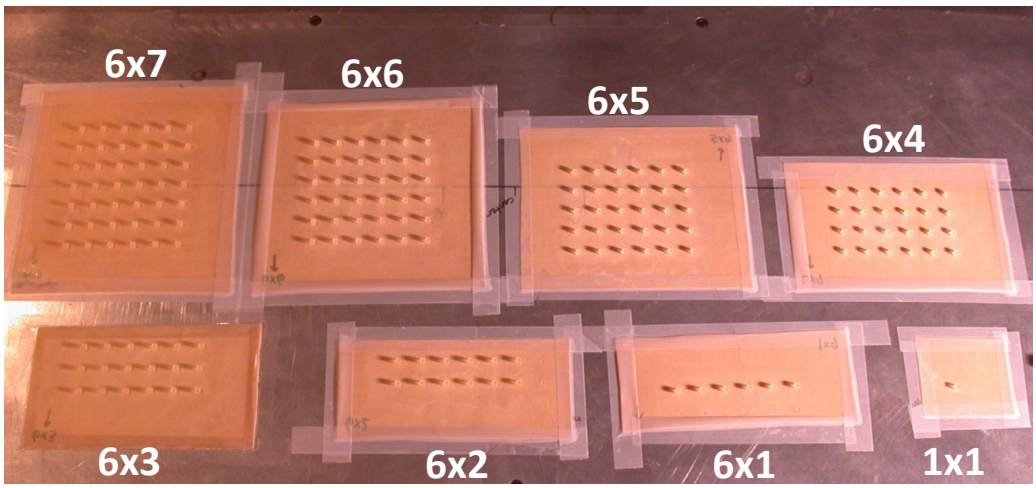

Figure 2-24. Arrangements of cubic element fetches

Wall pressure measurements and single point far field measurements were made separately inside the 42 element fetches by punching holes in the surface. Figure 2-25 shows a diagram of these measurement locations and their relative position to the roughness elements. Wall pressures were recorded at fourteen positions in the cubic element fetch and nine positions in the hemispherical element fetch. For these measurements, the surface was moved relative to a single microphone which was fixed in the wall at x=1358mm, z=-43mm. Therefore, the front spanwise center of the fetch's position varied from x= 1255-1366mm and z=-92.5-6.5mm. All holes at positions not being measured were covered with packing tape so as to not interfere with the measurement in progress. Table 2-5 and 2-6 give detailed descriptions of each wall pressure microphone location.

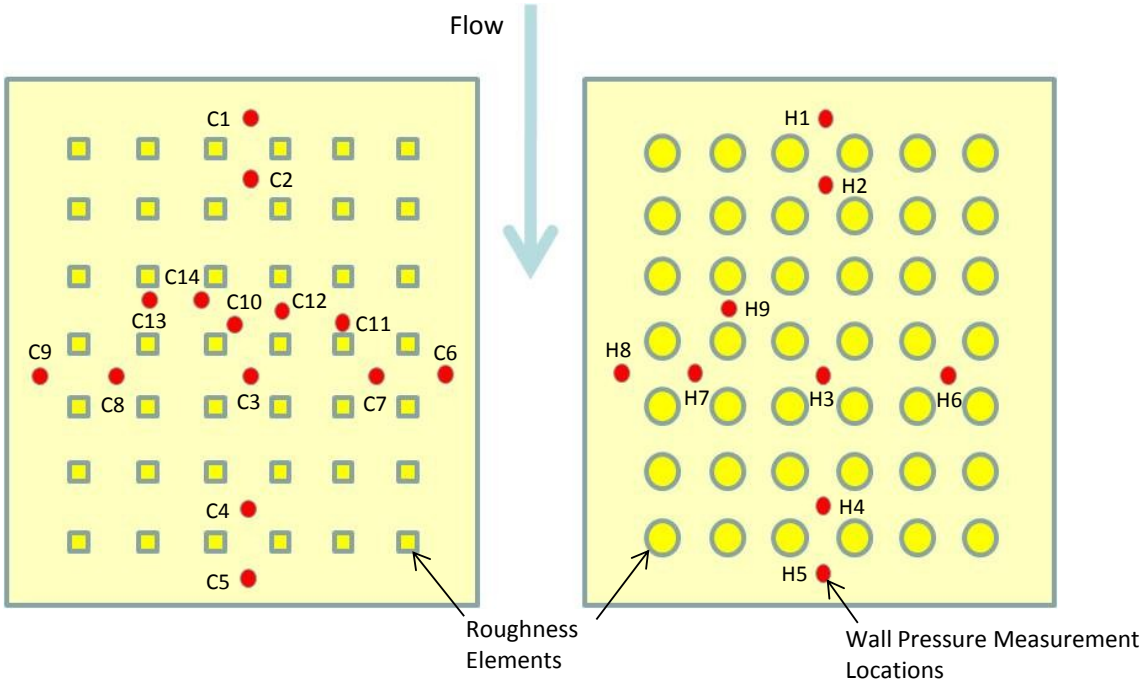

Figure 2-25. Wall pressure measurement diagram

	Location Description
C1	Centered 8.25mm upstream of elements
C2	Centered between elements
C3	Centered between elements
C4	Centered between elements
C5	Centered 8.25mm downstream of elements
C6	Centered between two rows 8.25mm outside of roughness
C7	Centered between elements
C8	Centered between elements
C9	Centered between two rows 8.25mm outside of roughness
C10	4.8mm upstream and 4mm to the right of the element center
C11	5.2mm upstream of roughness element center
C12	Centered between two elements
C13	4.8mm downstream of element center
C14	4mm downstream and 4.8mm left of the element center

Table 2-5. Description of wall pressure measurement locations inside the 3mm cubic element fetch

	Location Description
H1	Centered 8.25mm upstream of elements
H2	Centered between elements
H3	Centered between elements
H4	Centered between elements
H5	Centered 8.25mm downstream of roughness elements
H6	Centered between elements
H7	Centered between elements
H8	Centered between two rows 8.25mm outside of roughness
H9	Centered in-line streamwise between two elements

Table 2-6. Description of wall pressure measurement locations inside the 3mm hemispherical element fetch

2.6.2 610x305mm Fetches

Far field and wall pressure measurements were made for three different 610x305mm fetches of hemispherical elements. The first fetch was made of 3mm hemispheres spaced 16.5mm apart. There were a total of 703 elements with 19 spanwise rows and 37 streamwise columns. The second fetch was a similarly scaled fetch of 1mm hemispheres spaced 5.5mm apart increasing the number of rows and columns to 54 and 109, respectively. The third fetch was composed of 6209 randomly located 1mm hemispherical elements with a maximum spacing between two elements of 9.4mm. The element positions were exactly known but were distributed over the extent of the roughness fetch using the pseudo-random Mersenne Twister algorithm to generate values for the x and z locations. The locations of all the elements are given in Appendix A. The shorter dimension for all three fetches was aligned in the streamwise direction. Like the 42 element fetches, all wall pressure measurements were made from a single downstream location (x=1403mm, z=0) while the surface was moved in relation. The wall pressure was measured at only one location relative to the roughness elements in the random surface. This location, shown in Figure 2-26, was 163.5mm from the leading edge of the fetch and 25mm off of the spanwise center of the fetch in the $-z$ direction.

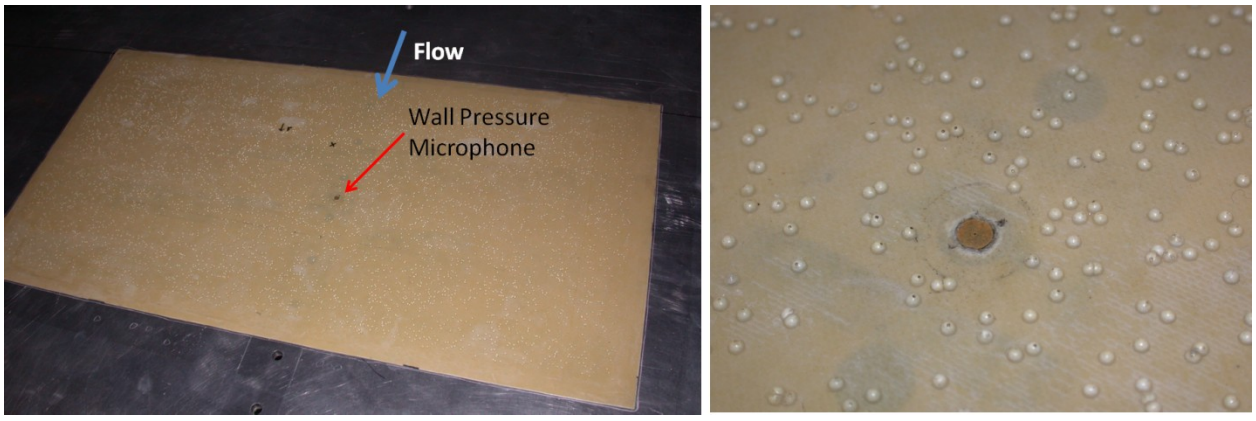

Figure 2-26. 1mm random hemispherical element array and detailed view of wall pressure microphone

The wall pressure was measured at four locations in the grid patterned 1mm hemisphere surface each with different relative positions to the nearest roughness elements. All four measurements were made between 143-148.5mm downstream of the leading edge and within the middle 15 spanwise columns of the roughness. Eight relative locations were measured in the 3mm hemisphere surface between the ninth and tenth spanwise rows 132-148.5mm downstream of the lead row of roughness. The wall pressure measurement locations for both grid patterned surfaces are shown in Figure 2-27. The locations are described in Table 2-7 and 2-8. Some of the wall pressure locations were less than a microphone radius away from the base of the nearest elements in the 3mm hemispherical element fetch. This was done by removing the conflicting element then installing the microphone flush with the substrate. The element was then reattached to the surface partially covering the brass face of the microphone. Figure 2-28 shows a detailed view of this microphone arrangement. Elements on the 1mm surface were not replaced if they conflicted with the microphone position. The elements were simply removed and the measurement taken without them. The missing elements are correctly omitted in Figure 2-27b.

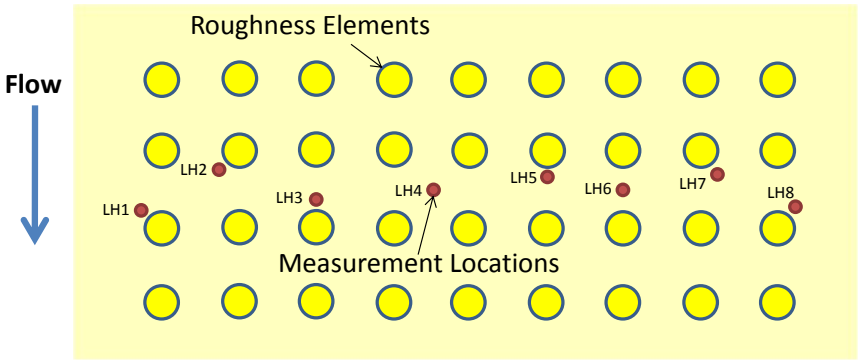

a)

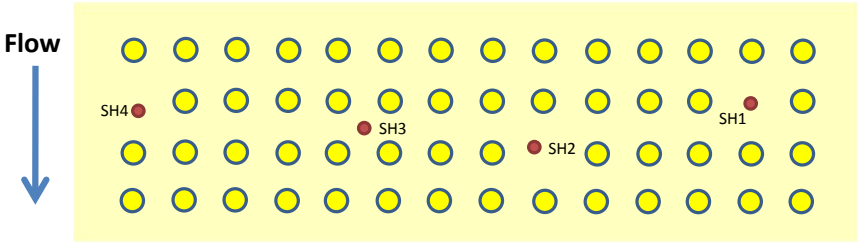

b)

Figure 2-27. Diagram of wall pressure measurement locations relative to the roughness elements of the a) 3mm hemispherical surface b) and the 1mm hemispherical surface

	Location Description
LH1	2.8mm upstream and 2.8mm to the left of the element center
LH2	2.4mm downstream and 3.2mm to the left of the element center
LH3	4.1mm upstream of element center
LH4	Centered between elements
LH5	4.3mm downstream of element center
LH6	Centered between two elements
LH7	3.1mm downstream and 2.7mm to the right of the element center
LH8	2.9mm upstream and 2.7mm to the right of the element center

Table 2-7. Description of wall pressure measurement locations inside the 610x305mm 3mm hemispherical element fetch

	Location Description
SH1	Microphone in location of roughness element
SH2	1mm upstream and 1mm to the left of the removed element center
SH3	Centered between elements
SH4	1mm downstream and 1mm to the right of the removed element center

Table 2-8. Description of wall pressure measurement locations inside the 610x305mm 3mm hemispherical element fetch

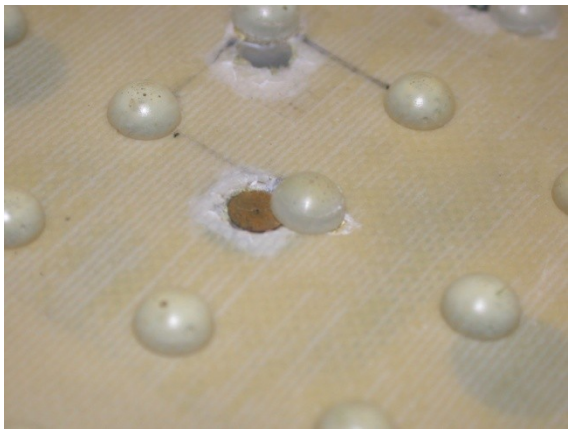

Figure 2-28. Detailed view of the wall pressure microphone configuration around a 3mm hemispherical element

Chapter 3 Roughness Wavenumber Analysis

Roughness noise is dependent upon the specific roughness geometry as observed in both Grissom (2007) and Alexander (2009). Therefore, the noise from roughness with different shapes will be unlikely to collapse using a simple inner or outer variable scaling even if the rough surfaces have equal roughness heights. Glegg & Devenport (2009) developed a relationship between the roughness geometry and the radiated far field noise. This relationship is dependent on the wavenumber content of the surface and its slope. The following section derives analytical solutions to the wavenumber content of the surface and slope for the hemispherical and cuboidal roughness used in this study. These solutions are used to make preliminary far field noise estimations. The noise from a 40 grit fetch of roughness is predicted and compared to the results presented in Alexander (2009).

3.1 Discussion of the *"Unified Theory of Roughness Noise"* from Glegg & Devenport (2009)

The generation of roughness noise as described in Glegg & Devenport (2009) is the result of interaction between the wavenumber surface pressure spectrum and the surface wavenumber content. The simplified form of their theory is shown in Equation 3-1 assuming a homogeneous wall pressure field.

$$\Phi_{PP}(\boldsymbol{x},\omega) \approx \frac{4\pi^2(k_o h)^2 \Sigma \Phi_{pp}(\omega)}{|\boldsymbol{x}|^2} \int \Psi_{pp}(\kappa_x,\kappa_z,\omega)\Gamma(\kappa_x,\kappa_z,k_o)d\kappa_x d\kappa_z \quad \text{Eq. 3-1}$$

where Ψ_{pp} is the wavenumber wall pressure spectrum normalized on the single point pressure spectrum and Γ is a non-dimensional wavenumber filter function defined by the rough surface characteristics as defined in Equation 3-2.

$$\Gamma(\kappa_x,\kappa_z,k_o) = \frac{1}{\Sigma h^2}\mathrm{Ex}\left[\left|\left(\frac{x\zeta^{(x)}}{|\boldsymbol{x}|}+\frac{z\zeta^{(z)}}{|\boldsymbol{x}|}\right)-ik_o h\zeta\right|^2\right] \quad \text{Eq. 3-2}$$

$\zeta^{(x)}$ and $\zeta^{(z)}$ are the Fourier transforms of the surface gradients in the *x* and *z* directions, ζ is the Fourier transform of the surface shape, *h* is the roughness height, k_o is the acoustic wavenumber, *x* and *z* are the observer location along the *x* and *z* axes, $\boldsymbol{x}$ is the observer's location vector, and Σ is the roughness area. Equation 3-2 is different from the equation given in Glegg & Devenport (2009). There is an error in their paper decreasing the magnitude of the filter function by a factor of 7. Several specific surface types are discussed in Glegg & Devenport (2009) and their wavenumber content analyzed including stochastic, deterministic, and wavy-wall surfaces. A thorough analysis of the noise produced by a wavy-wall surface is given in Devenport *et al*. (2010) showing that the far field noise produced can be used to probe the wavenumber surface pressure spectrum at regions currently immeasurable due to limits imposed by the size of existing sensors. Similarly, their results show the possibility of predicting the far field noise using measurements of a rough surface and the overriding wall pressure spectrum. The theoretical wavenumber solutions for a discontinuous stochastic surface as well as a surface composed of randomly located and sized hemispheres are given in Glegg & Devenport (2009). Sources on both surfaces are assumed

acoustically compact so that $k_o h$ is very small and therefore the wavenumber spectrum of the surface is negligible compared to the wavenumber spectrum of the surface slope. This surface slope dictates the shape of the theoretical collapse of the far field data when normalized by the measured single point wall pressure spectrum. Glegg & Devenport (2009) predict that a surface composed of randomly distributed hemispheres will produce an ω^4 collapse which is different from the theoretical and observed ω^2 collapse of noise from stochastic roughness shown in Alexander (2009).

A wavenumber analysis of three of the rough surfaces used in this study is detailed below giving some insight into the inherit differences of the examined surfaces. Also, estimations of produced far field noise will be compared to the expected results from Glegg & Devenport's (2009) theory.

3.2 Surface Wavenumber Spectrum of 42 Element Fetch of 3mm Cubes

A single cuboid of dimensions a, b, and c, as shown in Figure 3-1, protruding from a flat surface can be defined by a series of two-dimensional Heaviside functions along the *x* and *z* axes as given in Equation 3-3.

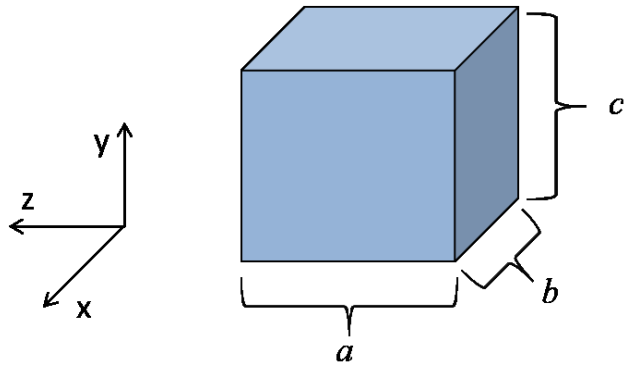

Figure 3-1. Cubic element

$$f(x,z) = c \cdot \mathrm{H}\left({}^{a}/_{2} - z\right)\mathrm{H}\left(z - {}^{a}/_{2}\right)\mathrm{H}\left({}^{b}/_{2} - x\right)\mathrm{H}\left(x - {}^{b}/_{2}\right) \qquad \text{Eq. 3-3}$$

The Fourier transform will be defined as in Equation 3-4 shown with its inverse pair.

$$F(\kappa_x, \kappa_z) = \frac{1}{(2\pi)^2}\int_{-\infty}^{\infty}\int_{-\infty}^{\infty} f(x,z)e^{i(\kappa_x x + \kappa_z z)}dx\,dz$$

$$f(x,z) = \int_{-\infty}^{\infty}\int_{-\infty}^{\infty} F(\kappa_x, \kappa_z)e^{-i(\kappa_x x + \kappa_z z)}d\kappa_x\,d\kappa_z \qquad \text{Eq. 3-4}$$

The equation for a three-dimensional box can be inserted into the transform and the limits of integration can be adjusted to the region where $f(x,z) > 0$.

$$F_{cuboid}(\kappa_x, \kappa_z) = \frac{c}{(2\pi)^2}\int_{-a/2}^{a/2}\int_{-b/2}^{b/2} e^{i(\kappa_x x + \kappa_z z)}dx\,dz \qquad \text{Eq. 3-5}$$

This can be integrated to yield the analytic Fourier transform solution for a single cuboid in Equation 3-6.

$$F_{cuboid}(\kappa_x, \kappa_z) = \frac{c}{\kappa_x \kappa_z \pi^2} \sin\left(\kappa_x {}^{b}/_{2}\right) \sin\left(\kappa_z {}^{a}/_{2}\right) \qquad \text{Eq. 3-6}$$

This solution in wavenumber space is shown in Figure 3-2 for a cube with $a = b = c = 3$mm. The flat vertical faces of the cube aligned on the x and z axes produce a highly directional wavenumber pattern indicating sound may be produced more efficiently in directions normal to the cubes faces.

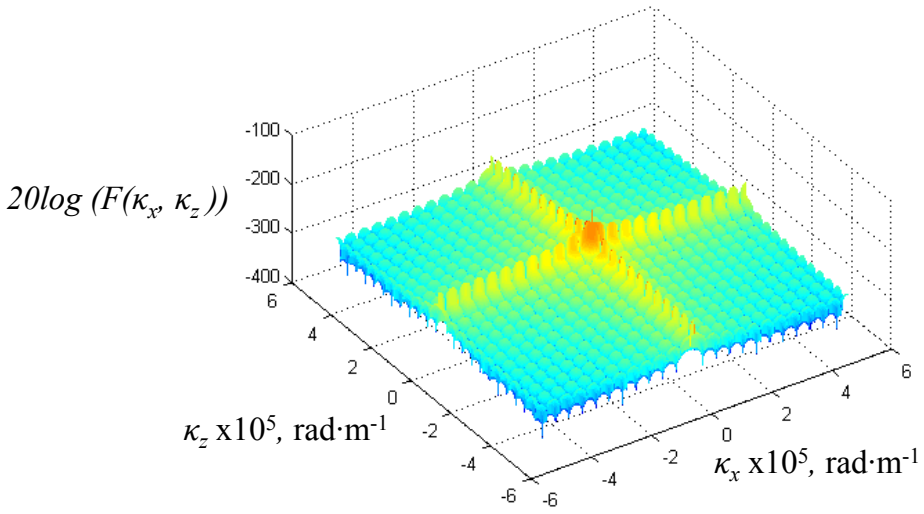

Figure 3-2. Wavenumber transform of a single 3mm cubic element

The Fourier transform of a fetch of cubes with dimensions a, b, and c can be calculated by a linear addition of Equation 3-6 offsetting each cube to a different (x_j, z_j) location using Equation 3-7.

$$F_j(\kappa_x, \kappa_z) = F(\kappa_x, \kappa_z) e^{i(\kappa_x x_j + \kappa_z z_j)} \qquad \text{Eq. 3-7}$$

This can be done to model a 42 element fetch of cubes spaced 16.5mm apart in a grid pattern simulating one of the fetches used experimentally in this study. The resulting Fourier transform is shown in Figure 3-3. The same directionality is observed, but the spectrum appears noisier because its smallest scale is now determined by the full size of the fetch rather than just a single element.

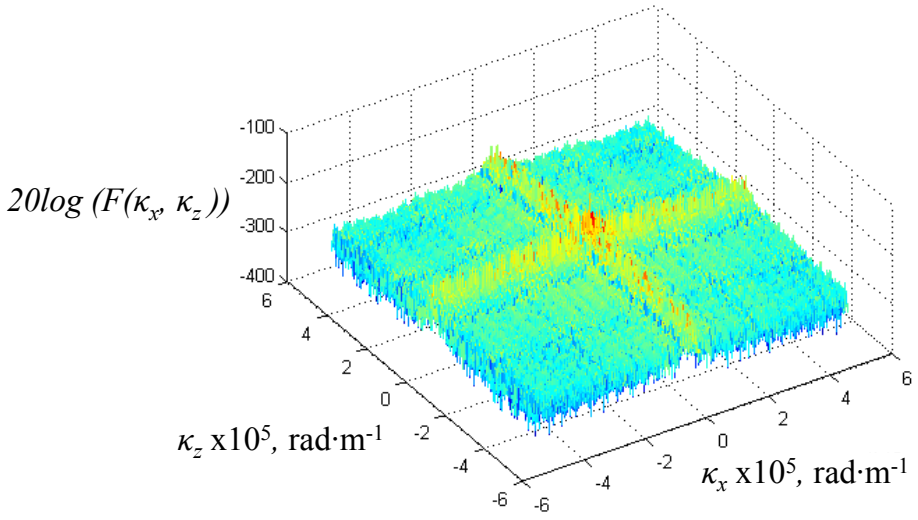

Figure 3-3. Wavenumber transform of a 42 element fetch of 3mm cubes spaced 16.5mm apart

Though the Fourier transform of these elements seems to indicate a specific directional efficiency, through the assumption of compact sources, it was determined that the wavenumber spectrum of the surface was negligible compared to the wavenumber spectrum of the surface slope. It can be shown that the Fourier transform of the surface can be related to the Fourier transform of the slope in the *x*-direction as in Equation 3-8.

$$\frac{1}{(2\pi)^2}\int_{-\infty}^{\infty}\int_{-\infty}^{\infty}\frac{\partial f(x,z)}{\partial x}e^{i(\kappa_x x+\kappa_z z)}dx\,dz = -i\kappa_x F(\kappa_x,\kappa_z) \qquad \text{Eq. 3-8}$$

The equation is similar in *z* and can be generalized for the slope in any direction with unit vector $\overrightarrow{e_s}$.

$$\frac{1}{(2\pi)^2}\int_{-\infty}^{\infty}\int_{-\infty}^{\infty}\overrightarrow{e_s}\cdot\nabla f(x,z) = \overrightarrow{e_s}\cdot[-i\vec{\kappa}F(\kappa_x,\kappa_z)] \qquad \text{Eq. 3-9}$$

Rearranging Equation 3-2 using the result of Equation 3-9 leaves a solution for the wavenumber filter function in terms of the surface wavenumber spectrum. The only assumption made is that the sources are compact so that the surface wavenumber term of Equation 3-2 vanishes.

$$\Gamma(\kappa_x,\kappa_z) = \frac{1}{\Sigma h^2}\mathrm{Ex}[|\overrightarrow{e_s}\cdot[-i\vec{\kappa}F(\kappa_x,\kappa_z)]|^2] \qquad \text{Eq. 3-10}$$

Figure 3-4 shows a 2D plot of the Fourier transform of the surface slope in the *x*-direction for the 42 element fetch of 3mm cubes.

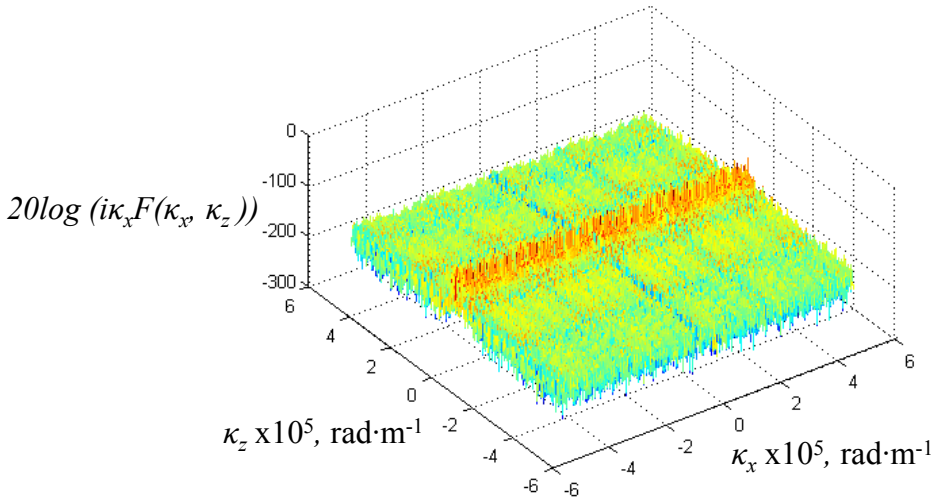

Figure 3-4. Wavenumber transform of slope of 42 element fetch of 3mm cubes

The result seems to be wavenumber white in the κ_x dimension, but the wavenumbers which will be most effective at scattering sound will be the wavenumbers that align with the convective ridge of the wavenumber wall pressure spectrum. This study will later show measured far field noise in a frequency range 250Hz-20kHz. This frequency range corresponds with a convective ridge that peaks between $\kappa_x \approx$200-14000 rad/m for κ_z=0 according to the wall pressure wavenumber spectrum models of Chase (1987) and Corcos (1964).

Figure 3-5 is a closer look at these much lower wavenumbers. The peak values are still seemingly flat in the κ_x direction but there is a grid pattern present in the wavenumber space due to the grid configuration and shape of the cubic elements.

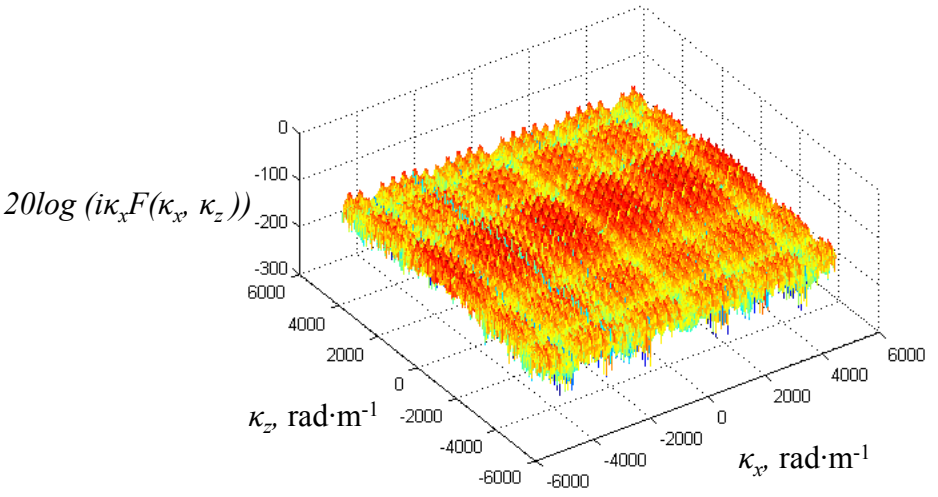

Figure 3-5. Low wavenumber region of wavenumber transform of surface slope of 42 3mm cubic element fetch

3.3 Surface Wavenumber Spectrum of 42 Element Fetch of 3mm Hemispheres

The fetch of hemispherical elements can be analyzed in the same way as the cubes using a Hankel transform. A Hankel transform of order zero can be used to express a two-dimensional Fourier transform of a radially symmetric function. Switching to polar coordinates, the Fourier transform of Equation 3-4 can be written as

$$F(u,v) = \frac{1}{(2\pi)^2}\int_{-\infty}^{\infty}\int_{-\infty}^{\infty} f(r)e^{2\pi i(ux+vz)}dx\,dz \qquad \text{Eq. 3-11}$$

where

$$\begin{aligned} r^2 &= x^2 + z^2 & x &= r\cos(\theta) & z &= r\sin(\theta) \\ q^2 &= u^2 + v^2 & u &= q\cos(\phi) & v &= q\sin(\phi) \end{aligned} \qquad \text{Eq. 3-12}$$

The Fourier transform can be reformulated using the definition of a Hankel transform into Equation 3-13.

$$F(q) = \frac{1}{2\pi}\int_0^{\infty} f(r)J_0(-2\pi qr)r dr \qquad \text{Eq. 3-13}$$

where $J_0(-2\pi qr)$ is a Bessel function of order zero. For a hemisphere of radius R, the function $f(r)$ can be defined as

$$f(r) = \begin{Bmatrix} \sqrt{R^2 - r^2} & \text{for } r < R \\ 0 & \text{for } r > R \end{Bmatrix} \qquad \text{Eq. 3-14}$$

Integration of Equation 3-13 then yields the solution

$$F_{hemi}(q) = \frac{1}{2\pi}\left(\frac{\sin(2\pi qR) - 2\pi qR\cos(2\pi qR)}{(2\pi qR)^3}\right) \qquad \text{Eq. 3-15}$$

Substituting

$$\kappa_x = 2\pi u \qquad \kappa_z = 2\pi v \qquad \boldsymbol{\kappa} = 2\pi q \quad \boldsymbol{\kappa}^2 = \kappa_x^2 + \kappa_z^2 \qquad \text{Eq. 3-16}$$

The final solution in wavenumber space is

$$F_{hemi}(\boldsymbol{\kappa}) = \frac{\sin(\boldsymbol{\kappa}R) - \boldsymbol{\kappa}R\cos(\boldsymbol{\kappa}R)}{(2\pi\boldsymbol{\kappa})^3} \qquad \text{Eq. 3-17}$$

Figure 3-6 shows this solution for a single 3mm hemispherical element. Unlike Figure 3-2, there is no strong directionality present, which is expected since a hemisphere is radially symmetric. The solution produces a spike around the origin and then decays as $\boldsymbol{\kappa}^2$ in all directions.

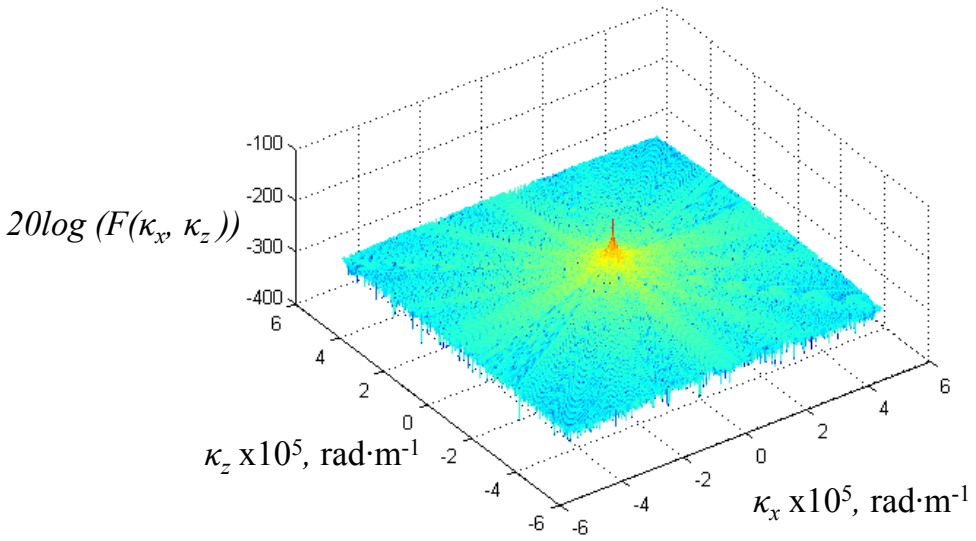

Figure 3-6. Wavenumber transform of a single 3mm hemispherical element

Using Equation 3-7 to simulate the 42 element fetch with a grid spacing of 16.5mm yields the solution shown in Figure 3-7. The addition results in a grid pattern present in the wavenumber in both the κ_x and κ_z directions. A similar pattern is present in Figure 3-3 generated using the 42 element fetch of cubic elements in a grid configuration.

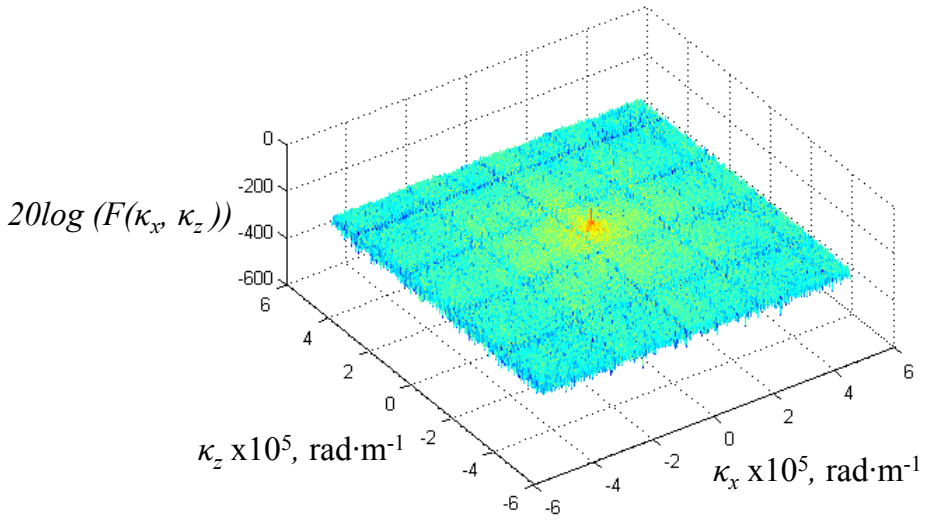

Figure 3-7. Fourier transform of 42 element fetch of 3mm hemispherical elements spaced 16.5mm apart

Using Equation 3-8, the wavenumber of the surface slope is generated for an observer in the *x*-direction as in Equation 3-18.

$$F_{hemi}(k) = \kappa_x \frac{\sin(\boldsymbol{\kappa}R) - kR\cos(\boldsymbol{\kappa}R)}{2\pi\boldsymbol{\kappa}^3} \qquad \text{Eq. 3-18}$$

This solution approaches zero in the limit as $\boldsymbol{\kappa}$ approaches zero but produces a singularity at the origin. The computation of the wavenumber field was corrected to satisfy the condition that $\Gamma(\boldsymbol{\kappa} = \mathbf{0})$ must be nil for a simple shape protruding from a flat surface. Figure 3-8 compares the wavenumber slope in the κ_x direction for both the large wavenumber and small wavenumber fields. The wavenumber of the surface slope in the κ_z direction behaves similarly.

At large wavenumbers, the solution appears relatively flat. The low wavenumber region shows that the solution is again radially symmetric except for the steep decline around κ_x=0. The hills and valleys of this slope wavenumber space will interact differently than the cubic element fetch with the wavenumber wall pressure spectrum scattering different portions of the wavenumber space for various frequencies.

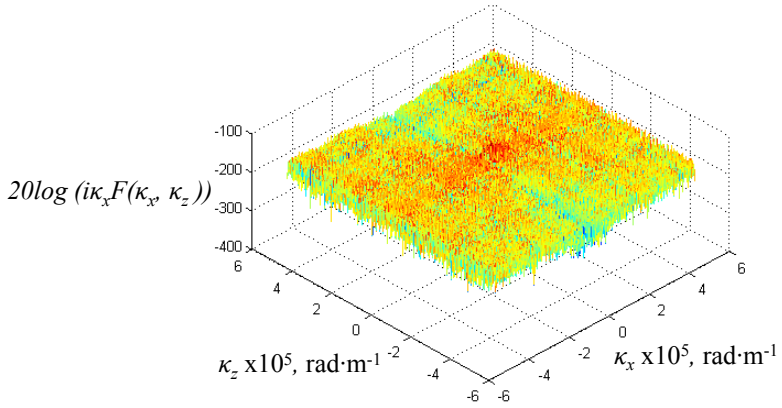

a)

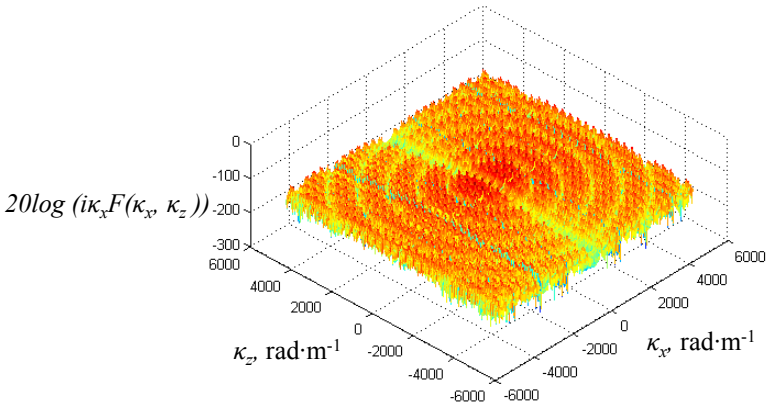

b)

Figure 3-8. Wavenumber transform of the surface slope of the 42 element fetch of 3mm hemispheres at a) high b) and low wavenumber regions

3.4 Surface Wavenumber Spectrum of 6209 Element Fetch of 1mm Randomly Distributed Hemispheres

The procedure for finding the wavenumber transform of the surface and the surface slope of the 610x305mm fetch of randomly distributed 1mm hemispheres directly follows that for the smaller fetch of 3mm hemispherical elements. Using the exact locations of all 6209 elements, the resulting Fourier transform of the surface is shown in Figure 3-9. An incorrect assumption of this procedure occurs when elements overlap. Linearly adding the Fourier transform of two overlapping hemispheres of exactly the same size would mathematically represent the Fourier transform of a single hemisphere of double the original height. It is assumed for this calculation that the total effect of this occurrence is negligible. On the entire fetch of 6209 elements only 560 overlap at all and no two elements have the exact same position. Just as the result of the single hemispherical element, the Fourier transform of this surface is radially symmetric in wavenumber space.

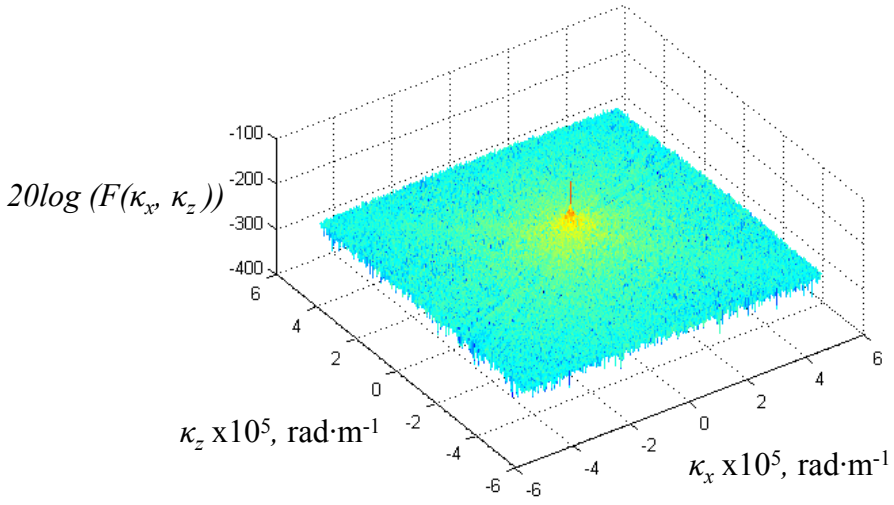

Figure 3-9. Wavenumber transform of fetch of 6209 randomly located 1mm hemispheres

The Fourier transform of the surface slope for large and small wavenumbers is shown in Figure 3-10. Again at large wavenumbers, the spectrum appears relatively flat, but at low wavenumbers a pattern emerges. This result looks similar to that in Figure 3-8 for the 3mm hemispheres except that the underlying grid pattern in the spectrum is removed. This is due to the random relative positioning of the elements. Also, the radially symmetric ridges are further spaced in the random surface as compared to the 42 element fetch of larger hemispheres. In Figure 3-8b, there are four concentric rings surrounding the origin producing hills and valleys in wavenumber space compared to only one over the same wavenumber range in Figure 3-10b.

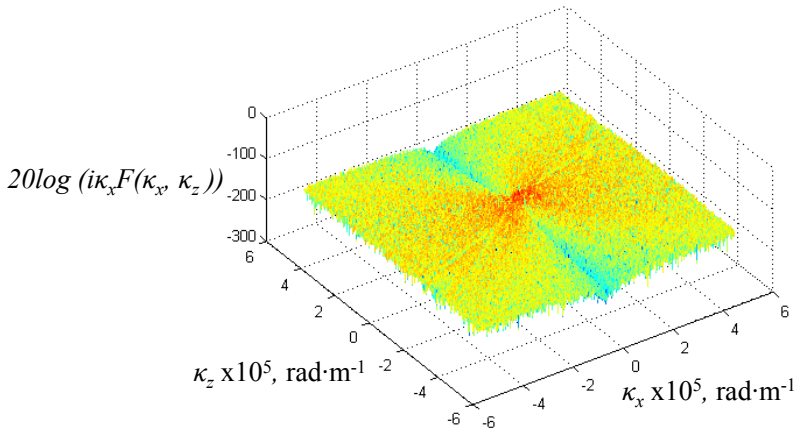

a)

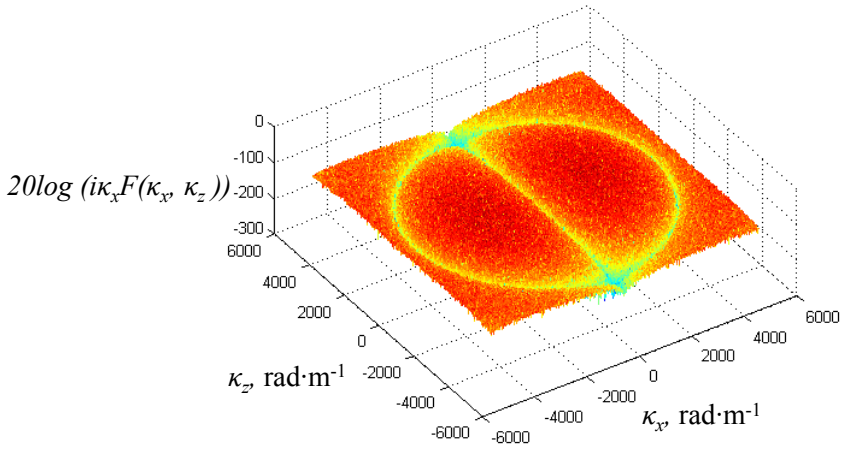

b)

Figure 3-10. Wavenumber transform of surface slope for random fetch of 1mm hemispheres at a) high b) and low wavenumbers

3.5 Sound Estimates from Deterministic Roughness

The wavenumber decomposition of the surface slope for each fetch of deterministic roughness can be used to make absolute estimates of the sound produced by these surfaces using the theory of Glegg & Devenport (2009). By dividing Equation 3-1 by the single point wall pressure spectrum, any assumption of the form of this spectrum can be removed. If the observer is located a unit distance away in the negative *x*-direction and assuming compact sources, Equation 3-1 can be simplified to

$$\frac{\Phi_{PP}(\boldsymbol{x},\omega)}{\Phi_{pp}(\omega)} \approx 4\pi^2 k_o^2 \int \Psi_{pp}(\kappa_1,\kappa_3,\omega)\Gamma(\kappa_1,\kappa_3,k_o)d\kappa_1 d\kappa_3$$

Eq. 3-19

$$\text{Where } \Gamma(\kappa_1,\kappa_3,k_o) = \left|\zeta^{(x)}\right|^2$$

The Corcos and Chase wavenumber wall pressure spectrum are both used to estimate the normalized wavenumber wall pressure spectrum, Ψ_{pp}, for comparison. The Corcos spectrum as given by Howe (1998) is shown in Equation 3-20.

$$\frac{\Phi_{pp}(\boldsymbol{\kappa},\omega)}{\Phi_{pp}(\omega)} = \frac{l_1}{\pi[1+l_1^2(\kappa_1-\omega/U_c)^2]}\frac{l_3}{\pi[1+l_3^2\kappa_3^2]}$$

Eq. 3-20

Where $l_1 \approx 9\,U_c/\omega$ and $l_3 \approx 1.4\,U_c/\omega$

The analytical form of the integrated single point spectrum is

$$\Phi_{pp}(\omega) = \frac{(\rho u_\tau^2)^2\left(\frac{\omega\delta^*}{U_e}\right)^2}{\left(\frac{U_e}{\delta^*}\right)\left[\left(\frac{\omega\delta^*}{U_e}\right)^2+\alpha_p^2\right]^{3/2}}$$

Eq. 3-21

Where $\alpha_p = 0.12$

The Chase spectrum, which is much more complicated than the Corcos spectrum, provides a better model of the wavenumber wall pressure spectrum at low wavenumbers. This model spectrum as given by Chase (1987) is

$$\Phi_{pp}(\boldsymbol{\kappa},\omega) = \frac{\rho^2 u_\tau^3}{[k_+^2+(b\delta)^{-2}]^{5/2}}\left\{C_T|\boldsymbol{\kappa}|^2\left[\frac{k_+^2+(b\delta)^{-2}}{|\boldsymbol{\kappa}|^2+(b\delta)^{-2}}\right]+C_M\kappa_x^2\right\}$$

Eq. 3-22

Where $h_C = 3 \quad C_T h_C = 0.014 \quad C_M h_C = 0.466 \quad b = 0.75$

And $$k_+^2 = \frac{\left(\frac{\omega}{U_C}-\kappa_x\right)^2}{h_C^2\left(\frac{u_\tau}{U_C}\right)^2}+\boldsymbol{\kappa}^2$$

Chase's single point spectrum is given as the summation of two parts defined separately in Chase (1980) and Chase (1987).

$$\Phi_{pp}(\omega) = \Phi_T(\omega)+\Phi_M(\omega)$$

Where $\Phi_T(\omega) = \pi C_T h_C \rho^2 u_\tau^4 \omega^{-1}\alpha^{-1}(1+\alpha^{-2})$ and
$\Phi_M(\omega) = r_M a_+ \rho^2 u_\tau^4 \omega^{-1}\alpha^{-3}(1+\mu^2\alpha^2)$

Eq. 3-23

$$\alpha = [1+(U_c/\omega b\delta)^2]^{-1/2} \qquad r_M = 1-C_T h_C/(C_T h_C + C_M h_C)$$

$$a_+ = (2\pi h_C/3)(C_T+C_M) \qquad \mu = h_C u_\tau/U_c$$

For both wall pressure spectrum models, the friction velocity of the wall jet flow was estimated using Bradshaw & Gee's (1960) skin friction relationship for a wall jet, $C_f = 0.0315\mathrm{Re}_\delta^{-0.182}$. The convection velocity was taken from the analysis of Devenport *et al*. (2010). They found, through analysis

of far field noise from rib roughness, that the convection velocity was approximately 41% of the edge velocity for a 60m/s nozzle flow. This is lower than values from conventional boundary layers, which have convection velocities around 60%, but the difference was attributed to interaction with the wall-jet's large slower moving mixing layer. All further input values and relationships used in this analysis to estimate the Corcos and Chase spectra for a nozzle exit velocity of 60m/s are given in Equation 3-24.

$$\rho = 1.102\,\mathrm{kg/m^3} \qquad u_\tau = U_e\sqrt{C_f/2} \qquad C_f = 5.137\times10^{-3} \qquad U_c = 0.41U_e$$

Eq. 3-24

$$\delta = 16.4\mathrm{mm} \qquad U_e = 22\mathrm{m/s}$$

A 3D plot of the Chase wall pressure wavenumber spectrum is shown in Figure 3-11. Isocontours are highlighted to show the shape of the convective ridge. Comparison of two slices through the wavenumber spectra models of Corcos and Chase as a function of frequency are shown in Figure 3-12 at κ_x =2000 rad/m and κ_z =0. The Chase spectrum has a broader convective ridge and decays more rapidly at higher and lower frequencies, but both spectra produce a convective peak at the same approximate location.

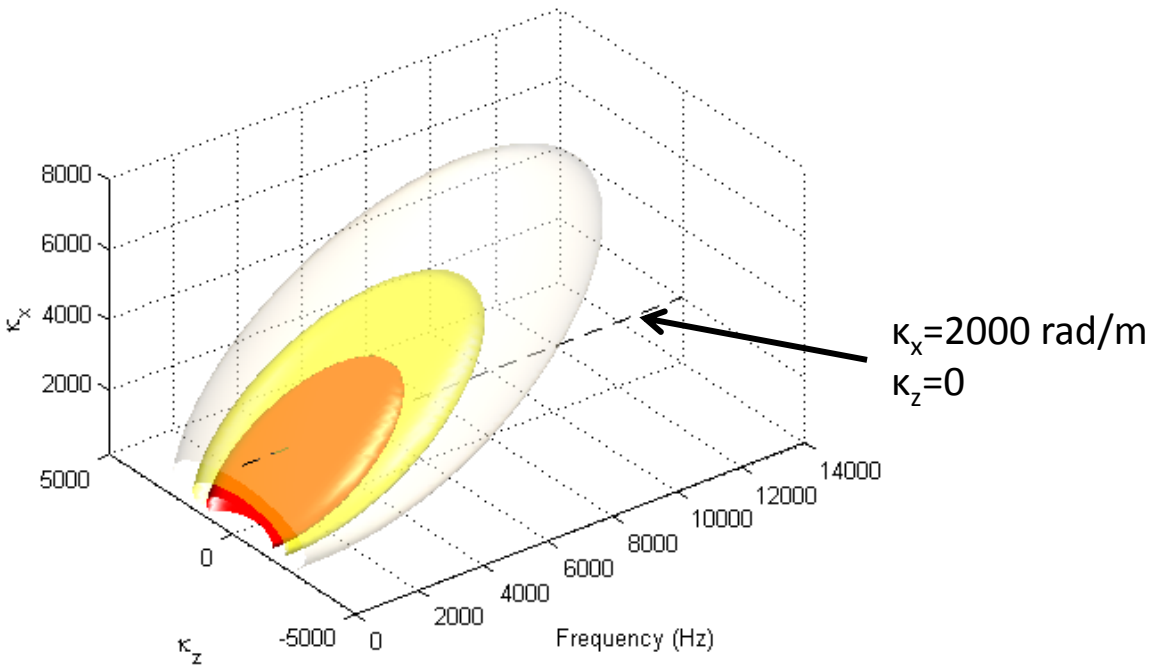

Figure 3-11. Convective ridge in wavenumber wall pressure spectrum

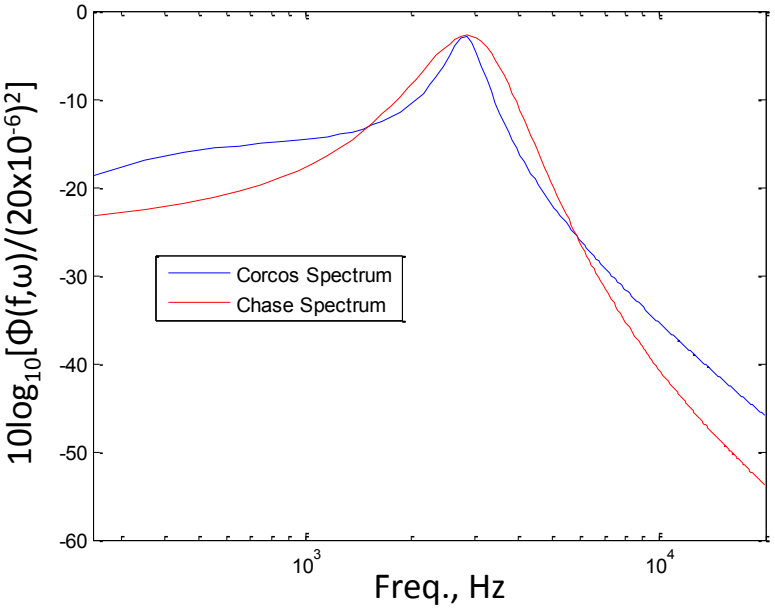

Figure 3-12. Comparison of the Corcos and Chase wavenumber wall pressure spectra at κ_x=2000, κ_z=0

The wavenumber pressure spectrum models can now be combined with the wavenumber of the surface slope and integrated to produce the estimated far field noise. Although the Fourier transforms of the surface slopes were computed analytically, the integration in Equation 3-19 was done numerically over a range of κ_x= [0 20000]rad·m^{-1} and κ_z= [-10000 10000]rad·m^{-1} with a resolution of 10 rad·m^{-1}. The resolution of this integration was examined to make sure the solution was converged. Also, the limits of the integration were studied and were found to be sufficient so that any extension did not significantly affect the results. Figure 3-13 to Figure 3-15 show the predicted noise from each fetch of deterministic roughness under the described condition for an observer located 1m upstream from the lead of the roughness fetch. Each figure has the predicted noise calculated using the Corcos and Chase wall pressure spectra as well as lines with slopes of ω^2 and ω^4 for comparison. None of the deterministic surfaces produce a clearly defined region where the normalization produces an ω^2 curve. Each surface produces a collapse that resembles an ω^4 region at low frequencies and then transitions to shallower slopes. For the cubic element fetch, the result approaches a straight line with an ω slope. Both normalizations from the hemispherical fetches resolve to a flat spectrum at higher frequencies above approximately 1kHz for the 3mm hemispheres and 5kHz for the 1mm hemispheres. The predicted normalization from the randomly positioned element fetch is much smoother, especially at lower frequencies, than the results from the grid patterned fetches. This is because the grid patterned fetches produced slope wavenumber solutions with frequent hills and valleys due to the patterned spacing of elements. The integrated spectrum is reflecting the result of the convective ridge passing through this wavenumber pattern as the frequency is increased. At higher frequencies, the associated convective ridge is less narrow smoothing the hills and valleys in the slope wavenumber that are radiated to the far field.

An interesting note is that the estimates using the Corcos and Chase spectra produce very similar results. The Corcos spectrum is more sensitive to changes in the slope wavenumber spectrum because of its narrow convective ridge which produces lumps in the predicted noise normalization. The Chase spectrum with its broad convective ridge tends to smooth this effect.

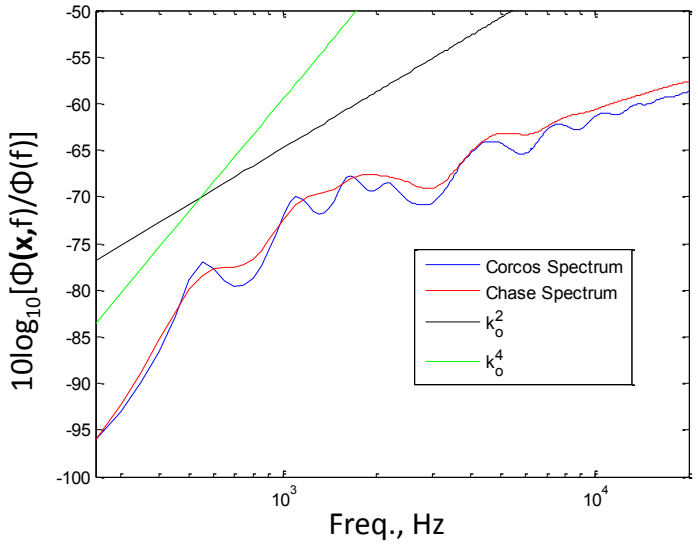

Figure 3-13. Normalized noise estimate from 42 element fetch of 3mm cubic elements

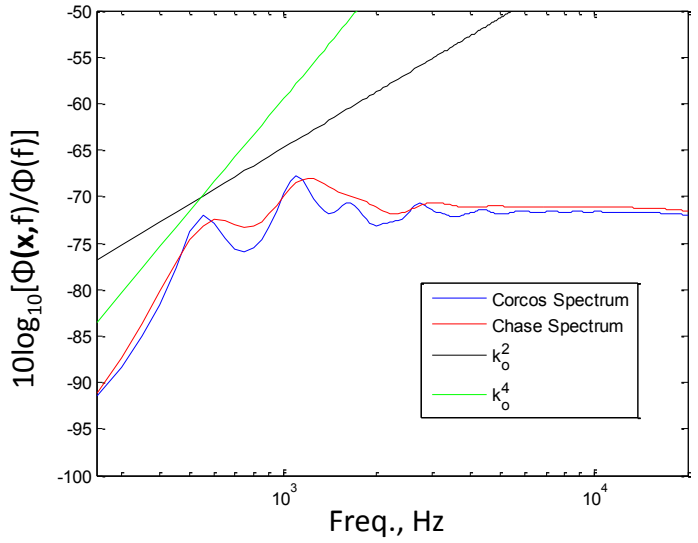

Figure 3-14. Normalized noise estimate from 42 element fetch of 3mm hemispherical elements

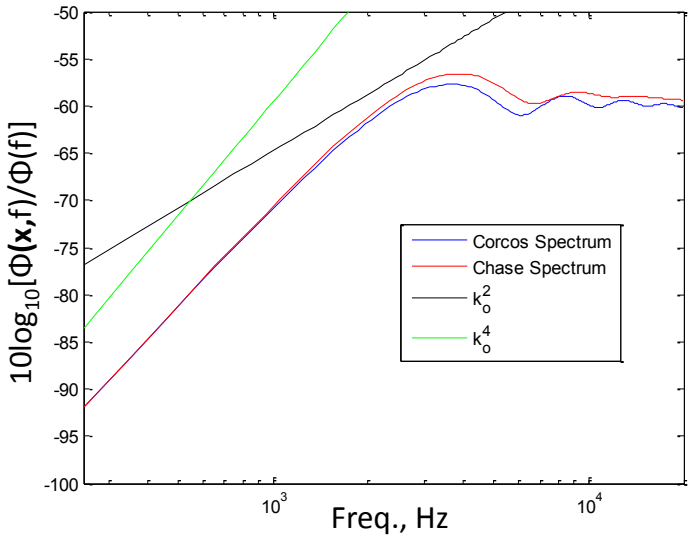

Figure 3-15. Normalized noise estimate from fetch of randomly located 1mm hemispherical elements

The assumption of compact sources can be tested by comparing the estimate in Figure 3-14 for the fetch of 42 3mm hemispherical elements with a similar estimate using the full form of Equation 3-2. This calculation does not ignore the $ik_o h\zeta$ term in the wavenumber filter function where ζ is the wavenumber of the surface shape normalized on the roughness height. This comparison is shown in Figure 3-16 using the Chase model of the wavenumber wall pressure spectrum. The two spectra are almost identical over the considered frequency range indicating that the assumption of compact sources is valid. The 3mm hemispherical elements are the largest used in this study. Therefore, the assumption of compact sources can be extrapolated to the other studied surfaces.

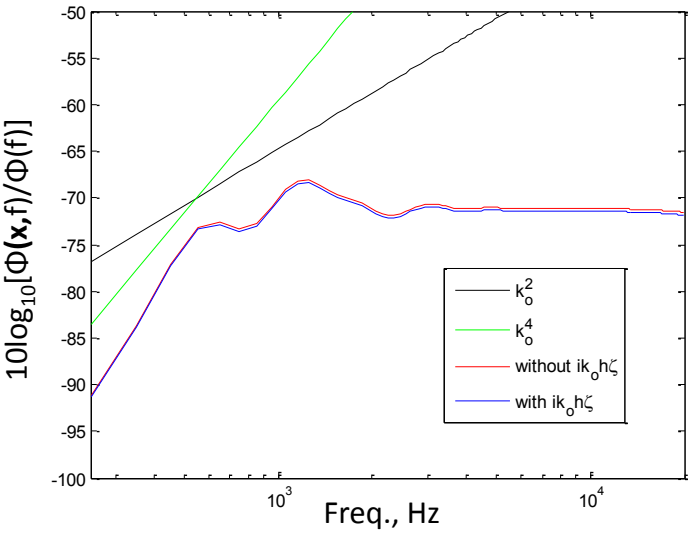

Figure 3-16. Comparison of noise estimate using assumption of compact and non-compact sources

3.6 Comparison with Data of Alexander (2009)

Figure 3-13 to 3-15 show only a very narrow ω^2 region unlike the observed normalizations of stochastic surfaces in Alexander (2009). These stochastic surfaces differ from the deterministic surfaces considered here in the element size and randomness of the elements' shape. The 40 grit surface in Alexander (2009) contained elements that were nominally 0.425mm, less than half as large as the smallest considered deterministic surface in this analysis. To study the effect of extremely small element size, the same method as given in Equation 3-19 was used to estimate the normalized noise from a single cubic and hemispherical element with characteristic dimensions of 0.425mm. The results are shown in Figure 3-17 for an observer at $\boldsymbol{x}$=(-1m, 0, 0). The predicted noise from both elements follows a slope slightly less than ω^4. The form of this normalization appears to be almost independent of element shape. This can be explained in the limit as the roughness element size goes to zero. When considering elements which are very small compared to the wavelengths of disturbances on the convective ridge, the surface slope of any elementary shape will appear as two Dirac delta functions of opposite signs separated by a distance $2a$ regardless of the actual element shape. This is essentially a low resolution view of the increasing slope on one side of the element and the decreasing slope on the other side. The low wavenumber region of the Fourier transform of the surface slope will appear similar between the two shapes. The resulting spectral shape is then only a function of the wavenumber wall pressure spectrum.

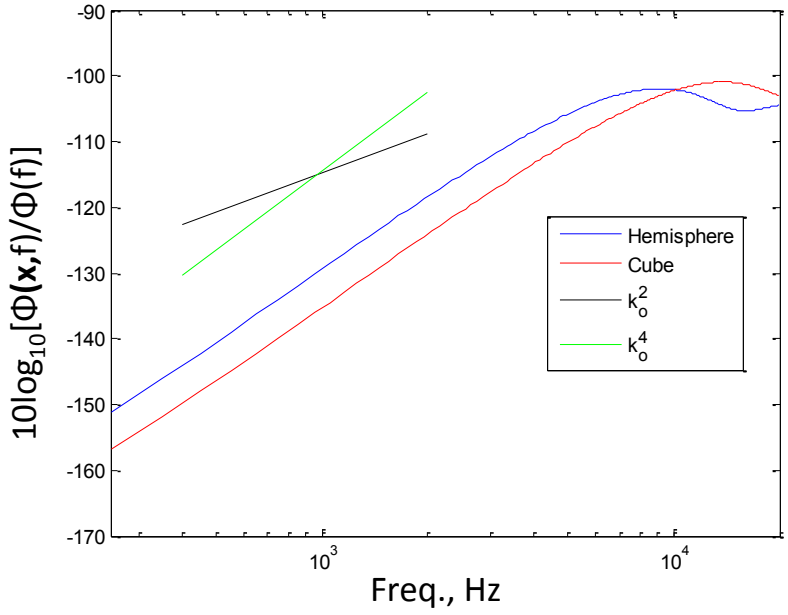

Figure 3-17. Estimated noise from a single 0.425mm hemispherical and cubic element at a nozzle exit velocity of 60m/s

To model the effect of the various grain sizes on a single fetch and their scattered positions, the entire 40 grit surface can be crudely approximated as a combination of randomly sized hemispheres and cuboids scattered over an area 610x305mm to match the fetch size studied in Alexander (2009). The grain heights were assigned randomly between values of 0.325 and 0.525mm. The total number of elements used to simulate the surface was calculated by counting the grains in two 5x5mm white light profilometry scans of 40 grit sandpaper to find the grain density. The computed grain density was 1.36 grains per mm^2, resulting in 253026 elements on the simulated fetch. An even number of cubes and hemispheres were

used. The resulting noise prediction is shown in Figure 3-18 compared with the data of Alexander (2009). The prediction has been computed for an observer at $\boldsymbol{x}$=(-0.2283, 0.473, 0)m, which is the far field microphone location used in Alexander (2009).

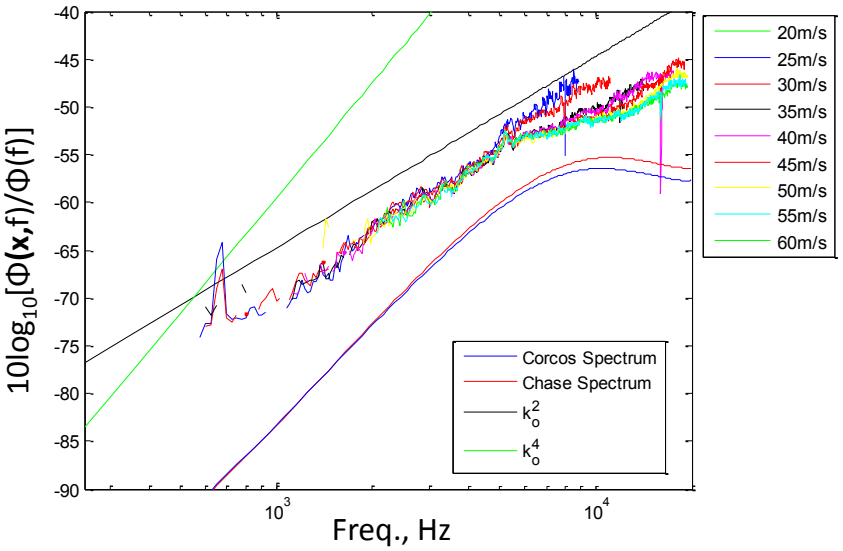

Figure 3-18. Noise prediction for a 610x305mm fetch of 40grit sandpaper at a nozzle exit velocity of 60m/s compared to the results reported in Alexander (2009) at a range of nozzle exit velocities

The result of Alexander (2009) clearly follows an ω^2 collapse unlike the prediction. The prediction is closer to the ω^4 curve especially at lower frequencies. This could be a result of inadequately modeling the surface as discrete cubes and hemispheres. A 5x5mm scan of the 40 grit surface is shown in Figure 3-19. There doesn't appear to be a truly flat substrate at any point in the scan. Therefore, the slope is never consistently zero for any distance on the surface. Also, the opposing Dirac delta functions may not accurately represent the slopes of each grain on the stochastic surface. The elements themselves do not have a simply approximated slope over their surface. The slope changes from sharply positive to negative not just at the front and back of each grain but over their entire surface area. Though, for the frequency range considered here, the low wavenumber region of the surface slope will dominate, 200 rad/m to 13000 rad/m, and the smallest details on the surface should be negligible. Details such as element spacing could be more important contributors in this region. The stochastic surfaces may be best described by a random distribution of slopes in wavenumber space which would be wavenumber white and produce the observed ω^2 normalization.

The difference between the estimated and measured normalizations is not just the spectral shape but also the 5-9dB difference in magnitude. Although this analysis is only an approximation of the noise and does not collapse on the same curve, it may provide some insight into the "break frequency" described in Alexander (2009) where the normalization ceases to collapse the data. The estimated and measured normalization begin to "break" from their respective curves at approximately the same frequency around 5kHz. This indicates the "break frequency" could be dependent on the convective ridge passing through the wavenumber space of the surface slope. Since the error between the estimated and measured curves in Figure 3-18 could be due to the modeling of the stochastic roughness, a more accurate measure of the capabilities of the theory proposed in Glegg & Devenport (2009) may be derived from a

comparison between the estimates and measurements of the deterministic surfaces. These results are analyzed in the following chapter.

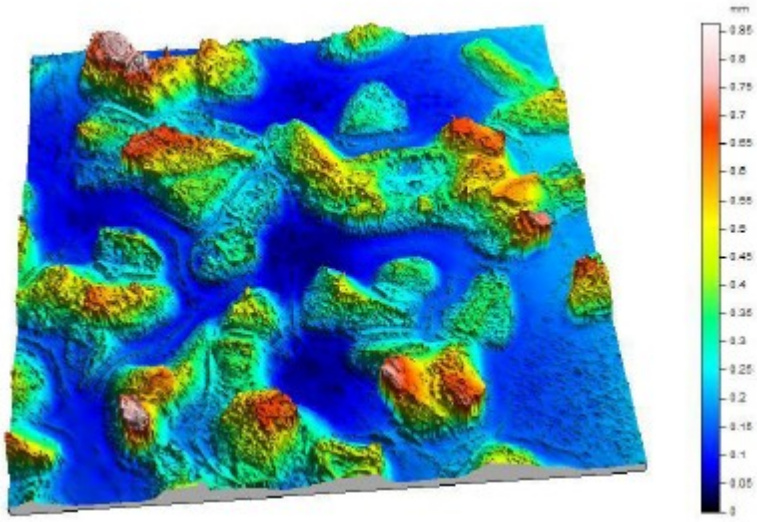

Figure 3-19. 5x5mm scan of the 40 grit sandpaper surface

Chapter 4 Estimations of Far Field Noise

Wall pressure and far field measurements were recorded from cuboidal and hemispherical roughness with various configurations and roughness heights. Unlike the previously studied stochastic surfaces in Grissom (2007), Alexander (2009), and Devenport *et al.* (2011), the exact analytical Fourier transforms of these surfaces can be calculated so that the accuracy of Glegg & Devenport's (2009) roughness noise theory can be examined. This section details the measurement of the wall pressure field in the deterministic roughness along with the radiated far field noise. Estimations are made of the wall pressure normalized far field noise and the absolute far field noise from the deterministic roughness. Also, the form of the wavenumber wall pressure spectrum is studied as it relates to the estimation of roughness noise.

4.1 Measurements from 42 Element 3mm Cubic Roughness

4.1.1 Wall Pressure

The smooth wall pressure spectrum of the wall-jet behaves as a conventional turbulent boundary layer as according to Blake (1986). The low frequency region varies as ω^{-1} and the high frequency approaches ω^{-5}. The wall pressure spectra measured in the wall-jet differ from conventional turbulent boundary layers most notably in the low frequency region. Figure 4-1 shows a comparison between the undisturbed wall pressure spectrum measured in the wall-jet at x=1358mm and U_o=60m/s with the unperturbed wall pressure spectrum from the computational study of Yang & Wang (2011) and the experimental studies of Rusche (2011) and Farabee & Cassarella (1986). These spectra are normalized on outer boundary layer variables to collapse the low frequency regions. Due to the wall-jet's large slow moving mixing layer, the low frequency region of the wall pressure spectrum rises above the wall pressure spectrum continuing the ω^{-1} slope to the extent of the measured frequencies. The data of Rusche (2011) and Farabee & Cassarella (1986) collapse well at lower frequencies at a slope shallower than ω^{-1} common due to the low Reynolds numbers achievable in laboratory experiments. The Reynolds numbers of the compared wall pressure spectra are shown in Table 4-1. The shift of the transition region to higher frequency for the data of Rusche (2011) is due to the comparably higher Reynolds number which extends the length of the ω^{-1} region due to the convected turbulence in the logarithmic portion of the boundary layer. The LES data of Yang & Wang (2011) have a similar magnitude in the low frequency region but drop off at a much lower non-dimensional frequency than any of the experimental measurements. This is most likely due to insufficient resolution of the LES study at these high non-dimensional frequencies. Although the low frequency regions differ, the shape of the wall-jet's spectrum at high frequencies is similar to that of Rusche (2011) and Farabee & Cassarella (1986).

	Wall-Jet at x=1358mm U_o=60m/s	Farabee & Cassarella (1986)	Rusche (2011)	Yang & Wang (2011)
Re_ϑ	1021	4079	7281	3065

Table 4-1. Previous studies and their corresponding momentum thickness Reynolds numbers

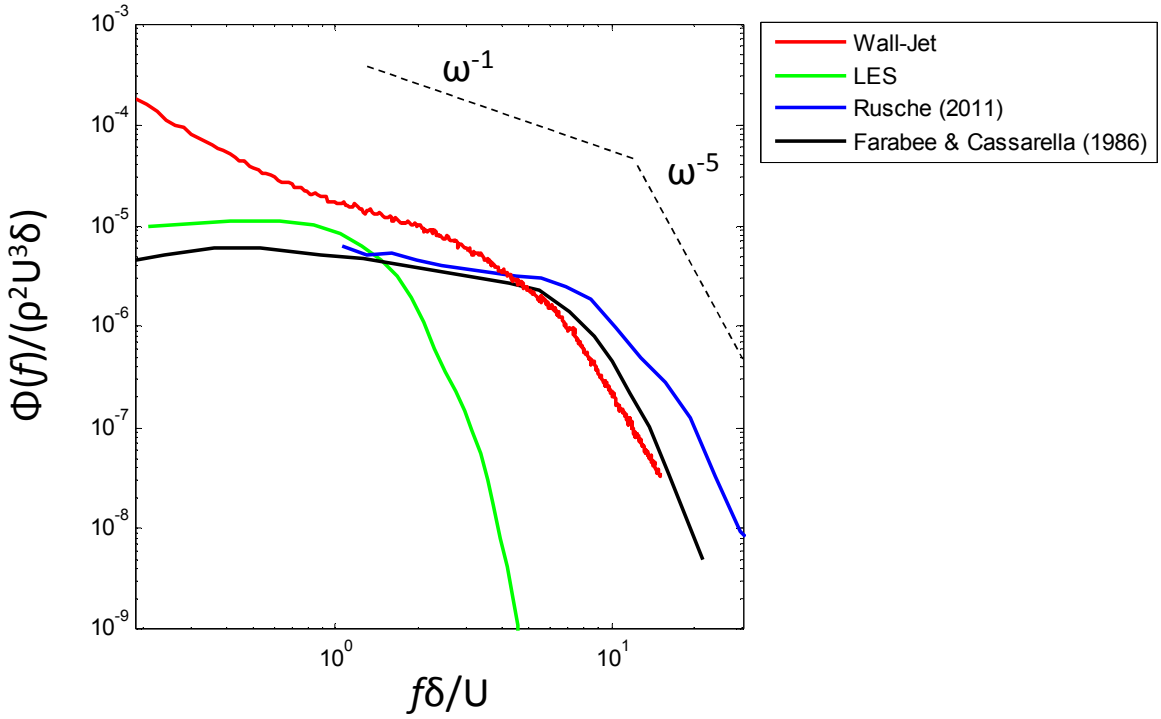

Figure 4-1. Comparison of normalized smooth wall pressure spectra from several studies with the unperturbed wall pressure spectrum of the wall-jet at U_o=60m/s

The wall pressure was recorded at 14 locations in and around the fetch of 42 cubic elements as shown in Figure 4-2. The same notation as in Figure 4-2 will be used to identify the results at each measurement location. The wall pressure measurement location was held fixed at x=1358mm and z= -43mm as the rough surface wave moved in relation. The streamwise variation through the fetch can be analyzed by focusing on positions C1-C5. Figure 4-3a shows the wall pressure recorded at these positions for U_o=60m/s compared to the smooth wall undisturbed wall pressure fluctuations. At position C1, which is 8.25mm upstream of the fetch, the wall pressure is slightly elevated from the smooth wall at all frequencies. The three internal measurement locations, C2, C3, and C4, all produce similar results below 5kHz which are significantly elevated from the upstream position. The scale of the wall pressure fluctuations on the convective ridge at 5kHz are approximately 1.8mm, roughly half the size of the roughness elements. Above 5kHz, the pressure fluctuations which begin 4dB above the smooth wall fluctuations at C2 tend back to the smooth wall spectrum with increasing streamwise distance. The wall pressure at Position C5, 8.25mm behind the roughness fetch, does not continue this trend. Behind the roughness fetch the wall pressure fluctuations increase at all frequencies and are above the smooth wall spectrum by up to 6dB. This suggests that the boundary layer is being displaced by the fetch of cubic roughness elements and that the presence of the downstream elements affects the upstream pressure fluctuations. The flow reattaches downstream of the roughness fetch creating a region of increased wall pressure fluctuations, especially in the frequency region 1kHz to 10kHz.

Positions C3 and C6 to C9 were recorded to analyze the spanwise change of wall pressure fluctuations over the fetch. These measurement locations have the same relative spacing among the nearest elements but are displaced spanwise between element rows. Positions C6 and C9 are located outside of the fetch, therefore, these positions only have elements in one spanwise direction. Figure 4-3b

shows the recorded wall pressure at these various locations for U_o=60m/s. There is very little change between positions. The two outside locations, C6 and C9, have slightly weaker low frequency fluctuations, approximately 1.5dB. At higher frequencies the opposite is true, and these outside positions have a slightly stronger response.

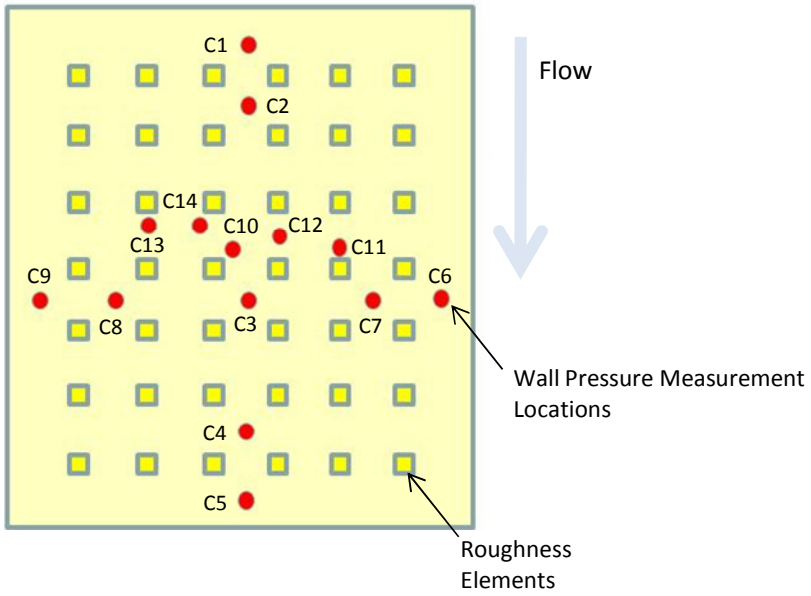

Figure 4-2. Wall pressure measurement locations inside 42 element fetch of cuboidal roughness

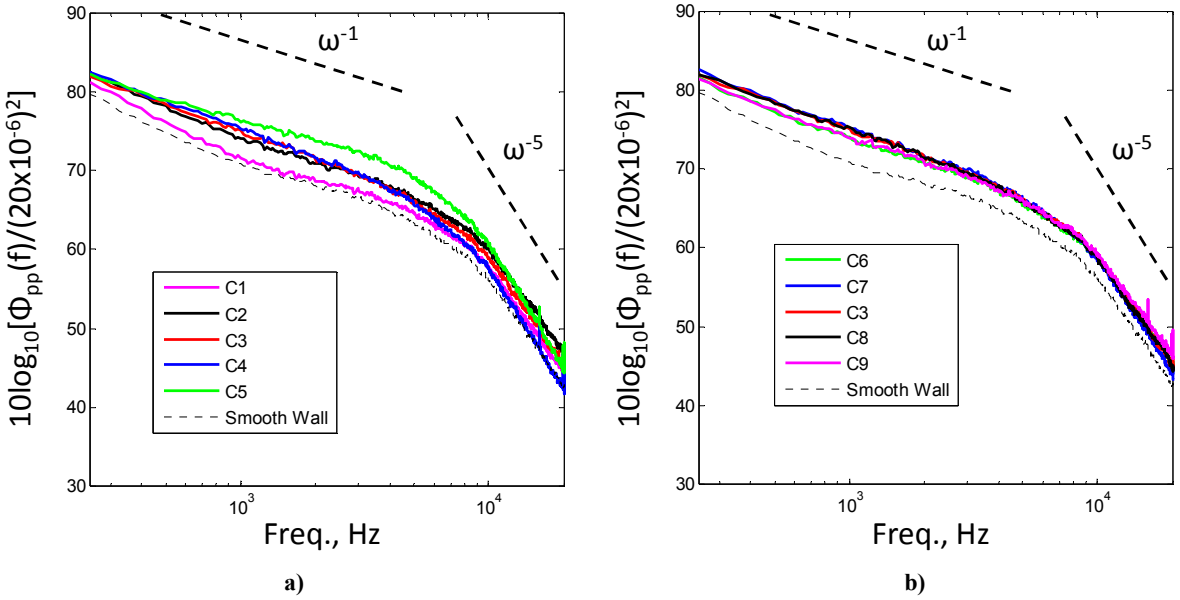

Figure 4-3. Variation of wall pressure in fetch of 3mm cubic elements at U_o=60m/s in the a) streamwise direction b) and spanwise direction

Since the relative wall pressure spectra recorded at similar interior locations across the span of the roughness fetch produce consistent results, positions C3 and C10 to C14 can be combined to compare the wall pressure around a single representative central element. Figure 4-4 compares the wall pressure spectra recorded at these locations with the smooth wall spectrum at U_o=60m/s. The wall pressure over this large element surface is clearly not homogeneous. The spectra not only differ in magnitude but in shape as well. Devenport *et al.* (2010) estimated the convection velocity of the smooth wall flow to be approximately 9m/s for U_o=60m/s. Therefore, frequencies below 7kHz correspond to flow structures convected with a characteristic dimension greater than 1.3mm. Below this frequency, the wall pressure fluctuations at every position were increased relative to the smooth plate. Above 10kHz, equivalent to flow structures smaller than 0.9mm, only the C13 and C14 positions, which are the closest measured downstream positions, recorded significantly elevated pressure fluctuations. The C11 position directly in front of the element showed a decrease in the high frequency pressure fluctuations. All others resembled the smooth wall data in this region with levels increased by approximately 2dB. Comparing positions C11 and C13, which are 1.7 element heights directly upstream and downstream of an element center, shows the wall pressure fluctuations at the upstream position are significantly lower than a similar distance downstream of the element center over all observed frequencies. These recorded wall pressure spectra are consistent with a horseshoe vortex wrapped around the base of the elements along with a region of separation behind the elements as seen in the LES results of Yang & Wang (2010). An upstream recirculation region produces an increase in low frequency pressure fluctuations and diminishing high frequency fluctuations as shown in wall pressure spectra of Farabee & Cassarella (1986) for the flow in front of a forward facing step. This is exactly the phenomenon as observed at position C11 upstream of the nearest roughness element. A similar effect is shown in the downstream separation region of a backward facing step in Farabee & Cassarella (1986). Position C13, downstream of the roughness element, has significantly increased low frequency fluctuations, but the high frequency fluctuations are also slightly greater than the smooth wall spectrum. This may be due to the relatively shorter separation region behind the roughness elements as compared to the step flows studied in Farabee & Cassarella (1986). Above 3kHz, pressure fluctuations recorded at the C14 position were greater than the recorded spectra at any other location. This position is downstream of the leading edges of the cubic roughness element from which the trailing legs of the horseshoe vortex would extend. Fluctuations above 3kHz correspond with structures equal to and smaller than the size of the roughness element, 3mm.

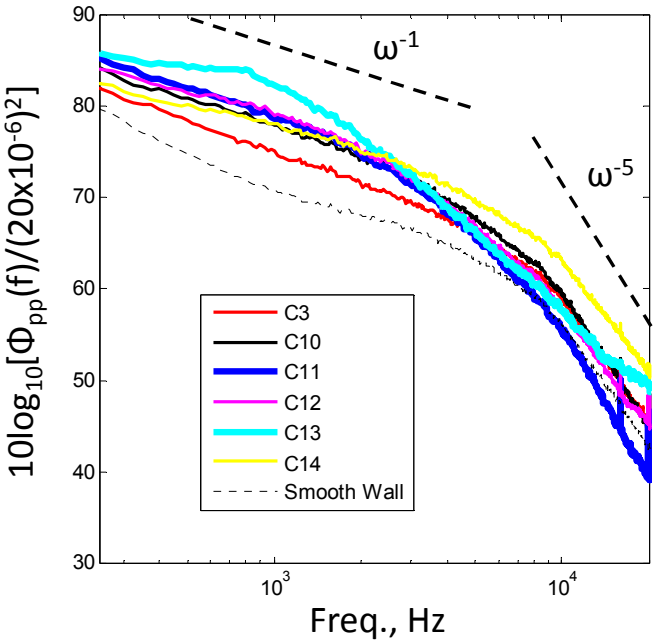

Figure 4-4. Wall pressure at various positions relative to nearest 3mm cubic element in 42 element fetch at U_o=60m/s

Figure 4-5 shows a direct comparison of the measured wall pressure spectra with the LES results of Yang & Wang (2011) at similarly scaled locations around cuboidal roughness. The cuboidal roughness in the LES study had a roughness height of 0.17", and elements were spaced 1". The incoming boundary layer thickness was 1.304" with an edge velocity of 45ft/s and the roughness Reynolds number was 168. These spectra are normalized on outer variables to collapse the low frequency region. The difference between measured spectra in the low frequency region is similar to the difference shown for the unperturbed wall pressure spectra shown in Figure 4-1 due to the mixing layer of the wall-jet. Like the unperturbed wall pressure spectra, the LES spectra roll-off at a much lower non-dimensional frequency than the measured wall-jet data. Again, this is most likely due to the large grid-scale of the LES unable to fully resolve the high frequency region. In the lower frequency region, the LES results produce more separation between the various measurement locations. This may indicate that the mixing layer of the wall-jet influences the roughness generated wall pressure fluctuations in this region while the local roughness has more of a dominating effect on the low frequency pressure fluctuations in a conventional turbulent boundary layer.

Comparison with the wall pressure spectra of Rusche (2011) shows the difference in experimentally measured wall pressure under a conventional turbulent boundary layer using the same configuration of cuboidal roughness used in this study with roughness heights of 3mm and a grid spacing of 16.5mm. The boundary layer in Rusche was 60mm thick and the edge velocity was 26.5m/s. The spectra in Figure 4-6 show the streamwise variation through the fetch of roughness. The low frequency regions of the recorded spectra show some differences between the two flows. The wall pressure fluctuations at position C2, one row into the roughness, do not rise significantly above the levels recorded in front of the fetch, C1, for the conventional turbulent boundary layer. Also, the data of Rusche (2011) do not show the same increased pressure fluctuations behind the fetch indicating a separated boundary

layer. This is most likely due to the larger boundary layer thickness in Rusche's experiment, 60mm, compared to the wall-jet's 16.4mm thickness at U_o=60m/s.

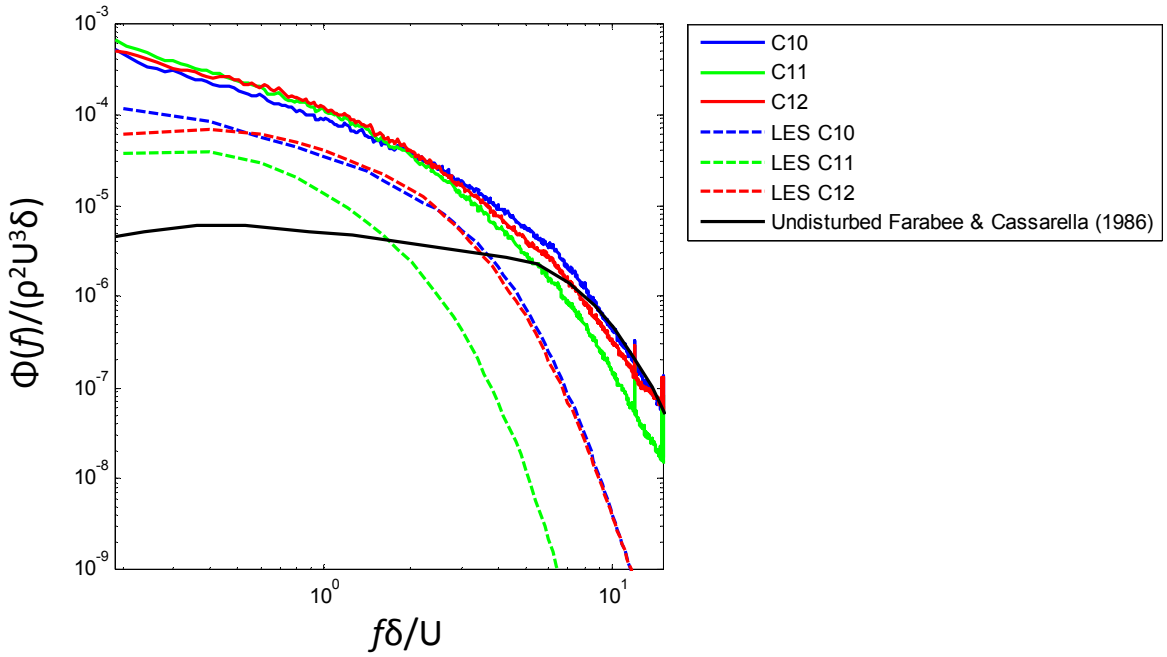

Figure 4-5. Comparison of measured normalized wall pressure spectra from a fetch of 3mm cuboidal roughness compared to similar cuboidal roughness relative locations from the computational study of Yang & Wang (2011)

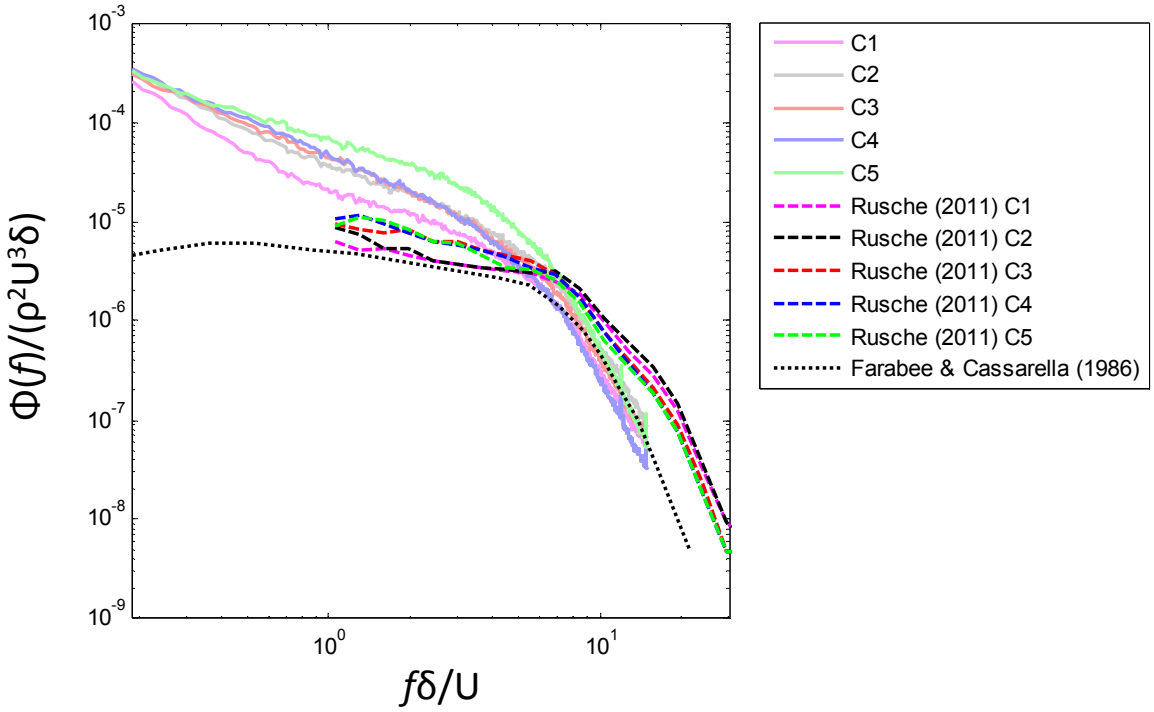

Figure 4-6. Normalized wall pressure spectrum through a fetch of 3mm cuboidal roughness compared to the streamwise variation presented in Rusche (2011)

To apply Glegg & Devenport's (2009) theory of roughness noise as given in Equation 3-19, a representative single point wall pressure spectrum is needed, particularly, a spectrum that is representative of the portion of turbulent pressure fluctuations that are scattered into radiated noise. Since this large element fetch has a highly inhomogeneous wall pressure field, no single point wall pressure spectrum could perfectly represent the portion of wall pressure fluctuations scattered to the far field. Instead, an approximation is assumed using the average of the wall pressure spectra measured at each of the presented locations. The average wall pressure was calculated using the recorded pressures at positions in Figure 4-4 along with the upstream and downstream fetch locations, C1 and C5, for nozzle exit velocities between 20 and 60m/s. These averaged spectra are shown in Figure 4-7. The recorded pressures at positions C2, C4, and C6 to C9 were ignored so that the central location between elements was not biased over other positions in the average.

Another approach would be to use the wall pressures recorded at the C11 position to represent the scattered turbulent fluctuations. According to Yang & Wang (2009), the pressure fluctuations on the front of the roughness element are the most efficient scatterer of sound in the streamwise direction. These pressure fluctuations recorded at various nozzle exit velocities are also shown in Figure 4-7 compared to the averaged spectra.

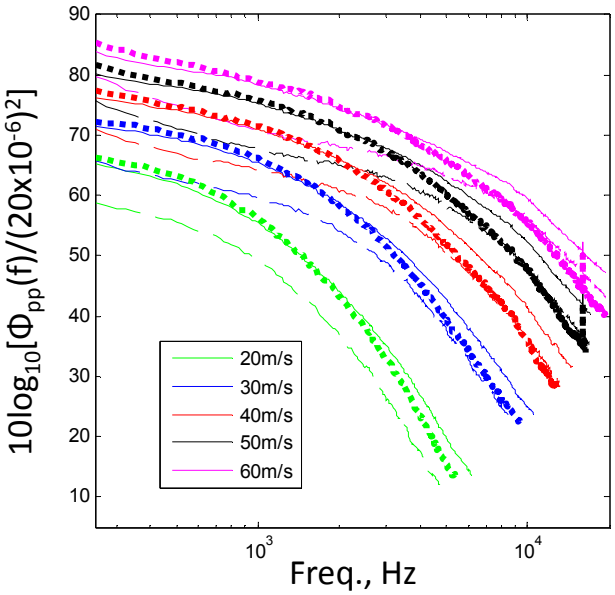

Figure 4-7. Wall pressure spectra for cubic element fetch at various nozzle exit velocities recorded at position C11 (dot) and averaged over the surface (solid) compared to the smooth wall (dash)

4.1.2 Far Field Noise

Far field noise was recorded during each separate wall pressure measurement. The far field microphone was located upstream of the roughness at x=1029mm, y=469mm and z=0mm. The position of the roughness fetch was shifted for each wall pressure measurement so that the lead row of roughness began at x= 1255mm to 1366mm and the spanwise center varied from z= -92.5mm to 6.5mm. Even though the fetch location was shifted for each near field measurement, the recorded far field noise was not significantly altered. The measured noise from the cubic element fetch is shown in Figure 4-8a compared

to the background levels of the tunnel. At 20m/s there is very little significant sound produced by the 3mm cubic roughness fetch. As the nozzle velocity is increased, the signal-to-noise ratio increases to a maximum of 18dB at U_o=60m/s. Figure 4-8b shows the background-subtracted noise. To reduce uncertainty of the presented data, only roughness noise with a signal-to-noise ratio over 1dB is plotted. The uncertainty for the subtracted noise is 3.5dB, 1.5dB, and 1.1dB for regions with signal-to-noise ratios of 1dB, 5dB, and 10dB, respectively. As the nozzle velocity is increased from 20-60m/s, the maximum recorded far field produced by the rough surface increases by 26dB.

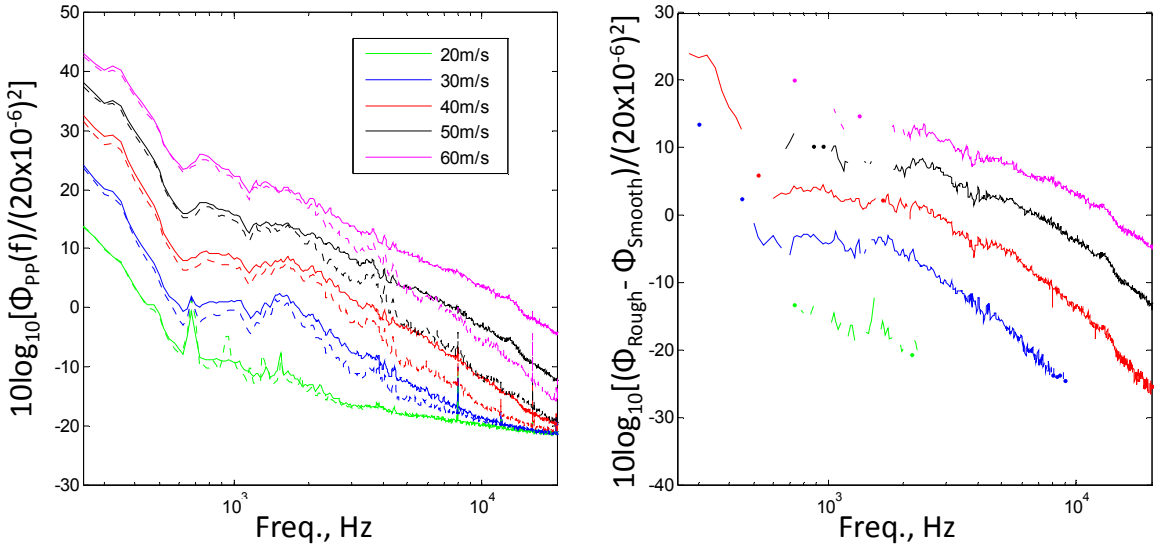

a) b)

Figure 4-8. Far field sound from cubic element fetch at various nozzle exit velocities compared to the background noise a) raw b) and background subtracted

4.1.3 Radiated Noise Normalization and Estimate Comparison

Figure 4-9 and Figure 4-10 show the far field noise of Figure 4-8b normalized on the average wall pressure spectra and the wall pressure measured just in front of the roughness element, respectively. The averaged wall pressure spectra collapse the radiated noise on a slope of $\omega^{1.25}$. The single-point wall pressure spectra recorded in front of the element produces an ω^2 collapse over the majority of the analyzed frequency range. As the frequency increases above 4kHz, the collapse begins to break down and the data fan out in order of velocity using both methods. These measured normalizations have uncertainties of 3.64dB, 1.8dB, and 1.5dB for regions where the measured far field has a signal-to-noise ratio of 1dB, 5dB, and 10dB, respectively.

Noise estimates computed similarly as before in Chapter 3 are shown on each figure for comparison assuming acoustically compact sources. These estimates use Chase's (1980, 1987) wavenumber wall pressure spectrum and the local conditions for nozzle exit velocities of 40 and 60m/s for a smooth wall at x=1257mm. This includes the convection velocities as determined by Devenport *et al*. (2010) of 44% and 41% for U_o=40 and 60m/s, respectively. The estimations have been calculated for the far field measurement location using observer distances in Equation 3-1 measured relative to the spanwise center of the plate at x=1257mm.

The estimated normalized spectral shapes more closely resemble the measured normalization in Figure 4-9 using the averaged wall pressure spectra, although, the absolute results are approximately 5-9dB below the measured normalization. The error could be due to the assumption of a homogeneous wall pressure field inherent in Equation 3-19 which is obviously not the case as shown in Figure 4-4. The absolute levels of the normalized curves will be highly dependent on the measurement location of the single point wall pressure spectrum chosen to collapse the data. The 40m/s and 60m/s estimations do not produce a collapse as tight as the measured spectra, but only differ by approximately 2dB above 6kHz. At frequencies below 6kHz, the normalizations have large humps in them created by the convective ridge of the wall pressure wavenumber spectrum as it amplifies various regions of the surface slope wavenumber spectrum at different frequencies. The two estimated spectra only collapse within 5dB in this region. At higher frequencies, the convective ridge is much broader amplifying larger regions of the wavenumber space of the surface slope and the estimated normalized result becomes more linear.

The assumption of a homogeneous wall pressure spectrum depends on the scale of the pressure fluctuations scattering to the far field. The dominate portion of these scattered fluctuations are those on the convective ridge of the wavenumber wall pressure spectrum. Therefore, fluctuations at 500Hz and 20kHz are dominated by structures with sizes of 18mm and 0.45mm, respectively. The cubic roughness has dimensions of 3mm. Eddies of a similar size would pass at a frequency of 3kHz. Consequently, the assumption of a homogeneous wall pressure spectrum may be more valid at frequencies below 3kHz where the fluctuations are larger than the roughness elements. There isn't a clear difference between the higher and lower frequency regions showing that the estimated values are closer to the measured normalizations at lower frequencies in Figure 4-9 which uses the average wall pressure spectra, but Figure 4-10, using the single point measurement, shows a clear deviation from the estimation at approximately 3kHz. The lower frequency side of the measured data in both figures has a higher uncertainty, near 3.64dB, slightly less than the difference in the spectra showing that these estimations are quite reasonable below 3kHz. Dividing the spectra in this way according to structure size implies that the low frequency fluctuations encountered by the element would be dominated by the large eddies in the turbulent boundary layer and that the high frequency would be attributed to local effects of the roughness. The shapes of the measured spectra are correctly estimated using the average wall pressure spectra. This suggests differences in the long eddy wavenumber regions and short eddy wavenumber regions associated with the average local flow must still behave in a form consistent with the Chase wavenumber wall pressure spectrum having a convection velocity that is approximately 41% of the edge velocity.

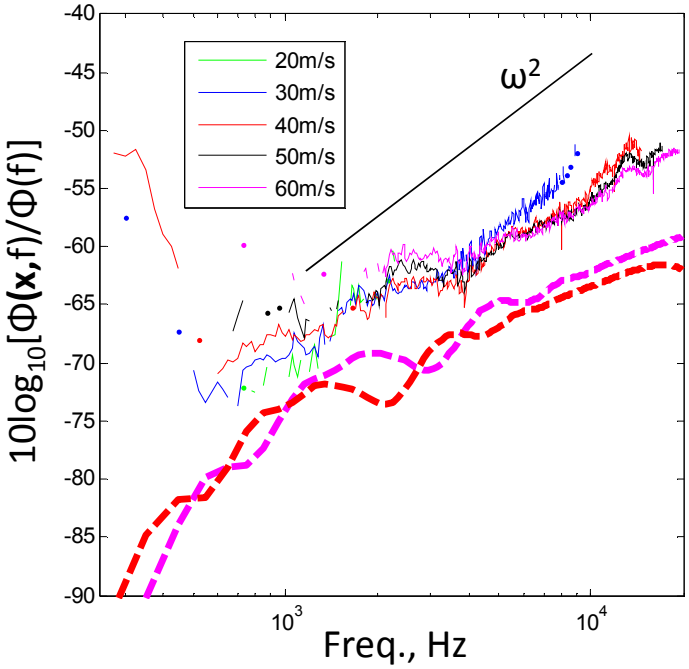

Figure 4-9. Measured far field normalization using average wall pressure compared to estimation

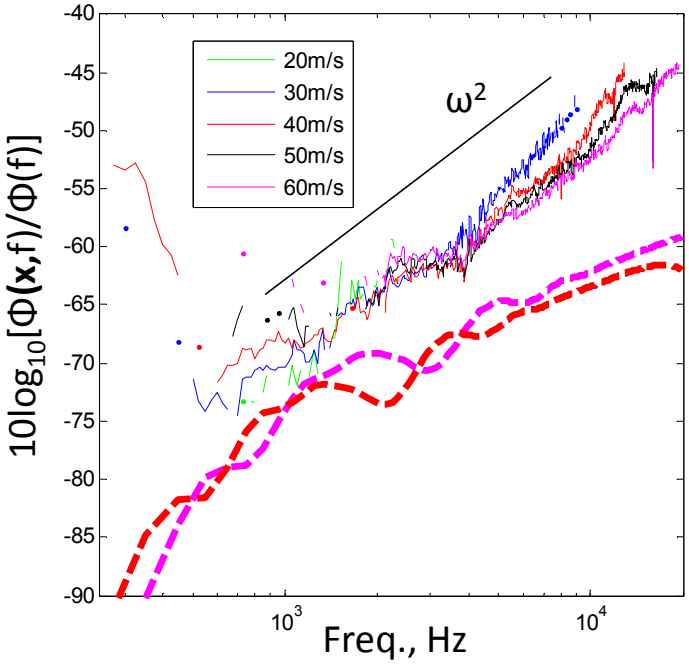

Figure 4-10. Measured far field normalization using single point wall pressure compared to estimation

4.2 Measurements from 42 Element 3mm Hemispherical Roughness

4.2.1 Wall Pressure

A similar analysis of the wall pressure variation throughout a 42 element fetch of 3mm hemispheres was conducted. The wall pressure measurement locations are given in Figure 4-11. Figure 4-12 shows the streamwise and spanwise variation through the roughness fetch at similar locations as measured in the cubic element fetch. Figure 4-12a shows, as the streamwise position increases, the wall pressure fluctuations increase as well until midway through the fetch at position H3. Beyond this streamwise point there is little variation in the measured spectra. Downstream of the fetch at position H5, the pressure fluctuations remain the same as the upstream values. An increase at all frequencies, as observed in the cubic element fetch, is not measured. This indicates that a similar boundary layer displacement effect may not be present for the hemispherical fetch. This agrees qualitatively with the findings in Yang & Wang (2011) that observes the difference between fetches of hemispherical and cuboidal roughness using LES. The LES shows that the cuboidal roughness creates a larger disturbance in the flow having a bigger separation region downstream of the elements.

There is little spanwise variation of the wall pressure as measured through the center of the roughness fetch shown in Figure 4-12b. Similar to the cubic roughness, position H8, which is bound by roughness elements in only one spanwise direction, has a slightly suppressed lower frequency region and increased higher frequency region. The measurements at all frequencies are 2 to 5dB above the smooth wall pressure fluctuations.

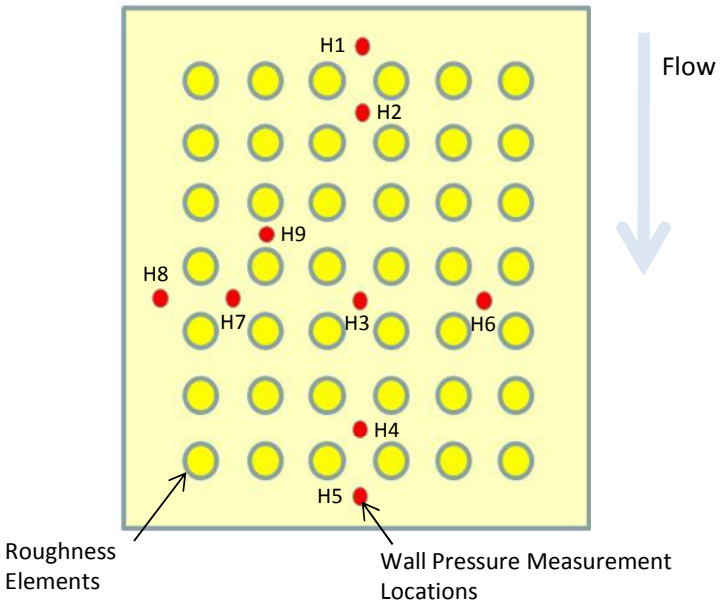

Figure 4-11. Wall pressure measurement locations inside 42 element fetch of 3mm hemispheres

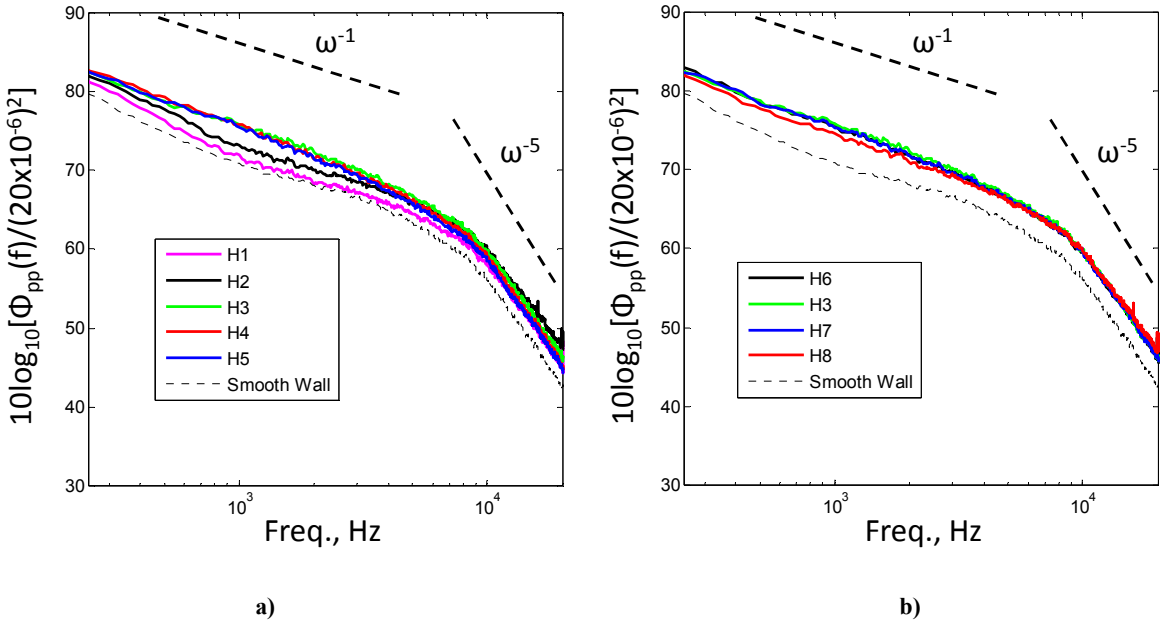

Figure 4-12. Variation of wall pressure in fetch of 3mm hemispherical elements at U_o=60m/s in the a) streamwise direction b) and spanwise direction

The uniformity of the spanwise measured wall pressure enables a comparison of the varying element relative positions as if they were recorded in relation to similar elements. Figure 4-13 shows a comparison between a measurement at a central position of the roughness fetch, H3, and a position located in-line streamwise between two elements, H9. The wall pressure fluctuations are greater for all measured frequencies in the wake of an element at H9 by up to 9dB. This is consistent with the findings of Yang & Wang (2010) which show that the RMS pressure fluctuations are greater in the wake of the elements than between streamwise columns. Again, this figure highlights the great inhomogeneity of the wall pressure fluctuations in large element surfaces as compared to the previously studied small boundary layer to roughness height ratio stochastic roughness in Alexander (2009) and Devenport *et al*. (2011).

Figure 4-14 shows a comparison of the measured data with the streamwise variation through a hemispherical roughness fetch with equivalent dimensions as recorded by Rusche (2011). Rusche shows a dip in the high frequency pressure fluctuations downstream of the lead row of roughness at a non-dimensional frequency of 10 that is not observed in the wall-jet data. The low frequency region of Rusche's spectra do not sequentially increase with streamwise distance into the roughness fetch, but the large fluctuations in his presented spectra, especially for the H2 position, suggest that the trend differences with the wall-jet may be due to uncertainty associated with the measurements given in Rusche (2011).

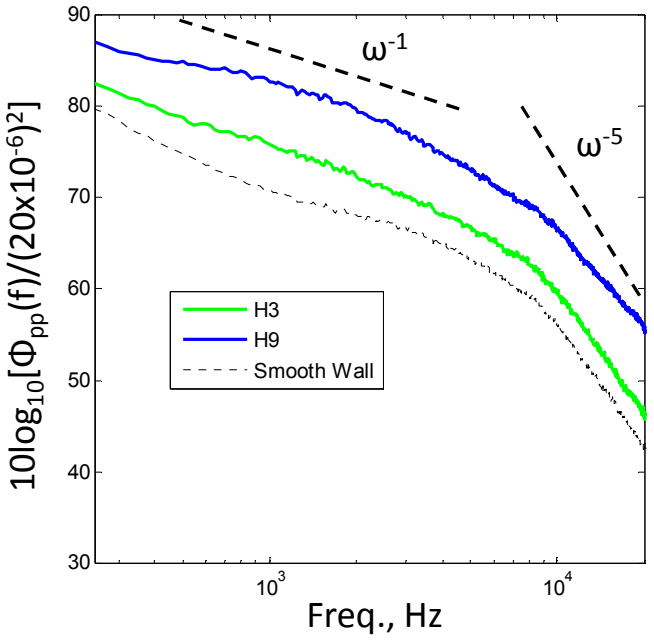

Figure 4-13. Wall pressure at various positions relative to nearest 3mm hemispherical element in 42 element fetch at U_o=60m/s

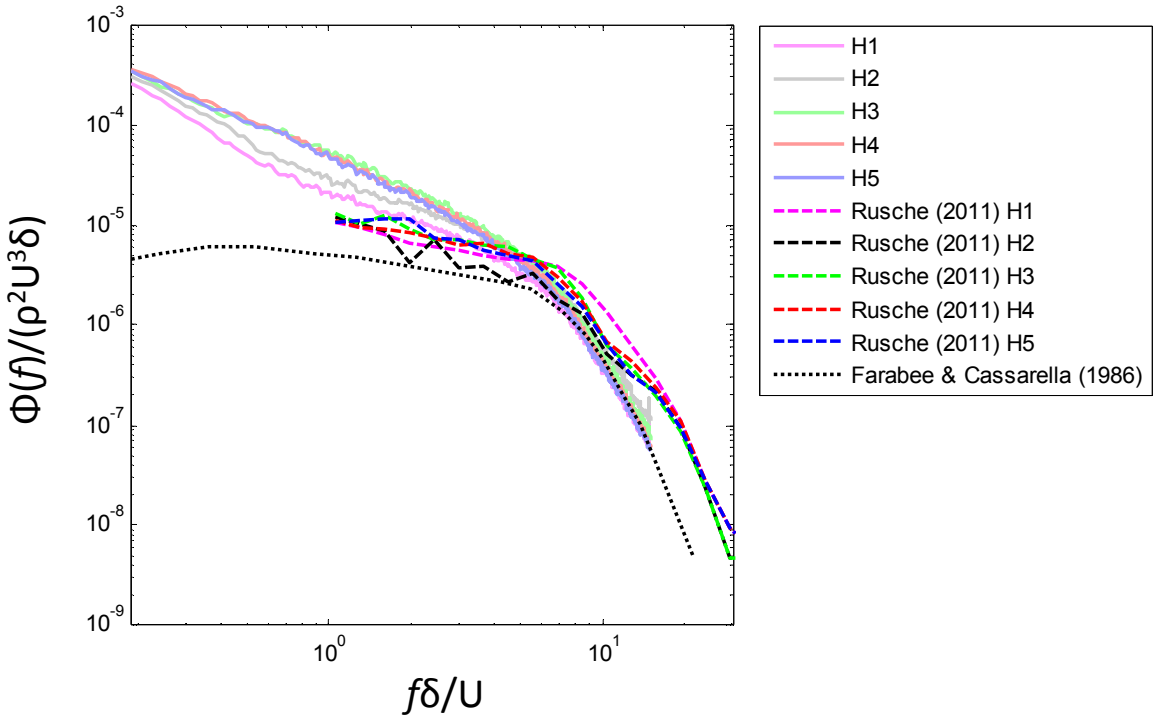

Figure 4-14. Comparison of the normalized wall pressure spectrum from the fetch of 3mm hemispherical roughness with the study of Rusche (2011)

The average wall pressure over the hemispherical element fetch was calculated using the spectra recorded at positions H1, H3, H5, and H9 for each nozzle exit velocity. These average spectra are compared to the measured smooth wall undisturbed pressure fluctuations in Figure 4-15. The smooth and rough wall spectra have a similar shape but are increased by approximately 4-5dB for all frequencies and velocities. These calculated average wall pressures will be used to normalize the recorded far field spectra from the hemispherical roughness.

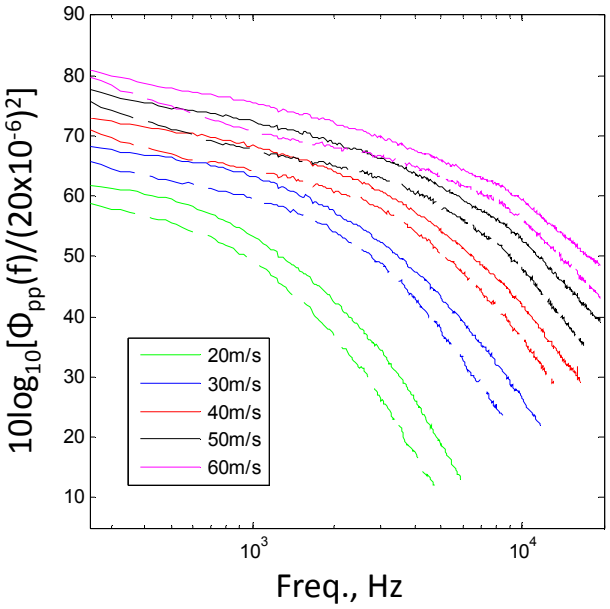

Figure 4-15. Average wall pressure spectra for hemispherical element fetch at various nozzle exit velocities averaged over the surface (solid) compared to the smooth wall (dash)

4.2.2 Far Field Noise

The hemispherical element fetch produced very little measurable far field noise discernable from the tunnel's background noise. Figure 4-16 shows the raw and background subtracted noise from the hemispherical element fetch as measured from the same far field position as the cuboidal roughness at x=1029mm, y=469mm and z=0mm. Again, the location of the lead spanwise center of the fetch varied over x= 1255mm to 1366mm and z= -92.5mm to -10mm and made a negligible difference in the recorded far field. The signal-to-noise ratio was very low for this surface, so that Figure 4-16b uses a lower limit of 0.5dB to exclude noise from the presented data instead of the 1dB limit that was used for the far field results from the cuboidal roughness. This lower tolerance is responsible for the noisier appearance of Figure 4-16b as compared to Figure 4-8b. This increases the maximum uncertainty level of the presented spectra in Figure 4-16b to 5.3dB for frequencies where the signal-to-noise ratio is 0.5dB.

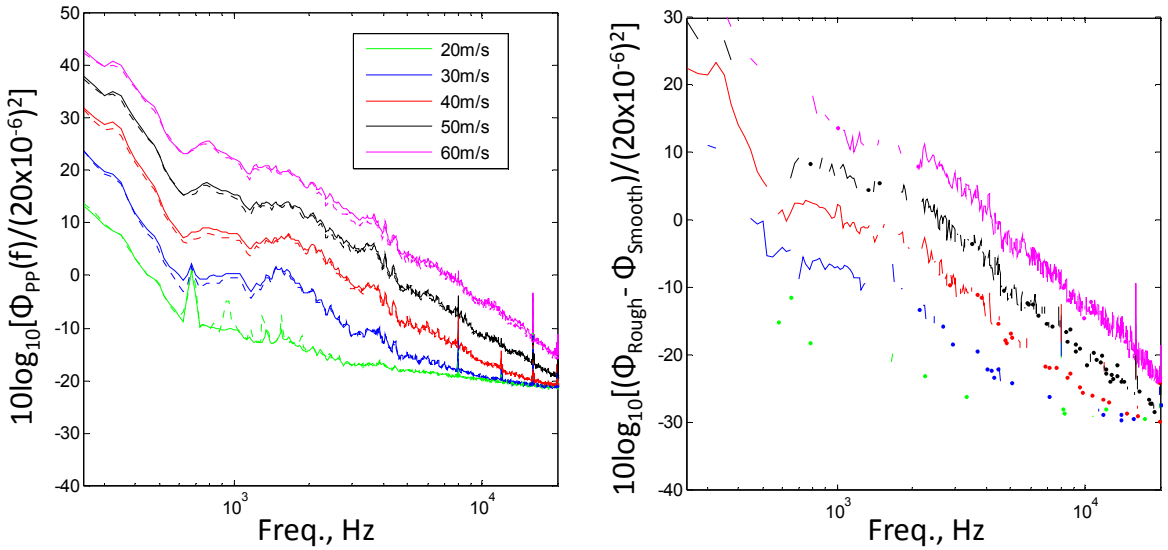

a) b)

Figure 4-16. Far field sound from hemispherical element fetch at various nozzle exit velocities compared to the background noise a) raw b) and background subtracted

4.2.3 Radiated Noise Normalization and Estimate Comparison

Using the averaged measured wall pressure, the far field/near field normalization is computed in Figure 4-17 for the 42 element fetch of 3mm hemispherical roughness. The normalization is flat unlike the cuboidal roughness results. These normalized results are similar to those found in Alexander (2009) from a 3mm hemispherical surface. In this previous study, the reason for the flat spectral shape and lack of collapse was attributed to an inaccurate representation of the inhomogeneous wall pressure field of the surface. Again, shown on Figure 4-17, Glegg & Devenport's (2009) roughness noise formulation was implemented to provide estimates of the normalization using the Chase single point wall pressure spectra for nozzle exit velocities of 40m/s and 60m/s. Like the cuboidal roughness fetch, the estimated results correctly predict the shape of the spectra but do not accurately predict the magnitude. The estimated and normalized spectra only agree within 11dB at lower frequencies, but are more accurately predicted at higher frequencies above 7kHz. These measured spectra have a higher uncertainty than the cubic fetch data presented in Figure 4-9 due to the extended lower limit of the signal-to-noise ratio of the presented data, 0.5dB. For the spectra in Figure 4-17 corresponding to regions where the signal-to-noise ratio of the far field data is approximately 0.5dB, the uncertainty is as large as 5.5dB. This resolves some of the difference between measurement and estimation. Unfortunately, there is not a sufficiently large frequency range of measurable roughness noise to make any further conclusions on the quality of the prediction, specifically regarding the relation of the 40m/s and 60m/s normalizations, but clearly the functional relationship of the roughness geometry and radiated far field noise is being captured by the theory of Glegg & Devenport (2009) to predict this dramatic shift in expected normalized shape between the cuboidal and hemispherical roughness. Combined with the results of Figure 4-9 and Figure 4-10 for the cuboidal roughness, these estimations show that predictions of roughness noise for surfaces with even large h/δ can produce reasonable results within approximately 5dB for regions where the turbulent structures of the boundary layer are significantly larger than the roughness elements.

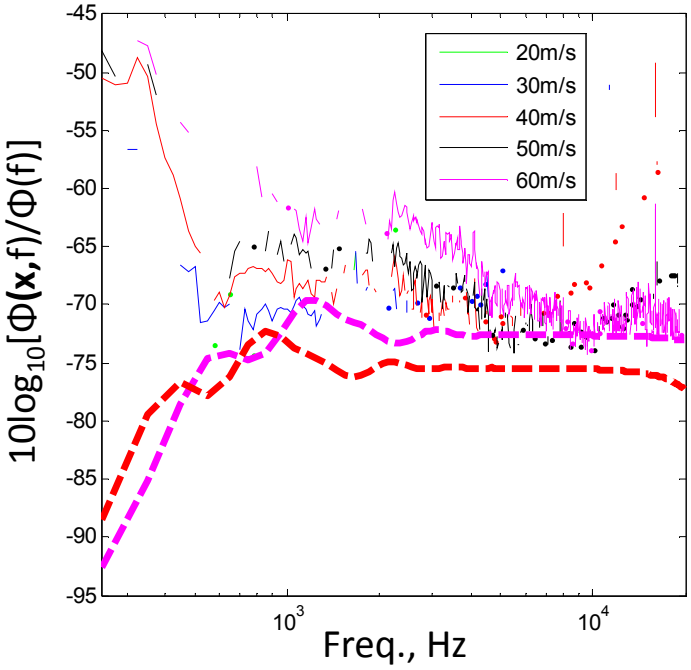

Figure 4-17. Measured far field normalization using average wall pressure compared to estimation

4.2.4 Comparison of 42 Element Surfaces of Hemispherical and Cuboidal Roughness

Figure 4-18 shows a comparison between similar element relative wall pressure measurement locations, between the final two spanwise rows of the roughness centered between elements, in the cuboidal and hemispherical roughness fetches. The low frequency fluctuations up to 5kHz are approximately equivalent. Above 5kHz, the pressure fluctuations produced by the hemispherical surface rise above the cubic element spectra by 5dB. This could be due to the proximity of the wall pressure measurement location to the roughness elements. Although the roughness heights and grid spacings are equivalent between the two surfaces, the base of the hemispherical elements is twice that of the cuboidal elements. Therefore, the space between streamwise columns of hemispherical roughness is 3mm narrower than the cuboidal roughness. This difference in relative distances may influence the results above 5kHz, especially since the size of the eddies in this frequency range are smaller than the roughness elements.

The far field sound from the cuboidal roughness is greater than that produced by that hemispherical roughness for the entire frequency range where noise was discernable above the background as shown in Figure 4-19. The difference increases with frequency by up to 18dB at 20kHz. At lower frequencies, below 1kHz, the noise from the hemispherical elements may surpass that of the cuboidal roughness, but no definitive conclusion can be made about the shape of the spectra in this region. Referring back to the measured wall pressure spectra in Figure 4-18, it can be concluded that the far field sound of a discrete large element rough surface cannot be inferred from the surrounding wall pressure alone. The hemispherical roughness produces more intense pressure fluctuations in the same frequency range that the cuboidal roughness has an 18dB advantage in the far field.

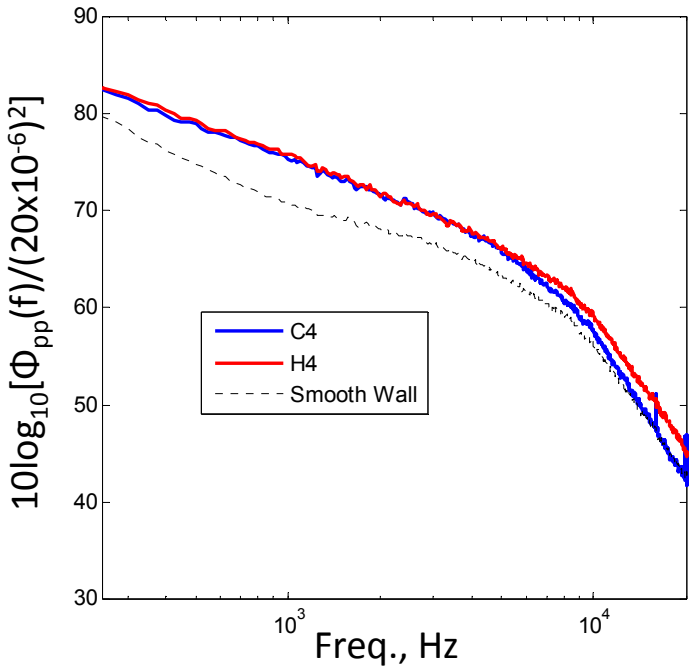

Figure 4-18. Comparison of wall pressure in cubic and hemispherical element fetch at U_o=60m/s

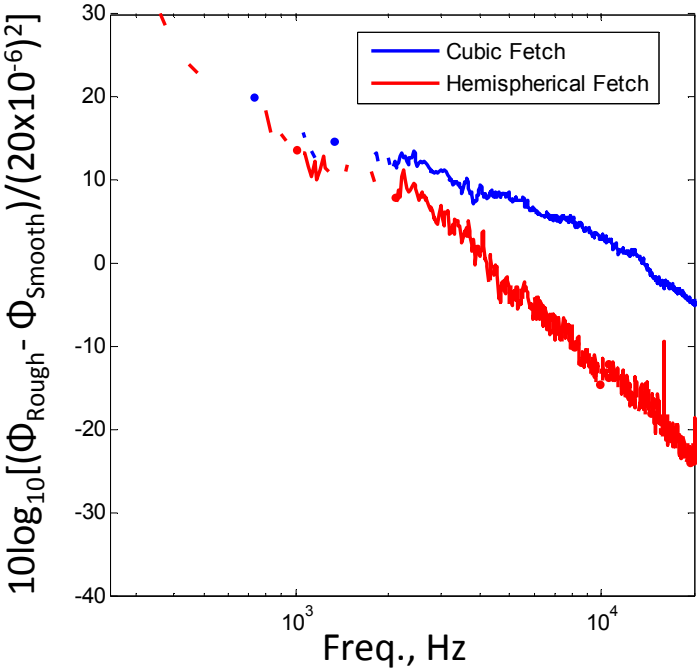

Figure 4-19. Background subtracted far field noise from cubic and hemispherical roughness fetch at U_o=60m/s

4.3 Measurements from 610mmx305mm Fetch of 3mm Hemispherical Roughness

4.3.1 Wall Pressure

A closer analysis of the variation in wall pressure around 3mm hemispherical elements was conducted using a 610x305mm fetch with 703 elements arranged with the same grid spacing as the 42 element fetch, 16.5mm. The wall pressure measurement locations are shown in Figure 2-27a. These element relative measurement locations are at a greater distance into the rough surface as compared to the similar measurements in the 42 element fetches, roughly 140mm as compared to 50mm from the leading edge. The wall pressure results from these positions at U_o=60m/s are shown in Figure 4-20. Locations LH7 and LH8 are omitted from this figure because these results were equivalent to those recorded at locations LH2 and LH1, respectively, due to the symmetry of the flow. Like the 42 element fetch, the local elements dominate the surrounding wall pressure field producing widely varying spectral shapes and magnitudes over the roughness area. The spectra vary less at lower frequencies especially below 1kHz where the structure scale on the convective ridge have length scales of approximately 9mm, much larger than the size of the roughness. These larger eddies are less impacted by individual roughness elements, and therefore, the measured wall pressure spectra in this region should be more uniform. The magnitudes differ by up to 12dB at 20kHz depending on the measurement location. The spectra at positions LH3 and LH5 may indicate a separation region just upstream and downstream of the roughness elements which produce greater low frequency fluctuations with high frequencies similar to or below the smooth wall spectrum. Unlike the pressure spectra recorded from the cubic roughness, the upstream position produces stronger pressure fluctuations for all frequencies than at a similar distance downstream of an element.

Figure 4-21 displays a wall pressure comparison between similar roughness element relative measurement positions for the 42 element and 703 element fetches. Although very little difference was observed in the streamwise development of the wall pressure spectrum beyond the halfway point of the roughness in Figure 4-12a, the comparison in Figure 4-21 shows some variation between the recorded spectra at the H3 and LH4 measurement positions which only differ in streamwise distance from the leading edge. The difference between the two spectra is no greater than 3dB. The difference between the H9 and LH6 positions is greater. These positions are recorded in-line streamwise between two roughness elements. The spectra are similar at lower frequencies but differ by 4dB above 5kHz. These results indicate that the flow is still developing over the 42 element fetch only at a much slower rate than observed over the initial four rows of roughness as measured in the 42 element fetch.

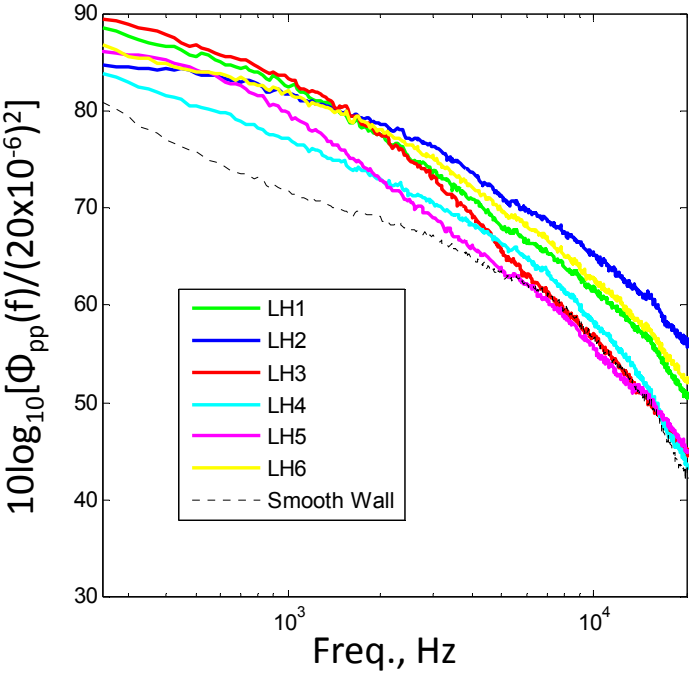

Figure 4-20. Wall pressure variation around elements in the 610x305mm element fetch of 3mm hemispherical roughness at U_o =60m/s

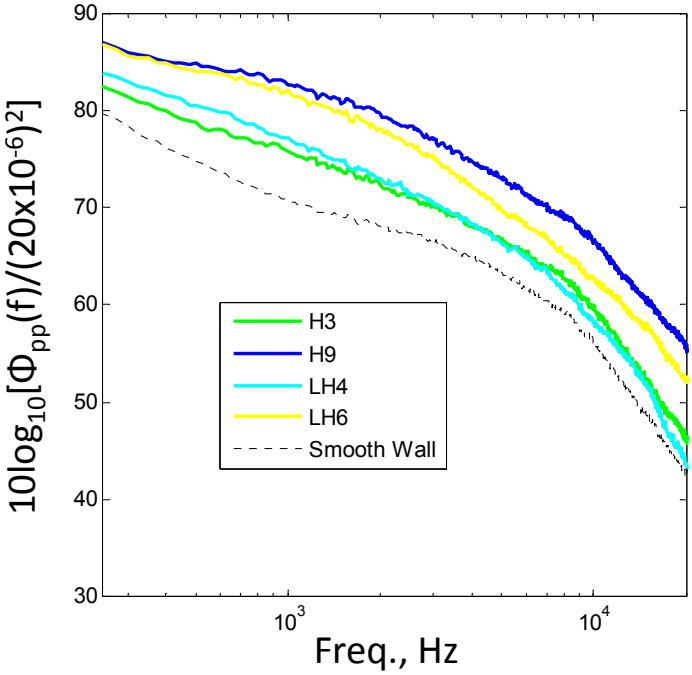

Figure 4-21. Wall pressure spectra comparison of 42 element and 703 element fetch of 3mm hemispheres at U_o =60m/s

4.3.2 Far Field Noise

The far field noise, as recorded from x=1029mm, y=469mm and z=0mm, produced by the larger fetch of 3mm hemispheres is shown in Figure 4-22. The spanwise center of the lead row of roughness was located at x=1255mm to1271mm and z= -66mm to 66mm. The increase in number of roughness elements increases the level of radiated noise, therefore, only data with a signal-to-noise ratio above 1dB is shown in Figure 4-22b. This is the same far field measurement position as used to record the far field data from the 42 element fetches. At nozzle exit velocities of above 40m/s there is a broad spike in the data at 13kHz. The magnitude of the lump increases with velocity, but the frequency does not vary. This is a similar phenomenon as observed in Alexander (2009). Alexander (2009) recorded a pair of these spectral peaks at 9kHz and 13kHz. An explanation of these peaks could not be given and were thought to be an error in the measurement, but the consistency of the occurrence indicates that it is a function of the surface. The surfaces used in each study contained exactly the same number of 3mm hemispherical elements with the same element spacing. The only difference between the surfaces was the manufacturing process. The surfaces used in this study were made from epoxy molded onto a Kevlar backing producing a substrate 0.30mm thick. The surfaces used in Alexander (2009) were created by molding a thicker rubber material and therefore had a 1.6mm thick substrate.

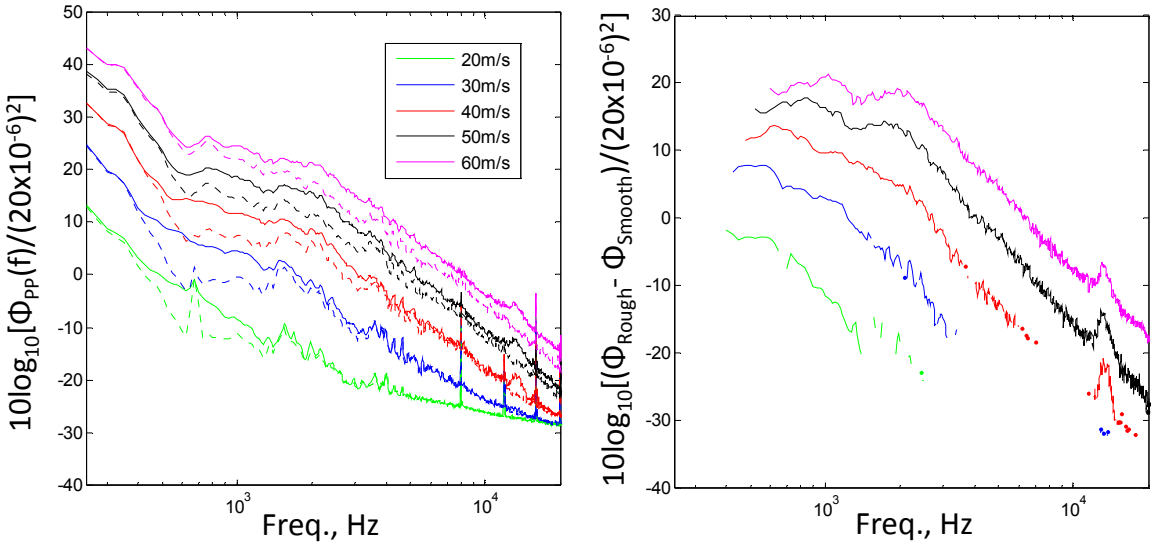

Figure 4-22. Far field sound from 3mm hemispherical element fetch at various nozzle exit velocities compared to the background noise a) raw b) and background subtracted

The same spectral peak at 13kHz is not seen in the recorded far field noise from the 42 element fetch of 3mm hemispherical roughness, but the cuboidal roughness produces a very slight lump in the far field spectra at a similar frequency as shown in Figure 4-8b. Figure 4-23 shows a comparison between the 42 element fetch and 703 element fetch of 3mm hemispherical roughness at a nozzle exit velocity of 60m/s. The magnitude of the far field noise is increased with the addition of more elements by approximately a factor of four while the number of elements increased by a factor of nearly seventeen. Therefore, unlike the far field noise recorded by Rasnick (2010) from large rock and cubic roughness,

these data from 3mm hemispherical roughness would not scale similarly on number of elements even within 3-4dB. As observed in the previous wall pressure measurements of Figure 4-21, the flow is still developing in the streamwise direction through the 42 element fetch. Therefore, the trailing elements in the larger 610x305mm fetch of roughness may produce different noise spectra than that of the leading elements as the flow develops through the roughness in the streamwise direction. Rasnick (2010) collapsed the noise from 610x305mm fetches of roughness with heights double the size of the 3mm hemispheres. Use of these larger elements may explain the unvarying per element source strength calculated in his study for multiple fetch sizes. The larger elements may have a more even source strength distribution because their noise is dominated by self-generated unsteady forces and not a scattering mechanism. Rasnick examined only smaller fetches of 3mm roughness elements and therefore may not have measured this change in streamwise source strength due to the developing flow field.

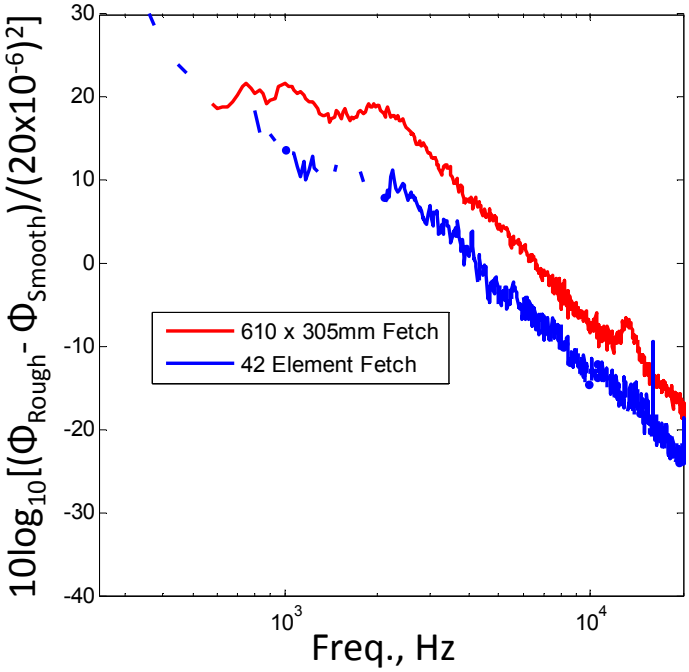

Figure 4-23. Far field comparison of noise from 42 element and 703 element fetch of 3mm hemispheres at U_o =60m/s

4.3.3 Radiated Noise Normalization and Estimate Comparison

The normalizations of the measured far field spectra on the average wall pressures recorded at positions LH1 through LH6 are shown in Figure 4-24 for multiple nozzle exit velocities. Again, the estimated spectra using Glegg & Devenport (2009) are shown alongside the measured data. For this larger fetch the estimated normalization more accurately predicts the observed data below 3kHz, where turbulent structures are larger than the roughness height, but estimations differ from measurement by up to 9dB at higher frequencies. Still, these differences are reasonable considering the inhomegeneity of the wall pressure fluctuations and that even approximate estimations of roughness noise have been unattainable until now. The levels of the average measured wall pressure spectra changed similarly to the levels of the measured far field in relation to the results from the 42 element fetch. Therefore, the measured normalized values of the two rough surfaces remained closely the same magnitude. The

estimated spectral levels increased because the magnitude of the wavenumber filter function, Γ, was increased due to the addition of more roughness elements. Although, the agreement between measurement and estimation seems to have increased for low frequencies, this is a poor indicator of the accuracy of this method. Calculating the measured far field normalizations for these large discrete element surfaces that produce highly inhomogeneous wall pressure fields entails choosing the proper single point wall pressure spectrum to collapse the data. This choice greatly impacts the level of the normalization. If the average used to normalize Figure 4-24 included the wall pressure at the front of the fetch, which has a magnitude comparable to the smooth wall spectrum, the disagreement between estimation and measurement would change. Therefore, the absolute level of the measured normalization is highly dependent on the chosen normalization spectrum.

The estimation fails to reproduce the peak created at 13kHz. The measured normalization produces the tightest collapse in this region, 6-20kHz, disregarding the peak magnitude at 13kHz. This spike may be an effect of the roughness geometry manipulating the flow field. This type of effect would not be reproduced by the simplified scattering theory of Equation 3-1, especially when applying a homogeneous smooth wall wavenumber spectrum to estimate the normalized results. Since the spike frequency does not depend on velocity, it must be related to a characteristic dimension of the surface. The characteristic acoustic lengthscale of a 13kHz signal is approximately 26mm. This is almost twice the element spacing of the rough surface but does not have a direct relation with any physical size of the surface. Also, this frequency gives a Strouhal number based on element height of 1.8 for U_o=60m/s which is exceedingly higher than the expected value for bluff body shedding, roughly 0.2. Aerodynamic measurements by Morton (2011) over the 42 element fetches show that the $\overline{v^2}$ and $\overline{u^2}$ turbulence levels, corresponding to the *y* and *x* directions, respectively, increase with streamwise distance through the fetch, but the $\overline{w^2}$ values, corresponding to the *z* direction, decrease. This suggests the flow is being channeled between rows. Although the 13kHz spike was not seen for the 42 element roughness, the increased streamwise length of the larger fetch may allow additional development of this effect creating this resonant peak.

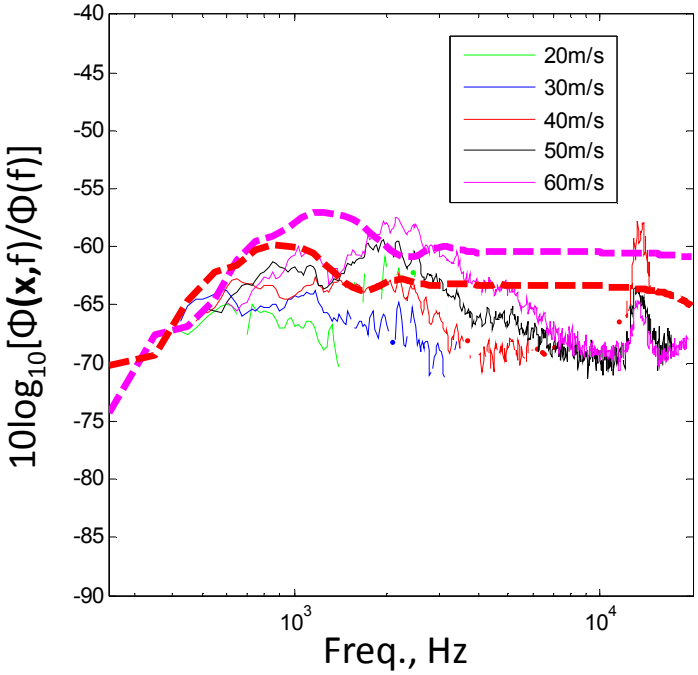

Figure 4-24. Measured far field normalization using average wall pressure from 610x305mm fetch of 3mm hemispherical roughness compared to estimation

4.4 Measurements from 610mmx305mm Fetch of Ordered 1mm Hemispherical Roughness

4.4.1 Wall Pressure

The inhomogeneous wall pressure fluctuations generated by the 3mm roughness made the application of Glegg & Devenport's (2009) theory given in Equation 3-1 contradictory to the main assumption in its derivation that the wall pressure field was uniform over the rough surface. To improve the comparison between the experimental conditions and the assumptions inherent in the applied theory, the roughness size was reduced to create a more homogeneous wall pressure field. Fetches of 1mm hemispherical roughness were chosen as this element size provided a deterministic roughness on the scale of the largest stochastic roughness studied in Alexander (2009), which was a 20 grit sandpaper surface. The sizes of the elements (1mm) and their spacing (5.5mm) were scaled similarly, but the number of elements was increased to 5886 keeping the planar area of the roughness fetch the same. Four wall pressure measurement locations were measured inside of this fetch and are diagramed in Figure 2-27b. Figure 4-25 shows the wall pressure spectra recorded at these four locations for U_o=60m/s. At this condition, h^+=66 and therefore, this flow is still in the fully rough regime, but h/δ is reduced from 18% for the 3mm case to 6%. The wall pressure spectra are not completely homogeneous, but show less variation than from the larger hemispherical roughness. Although, measurements were not completed at all the same locally scaled distances around individual elements as in Figure 4-20 for the 3mm hemispherical roughness. For the measured locations, the wall pressure spectra above 3kHz begin to differ by approximately 3dB. Eddies 1mm in size are associated with frequencies of 9kHz. The observed

effect of the roughness location extends down to 3kHz which corresponds to structures three times as large as the roughness height. At lower frequencies, the spectra appear to be uniform as expected.

The only direct comparison between similarly scaled element relative locations for the 3mm and 1mm 610x305mm hemispherical element fetches can be made between the LH4 and SH3 positions, which were both centered among a group of 4 elements. This comparison is shown in Figure 4-26. The wall pressure spectrum in the 1mm hemispherical roughness does provide less of a disturbance from the smooth wall at frequencies below 3kHz. Above this, both rough surfaces produce similar spectra. It was assumed that the smaller disturbances generated by the 1mm roughness translated to smaller disturbances on the wall pressure field as a whole. In this way, the wall pressure field could more justifiably be approximated as homogeneous over the considered frequency range. This assumption includes the wall pressure field over the surface of the roughness elements since this would be the part of the wall pressure field associated with the unsteady drag radiated to the far field.

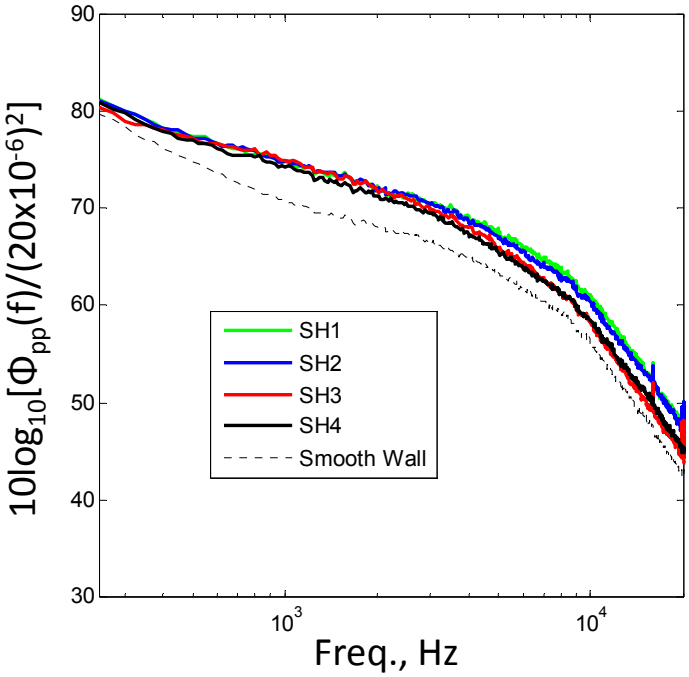

Figure 4-25. Wall pressure variation in a grid patterned fetch of 1mm hemispherical roughness at U_o=60m/s

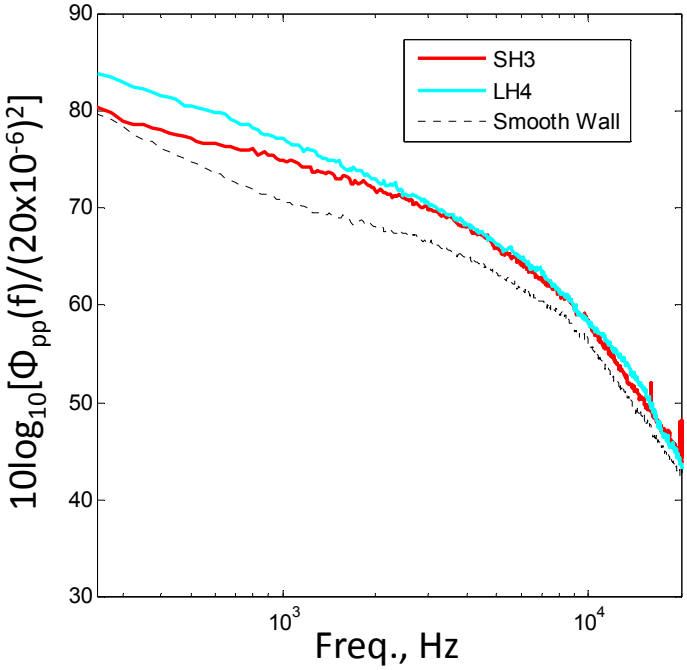

Figure 4-26. Comparison of wall pressure measured at similar locations in fetch 1mm and 3mm hemispherical roughness at U_o=60m/s

4.4.2 Far Field Noise

The far field noise was measured in an upstream position, the same as used for the previously presented far field measurements, and is shown in Figure 4-27. The lump at 13kHz, as observed from the 3mm hemispherical roughness in Figure 4-22b, is not seen for this surface, but if the phenomenon is a function of the roughness geometry or manipulation of the flow around the large roughness elements, it should not be expected for this smaller element roughness. If the broad spike in Figure 4-22b were to have a similar dimensional scaling of its wavelength as compared to the roughness size and spacing for this surface of 1mm hemispheres, the frequency of the phenomenon would be beyond the limits of this figure at 39kHz. There was very little signal-to-noise ratio at a nozzle exit velocity of 20m/s, but the noise shows a clear rise from the background at all other velocities. The maximum far field noise and peak frequency increase with velocity, similarly to the noise from the previously studied surfaces, but in this case, the shape of the spectra also change. A lump begins to appear at higher velocities between 2kHz and 3kHz altering the shape of spectra. As is all roughness noise, this lump is either generated by the unsteady loading due to vortex shedding or a scattering mechanism due to the imposed long wave pressure fluctuations of the overriding boundary layer flow. If the simplified theory of Glegg & Devenport (2009) correctly predicts this result than the scattering mechanism is confirmed.

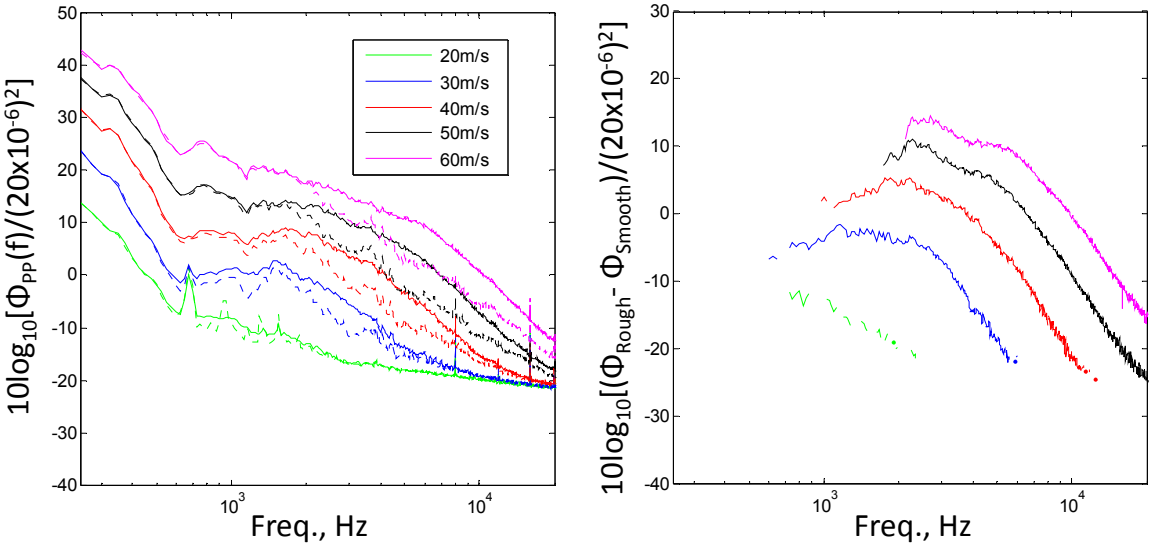

a) b)

Figure 4-27. Far field sound from 1mm hemispherical element grid patterned fetch at various nozzle exit velocities compared to the background noise a) raw b) and background subtracted

4.4.3 Radiated Noise Normalization and Estimation Comparison

The subtracted radiated far field noise in Figure 4-27b was normalized on the average wall pressure spectra computed from the four measurement positions for each nozzle exit velocity. The smaller roughness produces an ω^2 region that then deviates from this slope at approximately 2kHz. Above 2kHz, the data fan out in order of velocity. The estimations using Glegg & Devenport (2009) are very accurate over the measured frequency range within 5dB of the measured normalization at all frequencies and show a similar spectral behavior. Although the lump in the 60m/s spectra is not exactly predicted, the estimated 60m/s spectrum comes very close to recreating this behavior. The estimated spectrum produces a wavy normalized spectral shape that resembles the measured spectrum. A similar wavy pattern is estimated for the 40m/s spectrum but is shifted to lower frequencies. This may explain the presence of the suspect lump in the 60m/s spectrum that is absent for the 40m/s case. The lump may be beyond the extent of the measured data. The estimated and measured spectra are very similar and indicate that the sound production mechanism for roughness that is a small fraction of the boundary layer thickness is correctly captured by Glegg & Devenport's (2009) scattering theory. Differences between the estimated and measured spectra may be attributed to inaccurate modeling of the wavenumber wall pressure spectrum. Like the analysis in Devenport *et al.* (2010) using a wavy wall roughness, these rough wall results may provide an opportunity to probe the wavenumber wall pressure spectrum's form in the low wavenumber region.

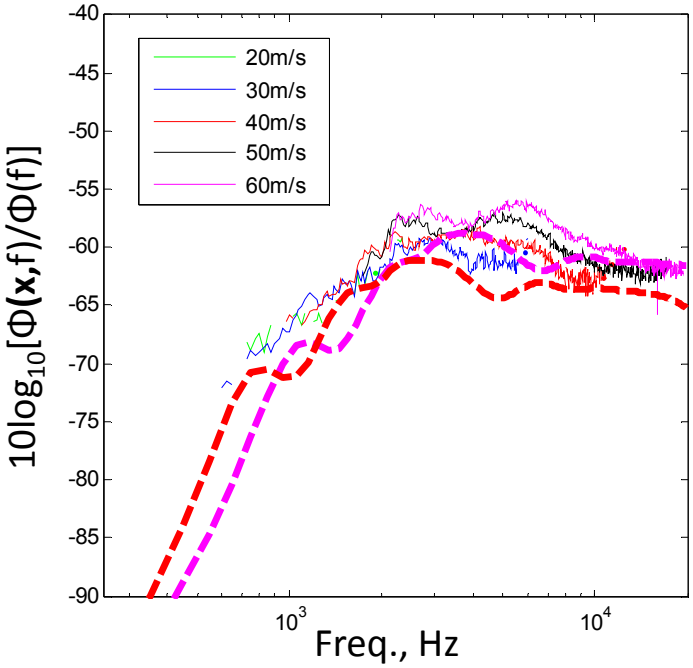

Figure 4-28. Measured far field normalization using average wall pressure compared to estimation

4.5 Measurements from 610mmx305mm Randomly Distributed 1mm Hemispherical Roughness

4.5.1 Wall Pressure

The wavenumber spectra of the ordered arrays are discrete at multiples of the element spacing wavenumbers. A randomly distributed roughness of 1mm hemispheres was tested to examine the difference between the continuous wavenumber spectrum of a random surface and these ordered surfaces. This is also a more accurate representative case of roughness encountered in engineering applications which are likely to be random in nature. The element locations were chosen randomly but their locations were known so that the exact analytical Fourier transform could still be determined as presented in Section 3.4.

The wall pressure was only recorded in one central location of the random 1mm hemispherical element fetch due to limits imposed by the size of the surface pressure microphone. This location was central to the roughness fetch and is shown in Figure 2-24. The position is 163.5mm from the leading edge of the roughness. The wall pressure fluctuations recorded in this location resemble the smooth wall spectral shapes but are elevated by 4-7dB for all velocities and frequencies.

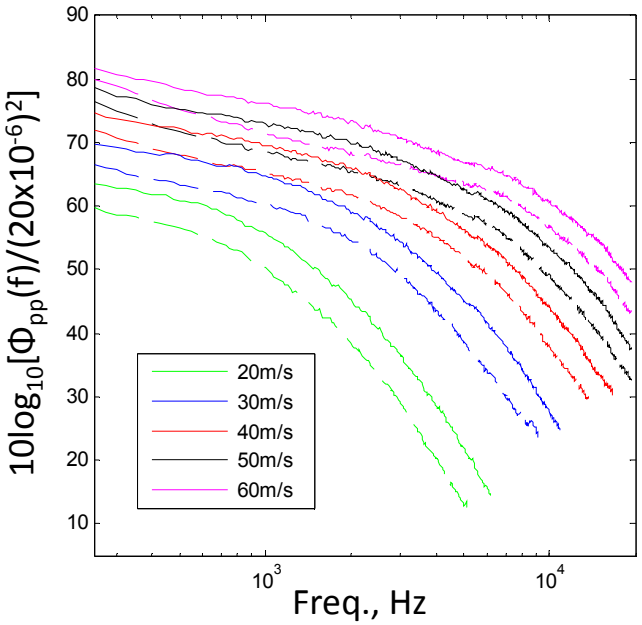

Figure 4-29. Wall pressure spectra for 1mm hemispherical element fetch at various nozzle exit velocities (solid) compared to the smooth wall (dash)

Figure 4-30 is a comparison of the wall pressure measured inside of the fetch of randomly located 1mm hemispherical roughness to that of the averaged wall pressure spectrum from the ordered 1mm roughness. The fluctuations at this single position are slightly elevated from this averaged spectrum but the two spectra have approximately the same shape.

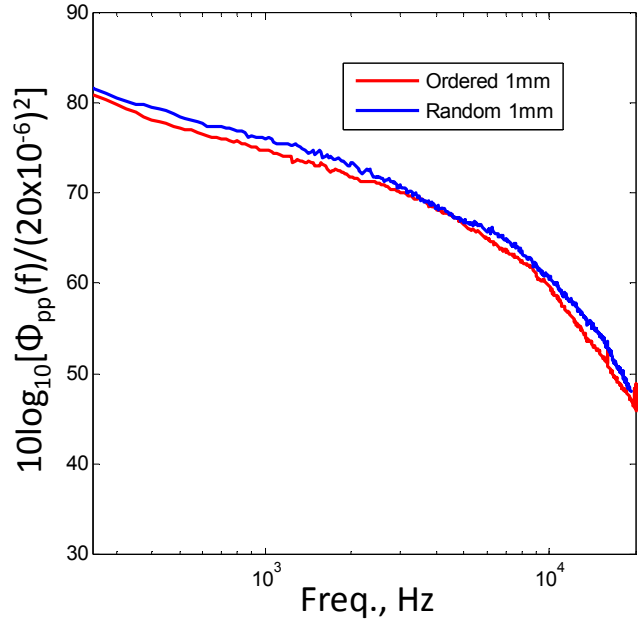

Figure 4-30. Comparison of average wall pressure measured in ordered fetch of 1mm hemispherical elements and the wall pressure measured inside of the random 1mm element fetch at U_o=60m/s

4.5.2 Far Field Noise

Far field noise from the random fetch of 1mm hemispherical roughness recorded upstream of the roughness at the same location as presented for the other surfaces, x=1029mm, y=469mm and z=0mm, is displayed in Figure 4-31. The background-subtracted spectra have a different spectral shape than that of the ordered fetch of 1mm hemispherical roughness.

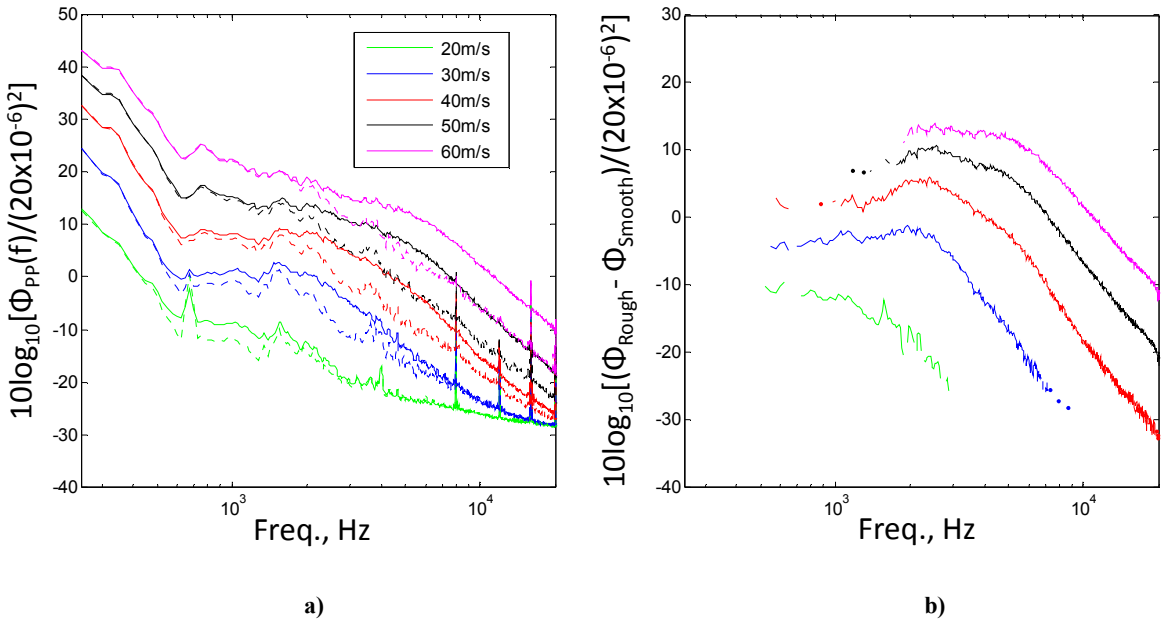

Figure 4-31. Far field sound from randomly distributed 1mm hemispherical element fetch at various nozzle exit velocities compared to the background noise a) raw b) and background subtracted

Figure 4-32 shows a comparison of the background noise from the two 1mm element fetches at U_o = 40m/s and 60m/s. The random fetch has slightly more elements 6209 as opposed to 5886 in the ordered fetch, but the spectra are not just scaled versions of each other due to this difference in number of elements. The disagreement between the far field spectra grows with frequency. The ordered fetch has a steeper roll-off with frequency so that the far field from the random fetch is 4dB greater than that of the ordered fetch at 20kHz for the U_o = 60m/s spectrum. Also, the lump in the ordered U_o = 60m/s spectrum between 2kHz and 3kHz is not present in the random fetch spectrum. Therefore, this demonstrates that the element size is not the only important factor that determines the level of the radiated noise, but that the roughness element configuration is a formative property in predicting the radiated levels.

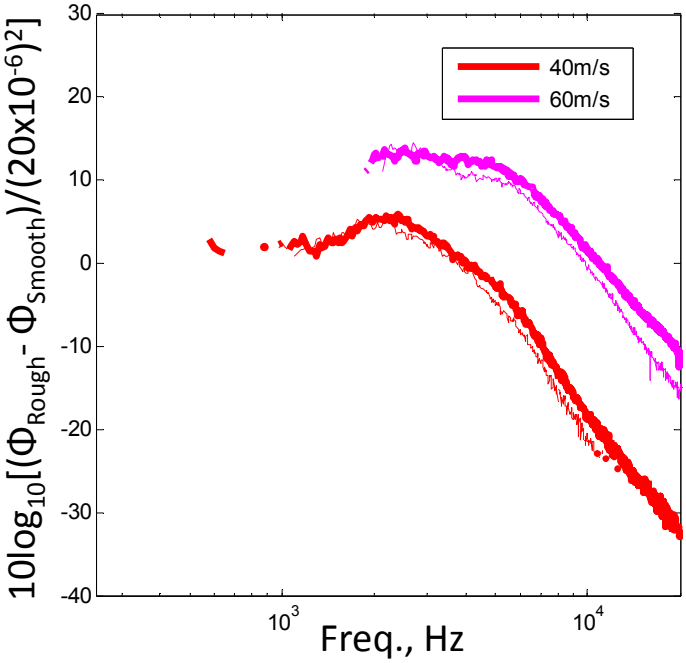

Figure 4-32. Far field comparison of noise from 1mm hemispherical elements in grid configuration (thin) and random configuration (thick)

4.5.3 Radiated Noise Normalization and Estimation Comparison

The far field noise of Figure 4-31 can be normalized on the measured wall pressure spectra at all velocities producing the collapse shown in Figure 4-33. This normalization works poorly to collapse the data onto a single curve and fans out in order of velocity above 2kHz as observed for the ordered fetch of 1mm roughness, but this clear ω^2 normalization and break frequency resemble the break frequency discussed in Alexander (2009) with respect to stochastic roughness. The estimated spectra shown on this figure predict the spectral values remarkably well. The spectral shape is correctly estimated with the absolute predicted the levels within 2dB below 2kHz. Above this, the difference between estimation and measurement grows up to 5dB, but as stated earlier, the difference may be attributed to inaccurate modeling of the wavenumber wall pressure spectrum. The estimated spectra appear to roll-off at a lower frequency. Although, the estimated normalizations show that the break frequency is a predictable function of the wavenumber wall pressure spectrum and the roughness geometry. The relative difference in break frequency is correctly predicted for the 40m/s and 60m/s spectra as well as the shape of the break. The estimations fan out in order of velocity with the higher velocity rising above and holding on to the ω^2 shape slightly longer than that of the slower case.

Figure 4-34 illustrates the reason for the break frequency. This figure shows a slice through the wall pressure wavenumber spectrum at 3000Hz and 500Hz for the local conditions at the leading edge of the roughness fetch with U_o = 60m/s. The peak produced in the map corresponds to the convective ridge. At these frequencies, the convective ridge peaks at a wavenumber of κ_x=2100 rad/m and κ_x=350, respectively. Figure 4-34 also shows the filter function, Γ, from Equation 3-2 derived from the Fourier transform of the surface slope for the random fetch of 1mm hemispheres. The voids in Γ are a function of the diameter of the roughness so that the 3mm hemispheres would have three times as many voids over

the same wavenumber space. The filter function is an exact Fourier transform calculated by displacing the Fourier transform of a single hemisphere's surface slope as calculated in Chapter 3 using the known location of each roughness element. Highlighted on this figure are two locations corresponding to the peak of the convective ridge of the wall pressure wavenumber spectrum for two different frequencies, 500Hz and 3000Hz. Increasing from 500Hz, the convective ridge peaks at lower wavenumbers and corresponds with an increasing region in the surface slope wavenumber spectrum. At 3kHz, the convective ridge aligns with a maximum in the surface slope wavenumber spectrum. As the frequency is increased further, the convective ridge will coincide with a sharp decline in the surface slope wavenumber spectrum associated with increasing κ_x. The shape of the estimated normalization is highly dependent on the interaction between the integrated product of the Γ function and the shape of the convective ridge at each frequency. Referring back to Figure 4-33, the estimated spectrum for the U_o = 60m/s case breaks from the linear slope at approximately 3kHz precisely where the plot of the Γ function indicates it should. To more accurately match the measured 60m/s normalized spectrum, this break needs to be shifted to a higher frequency. This could be accomplished by changing the characteristics of the model wavenumber wall pressure spectrum so that the integrated value of the normalized wavenumber pressure spectrum, Ψ, and wavenumber filter function of the surface, Γ, from Equation 3-2 peak at a higher frequency.

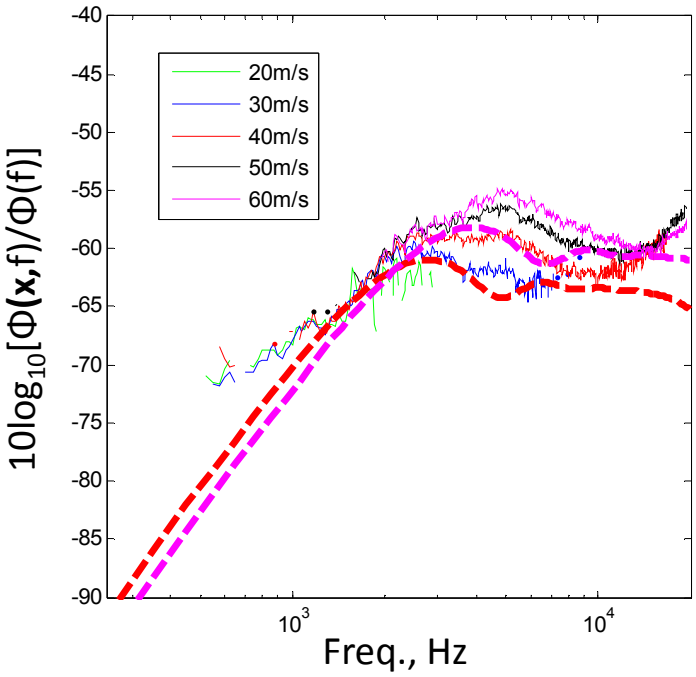

Figure 4-33. Measured far field normalization compared to estimation

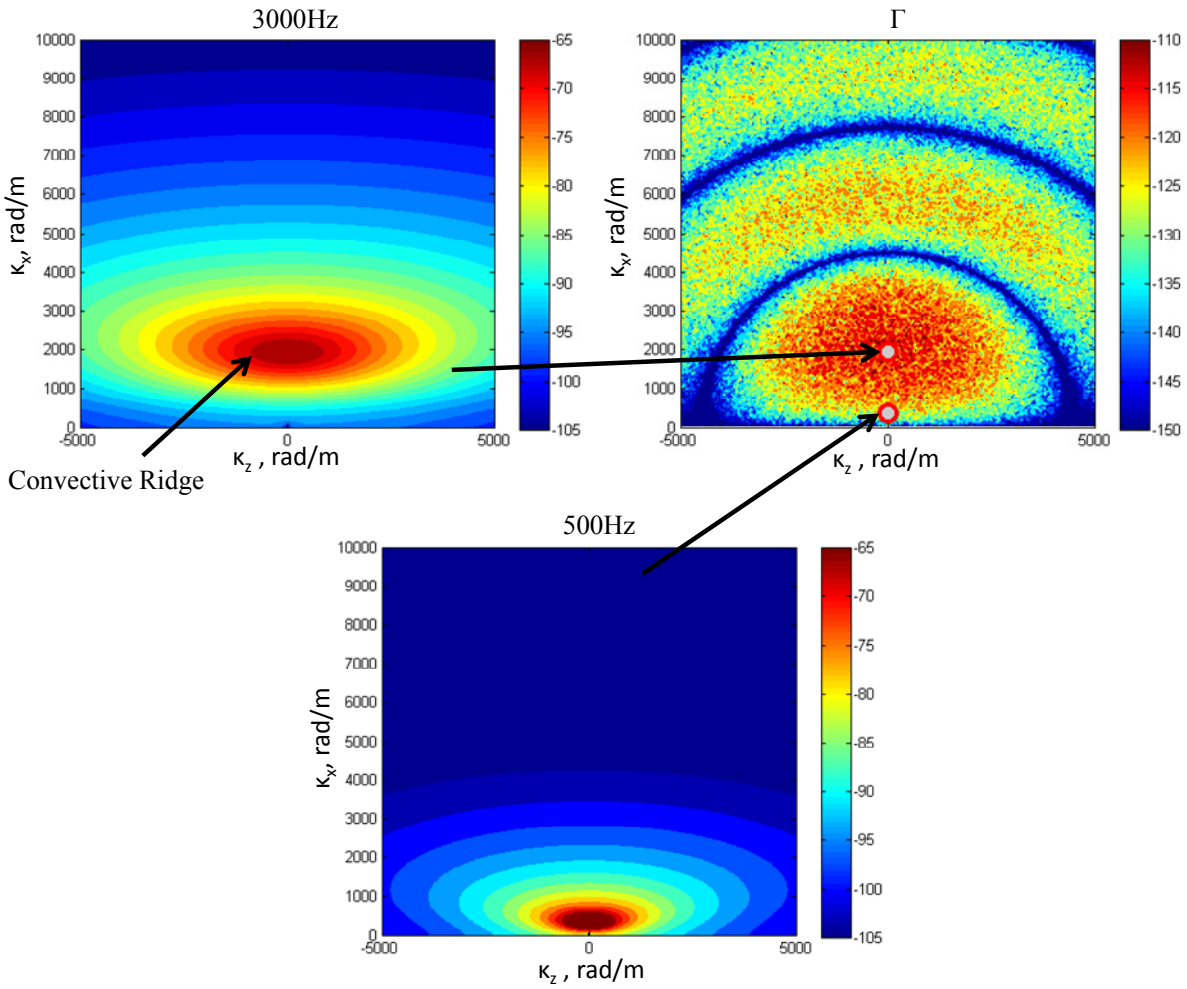

Figure 4-34. Cut through Chase wavenumber spectrum at 3000Hz, 500Hz, and the Γ function for random fetch of 1mm hemispheres

4.6 The Chase Spectrum - Application in Glegg & Devenport (2009)

Although the magnitudes of the estimations differ from measurement for the larger deterministic roughness, the accuracy of the predicted spectral shapes (and magnitudes for the *h*=1mm surfaces) for all of the different rough surfaces and velocities indicates that the produced far field noise, even from these transitionally to fully rough surfaces, is highly dependent on the wavenumber spectrum of the surface slope. Also, the form of the unsteady drag on the roughness elements associated with the self-generated and incoming wall pressure field is characterized well by the Chase (1980, 1987) wavenumber wall pressure spectrum. The full unreduced form of Glegg & Devenport (2009), Equation 1-3, which does not assume a homogenous wall pressure spectrum, cannot be used experimentally because it would involve integrating the wavenumber pressure spectrum over the entire rough surface. This is not currently feasible due to technological limits on sensor size. Using the simplified version, given in Equation 3-1, the error in magnitude between measurement and estimations appears to rely on the accuracy of the assumption of a homogeneous wall pressure field. Although the roughness elements do produce self-generated turbulence, the wavenumbers important in generating the observed far field noise are in the low wavenumber range 2000 to 14000 rad/m associated with disturbances ½ to 3 times as large as the 1mm roughness. Therefore,

the majority of the observed noise spectra from these 1mm surfaces are due to the incoming pressure field from large upstream disturbances, relative to the size of the roughness elements, being scattered by the rough wall geometry.

The single point wall pressure spectrum produced by the integration of the Chase's wavenumber spectrum is compared to the measured smooth wall undisturbed wall pressure fluctuations and the averaged wall pressure spectrum for the 42 element cubic roughness fetch case in Figure 4-35. The Chase model does not incorporate viscous terms and therefore does not produce the ω^{-5} roll-off at high frequencies associated with the dissipation region. The shape of the lower frequency region is captured, but the estimated results fall below the measured smooth wall pressure spectra for both the 40m/s and 60m/s cases. The estimated and measured smooth wall spectra differ by approximately 4-5dB over this range except at the lowest frequencies of the 60m/s spectra where the difference grows to 9dB. The Chase spectra perform much worse representing the averaged measured rough wall spectra. Differences are as great as 12dB. The slopes are approximately the same at the lowest frequencies, but again the estimates do not represent the shape of the dissipation region. Even though Chase's formulation does a poor job of estimating the single point rough wall pressure spectra, the model wavenumber wall pressure spectrum still accurately reproduces the shape of the far field normalizations for all roughness geometries and sizes. These estimations are accurate because the single point wall pressure spectrum is normalized out of the equation and therefore Chase's single point model does not directly factor into the result.

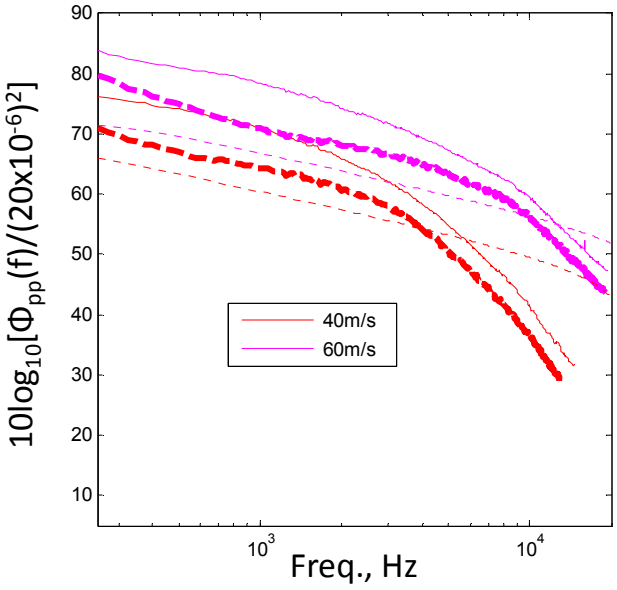

Figure 4-35. Smooth wall (dashed) and averaged rough wall pressure spectra (solid) compared to integrated Chase wavenumber wall pressure spectra (dotted)

Referring to Equation 3-1, the Ψ function, which contains the wavenumber wall pressure term, is normalized on the single point wall pressure spectrum. This means that the integrated value of the wavenumber wall pressure spectrum does not factor into the normalization of the far field because the Ψ function will always have an integrated value of unity at each frequency. The Ψ function's only operation is essentially that of a shape function that amplifies different regions of the surface slope wavenumber spectrum that creates the resulting spectral form of the normalization. Minor adjustment of the

wavenumber wall pressure spectrum cannot increase or decrease the levels of the estimated far field normalization significantly without a filter function, Γ, that varies dramatically over wavenumber space aligning perfectly with the convective ridge. Simple manipulations of Chase's spectrum were examined to study the effects on the normalized outcome.

Chase (1980, 1987) gives suggested values for the constants in Equation 3-22. If the constant μ from Equation 3-23 is assumed to be the same as used in Chase (1987), 0.176, instead of being determined from the constant value of h_C=3, the value of h_C changes correspondingly. The constant value of h_C in Chase's formulation is described as the velocity dispersion coefficient determined from space-time correlations. Using the relationship in Equation 4-1 from Chase (1987), h_C falls to 1.4 for the wall jet at U_o=60m/s assuming a convection velocity of 41%.

$$h_C = \frac{\mu(U_C)}{u_\tau} \qquad \text{Eq. 4-1}$$

The change in h_C manipulates the levels of the subconvective and convective regions of the wall pressure wavenumber spectrum through changes in the constants C_T and C_M, respectively. The adjustment of these constants changes the cross-section of the wavenumber wall pressure spectrum as shown in Figure 4-36**.** The narrowing of the convective ridge with a decrease in h_C manipulates the shape of the normalization through the integral in Equation 3-1.

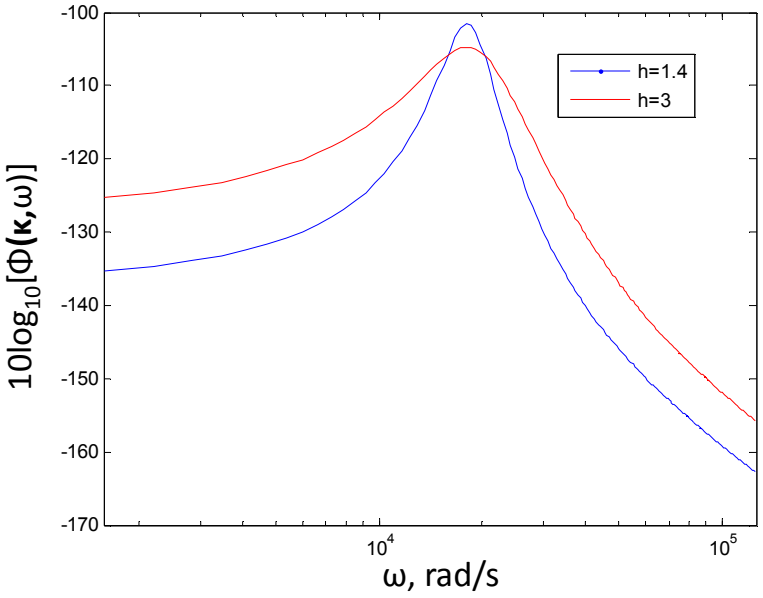

Figure 4-36. Comparison of Chase wavenumber wall pressure spectrum with various constants at κ_x=2000 and κ_z=0

Figure 4-37 shows the estimated normalization for the 42 element fetch of cubes for U_o=60m/s from Figure 4-9 compared to the estimated normalization using the manipulated constants for the Chase wall pressure wavenumber spectrum given in Equation 4-2.

$$h_C = 1.4 \quad C_T h_C = 0.014 \quad C_M h_C = 0.466 \quad b = 0.75 \qquad \text{Eq. 4-2}$$

The result using Chase's suggested value of h_C=3 fits the spectral shape better than the modified version. The narrower convective ridge peak of the modified Chase spectrum produces a lumpier normalization amplifying all of the small details in the Γ function of the 42 element fetch. Even though the shape of the normalized results is altered, the mean magnitude of the estimated curve is unchanged.

The *b* value in the Chase model can also be modified. This value controls the source layer thickness as a fraction of the boundary layer, but analysis showed that increasing or decreasing this value from 0.5 to 1 had an insignificant effect on the estimated outcome.

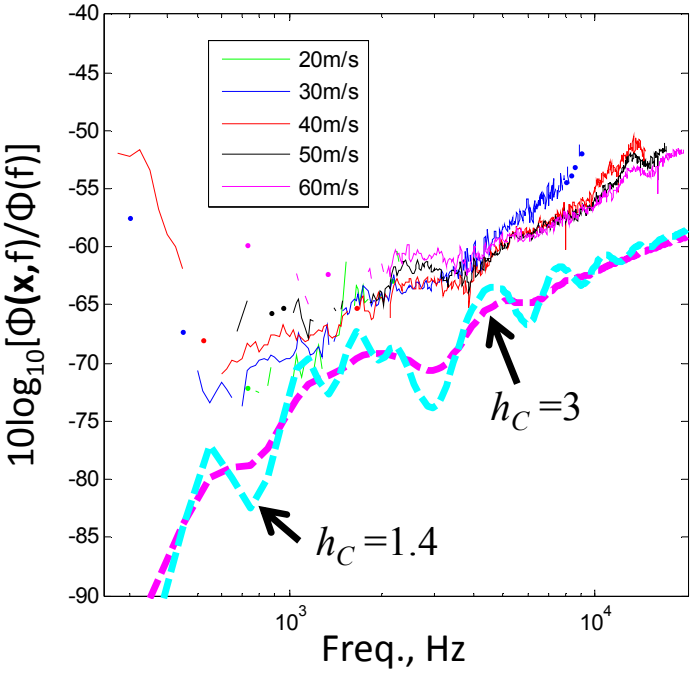

Figure 4-37. Comparison of normalization shape with adjusted Chase spectrum values

The estimation in Figure 4-33 for the random distribution of 1mm hemispheres deviates from the linear slope of ω^2 at a lower frequency then the measured normalization. The cause of the "break frequency" was explained using Figure 4-34 which shows that the normalization will deviate at the frequency that aligns the convective ridge with the maximum location in the Γ function. Therefore, to improve the estimation, the convection velocity can be increased which decreases the slope of the convective ridge in the wavenumber wall pressure spectrum. With a higher convection velocity, eddies on the convective ridge at any given frequency are larger and therefore have a lower wavenumber. This affects the estimation by moving the "break frequency" to a higher value. Figure 4-39 shows the measured normalization for the random fetch of 1mm hemispheres at U_o=60m/s compared to the original calculated estimation using a convection velocity that is 41% of the edge velocity and a higher value of 52%.

Moving the convection velocity to a higher percentage of the edge velocity reduces the disagreement between measurement and estimation, but this is an arbitrary adjustment based on the desire to fit the measured and estimated values. The convective velocity of $0.41U_m$ was calculated in Devenport *et al.* (2010) using the noise radiated from a hydrodynamically smooth surface. The presence of the 1mm roughness should lower this convective velocity, not increase it. Also, the roughness used in this

measurement has a surface slope wavenumber spectrum that is not single valued as did the rib roughness used in Devenport *et al.* (2010). Therefore, the estimated values are affected by larger regions of the wavenumber wall pressure spectrum. Differences between the estimated and measured normalizations could be due to the assumed form of the wall pressure wavenumber spectrum.

To test the effect of the shape of the wall pressure wavenumber spectrum, the estimated normalization was calculated using a wavenumber wall pressure spectrum with a rectangular cross section. The cross-section was centered on the peak of the Chase spectrum, assuming the convective velocity of $0.41U_m$, for each frequency so that the slopes of the two spectra were the same. The rectangle was $2000\kappa_x$ x 6000 κ_z rad/m in wavenumber space. The contained area had an integrated value of unity and all points outside this area had values of zero. Figure 4-38 shows an illustration of a cut through the Chase wavenumber wall pressure spectrum at a frequency of 3kHz with the outline of the rectangular wall pressure spectrum at this frequency.

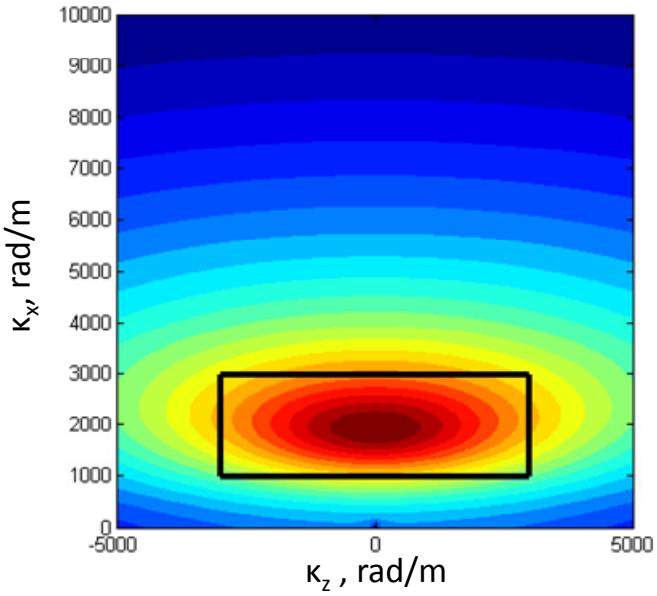

Figure 4-38. Rectangular wavenumber wall pressure spectrum cross-section compared to the Chase wavenumber wall pressure spectrum at 3kHz

The normalized curve produced by this crude wavenumber wall pressure spectrum is also shown in Figure 4-39. Above 1kHz, the rectangular spectrum produces values similar to that of the Chase spectrum. This suggests that the exact shape of the wavenumber wall pressure spectrum is not that important as long as the location of the convective ridge is approximately accurate. Crude forms of the wavenumber wall pressure spectrum can produce reasonable results at least over the frequency range observed in this experiment. Below 1kHz, the rectangular cross-section produces a normalized spectrum that follows a shallower slope of approximately ω^2. This slope may actually fit the lower frequency region of the measured normalization better than that produce by the Chase spectrum. The data from other velocities in Figure 4-33 clearly show the measured normalization at a shallower low frequency slope than the estimated spectra. The "break frequency" using this rectangular cross-section also changes shifting to a slightly higher frequency. This indicates that the earlier adjustment of the convective velocity might not be justified to settle the disagreement between measurement and estimation, but that the difference may be due to the shape of the assumed wavenumber wall pressure spectrum.

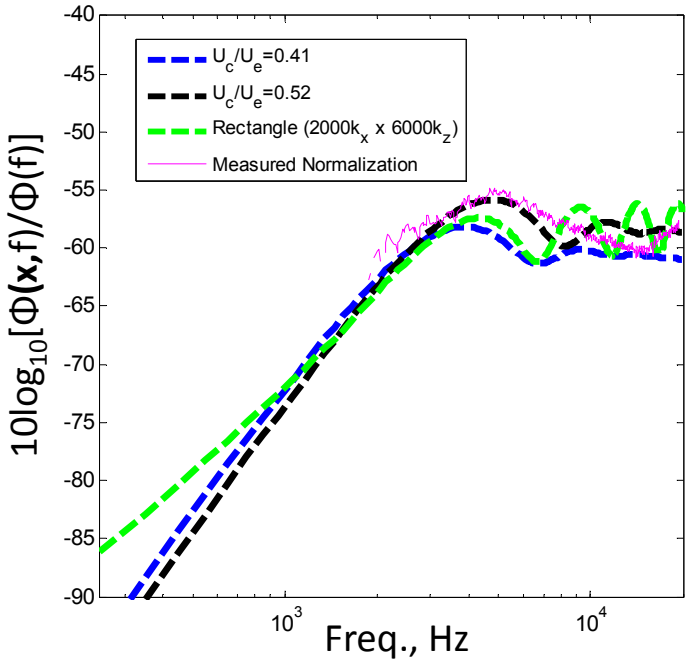

Figure 4-39. Change of convection velocity on Random norm fetch

4.7 Total Sound Far Field Estimates

Glegg & Devenport's (2009) theory can more usefully be applied to estimate the radiated far field noise from a rough surface and not just the normalized spectral shape. The previous comparisons of measured and estimated far field/near field normalizations were convenient because they excluded assumptions of the estimated single point wall pressure spectra. However, comparison with recorded normalized values required the measurement of the rough wall pressure spectra. In the following total far field sound estimates, a single point wall pressure spectrum is assumed in the estimated far field spectra instead. These estimations are calculated using the Chase wavenumber wall pressure spectrum and the analytical form of Chase's (1980, 1987) single point wall pressure spectrum given in Equation 3-23 with appropriate inputs for the U_o = 40m/s and 60m/s cases. The compared results for the five discussed deterministic rough surfaces are shown in Figure 4-40 to Figure 4-44 compared to the measured background subtracted roughness noise data.

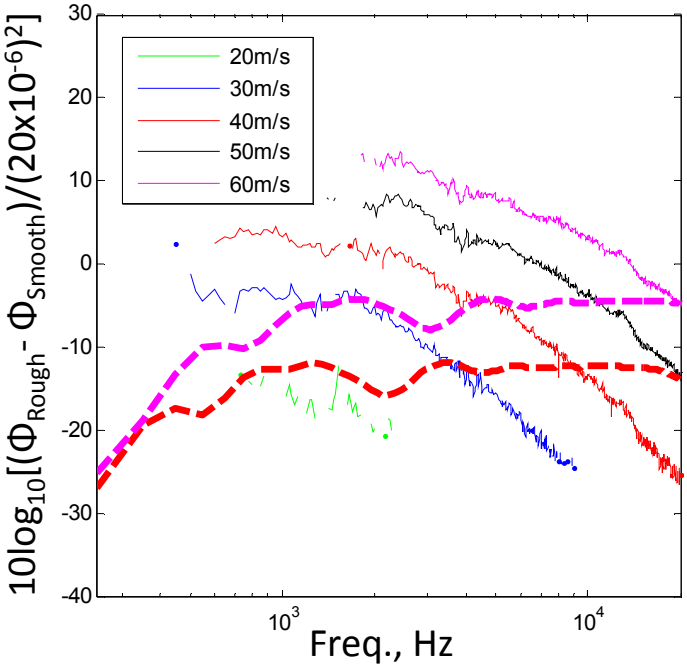

Figure 4-40. Far field noise estimation using the Chase single point wall pressure spectrum compared to measured sound spectra from 42 element fetch of 3mm cubic roughness

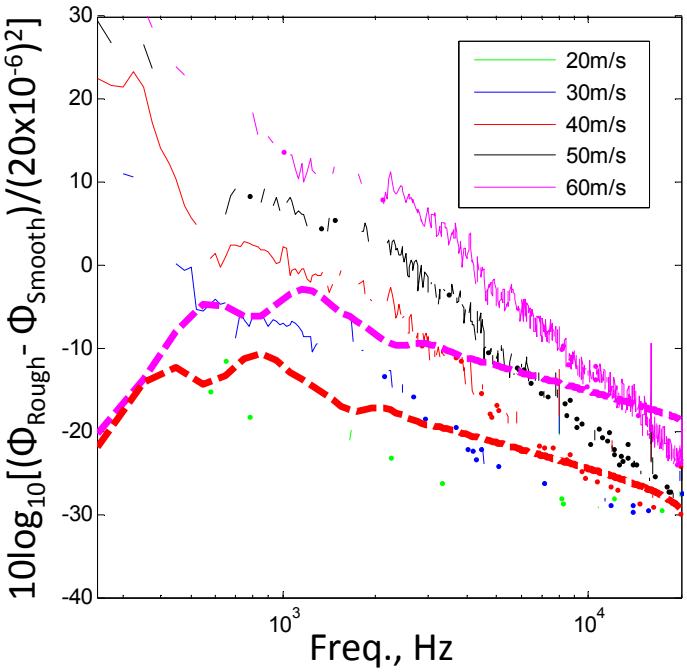

Figure 4-41. Far field noise estimation using the Chase single point wall pressure spectrum compared to measured sound spectra from 42 element fetch of 3mm hemispherical roughness

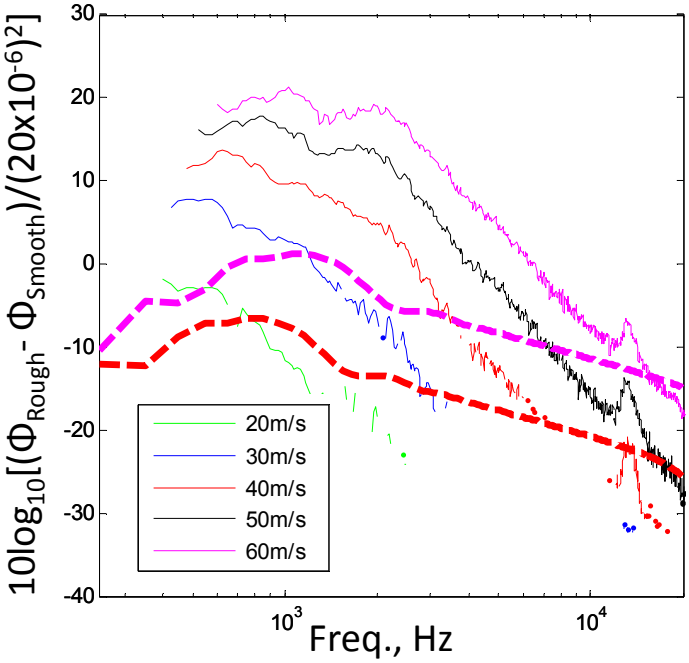

Figure 4-42. Far field noise estimation using the Chase single point wall pressure spectrum compared to measured sound spectra from 703 element fetch of 3mm hemispherical roughness

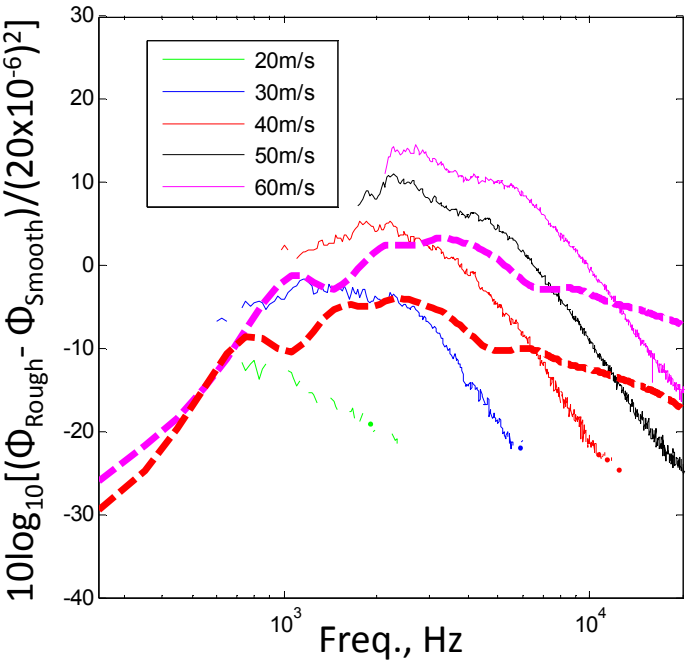

Figure 4-43. Far field noise estimation using the Chase single point wall pressure spectrum compared to measured sound spectra from fetch of ordered 1mm hemisipherical roughness

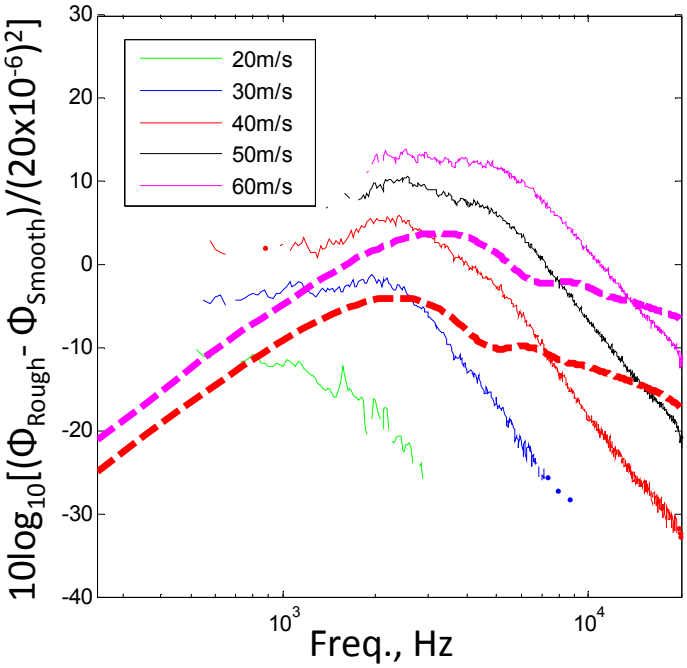

Figure 4-44. Far field noise estimation using the Chase single point wall pressure spectrum compared to measured sound spectra from fetch of randomly distributed 1mm hemisipherical roughness

For all far field estimates, the measured spectral slope of the high frequency region above 2kHz is underpredicted due to the exclusion of viscous effects in the Chase single point wall pressure spectrum as shown in Figure 4-35. This is most apparent in the results for the 703 element fetch of 3mm hemispherical roughness in Figure 4-42. The high frequency slope of the estimation follows an ω^{-1} curve while the measured far field produces a slope nearly ω^{-5}. The steep roll-off observed in the far field noise is controlled by the viscous effects in the near field damping the pressure fluctuations on the surface of the elements.

The smooth wall pressure spectrum model of Goody (2004) is a modified form of the Chase model but empirically accounts for the dissipative ω^{-5} region. His formulation is shown in Equation 4-3.

$$\Phi_{pp}(\omega) = \frac{3\left(\frac{\omega\delta}{U_e}\right)^2 \tau_w^2 \delta}{U_e\left[\left[\left(\frac{\omega\delta}{U_e}\right)^{0.75} + 0.5\right]^{3.7} + \left[\left(1.1R_T^{-0.57}\right)\left(\frac{\omega\delta}{U_e}\right)\right]^7\right]}$$

Eq. 4-3

$$\text{where} \qquad R_T = \left(\frac{\delta}{U_e}\right) / \left(\frac{\nu}{u_\tau^2}\right)$$

Comparison of the Goody (2004) model with the wall-jet's measured smooth wall spectra and the average rough wall pressure fluctuations measured in the 42 element fetch of cuboidal roughness is shown in Figure 4-45.

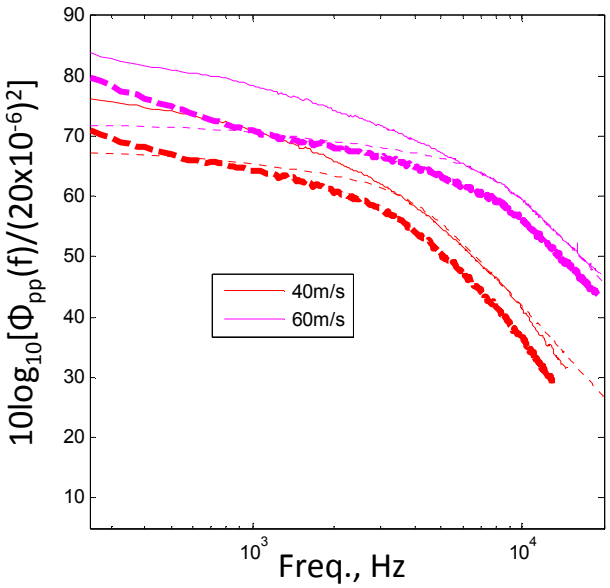

Figure 4-45. Smooth wall (dashed) and averaged rough wall pressure spectra from the cuboidal roughness fetch (solid) compared to the Goody (2004) wall pressure spectra model (dotted)

The Goody (2004) does a much better job than the Chase spectrum reproducing the shape of the measured wall pressure fluctuations. The low frequency region does not have the increased slope of the wall-jet near ω^{-1}, but the high frequency region is much better modeled. The Goody model is a smooth wall pressure spectra model but overpredicts the smooth wall spectral levels of the wall-jet in the dissipative region by up to 5dB. Coincidentally, the difference in the smooth wall spectra is similar to the increased pressure fluctuations due to the addition of the roughness. Therefore, total far field estimations using this single point wall pressure model along with the Chase wavenumber wall pressure spectrum should produce better estimates of the measured far field spectra especially in the higher frequency region. The estimated far field results for all five of the studied deterministic surfaces are shown in Figure 4-46 to Figure 4-50. The results of the estimations are quite accurate over the frequencies associated with dissipation region in the single point wall pressure spectra. The accuracy of the predictions is greatest for the 1mm roughness.

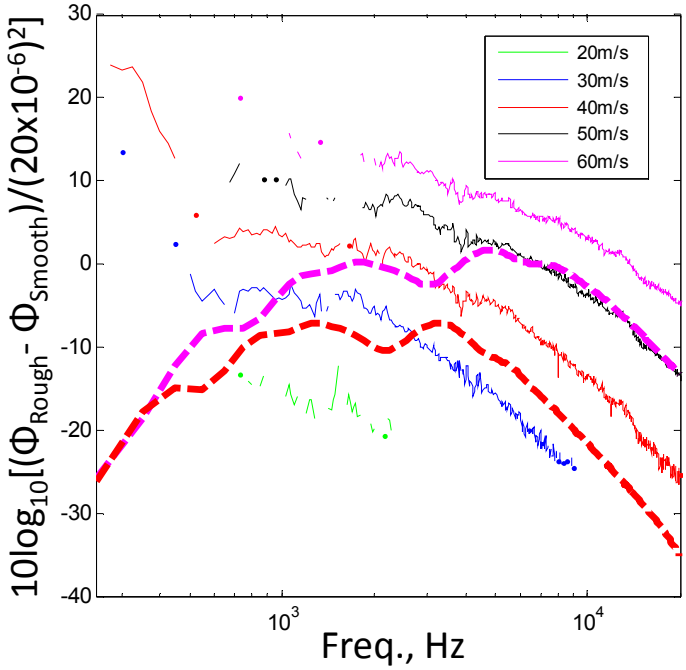

Figure 4-46. Far field noise estimation using the Chase single point wall pressure spectrum compared to measured sound spectra from 42 element fetch of 3mm cubic roughness

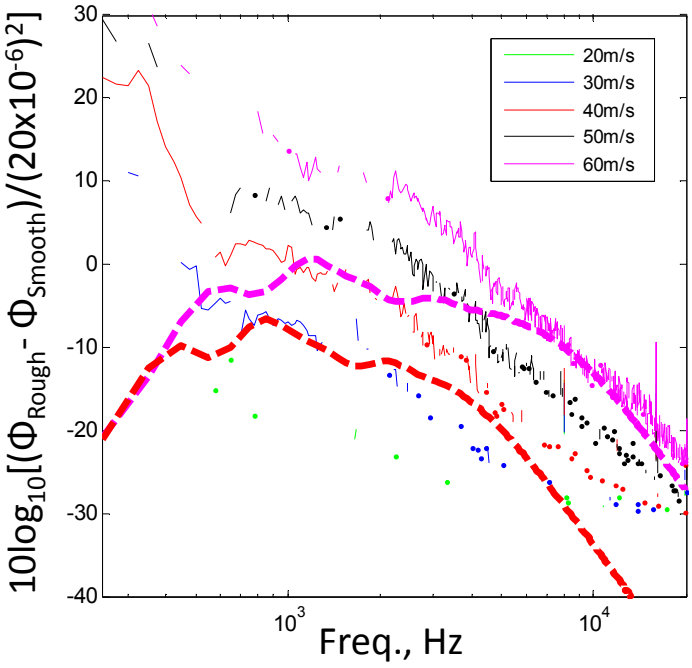

Figure 4-47. Far field noise estimation using the Chase single point wall pressure spectrum compared to measured sound spectra from 42 element fetch of 3mm hemispherical roughness

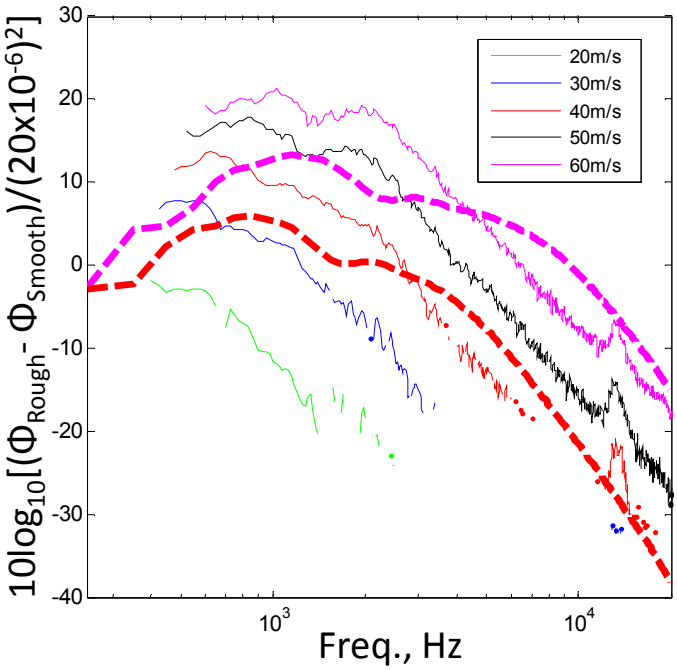

Figure 4-48. Far field noise estimation using the Chase single point wall pressure spectrum compared to measured sound spectra from 703 element fetch of 3mm hemispherical roughness

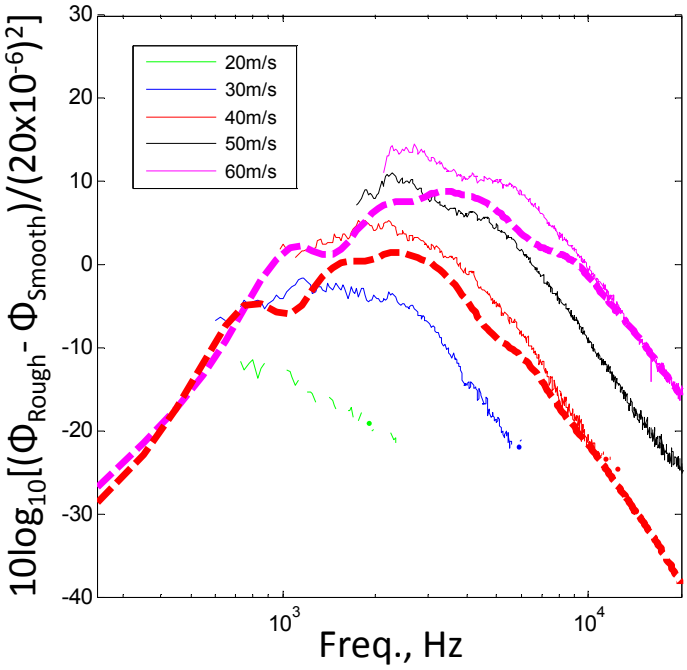

Figure 4-49. Far field noise estimation using the Chase single point wall pressure spectrum compared to measured sound spectra from fetch of ordered 1mm hemisipherical roughness

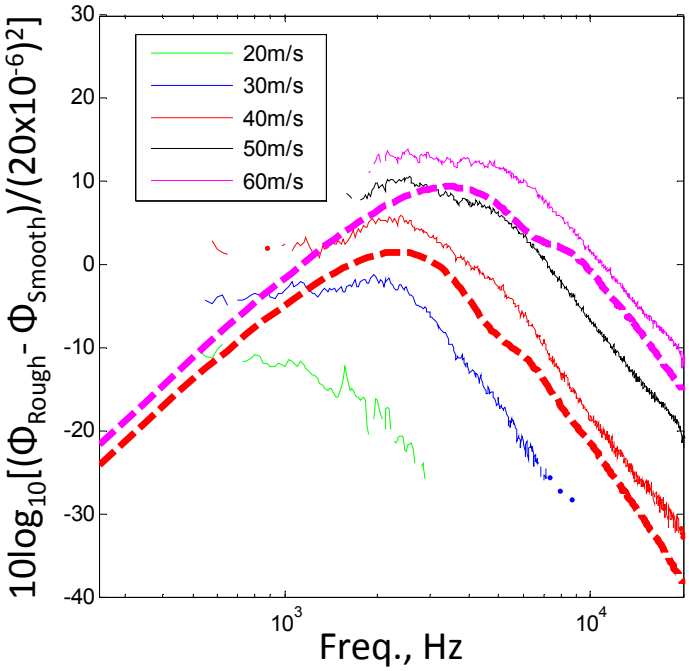

Figure 4-50. Far field noise estimation using the Chase single point wall pressure spectrum compared to measured sound spectra from fetch of randomly distributed 1mm hemisipherical roughness

The total far field estimations using the Chase (1987) and Goody (2004) single point wall pressure spectra qualitatively predict the spectral peak shift to greater frequencies and the increase in far field noise produced by higher velocities, but the estimated spectral magnitudes differ with the far field measurements. The magnitude of the far field estimation is dependent on the wall pressure spectrum used in the estimation. Figure 4-35 shows the Chase single point spectrum well below the average recorded rough wall pressure spectra from the 42 element cubic roughness case. The relatively close resemblance of the Goody (2004) spectrum to the average recorded rough wall pressure spectra at high frequencies for the 1mm surfaces resulted in the exceptional accuracy of the estimations in this region. Use of the elevated rough wall pressure spectra in the measurements would bring the estimated far field closer to agreement with the measured values. The estimated normalizations in the previous sections for the 3mm roughness show that use of the recorded average rough wall pressure spectra will still unsuccessfully recreate the measured data, but the measured rough wall pressure spectra from the 1mm surfaces should accurately recreate the measured far field data.

Figure 4-51 shows a prediction of the far field noise from the fetch of randomly located 1mm hemispheres using the recorded rough wall pressure spectra for the 40m/s and 60m/s nozzle exit velocities compared to the measured background-subtracted far field noise. The estimated results are within 5dB of the measured values. The largest observed difference is due to the dip created by the model convective ridge passing through the first void in the Γ function shown in Figure 4-34 for each velocity. The accuracy of this prediction demonstrates that the far field noise produced by roughness that is a small fraction of the boundary layer thickness can be determined if the surface geometry and rough wall pressure spectrum are known.

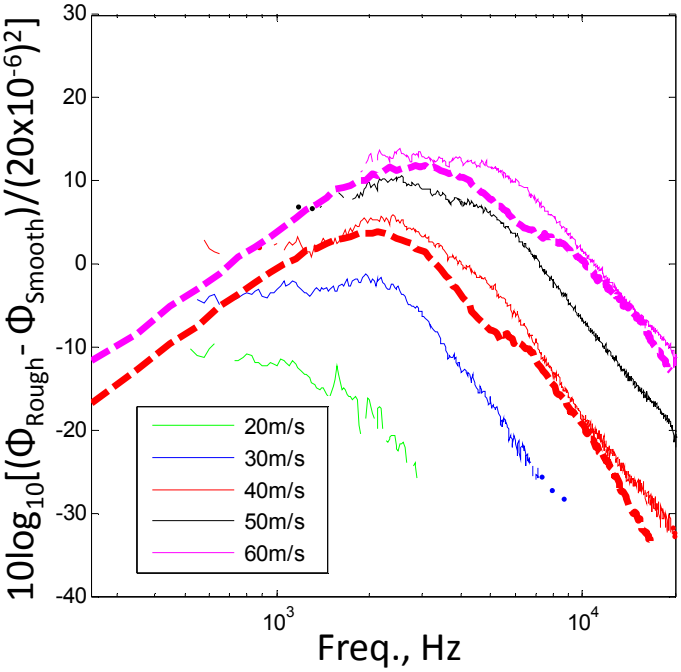

Figure 4-51. Farfield noise estimation of noise from random fetch of 1mm hemispheres using measured wall pressure spectra

4.8 Estimates of Average Pressure Fluctuations on Roughness Elements

Instead of trying to measure the wall pressure spectrum over the entire rough surface to calculate the true wavenumber wall pressure spectrum distribution, the average single point surface pressure spectrum that would exactly predict the radiated far field, assuming Chase's wavenumber wall pressure spectrum, can be calculated using the measured far field data as shown in Equation 4-4.

$$\Phi_{pp}(\omega) \approx \frac{\Phi_{PP}(\boldsymbol{x},\omega)|\boldsymbol{x}|^2}{4\pi^2(k_o h)^2 \Sigma \int \Psi_{pp}(\kappa_x,\kappa_z,\omega)\Gamma(\kappa_x,\kappa_z,k_o)d\kappa_x d\kappa_z} \qquad \text{Eq.4-4}$$

Figure 4-52 shows the estimated near field spectra needed to collapse the measured and estimated far field for the 703 element fetch of 3mm hemispheres. This estimation is compared to the measured wall pressures inside the rough surface. This estimated spectrum represents the single point surface pressure fluctuations responsible for the measured far field. A portion of these pressure fluctuations are responsible for the unsteady drag on the elements, but the surface pressure spectra also contain contributions from lengthscales unassociated with the unsteady drag. The frequency range of calculated values is limited to regions where background-subtracted data was available in the calculation. The estimated spectrum does not differ in magnitude greatly from the measured wall pressure spectra over the majority of the calculated frequency range. Ignoring the lump at 13kHz, the spectral shape is similar to some of the interior measurements positions, particularly LH3 and LH5 located just ahead and behind roughness elements, respectively.

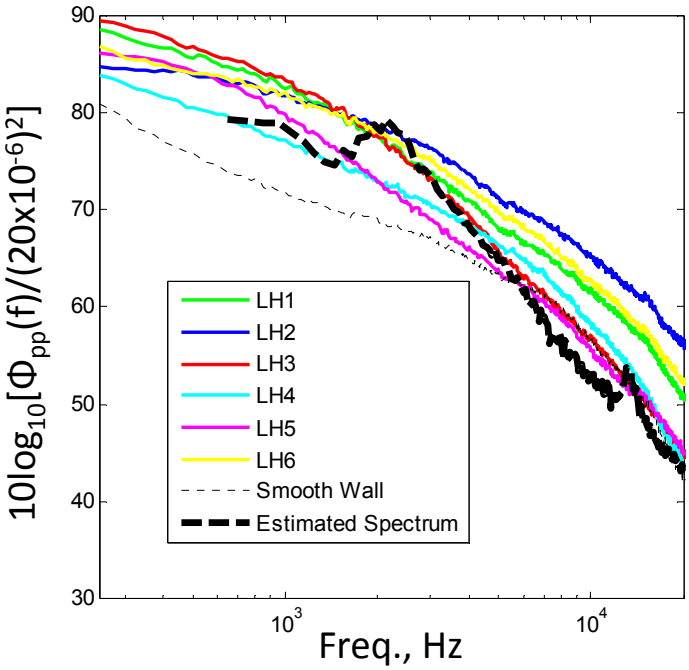

Figure 4-52. Estimated average pressure fluctuation on surface of roughness element for 703 element fetch of 3mm hemispheres compared to measure wall pressure fluctuations in the fetch at U_o = 60m/s

The estimated single point surface pressure fluctuations needed to resolve the difference between the predicted and measured spectra can be calculated for all five studied deterministic surfaces in a similar way. The results are shown in Figure 4-53 for a nozzle exit velocity of 60m/s. The majority of the spectra have a steep slope near or exceeding ω^{-5} above 6kHz. The cubic element fetch produces has the shallowest slope in this frequency range. The shapes of the curves seem to follow a slope closer to ω^{-1} below 2-6kHz. The 1mm surfaces deviate from the steeper slope at approximately 6kHz while the larger surfaces tend to become shallower at lower frequencies. The cubic element spectrum is also stronger than estimated results for the hemispherical surfaces. This is consistent with the observation that the cubic roughness produces greater far field noise. The 42 element hemispherical roughness spectrum shows that this smaller fetch is a more efficient producer of noise per element than the larger 703 element fetch. This could be due to the fact that the ratio of leading to trailing elements is decreased by a factor of 3 in the larger fetch. The increase in number of trailing elements, which produce less noise, decreases the per element efficiency of the fetch and therefore the strength of the estimated average single point wall pressure spectrum.

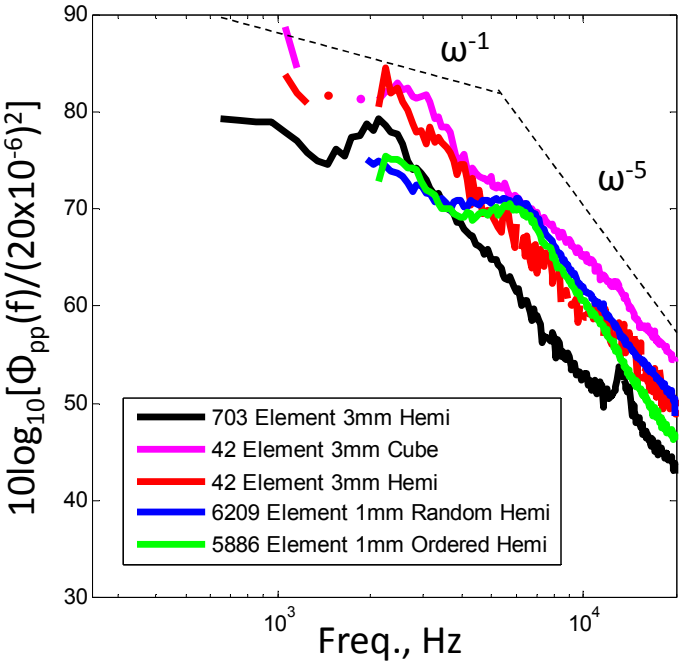

Figure 4-53. Estimated average pressure fluctuation on surface of roughness elements for all five studied deterministic surfaces at U_o = 60m/s

Chapter 5 Source Map Analysis

The directivity and variation of noise through a fetch of roughness fetch was analyzed using the linear microphone array discussed in Section 2.4. A delay and sum beamforming technique was used to solve for source strengths and distributions throughout fetches of h=3mm discrete element surface roughness. As observed in Figure 2-14, the configuration of the linear microphone array limits the use of the array in directions out of the axis of its sensors. Therefore, the array was positioned in several locations in the anechoic chamber to record the variation of source strengths along individual axes. These microphone array positions are shown in Figure 2-12. The following sections detail the source strength analysis for the single to 42 element fetches of cuboidal and hemispherical roughness using a delay and sum beamforming technique.

5.1 Cuboidal Roughness – Single Element to 42 Element Fetch

Figure 5-1 shows a diagram of a microphone array measurement of roughness noise from Array Position 1 whose exact sensor location is detailed in Section 2.4. The microphone array was positioned in the spanwise direction of the roughness with sensor locations only varying along the x-axis. The focal area was approximately 300mm square centered around x=1257mm, z=0. This area is large enough to contain all of the roughness elements in the single to 42 element fetches. The lead row of all roughness began at x=1257mm.

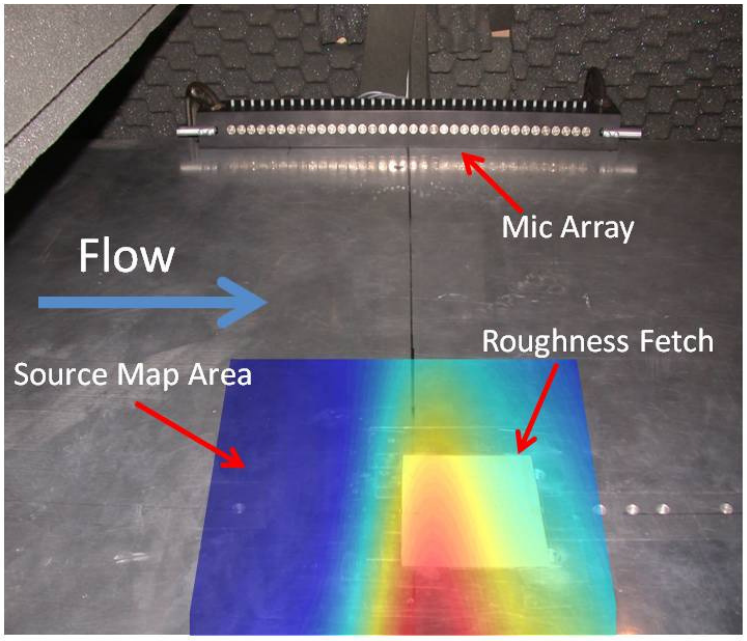

Figure 5-1. Diagram of Array Position 1 measurement and beamformed source map

The sensors of the linear array make a receiving angle of ±34° relative to the axis of a spanwise dipole emanating from x=1257mm, z=0, the central lead row location of the roughness noise measurements. The power of a dipole source varies as the cosine squared of the receiving angle.

Therefore, the calculated source maps will be dominated by measurement of the spanwise dipole strength but are not an exclusive measurement of this source. The microphones on either end of the microphone array will be more influenced by the streamwise dipole than the central sensors. Figure 5-2 shows two cosine squared functions representing equal strength dipoles aligned in the streamwise and spanwise directions. The thick black lines mark the maximum receiving angles drawn from source to sensor of the microphone array. Even at these largest receiving angles, the spanwise dipole efficiency exceeds the streamwise efficiency by over a factor of two.

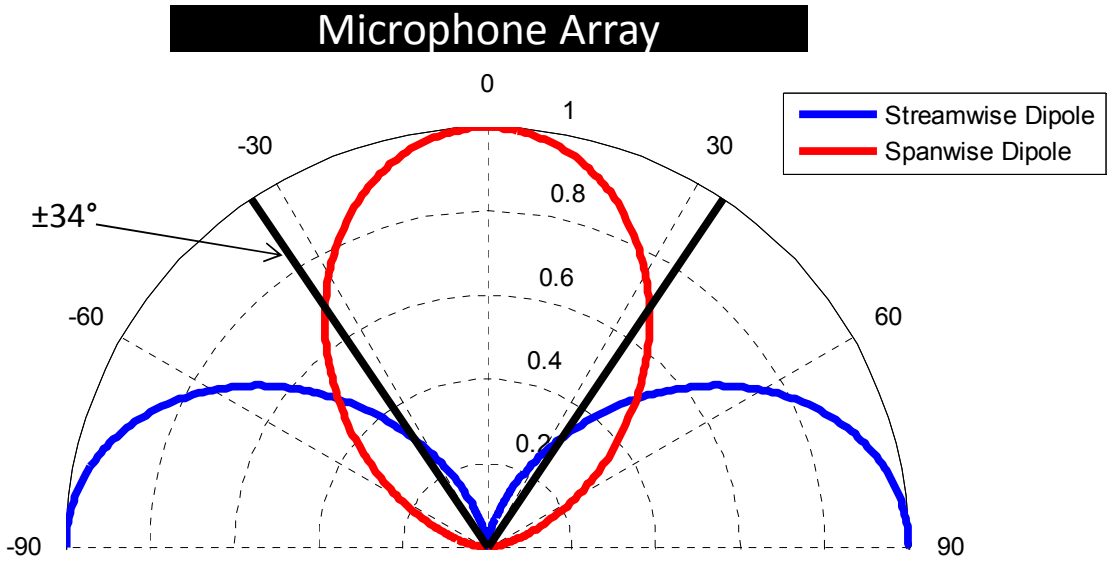

Figure 5-2. Directivity of theoretical streamwise and spanwise dipoles compared to receiving angles encountered by linear array sensors

Figure 5-3 shows the source map produced by measurement of the radiated far field noise at this spanwise position from a single 3mm cubic element located at x=1257mm, z=0 for U_o = 60m/s at three frequencies, 6336Hz, 10368Hz, and 13696Hz. Although the source maps produce no source peak in the z-direction because of the sensor alignment, the produced maps clearly show the peak source strength at the location of the roughness element in the x-direction. The resolution of the calculated source location increases with frequency. Comparing the width of the main lobe on each map, defined as the width at half the peak value through z=0, the size decreases by a factor of 2 from approximately 60mm to 30mm. The increase in resolution with frequency is a typical characteristic of this beamforming technique. Comparing magnitudes of the measured source maps, the strength of the spanwise source appears strongest at the lower frequency and decreases with increasing frequency.

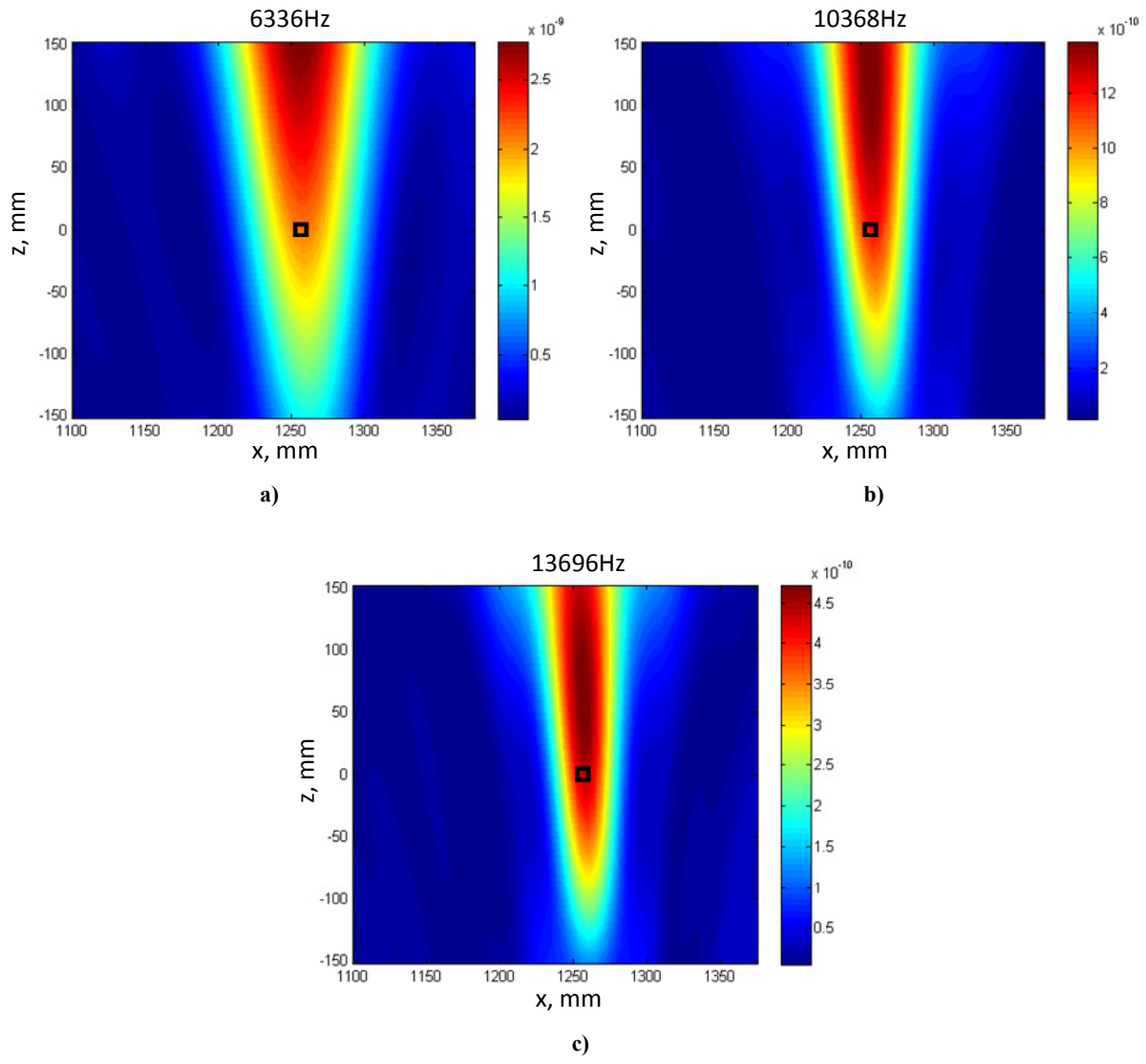

Figure 5-3. Source maps from a single 3mm cubic element at x=1257, z=0 using Array Position 1 with U_o = 60m/s for a) 6336Hz, b) 10368Hz, c) and 13696Hz in N^2/m^4Hz

A similar analysis of the streamwise dipole can be completed using the measured cross-spectrum with the microphone array at Array Position 2. The sensors at this position vary along the z-axis and the array is positioned upstream of the roughness in a position shielded from the jet noise produced by the nozzle. Figure 5-4 shows a diagram of the roughness noise measurements using Array Position 2. The source map focal area is the same size as that used in Array Position 1 and is centered about the same point, x=1257mm, z=0. This upstream microphone location is located 585mm above the flat plate of the wall jet and is angled down 56° from horizontal, so that points at the trailing edge of the focal area are 250mm further from the center of the microphone array than the leading edge. The sensors of the microphone array are centered around z=0 and have receiving angles that vary ±14° to the theoretical streamwise dipole axis of the single roughness element. Therefore, as shown similarly in Figure 5-2 for the spanwise dipole, the noise recorded at this position will be dominated by the streamwise radiating source.

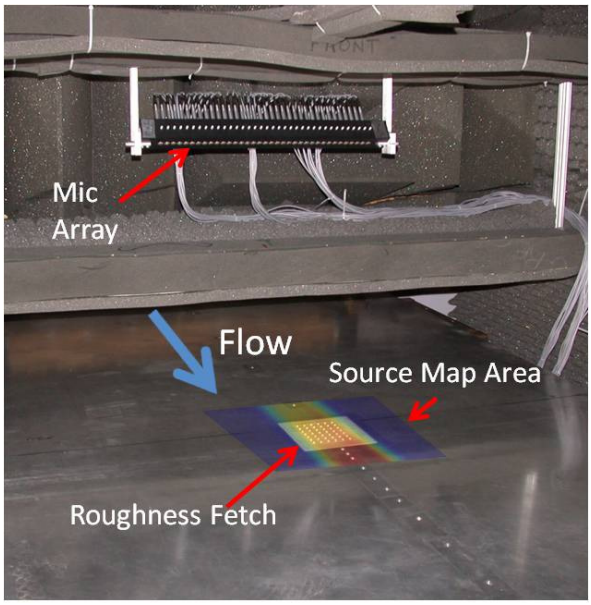

Figure 5-4. Diagram of Array Position 2 measurement and beamformed source map

Figure 5-5 shows the produced source maps for the single 3mm cubic element at x=1257mm, z=0 with U_o = 60m/s calculated using Array Position 2 for three different frequencies. The same narrowing effect of the main lobe is observed as the frequency is increased changing by a factor of two. The source strength decreases as well with increasing frequency. Like the source maps of the spanwise dipole shown in Figure 5-3, the peak source strength occurs at the location of the single roughness element. These source maps are given to show that the frequency variation only affects the resolution of the maps but that the main lobe even at the highest recorded frequencies is significantly wider than the width of the single element. The remaining analysis will be focused mainly at 10368Hz which is a central frequency of the measurable roughness noise.

Array Positions 3 and 4, which place the array nearly vertical over the single roughness element with sensors aligned in the streamwise and spanwise direction, respectively, produce source maps that again locate the correct position of the roughness element. Figure 5-6 shows the results as recorded from Array Positions 3 and 4 for the single cubic element at 10368Hz. These array measurement locations both produce a symmetrical stripe through the center of each map. If the sources coming from the single roughness element were a combination of only streamwise and spanwise dipoles sources, the resulting directivity pattern would have a void perpendicular to the plane of the wall above the roughness. This void is at a point perpendicular to both dipole axes. None of the sensors of the linear array are at exactly this point for Array Positions 3 or 4. In Array Position 3, the sensors are in a geometrical position that straddles this void point with all of the array's sensors in a position perpendicular to the origin of the spanwise dipole. Therefore, for the single element case, this is a measurement of the streamwise dipole solely. Array Position 4 is straddling the void point with sensors perpendicular to the streamwise dipole and is therefore a measurement of the spanwise source. Source convection effects due to the local flow velocity, discussed in Section 2.5.1.4, push the effective source location slightly downstream. As a result, the streamwise dipole will have some influence on the measurement at Array Position 4, but the receiving angle subtended from source to array for the streamwise source's axis is ~87° at the highest local velocity. Consequently, the streamwise source should be negligible compared to the spanwise source at this array position.

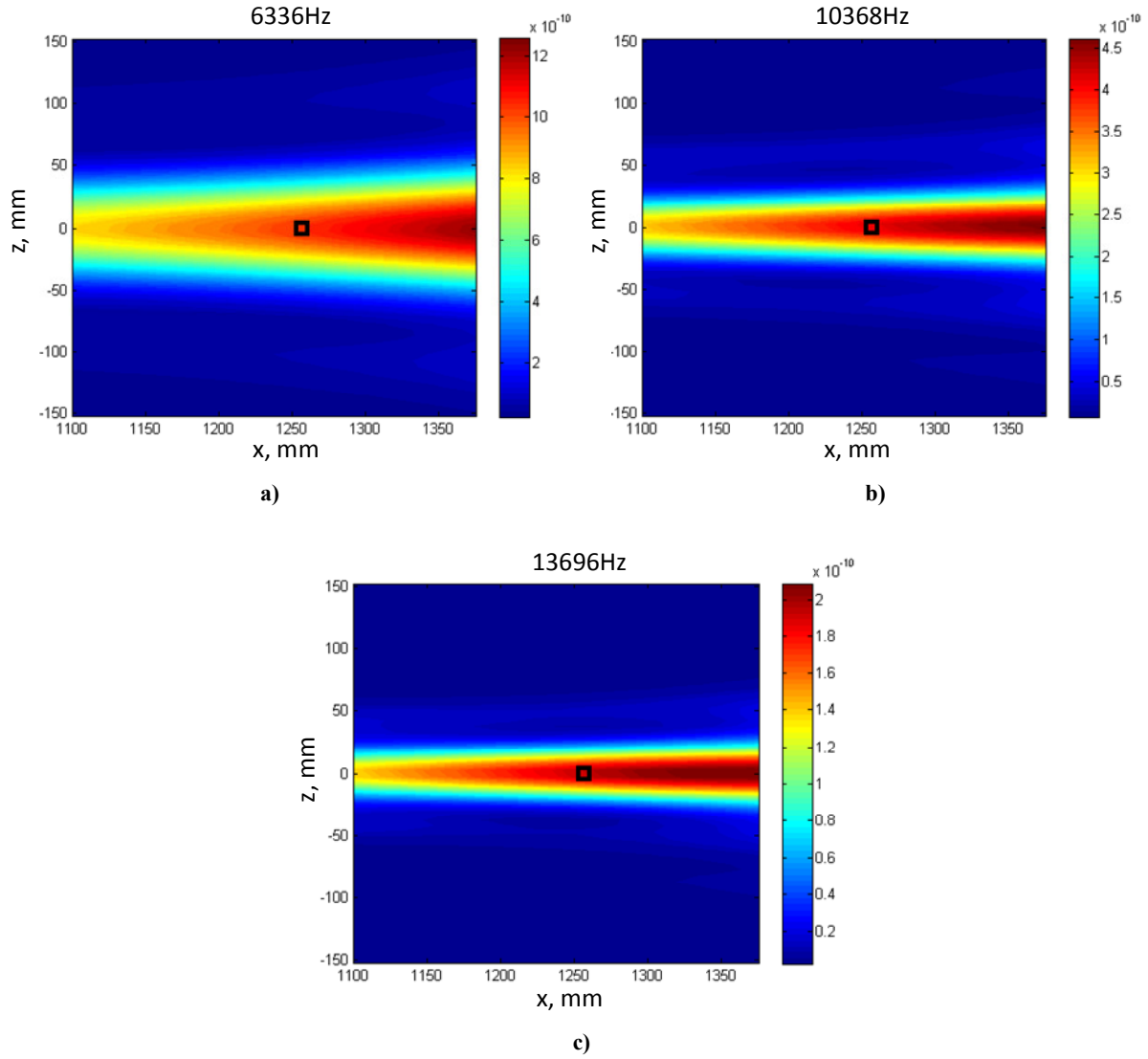

Figure 5-5. Source maps from a single 3mm cubic element at x=1257, z=0 using Array Position 2 with U_o = 60m/s for a) 6336Hz, b) 10368Hz, c) and 13696Hz in N^2/m^4Hz

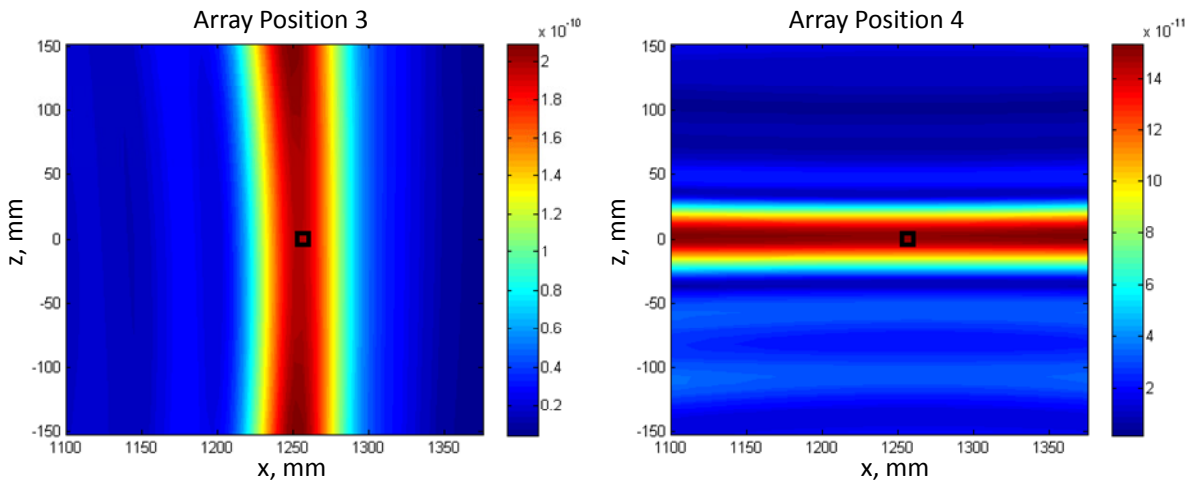

Figure 5-6. Beamformed source maps of single cubic element at 10368Hz using a) Array Position 3 b) and Array Position 4 with U_o = 60m/s in N^2/m^4Hz

To compare multiple source maps, sweeps through the maps at the roughness element location are taken in the direction of the array's sensor axis. This allows the shape and magnitudes of the maps from each array position to more easily be examined. Figure 5-7 and Figure 5-8 show sweeps through the source maps at z=0 and x=1257mm for Array Positions 1 and 2, respectively, calculated at various nozzle exit velocities. The results from Array Position 1, displaying the spanwise dipole, show that the source map peaks at the location of the roughness element for all velocities, and the magnitude of the peaks increases with velocity. At U_o=30m/s, the roughness noise is barely discernable above the background creating the large lumps in the normalized source maps away from the location of the roughness especially in the direction of decreasing x which is the towards the nozzle. The source maps recorded at Array Position 2, showing the streamwise dipole, also correctly identify the location of the roughness element at all measured velocities. For this array position, even at 30m/s, the background noise from the tunnel is well below the recorded roughness noise. This is due to the shielding of the array from the nozzle exit by the acoustically treated shelf as shown in Figure 5-4. There is no direct line of sight from nozzle exit to sensors as there is for the spanwise measurement position, Array Position 1. Both figures show that the shape of the measured source maps remain the same at all examined velocities. This single element analysis also demonstrates that the applied beamforming method works well isolating the roughness noise from the background and that the technique performs as expected identifying the source locations and the variation in source strengths.

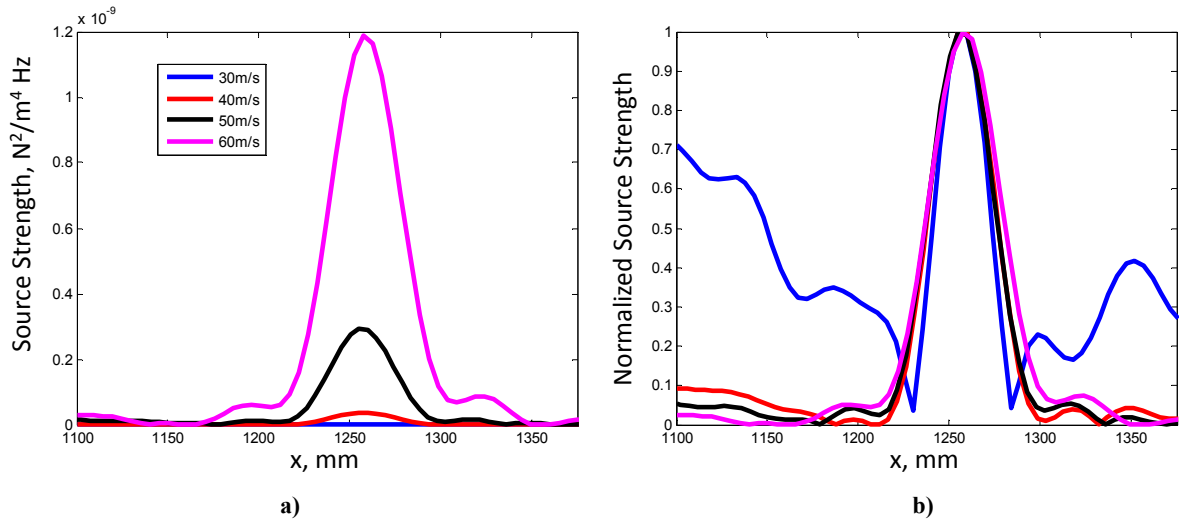

Figure 5-7. Sweeps through *z*=0 using Array Position 1 source maps of single cubic element at various nozzle exit velocities

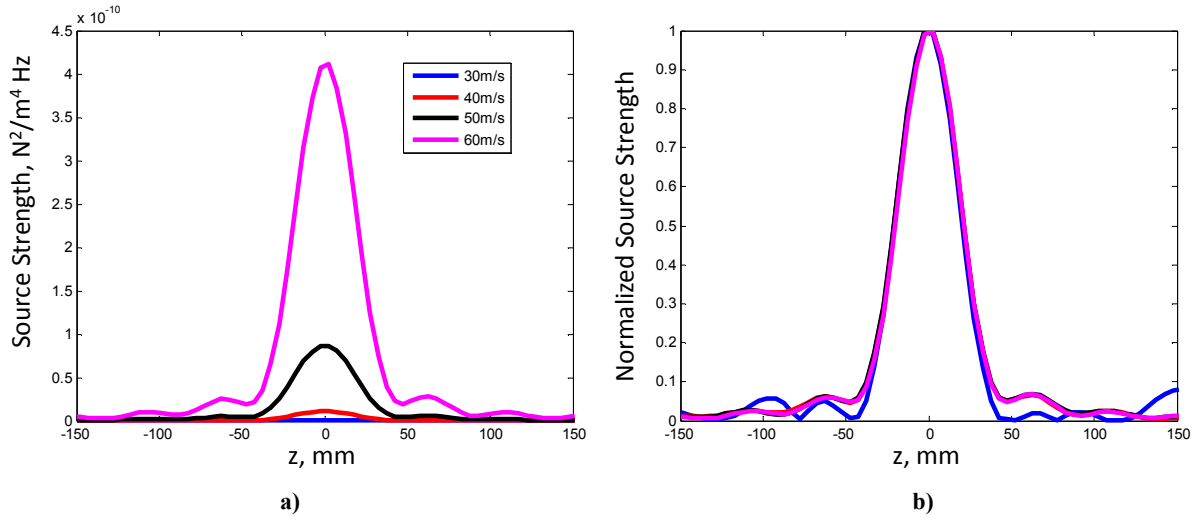

Figure 5-8. Sweeps through *x*=1257mm using Array Position 2 source maps of single cubic element at various nozzle exit velocities

If the number of elements is increased to a single spanwise row of six elements, the observed shape of the source maps is unaltered as measured from Array Position 1, but the source location becomes broader as observed from Array Position 2. This is due to the roughness elements being aligned along the same axis of the microphone array in Array Position 2 and out of axis in Array Position 1. These maps are shown for 10368Hz in Figure 5-9 along with the results as recorded from the two remaining microphone array locations. The source maps show that the array cannot distinguish between individual roughness elements which are all contained within one main source lobe. The resolution is not fine enough even at the highest observable frequency, 20kHz, to distinguish between individual roughness elements.

Figure 5-10 compares sweeps through the six element maps with the results from the single cubic element. For comparison, the single cubic element source map was manipulated by increasing its magnitude by a factor of six. Also, in Figure 5-10b and d, the measured single cubic element map was

displaced in the spanwise direction corresponding to each element location and summed to simulate a measurement of the 6x1 arrangement.

Figure 5-10a shows that the beamformed shape of the single cube and 6x1 arrangement are similar as measured from Array Position 1. The 6x1 configuration increased the peak level of the source map by approximately a factor of 6.7 from the single element result, slightly beyond the simple addition of six of the single element's sweep. The same enhancement in spanwise dipole strength is found in the measurement from Array Position 4. From this vantage point, the linear microphone records the spanwise variation of the spanwise dipole. Again, the results show that the spanwise noise of the 6x1 fetch is greater than that found from the addition of six individual sources. This indicates that the spanwise noise generated per element may be enhanced by the presence of spanwise adjacent elements, but it must be noted that these results do not account for the change in distance from the source-to-observer for the elements in the 6x1 configuration. The distributed single element map used for comparison is simply offset to simulate the 6x1 configuration of sources with no account for changes in the measured signals as would be recorded at each of the array sensors.

Alternatively, the streamwise dipole strengths of the 6x1 fetch, as measured from Array Positions 2 and 3, are approximately recreated by the addition of the single element results. There is no enhancement of the per element noise in the streamwise direction due to the addition of the spanwise elements. Array Position 2 shows the spanwise variation of the streamwise dipole is approximately constant. The source map is almost indistinguishable from the distributed single element results except for the slight asymmetry of the source map.

Both spanwise sweeps, in Figure 5-10b and d, show this asymmetric effect with spanwise and streamwise source strengths favoring the negative z-direction. This is believed to be due to variation of the in-flow conditions and is not a function of the surface geometry. This small variation in the flow in the spanwise direction was measured by Morton (2011) using a hotwire probe.

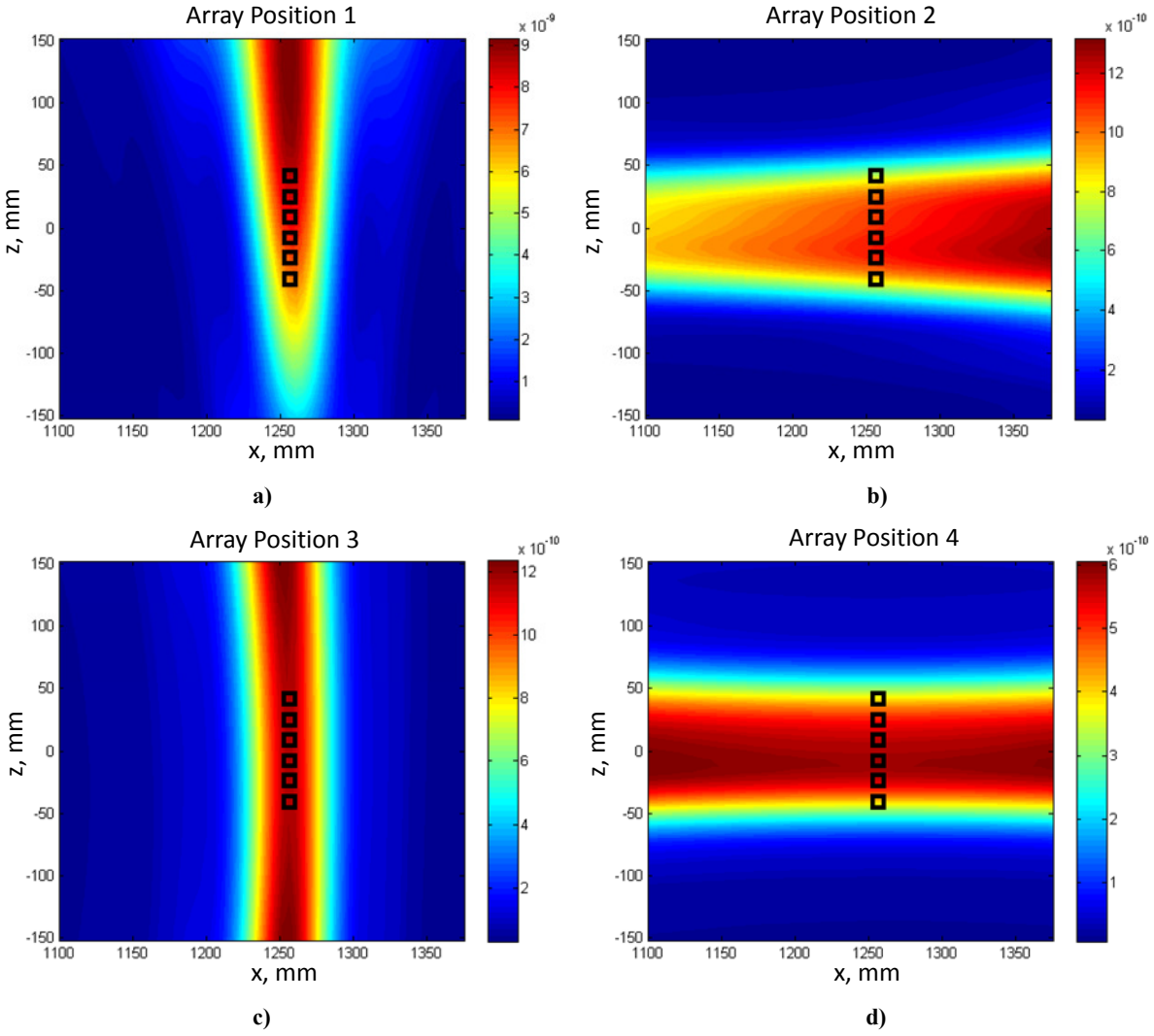

Figure 5-9. Beamformed source maps of a single spanwise row of six cubic elements at 10368Hz using a) Array Position 1 b) Array Position 2, c) Array Position 3, d) and Array Position 4 with U_o = 60m/s in N^2/m^4Hz

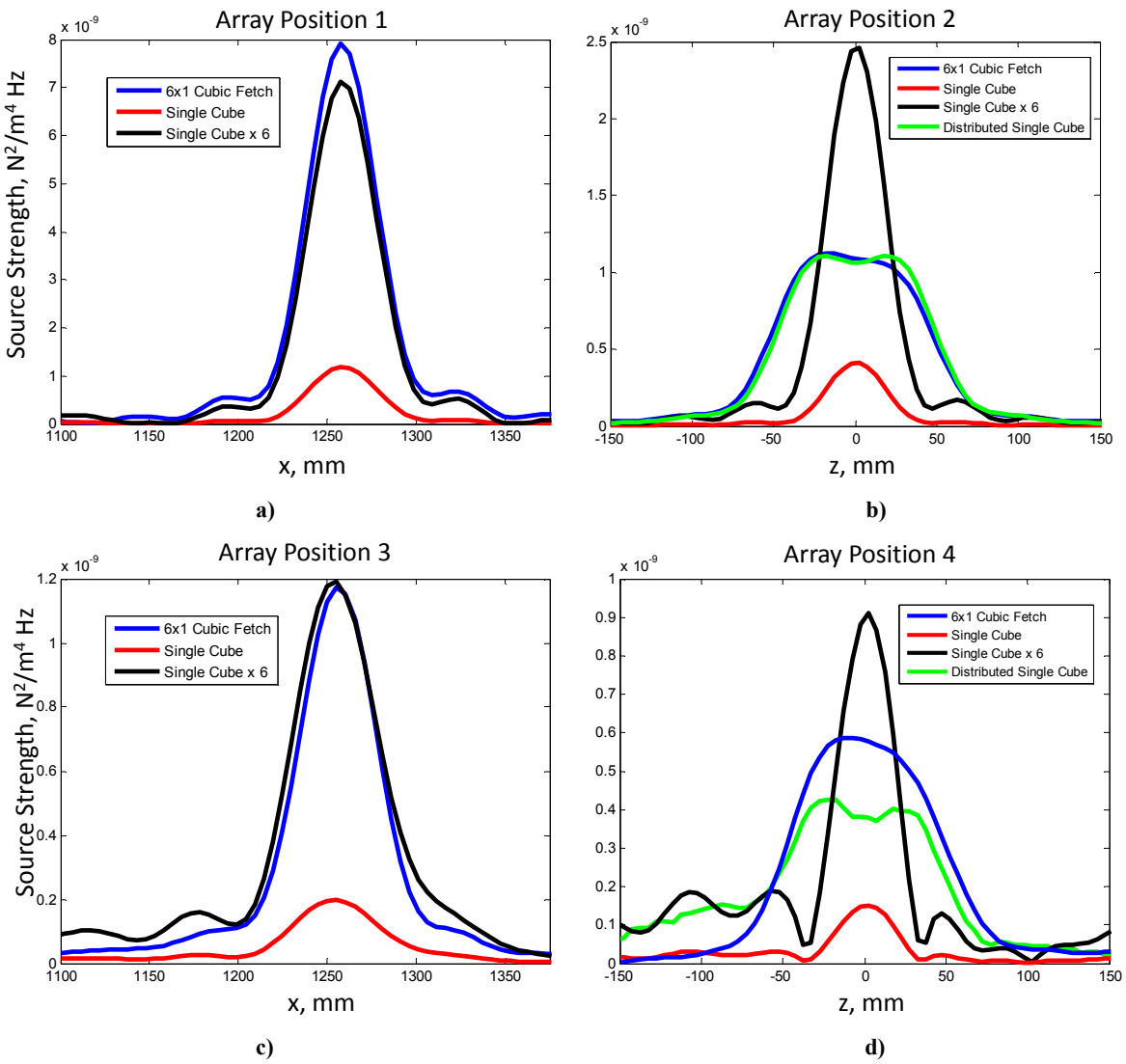

Figure 5-10. Comparison of sweeps through source maps of 6x1 and 1x1 cubic roughness fetches at U_o = 60m/s

Figure 5-10 shows the variation in beamformed source maps with the addition of spanwise adjacent roughness elements. The effect of downstream elements on the streamwise and spanwise dipoles was studied by incrementally increasing the number of trailing spanwise rows up from the 6x1 configuration to a 42 element fetch of cubic elements in a six spanwise by seven streamwise arrangement. Figure 5-11 shows a comparison of the source maps produced by measurements of all the multi-element cubic roughness fetches as recorded from Array Position 1 at U_o = 60m/s. These sweeps are through the spanwise center of the roughness fetch and show the streamwise variation of the spanwise dipole strength. Figure 5-11a shows that trailing rows of roughness increase the peak of the source map from the original 6x1 case, but a consistent increase with the total number of elements is not observed. The source map sweeps for fetches 6x2 to 6x7 have peaks that vary by 17% in a seemingly random order.

Figure 5-11b focuses on the shift in source map shape with the addition of trailing rows by normalizing the source maps on the peak values. The dashed lines indicate the streamwise location of the 1st and 2nd spanwise rows into the roughness. The addition of the trailing rows of roughness shifts the

peak of the source maps downstream. The 6x2 curve shows that the addition of a single trailing row of six spanwise elements produces a peak between the two rows. When a third row is added, the source map appears to peak at the location of the second row. The peak remains at this location with additional trailing rows, but the backside of the source map begins to widen further creating a broad base to the main lobe.

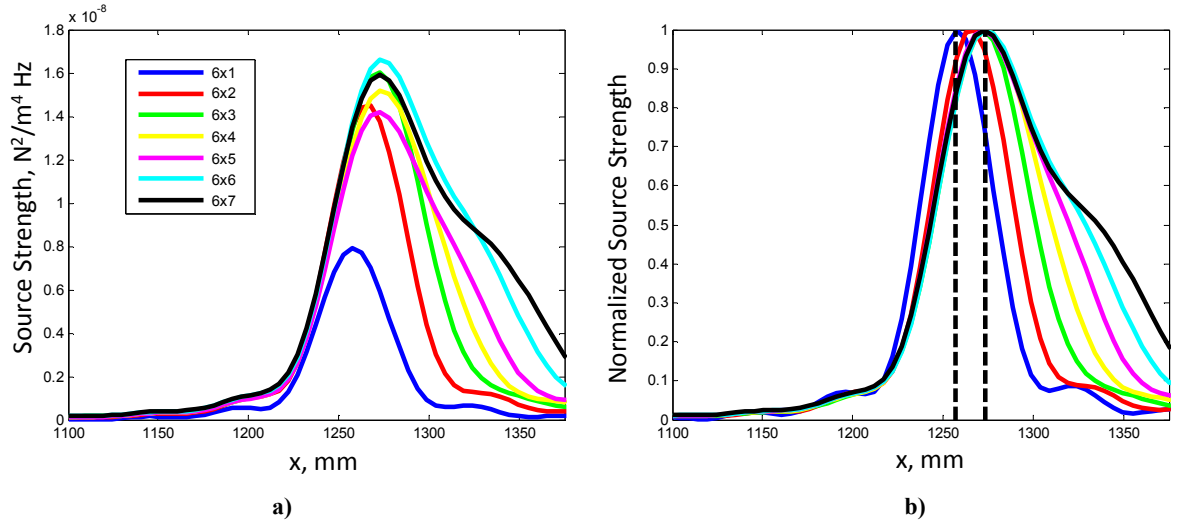

Figure 5-11. Sweeps through source maps at z=0 for the multi-element cubic fetches at U_o = 60m/s for Array Position 1 (dashed lines indicate the streamwise location of the 1st and 2nd spanwise rows)

Figure 5-12 shows a comparison of the source maps produced by the multi-element cubic fetches as recorded from Array Position 2. The compared sweeps are through the streamwise location of the lead row at x=1257mm and display the spanwise variation in the streamwise dipole. The shape of the source maps remains approximately constant with the small asymmetric effect becoming more pronounced with the increase in elements. In general, the source map magnitude increases with the addition of elements, but the magnitudes of the sweeps through the 6x3, 6x4, and 6x5 maps are relatively constant. The map strength then increases with the addition of 6th and 7th spanwise rows. The peak of all the maps is well contained within the boundaries of the roughness fetches shown as the two vertical dashed lines. For comparison, the single row source map was displaced streamwise accordingly to recreate the 6x7 configuration assuming each row produces a streamwise dipole strength equal to that of the 6x1 cubic fetch. The magnitude of the measured source map from the 6x7 fetch is significantly weaker than the summed result calculated assuming this equal strength. Therefore, this shows the per row strength distribution decreases with the inclusion of trailing rows in the roughness fetch. This indicates these trailing rows may have weaker streamwise dipole strengths than the lead row which lower the per row average strength of the radiated noise. To confirm this observation, the radiated noise needs to be analyzed from a vantage point that isolates the streamwise variation of the streamwise dipole.

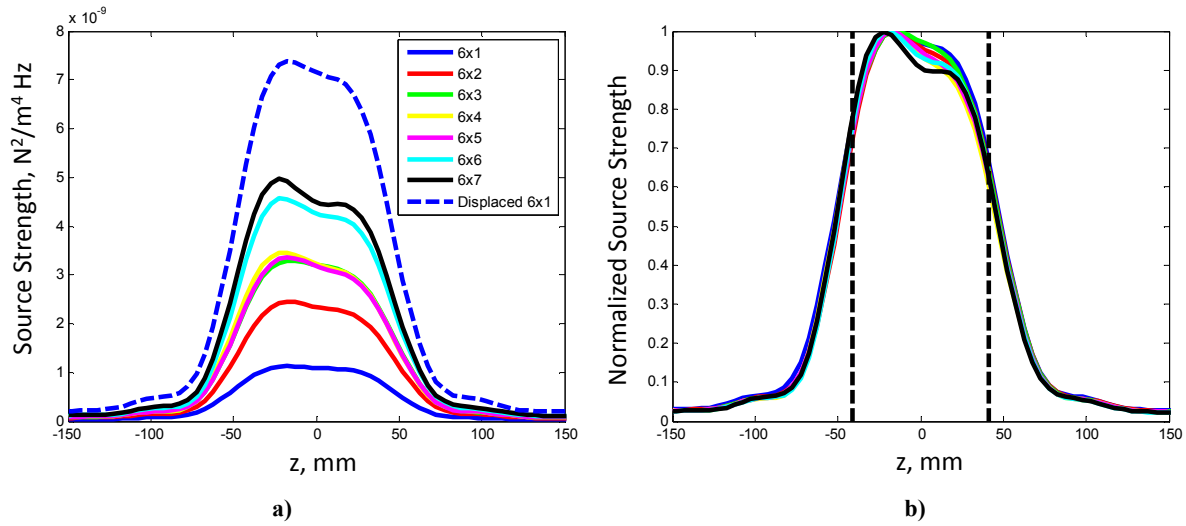

Figure 5-12. Sweeps through source maps at x=1257mm for the multi-element cubic fetches at U_o = 60m/s for Array Position 2 (dashed lines indicate the spanwise boundaries of the roughness fetch)

Figure 5-13 displays the results from Array Position 3 which is in a favorable position that isolates the streamwise variation of the streamwise dipole source. Like the spanwise dipole, the peak strengths occur near the front of the fetch, but again the peak magnitudes do not continuously increase with the number of elements. The peak levels rise and remain approximately constant beyond the addition the third row except for the 6x5 arrangement which has a magnitude similar to the 6x2 fetch. The shape of the source maps, indicating the relative source strength distribution through each roughness fetch, also resemble the spanwise dipole results in Figure 5-11. The peak of the map shifts downstream but remains within the lead two rows. The base becomes wider with increasing number of downstream elements creating a larger trailing side of the source map. A constant strength source distribution would produce a symmetrical source map different from the measured values. This suggests that the spanwise and streamwise dipole strengths throughout the fetch are not constant and favor the leading rows.

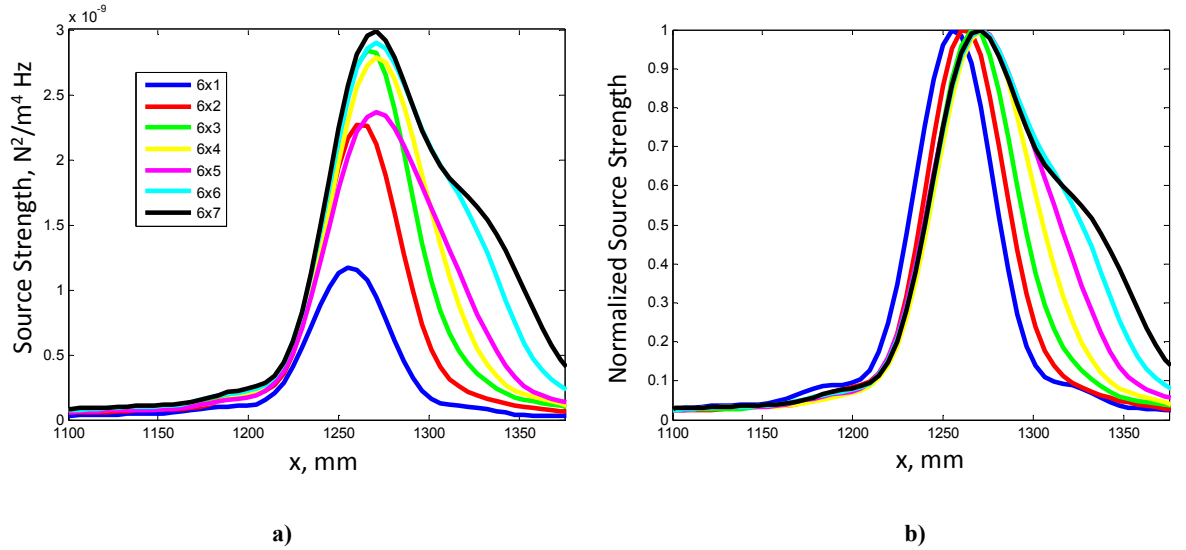

Figure 5-13. Sweeps through source maps at z=0 for the multi-element cubic fetches at U_o = 60m/s for Array Position 3

The fourth microphone array vantage point used in this study detects the spanwise variation of the spanwise dipole. These results for the multi-element cubic fetches are shown in Figure 5-14. The spanwise dipole behaves similarly to the streamwise dipole with an approximately even source distribution. Again, the slight asymmetric effect becomes more dominant as the number of elements increases. Like Figure 5-12, results from the 6x1 source map are distributed and summed to simulate a 6x7 fetch with spanwise source strengths equal to the 6x1 fetch for comparison. These results greatly overpredict the measured source map of the 6x7 fetch nearly doubling the observed peak value. This should be expected given the results of Figure 5-11 which show the trailing rows producing weaker spanwise dipole strengths. The streamwise source distributions of the spanwise and streamwise dipoles will be analyzed further in Section 5.4.

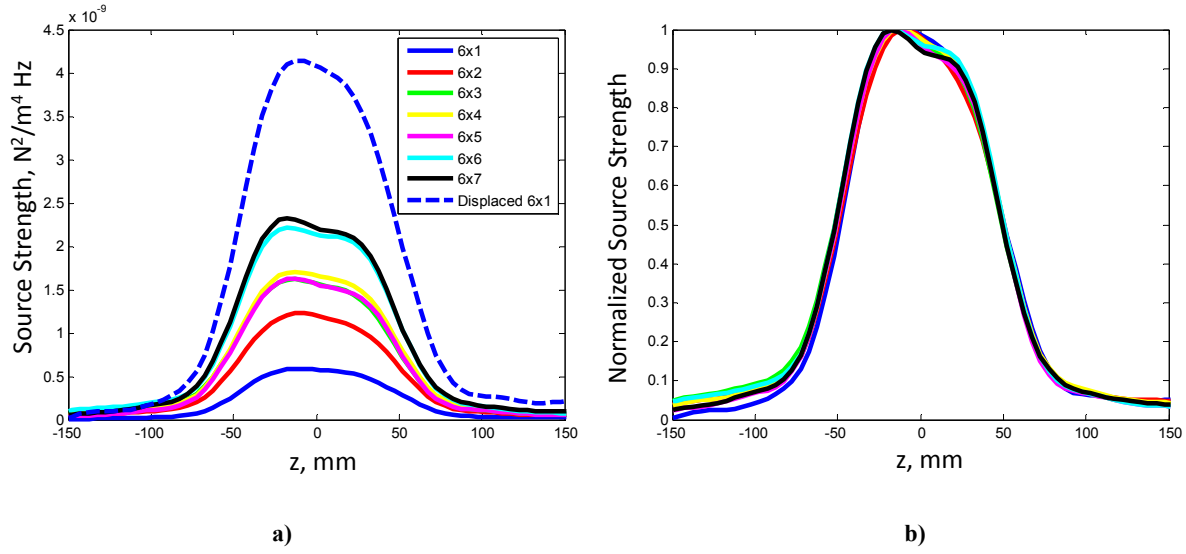

Figure 5-14. Sweeps through source maps at x=1257mm for the multi-element cubic fetches at U_o = 60m/s for Array Position 4

5.2 Hemispherical Roughness – Single Element to 42 Element Fetch

The far field noise from the hemispherical roughness was far below that produced by the cuboidal roughness as shown in Section 4.2.4. Beamformed maps of the noise from a single hemispherical element did not produce clearly defined peak over the focal area due to the extremely low signal-to-noise ratio of the measurement. Therefore, only source maps produced by the multi-element fetches are presented for the hemispherical roughness. Figure 5-15 and Figure 5-16 show sweeps through the multi-element source maps as recorded from Array Position 1 and Array Position 3. The source maps from both array locations are similar to the results from the cubic element fetch and display the streamwise variation of the spanwise and streamwise dipole strengths, respectively. The addition of trailing rows tends to shift the apparent peak source strength downstream and broaden the source area of both the spanwise and streamwise dipoles. Due to the low level sound produced by the hemispherical roughness, the background noise makes a greater appearance in the calculated source maps, especially from the direction of the nozzle in the negative x-direction. The source map shape of the streamwise dipole in Figure 5-16 appears to change with the size of the roughness fetch. The 6x5 fetch produces a broader peak than the 6x7 fetch

indicating a more even distribution of source strengths. No results are given for the 6x1 fetch in Figure 5-16 because the roughness noise was indistinguishable above the background levels.

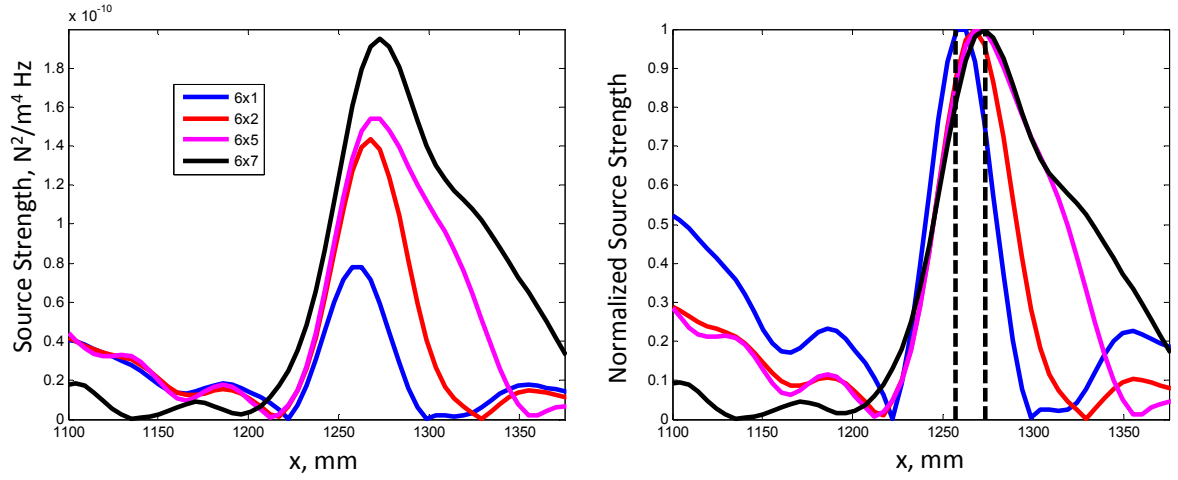

a) b)

Figure 5-15. Sweeps through source maps at z=0mm for the multi-element hemispherical fetches at U_o = 60m/s for Array Position 1

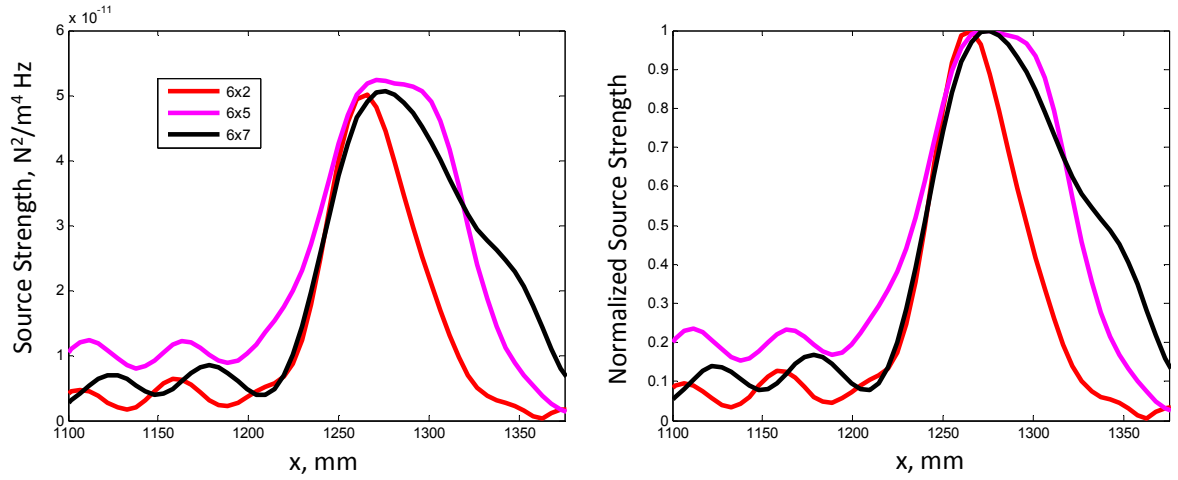

a) b)

Figure 5-16. Sweeps through source maps at z=0 for the multi-element hemispherical fetches at U_o = 60m/s for Array Position 3

Figure 5-17 displays the results from Array Position 2 measuring the spanwise variation of the streamwise dipole. Similar to the cuboidal roughness, an approximately constant source distribution is observed across the span of the roughness. The same slight asymmetric noise production is measured most notably for the larger fetches. It is also observed that the per element streamwise noise production is diminished with the addition of trailing rows compared to the summed solution of the distributed 6x1 source strengths. Plots of the spanwise variation of the spanwise dipole could not be produced because there was not sufficient signal-to-noise ratio as measured from Array Position 4.

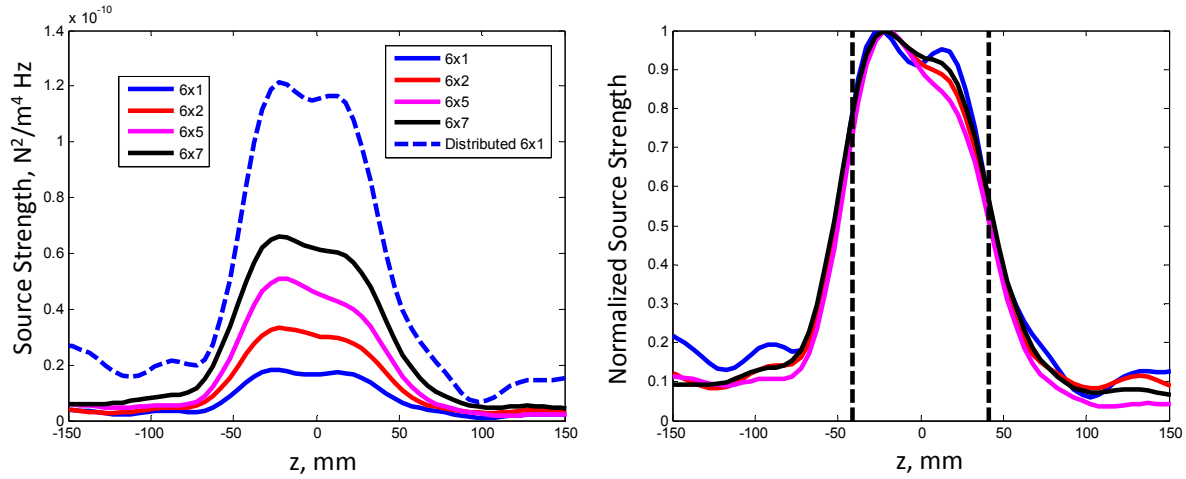

a) b)

Figure 5-17. Sweeps through source maps at x=1257mm for the multi-element hemispherical fetches at U_o = 60m/s for Array Position 2

5.3 Comparison of Cuboidal and Hemispherical Roughness

Although the source maps vary in magnitude greatly, the hemispherical and cuboidal roughness produce similarly shaped source maps. Figure 5-18 shows the comparison of the source maps as recorded by Array Positions 1. The similarity of the maps indicates that the spanwise dipoles vary similarly in the streamwise direction for both roughness fetches.

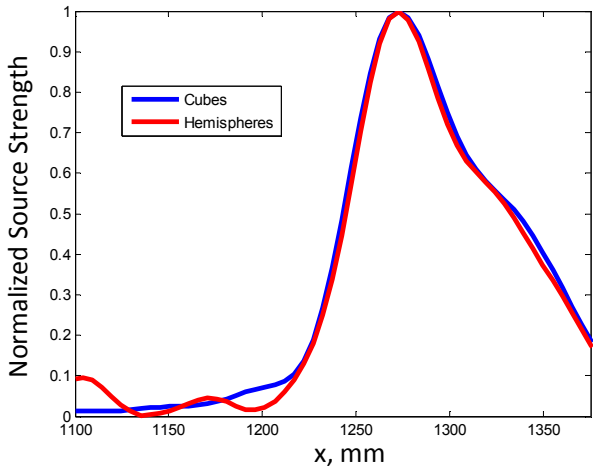

Figure 5-18. Comparison of 42 element source maps from cuboidal and hemispherical roughness as recorded from Array Position 1

The results from Array Positions 2 and 3 are used to observe the spanwise and streamwise variation of the streamwise dipole, respectively. These results are shown in Figure 5-19. The streamwise dipole distribution in the streamwise direction shown in Figure 5-19a varies between the two roughness

geometries. The hemispherical roughness has a broader peak that is shifted slightly further downstream than the result of the cubic roughness. This indicates that the streamwise source strength distribution in the hemispherical roughness may decrease at a slower rate than the cuboidal roughness even though their spanwise dipole strengths, shown in Figure 5-18, were almost identical. Although the streamwise distribution may be different for both surfaces, the spanwise variation of the streamwise dipoles is approximately the same as shown in Figure 5-19b.

A similar comparison from Array Position 4 of the spanwise variation of the spanwise dipole could not be completed because the hemispherical roughness did not produce a sufficient signal-to-noise ratio.

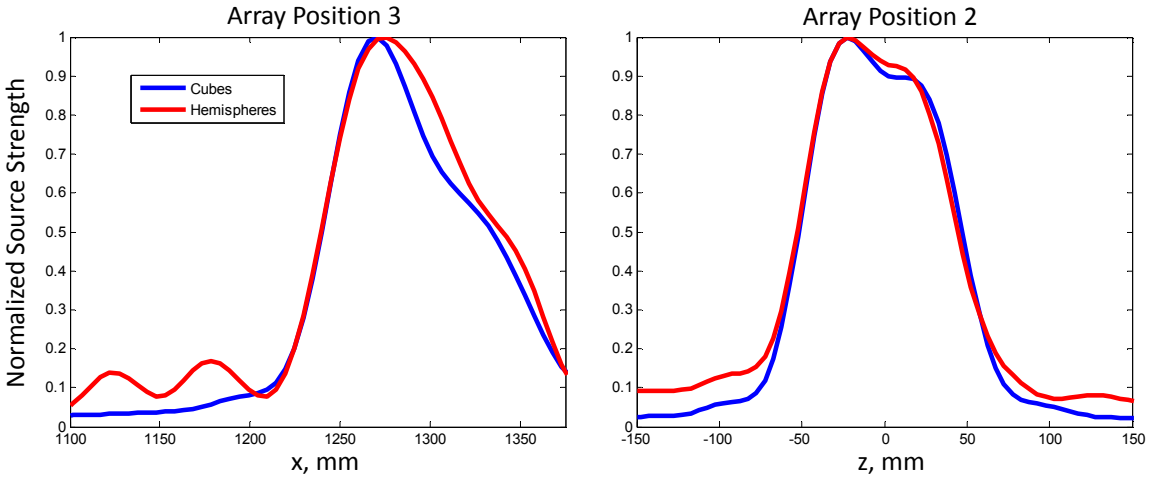

Figure 5-19. Array Position 3 and 2 comparison of noise from 42 element fetch of cubes and hemispheres at U_o=60m/s

5.4 Deconvolution of Source Maps

The source maps in Figure 5-18 and 5-19 show specific source strength distributions that vary slightly between the cuboidal and hemispherical roughness, but determining quantitative source strengths from the beamformed maps can be a difficult task. Conventional methods of determining source strengths from beamformed maps require the integration of the source map strength over a user defined area which is often a challenging choice especially in cases where the noise produced by individual sources cannot be isolated in the source map. The choice of integration area is an even greater problem when using a linear microphone array because of the lack of spatial resolution in the out of sensor axis direction. Although the source strength may be difficult to determine, the source strength variation can be easily deduced from the measured source maps. The shape of the measured maps can be recreated by computing source maps of distributed dipoles with similarly varying strengths to the actual case. By examining various source strength distributions and comparing them to the measured maps, the strength distribution through a fetch of roughness can be determined.

The simplest case would be that of a single roughness element. In this case, there is not a distribution of sources but only a single dipole source located at the roughness element location. Figure 5-20 shows the source map comparison between the measurement of a single cubic roughness element and the point source image generated by a dipole source at the same location. The maps have been

normalized on their peak strengths to compare shapes. The main lobes have a very similar shape, but the measured map is slightly wider and has elevated side lobes due to the background noise not present in the point source map.

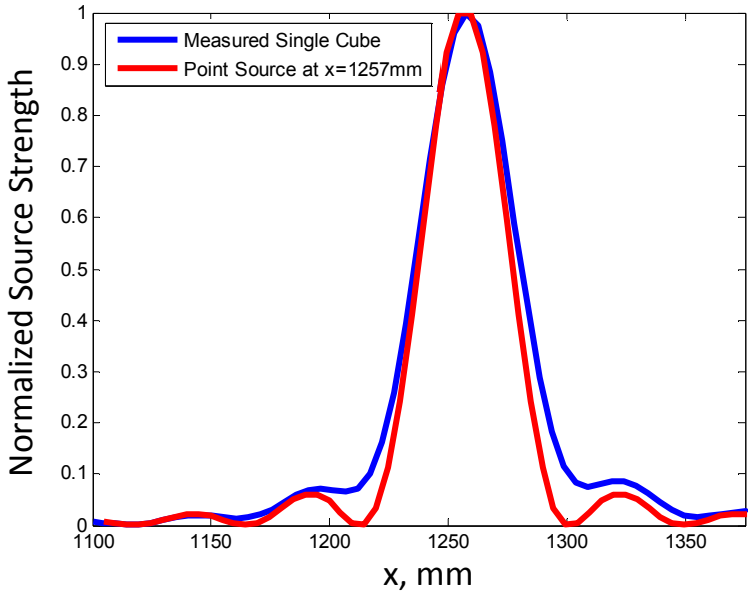

Figure 5-20. Comparison of measured single cubic element at U_o=60m/s spanwise dipole with dipole point source

A similar but more complex analysis can be done for the full 6x7 fetch of cubes in which a source strength distribution must be assumed. Figure 5-21 shows a few model source distributions by row for the streamwise variation of the streamwise and spanwise dipoles. Four different source distributions are studied for the strength of radiated noise in the streamwise and spanwise directions: a constant strength distribution, a linearly decreasing distribution, a dominant second row case, and the RMS force distribution as calculated by the LES of Yang & Wang (2011) for the corresponding streamwise or spanwise dipole. The RMS values reported in Yang & Wang (2011) may not be representative of the fluctuating forces at the frequencies where roughness noise was recorded in this study, and therefore, the comparison between generated source maps should not be considered a validation of the LES results. The RMS distribution was used solely as another distribution model shape. The absolute levels of the distributions are unimportant because the compared source maps will be normalized on their peak values the result being a contrast of the distribution alone.

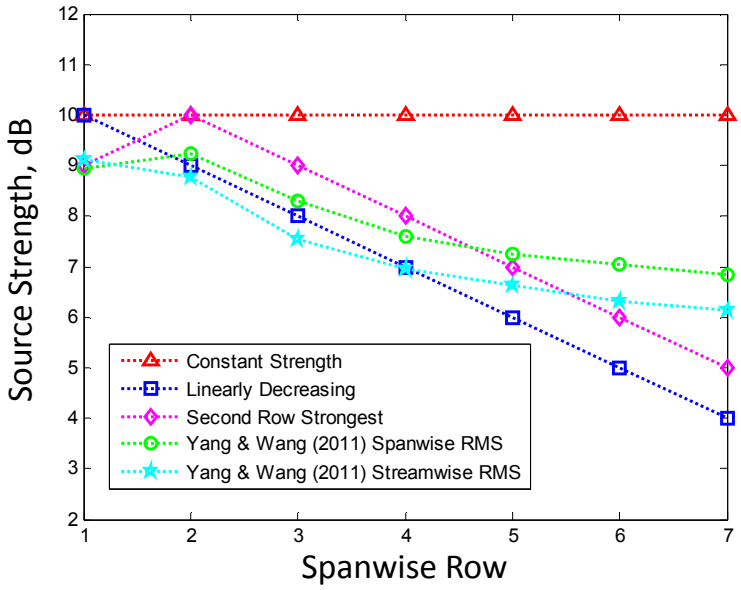

Figure 5-21. Model source strength distributions for streamwise variation of streamwise and spanwise dipoles in cubic roughness

Figure 5-22 shows the measured source map of the spanwise dipole sources from a 6x7 fetch of cubic roughness compared to the source maps produced by the model source distributions at three different frequencies. The estimated source maps assume a single source strength at the spanwise center of each row. Comparison with source maps having six spanwise distributed model source distributions showed negligible differences with the source map shape produced by assuming only a single spanwise central distribution. The peak of the source map for this fetch of elements peaks downstream of the lead row, but the linearly decreasing model clearly fits the measured sweeps the best at all frequencies. This shift in peak location is due to spatial broadening in the beamformed source map due to the low resolution of the source image. The relative difference between the linear source distribution and the measured source strengths differ by frequency. The strengths of the trailing rows are slightly underpredicted with the linear model at the lowest frequency, but as the frequency increases, the relative strength of the trailing rows diminishes. The linear model rises above the measured values on the backside of the main lobe peak at 13696Hz. The measured source distribution tends to level off towards the trailing rows similar to that of the Yang & Wang's (2011) RMS results but to a much less degree creating the hump on the backside visible at the two higher frequencies. The maximums in the normalized source maps produced by the second row dominant, the RMS distribution of Yang & Wang (2011), and the constant strength source distributions are all downstream of the maximum calculated in the measured map suggesting that the spanwise dipole is strongest for the lead row of cubic roughness.

Analyzing the streamwise dipole strength in a similar manner, Figure 5-23 shows that again the linear distribution of sources strengths decreasing by 1dB per row fits the measured maps best. The 6336Hz differs the most peaking upstream of all the model source distributions. The measured source map's relation to the model maps changes with frequency indicating that the distribution of streamwise dipole strengths, like the spanwise dipoles, varies with frequency. For all analyzed frequencies, the results indicate that the streamwise and spanwise dipoles are strongest for the lead row of the cubic roughness fetch and that the strength of the trailing rows decreases at an approximately linear rate of 1dB per row.

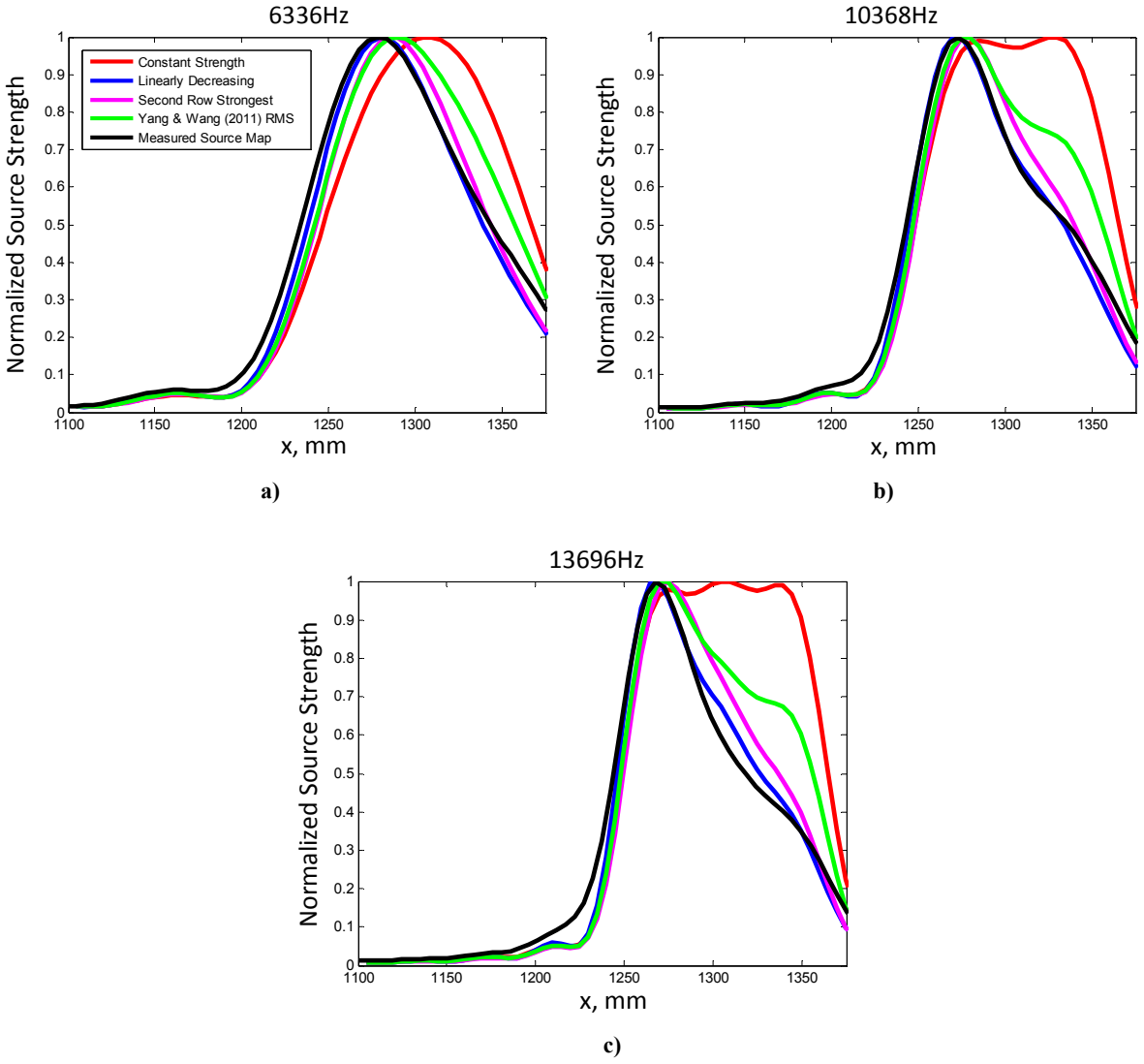

Figure 5-22. Comparisons of measured source map of 6x7 cubic fetch at z=0 with source maps of model source distributions for the spanwise dipole at U_o=60m/s

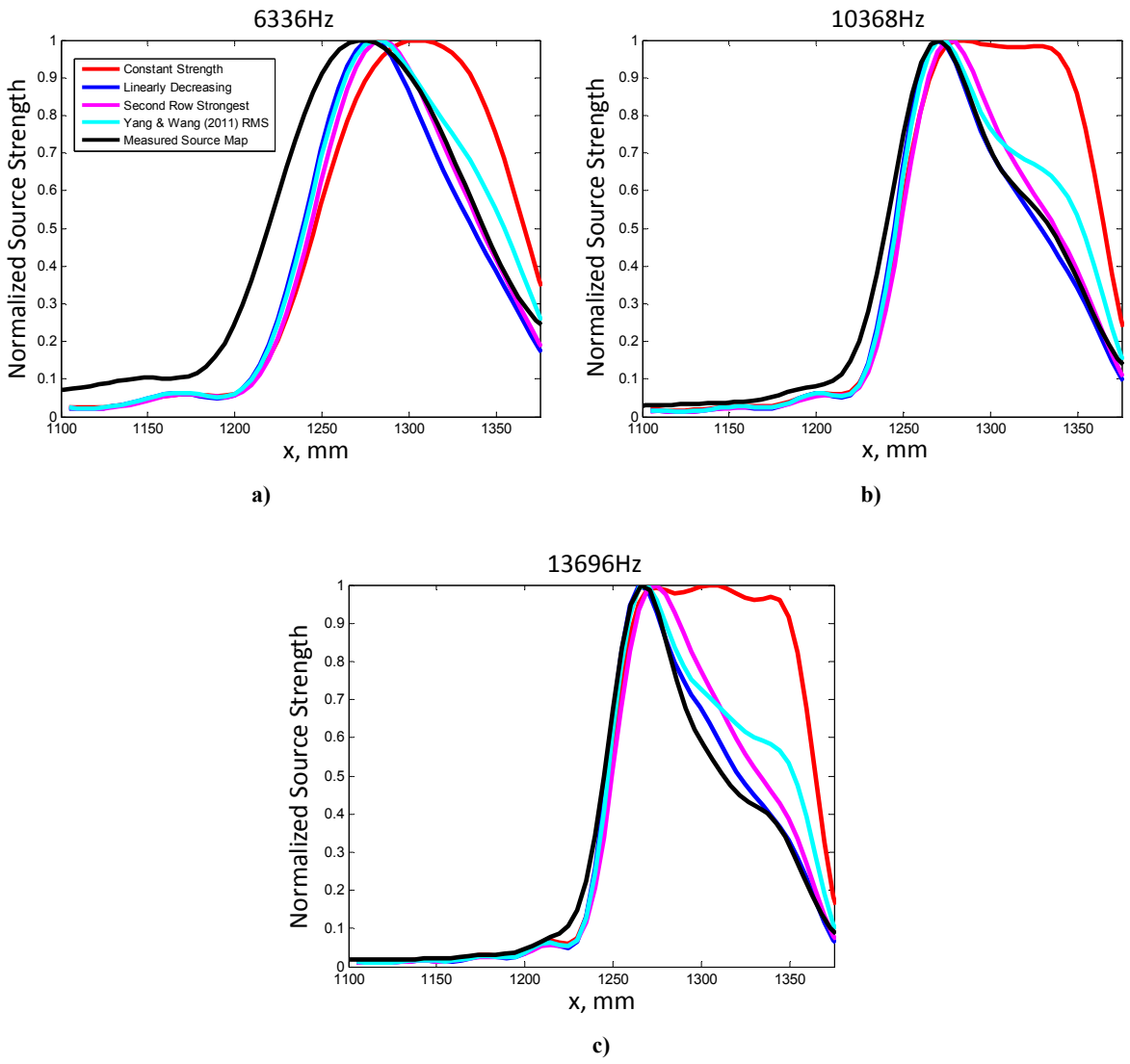

Figure 5-23. Comparions of measured source map of 6x7 cubic fetch at z=0 with source maps of model source distributions for the streamwise dipole at U_o=60m/s

A similar analysis of the streamwise variation of source strengths through a fetch of hemispherical roughness is completed using the source distributions in Figure 5-24. The second row dominant distribution and linearly decreasing distributions are considered similar to the cubic roughness analysis. The constant strength distribution is not considered further because, as shown in Figure 5-22 and 5-23, it provides a poor fit to the measured source maps. The Yang & Wang (2011) RMS unsteady force distributions are the result of an LES study for a 4x10 fetch of hemispherical roughness. The RMS distributions of the hemispherical roughness differ from that of the cuboidal roughness. The lead row of the hemispherical roughness produced the weakest spanwise and streamwise RMS dipole strengths over the entire rough surface. The source strength of the second row was strongest and then the calculated strengths quickly level off. Again, these distributions are used as shape functions only and should not be considered a validation of the LES study.

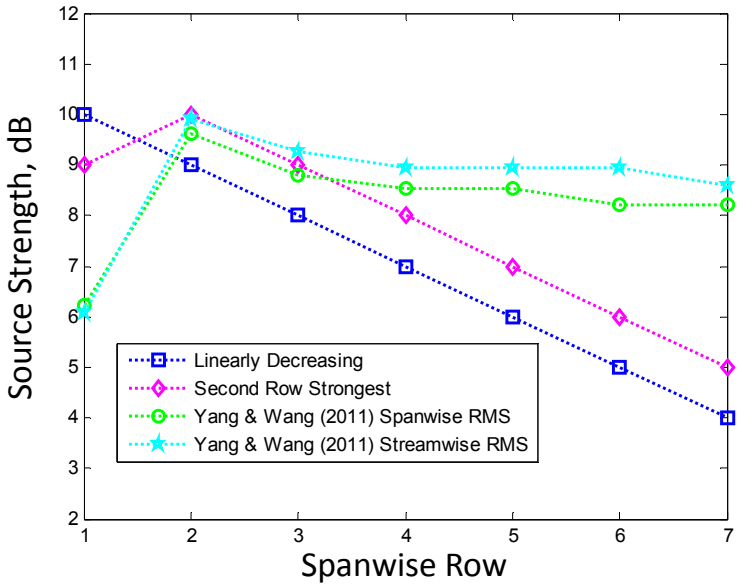

Figure 5-24. Model source strength distributions for streamwise variation of streamwise and spanwise dipoles in hemispherical roughness

The spanwise dipole results are shown in Figure 5-25 for three frequencies. The best fit of the measured source map is again the linearly decaying source distribution model. This is expected since the comparison in Figure 5-18a shows that the cuboidal and hemispherical source maps are very similar in the spanwise direction. The other source distribution models are too heavily weighted on the downstream elements. Like the cuboidal roughness fetch, the source distribution tends to favor the front of the roughness fetch with increasing frequency. The trailing rows become relatively weaker as the frequency is increased. This can be related back to measurements of the wall pressure spectra in both the cuboidal and hemispherical roughness in Figure 4-3a and 4-12a, respectively. These figures show that the recorded high frequency pressure fluctuations decrease in the streamwise direction. At 6336Hz, the spectra at all streamwise positions inside the roughness fetches vary only slightly in the streamwise direction, but at 13696Hz, there is a more dramatic reduction in pressure fluctuations between the front and rear of the roughness fetches.

Figure 5-26 shows the results of the streamwise dipole variation. The results of the hemispherical fetch in this case are different from that of the cuboidal roughness as shown in Figure 5-19. Comparing the model source distributions, none of the examples fit the measured source map precisely. The source strength appears to peak at the lead row like the linearly decreasing source distribution, but the shape of the measured distribution varies greatly for the three different frequencies. At the lowest frequency, 6336Hz, the peak occurs very near the lead row indicating that the trailing rows are significantly weaker with strengths decreasing much greater than 1dB per row as does the linearly decreasing distribution. At 10368Hz, the source seems evenly distributed around the lead rows of the fetch. The source distribution may be a cross between the results of the linearly decreasing model and the second row dominant model. The lead row appears to be the strongest producer of noise at 13696Hz but noise from the trailing rows generates an unusually shaped source map downstream that is not recreated by any of the model source distributions. These lumps on the trailing side of the source map, same as in Figure 5-25, may be an effect of background noise in the measurement and not due to the actual source distribution.

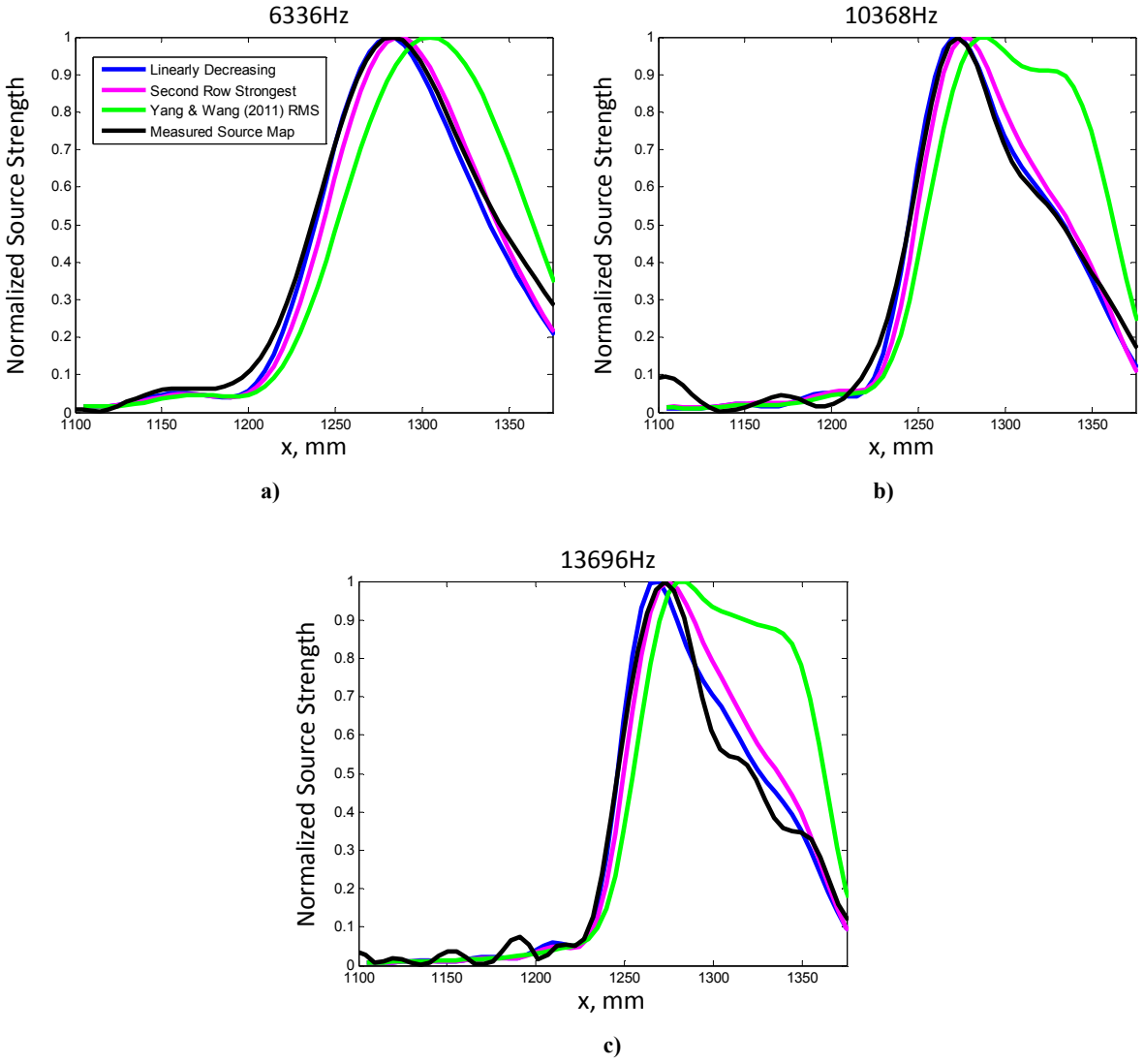

Figure 5-25. Comparions of measured source map at U_o=60m/s of 6x7 hemispherical roughness fetch at z=0 with source maps of model source distributions for the spanwise dipole

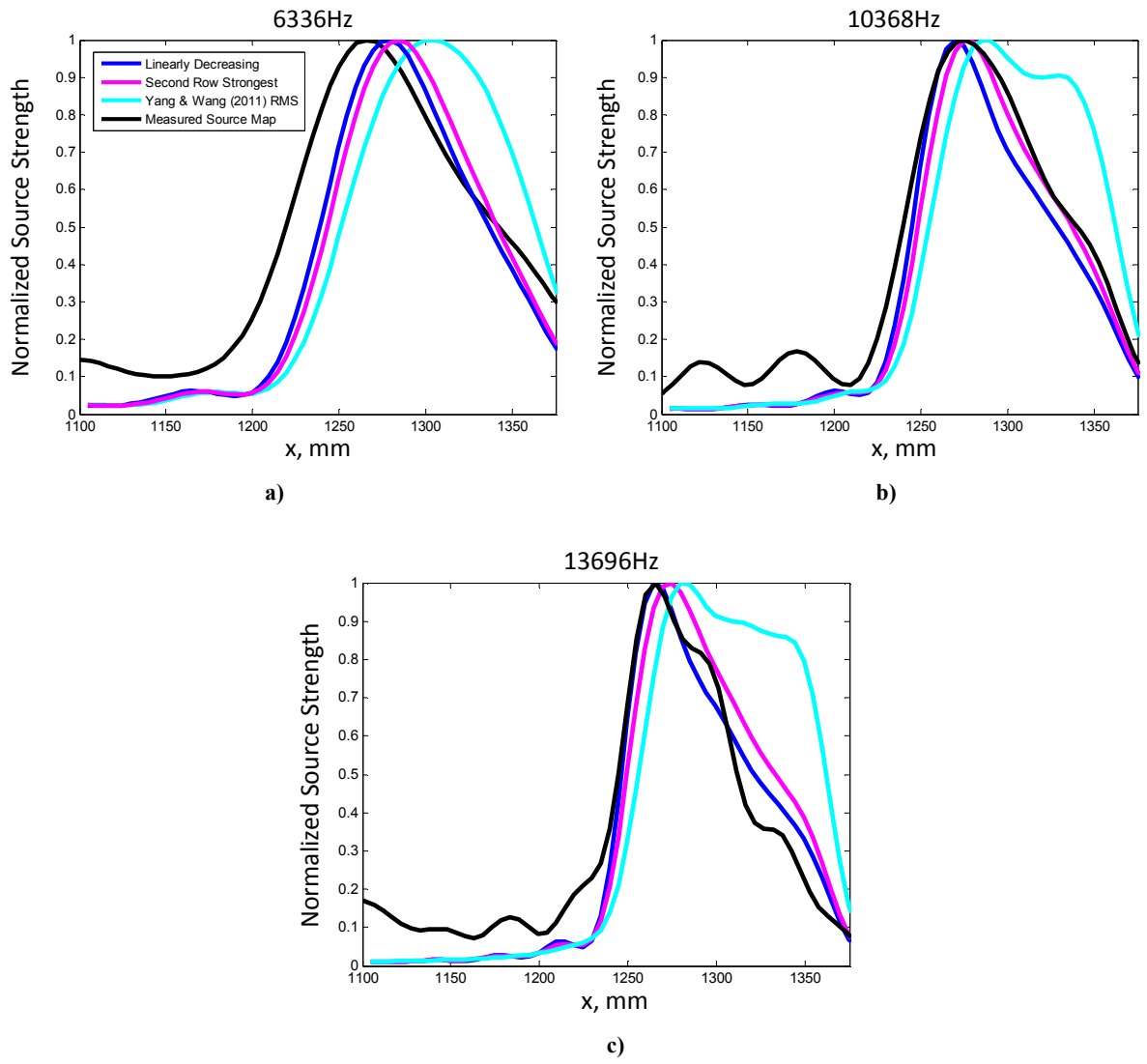

Figure 5-26. Comparions of measured source map at U_o=60m/s of 6x7 hemispherical roughness fetch at z=0 with source maps of model source distributions for the streamwise dipole

The shapes of the source maps have been approximately determined with this source distribution deconvolution method, but the absolute levels of the discrete source strengths have yet to be evaluated. To do this, a method needs to be developed that minimizes the error between the estimated and measured source maps. Using the measured source map results from Figure 5-3 and Figure 5-5 for a single cubic roughness element, assuming each figure is the result of either the spanwise or streamwise dipole alone, respectively, the strengths of the theoretical dipoles that would recreate the calculated source maps can be determined by a simple least-squares analysis. Figure 5-27 shows the source maps produced by the measurement of the single cube at Array Positions 1 and 2 compared to two curves produced by source maps of a dipole point source image with a source strength determined by a least-squares fit of the measured cross-spectral matrix assuming a dipole emanating from the location of the roughness element. The result for each source map was determined individually. The estimated and measured source maps agree very well showing the viability of the least-squares method to reproduce the measured source maps.

The calculated strength of the streamwise aligned dipole was 2.07×10^{-13} N^2/Hz and the strength of the spanwise aligned dipole was 3.82×10^{-14} N^2/Hz.

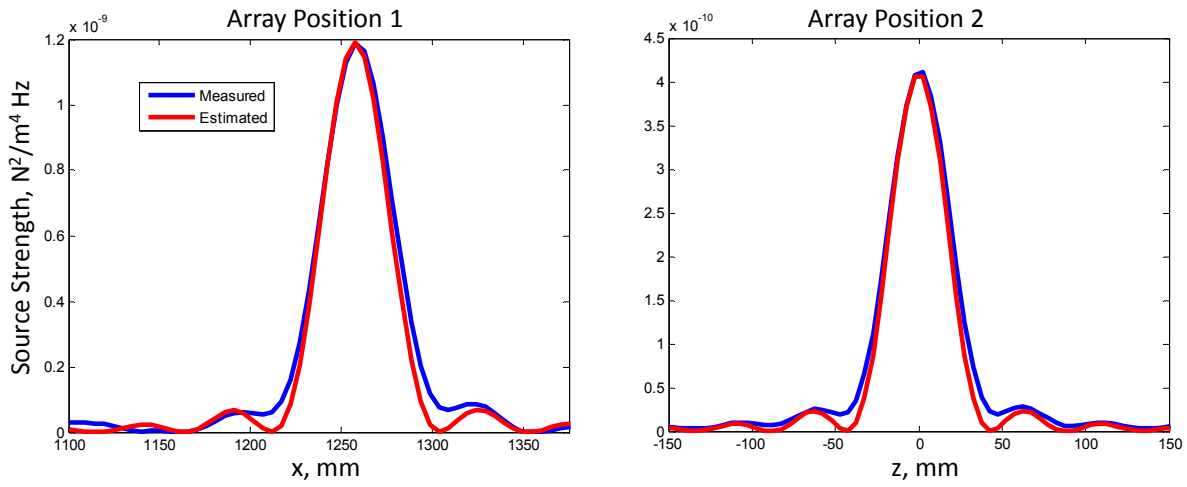

Figure 5-27. Measured and estimated source maps of single cubic elements from a) Array Position 1 b) and Array Position 2

This method seems to work well for the single cubic element, but as the number of sources is increased so does the error. When solving for seven independent source strengths the least-squares solution assigns source strengths of zero which is an artificial result, but the accuracy of this process can be improved by combining the array data from all four measurement positions. This process creates a highly overdetermined system of equations that solves for the separate streamwise and spanwise dipole strengths simultaneously. Chapter 6 details this least-squares analysis of the streamwise and spanwise dipole strengths.

Chapter 6 Least-Squares Analysis

Individual sources in the beamformed source maps of the noise from the cuboidal and hemispherical roughness fetches could not distinguished even at the highest measured frequencies. The desire to estimate individual source strengths inside multi-element fetches of discrete roughness led to the development of the least-squares analysis detailed in Section 2.5.2. This method is used to solve for the streamwise and spanwise source strengths using the data from all four array position simultaneously. The individual elements of the cross-spectral matrices were solved for assuming all of the roughness noise sources were uncorrelated. The following section details the least-squares calculation of source strengths from individual roughness elements in fetches of 3mm cuboidal and hemispherical roughness of various sizes. The roughness configurations range from single elements up to 42 elements.

6.1 Single Element Results

6.1.1 Spanwise and Streamwise Dipole Strengths

The measurements of noise from single cuboidal and hemispherical elements were the simplest cases studied since only two sources were assumed in the analysis: a spanwise and streamwise aligned dipole located at the position of the roughness element. The source strength analyses of the noise from single cubic and hemispherical elements reveal the large difference in source strengths of the two element shapes. Figure 6-1 shows the estimated spanwise and streamwise dipole strengths for both elements at a nozzle exit velocity of 60m/s. The estimated cubic element source strengths are over an order of magnitude stronger than that of the hemisphere. This agrees with the single point analysis of the far field noise in Figure 4-19 showing the large difference in radiated spectra from fetches of the two surface geometries. Comparison of the cubic element's spanwise and streamwise dipole show that the streamwise dipole is strongest for all frequencies and decreases at approximately the rate of $f^{-3.5}$. Although the conventional delay and sum beamforming method was unable to produce clear results at all of the microphone array positions for the single hemispherical element even at the highest studied velocity, the least-squares technique did converge over a limited frequency range. The results for the hemispherical element in Figure 6-1 are not as certain due to the very low signal-to-noise ratio and thus limited the frequency range over which a non-negative least-squares solution could be obtained. Further extensive analysis of the uncertainty of these estimations will be given in Chapter 7. A definitive conclusion cannot be made about the relative strengths of the hemisphere's spanwise and streamwise dipoles from this narrow frequency range of estimated data.

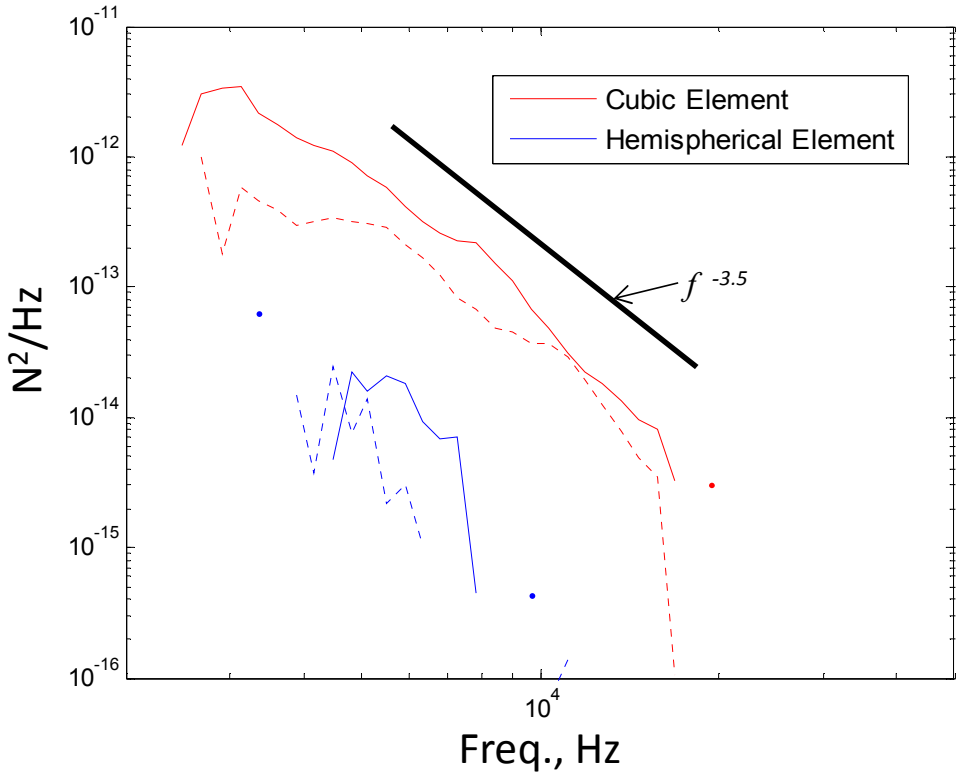

Figure 6-1. Streamwise (solid) and spanwise (dashed) dipole strengths of single cubic and hemispherical element at U_o=60m/s

The source strengths as determined by this least-squares method are in fact the unsteady drag and side forces on the element. Using the theory of Glegg & Devenport (2009), the single point pressure spectra needed to resolve the difference between the measured and estimated far field normalizations for the fetches of cuboidal and hemispherical roughness were calculated in Section 4.8. These wall pressure spectra results are given in Figure 4-53. They were calculated by dividing the measured far field recorded at an upstream location by the integrated value of the Chase wavenumber wall pressure spectrum and the surface filter function for each frequency. This analysis is shown in Equation 4-4. In the scattering model, the single point surface pressure spectrum measured in a rough surface may not accurately represent the unsteady drag on a surface's roughness elements because there is no account for the lengthscale of the boundary layer pressure fluctuations with respect to the roughness geometry which scatters only a portion of the fluctuations. Although, if the pressure fluctuations are the local result of unsteady forces on the element resulting from its own eddy shedding, then a more accurate representation might be expected. To examine this issue, the estimated single point wall pressure spectrum for the cuboidal roughness was converted to a crude approximation of the per element average unsteady drag by multiplying this spectrum by the cubes' frontal area, 9mm^2. The result of this calculation is shown in Figure 6-2 along with the least-square solution of the streamwise and spanwise dipole strength calculated for a single cubic element. The average estimatede unsteady pressure from the fetch of 42 elements overpredicts the average unsteady force from the single cubic element over much of the frequency range, but there is close agreement with the estimated streamwise dipole strength between 3-9kHz. Outside of this range, the disparity rises up to about 5dB. This surprisingly good agreement between the unsteady forces in the

streamwise direction and the surface pressure spectrum responsible for the noise projected in the streamwise direction suggests that eddy shedding from the cubic elements may play a significant role both in the generation of sound and of the pressure fluctuations. If the convection velocity of the shed vortices is similar to that of the unperturbed boundary layer, 9kHz correlates to structures 1/3 the size of the roughness element while 3kHz corresponds to eddies equal to the size of the element.

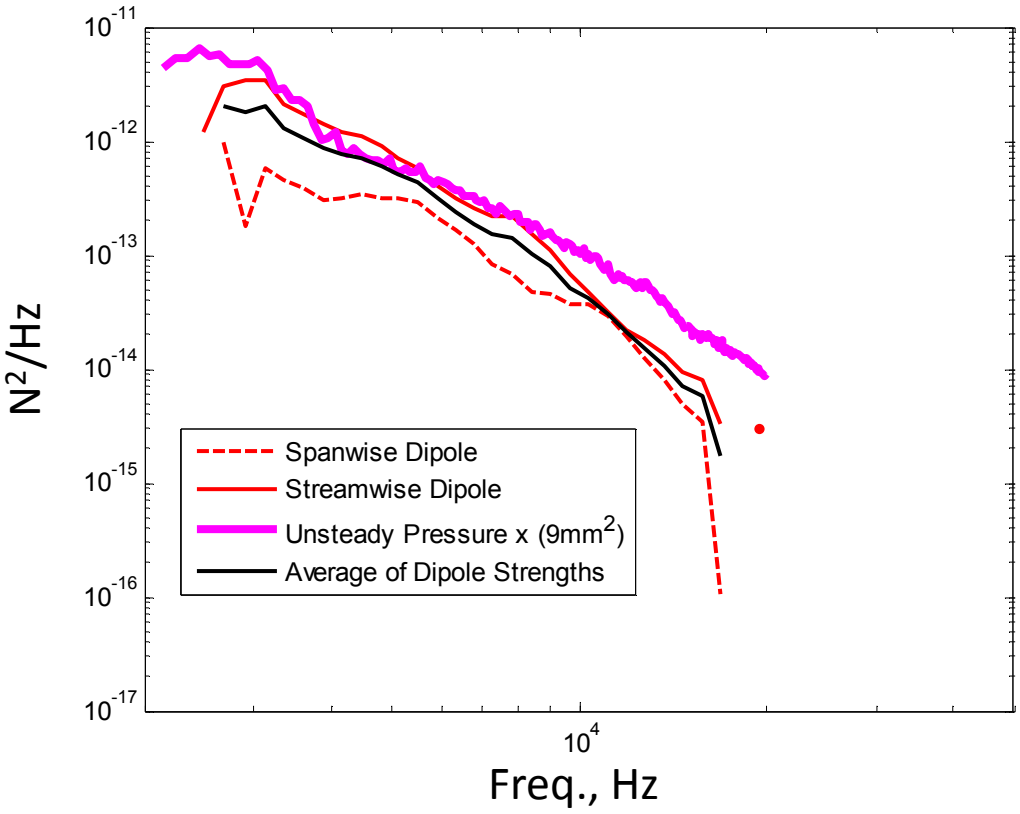

Figure 6-2. Estimated streamwise and spanwise source strengths of a single cuboid compared to the calculated average unsteady pressure on the roughness elements in a 42 element fetch of cuboids

A similar analysis can be done with the hemispherical roughness using the unsteady pressure spectra calculated in Figure 4-53 for the 42 element hemispherical roughness fetch. Again, the estimated single point wall pressure spectrum can be crudely converted to the unsteady drag spectrum by multiplying the wall pressure by the single hemisphere's forward projected area, $9\pi/2mm^2$. Figure 6-3 shows the least-squares estimated results for the single hemisphere's dipole strengths along with the unsteady drag force calculated using the forward projected area and estimated single point wall pressure spectrum. The great difference between the estimated spectral levels reveals that, unlike the cuboidal roughness, the far field produced by the hemispherical roughness may be created by a scattering effect and not vortex shedding over this compared frequency range. This analysis shows that the noise produced by the unsteady drag cannot be determined from the projected area and single point wall pressure spectrum alone. The scale of the pressure fluctuations must be taken into account through the form of the wavenumber wall pressure spectrum and Fourier transform of the surface slope to determine the portion of the wall pressure fluctuations that are scattered to the far field.

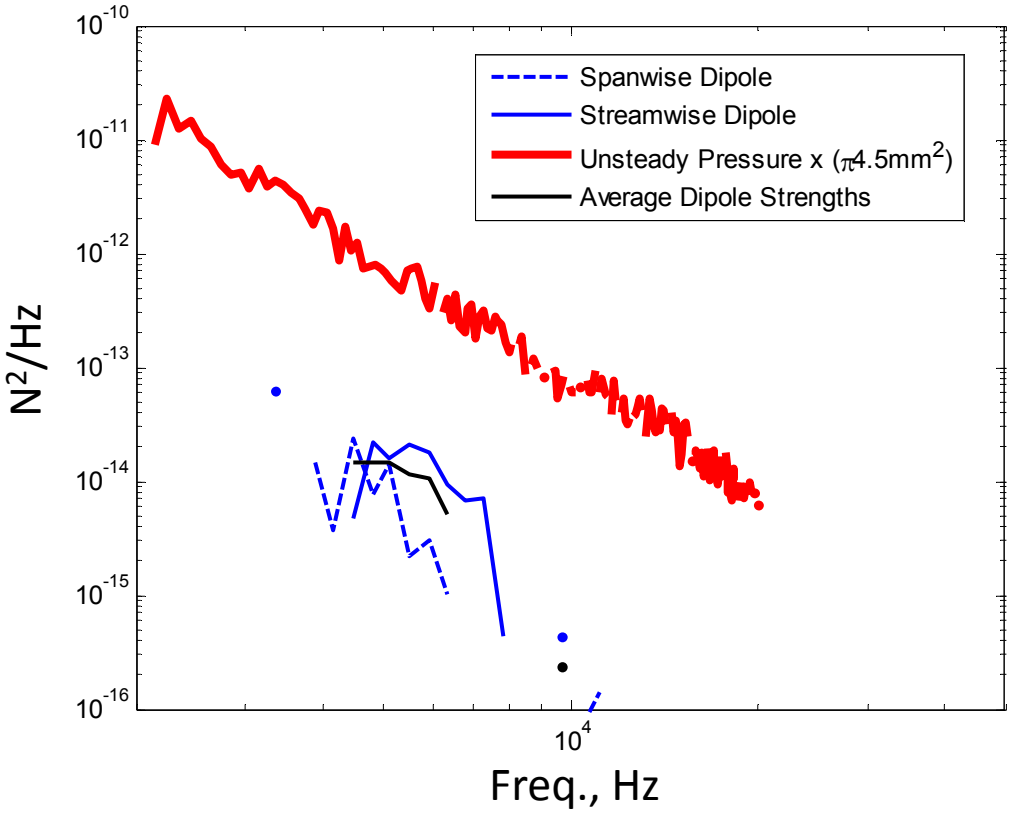

Figure 6-3. Estimated streamwise and spanwise source strengths of a single hemisphere compared to the calculated average unsteady pressure on the roughness elements in a 42 element fetch of hemispheres

6.1.2 Single Element Directivity

The source strengths determined for the cubic elements two dipole sources shown in Figure 6-1 have dissimilar spectral shapes. The spectra at 3kHz are separated by almost an order of magnitude. At 11kHz, the spectral values are nearly equal. This indicates that the directivity pattern of the noise from this single element varies with frequency. Figure 6-4 shows the implied radial directivity of noise in the plane of the wall at a distance of 0.65m produced by a single cubic element at U_o=60m/s for two frequencies, 3872Hz and 10368Hz. The given decibel levels are not absolute, but are shown on similar scales to show the relative difference in directivity. The streamwise axis is along the 0° and 180° directions and the spanwise axis is along 90° and 270°. At 3872Hz, the streamwise dipole is much stronger than the spanwise so that the radiation pattern is 7dB stronger in than streamwise direction. At 10368Hz, the dipoles are approximately equal and the directivity pattern is nearly constant in all directions varying by only 1dB.

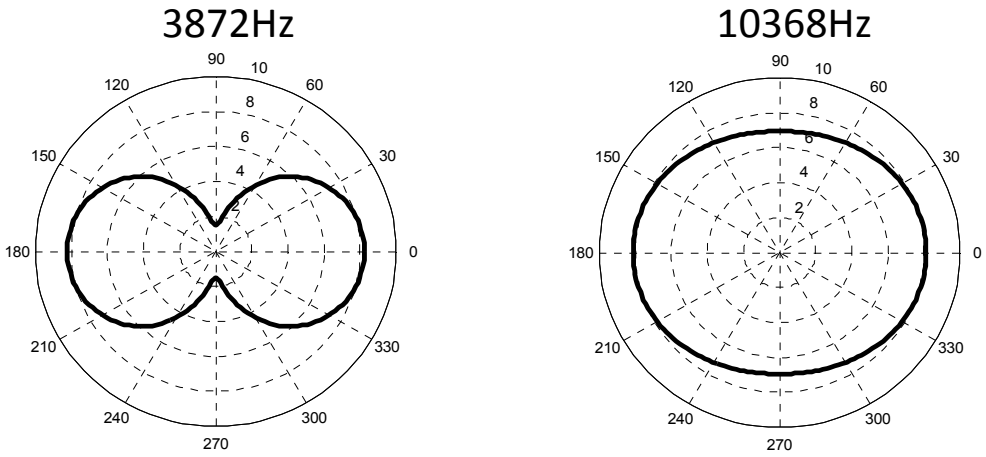

a) b)

Figure 6-4. Directivity of noise radiation from single cubic element at a) 3872Hz b) and 10368Hz on a decibel scale

6.1.3 Effect of Flow Speed on the Dipole Strength of a Single Cubic Element

The source strength spectra from the single cube were determined at multiple nozzle exit velocities and are shown in Figure 6-5. No estimation could be made for the 20m/s nozzle exit velocity because the signal-to-noise ratio was too low. At all velocities, the determined spanwise strength was less than the streamwise dipole strength. The strengths at each frequency increased by approximately three orders of magnitude with a doubling of the local velocity from 11-22m/s which corresponds to the nozzle exit velocity increase of 30-60m/s. Like the 60m/s case, the other nozzle exit velocities also produce spanwise and streamwise dipole spectra that vary in relation to each other.

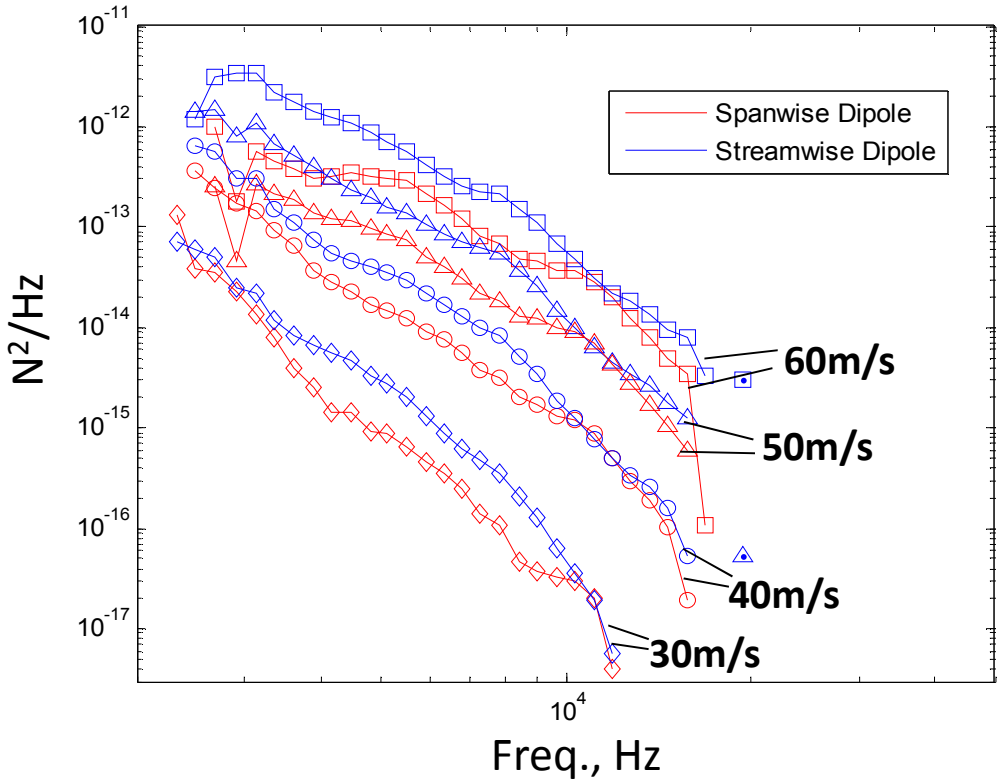

Figure 6-5. Streamwise and spanwise dipole strengths of single cubic element at various nozzle exit velocities

The estimated source strengths and frequencies can be normalized using the velocity of the unperturbed boundary layer evaluated at a height equivalent to the top of the roughness element, which is approximately 80% of the local edge velocity, and the roughness height. With this normalization, the three orders of magnitude spread shown in Figure 6-5 is reduced to a single order of magnitude as shown in Figure 6-6. Ignoring the U_o=30m/s spectra, the collapse of the three remaining curves reduces further within about 5dB over the majority of the non-dimensional frequency range.

The relative change in the strength of the spanwise and streamwise dipoles with velocity is analyzed by integrating the results of Figure 6-6 over the normalized frequency range $0.625 < fh/U < 2.5$. The ratio of this integration is shown in Figure 6-7 displaying an increase in the relative strength of the streamwise to spanwise dipole as the velocity is increased. The strength of the streamwise dipole grows more rapidly nearly doubling in relation to the spanwise dipole over this non-dimensional frequency range. The slope of this change can be approximated as linear with a slope of 0.12 per local velocity. The shape of this curve may be leveling off at higher velocities not following a continually linear slope, but more data is needed at different local velocities to make any further conclusion.

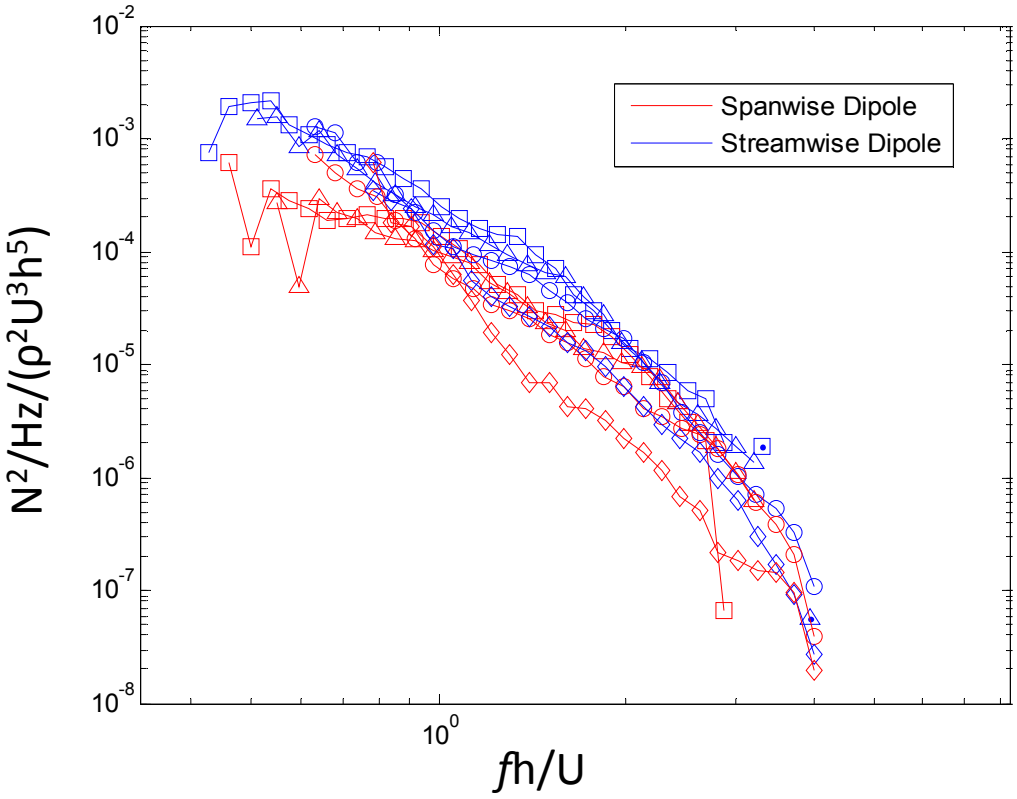

Figure 6-6. Normalized source strengths for the single cubic element at multiple nozzle exit velocities: 60m/s (square), 50m/s (triangle), 40m/s (circle), 30m/s (diamond)

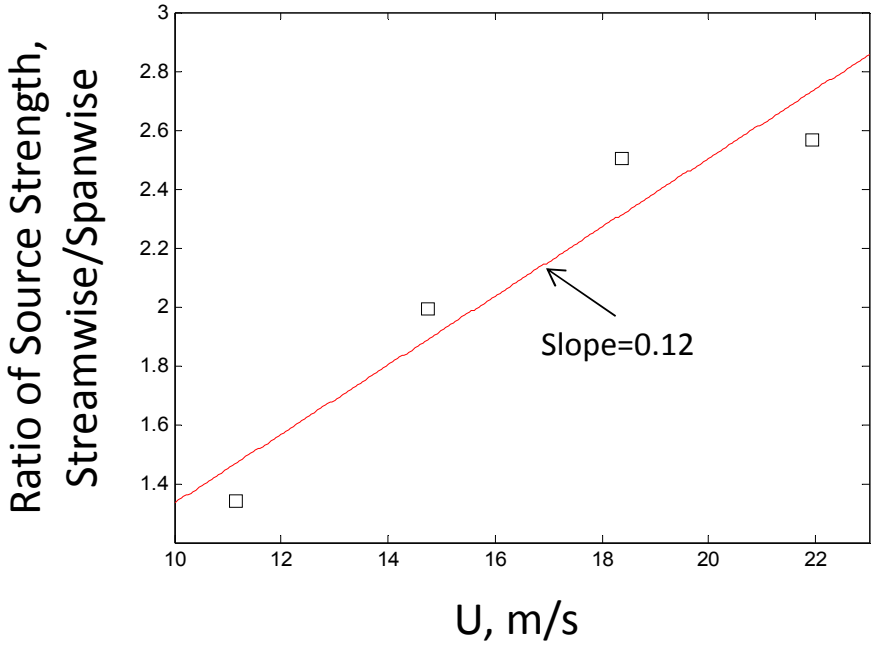

Figure 6-7. Integrated source strength ratio of dipoles produced by single cube at various maximum local velocities

6.1.4 Comparison with Rasnick (2010)

The least-squares method converges to produce source strength spectra even at frequencies where the roughness noise is indistinguishable in the measured autospectra. Rasnick (2010) estimated the source strength of an individual 3mm cubic element in an upstream position but was unable to estimate the source strength of a single hemisphere because he used only a single microphone to record the far field noise. The noise from the single hemisphere could not be separated from the background levels. A microphone array records information that exists in the cross-spectral data as well as the autospectra. These data were not available for Rasnick's calculation. To validate the use of the least-squares method, Rasnick's (2010) results for a single cubic element can be compared to the source strength spectra calculated from the least-squares method. Figure 6-8 shows this comparison for U_o=60m/s. Rasnick's data was corrected to account for the normalization using the velocity at the roughness height which was 80% of the edge velocity, and the half-space Green's function. The source strength for a single source was defined in Rasnick (2010) as given in Equation 6-7.

$$C_D^2 W_{ff} = \frac{(4\pi c_o)^2 \Phi(\boldsymbol{x},\omega)|\boldsymbol{x}|^2}{\left(\frac{1}{2}\rho U^2 A\right)^2 \omega_\tau \left(\frac{\omega}{\omega_\tau}\right)^2 \cos^2(\theta)} \qquad \text{Eq. 6-7}$$

where c_o is the speed of sound, $\Phi(\boldsymbol{x},\omega)$ is the recorded far field noise at vector position $\boldsymbol{x}$ from the roughness element, A is the projected frontal area, $\omega_\tau = \frac{U}{h}$, and θ is the receiving angle of the sensor to the roughness element. $C_D^2 W_{ff}$ represents the non-dimensional source strength and is the steady drag coefficient, C_D, multiplied by the source spectral shape function W_{ff}. The source strength definition used in this study is given in Equation 6-8.

$$Q = \frac{4\pi^2 |\boldsymbol{x}|^2 \Phi(\boldsymbol{x},f)}{\left(\frac{\omega}{c_o}\right)^2 \cos^2(\theta)} \qquad \text{Eq. 6-8}$$

Converting Φ to per angular frequency and normalizing this definition on $\rho^2 U^3 h^5$, Equation 6-8 can be rewritten as:

$$\frac{Q}{\rho^2 U^3 h^5} = \frac{(4\pi c_o)^2 \Phi(\boldsymbol{x},\omega)|\boldsymbol{x}|^2}{\left(\frac{1}{2}\rho U^2 A\right)^2 \frac{h}{U} \omega^2 \cos^2(\theta)} \left(\frac{2\pi}{16}\right) \qquad \text{Eq. 6-9}$$

Therefore, the relationship between the normalized data presented here and the strength spectra presented in Rasnick (2010) is a factor of 2π/16.The spectral data for the streamwise dipole and Rasnick's data agree well as shown in Figure 6-8. Since Rasnick's data was measured in an upstream position, the measured source strength was that of the streamwise dipole. This independent agreement corroborates the least-squares estimated results and verifies the use of the calculation method. The advantage of the least-squares method is apparent in Figure 6-8. The least-squares estimated results extend to a much lower frequency than calculated by Rasnick (2010). Also, the strengths of multiple sources are solved for simultaneously. Rasnick's method can only determine the strength of one source and therefore the streamwise and spanwise sources are combined in his calculation. To separate sources using the method of Rasnick (2010), far field microphones need to be placed in positions that isolate individual sources in

the directivity field. Of course, this microphone placement method would only work for individual roughness elements so that there are voids in the directivity pattern of the streamwise and spanwise dipole radiation. For multi-element fetches there is not a far field position that would eliminate the contribution from either the streamwise or spanwise dipoles completely. Also, Rasnick's single microphone method would be unable to separate the different streamwise or spanwise dipole strengths from multiple roughness elements.

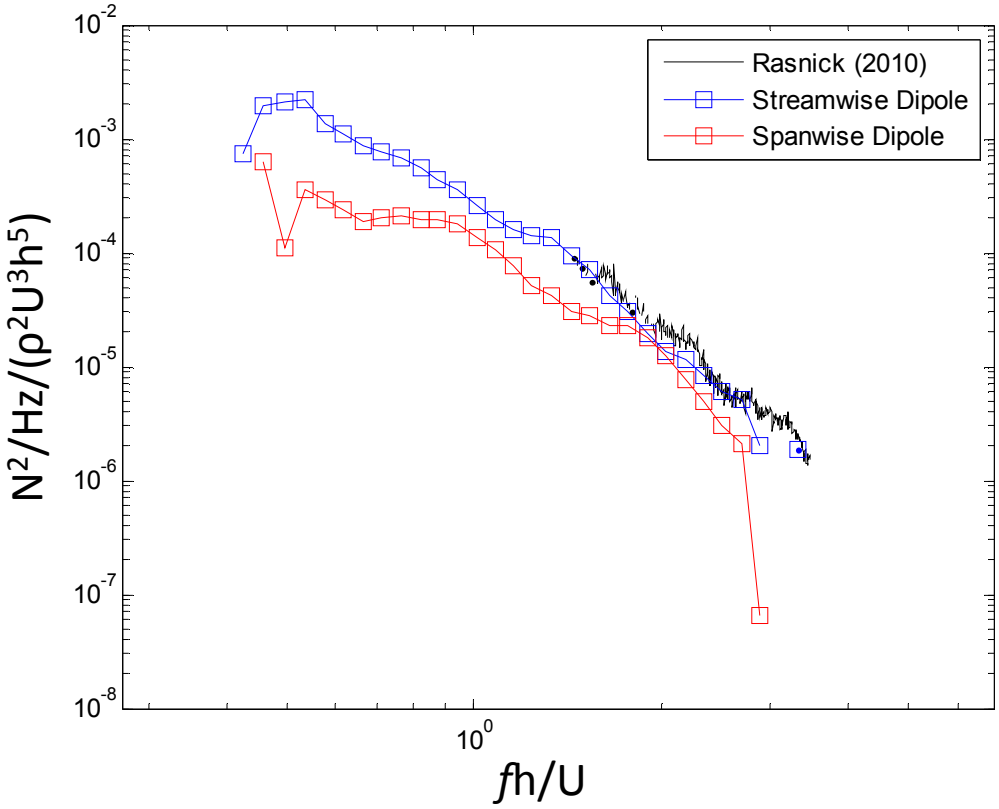

Figure 6-8. Single cubic element least-squares strength estimations compared to estimated strength from Rasnick (2010)

6.1.5 Comparison with LES

Yang & Wang (2011) completed a computational study of a wall flow involving fetches of cuboidal and hemispherical roughness arranged in a 4x10 pattern, 4 elements in the spanwise direction and 10 elements in the streamwise direction, in a conventional turbulent boundary layer. Their roughness height to boundary layer thickness ratio was 0.124 which is comparable to the ratio of 0.183 for the U_o=60m/s case presented in this study. Also, their momentum thickness Reynolds number was 3065 where as for the U_o=60m/s case the Re_θ=1021. Their roughness elements had a radius of 4.3mm and were spaced 25.4mm. The presented spectra in Yang & Wang (2011) are the average of the streamwise and spanwise source strengths across each spanwise row. The averaging was performed to reduce the uncertainty of the results. They found that the lead row of cuboidal roughness was the strongest producer of RMS sound in the streamwise direction and nearly the strongest in the spanwise direction following only the second row. For the hemispherical roughness, the RMS source strength of the lead row was the

weakest producer of noise in both the streamwise and spanwise direction. The least-squares estimated data only covers a small frequency range of the LES analysis near the highest calculated frequencies where LES analyses are typically most unreliable. Comparison between the results may corroborate both methods in this frequency range.

Figure 6-9 compares the per element streamwise and spanwise source strength results from the lead row of the cuboidal and hemispherical roughness compared to the least-squares estimated results for a single cuboidal and hemispherical element over the full presented LES range of data and a narrower range focusing on the region of comparison. Their calculated spectra in Yang & Wang (2011) was double sided and per angular frequency so their spectra have been adjusted by a factor of 4π. The velocity at the top of the roughness height was 70% of the edge velocity in their computation. Only the LES results from the lead row results are presented so that effects of upstream elements are not present in the comparison with the least-squares result for the single elements.

The least-squares estimated results are greater than the LES results at almost all non-dimensional frequencies. Disagreement between the LES estimated spectra and the least-squares calculated spectra grows with non-dimensional frequency up to approximately 15dB. At lower non-dimensional frequencies below $fh/U<1$, the estimated spectra agree much better within a factor of 5 or 8dB. The streamwise and spanwise dipoles calculated from the experimental cuboidal roughness split at a non-dimensional frequency of 0.8 for the U_o=50m/s and 60m/s cases. This split resembles the split in the LES results that occurs at a lower non-dimensional frequency of 0.5. These differences are large but may be attributed to differences in experimental conditions. The LES was conducted for a conventional turbulent boundary layer without the mixing layer present in the wall-jet. This mixing layer may be a significant influencing factor on the pressure fluctuations that are radiated to the far field. Also, the growing difference with frequency may be influenced by limits due to the resolution of the LES study. Although the absolute values differ, the difference in spectral magnitude between the hemispherical and cuboidal curves is the same for both the LES and experiment.

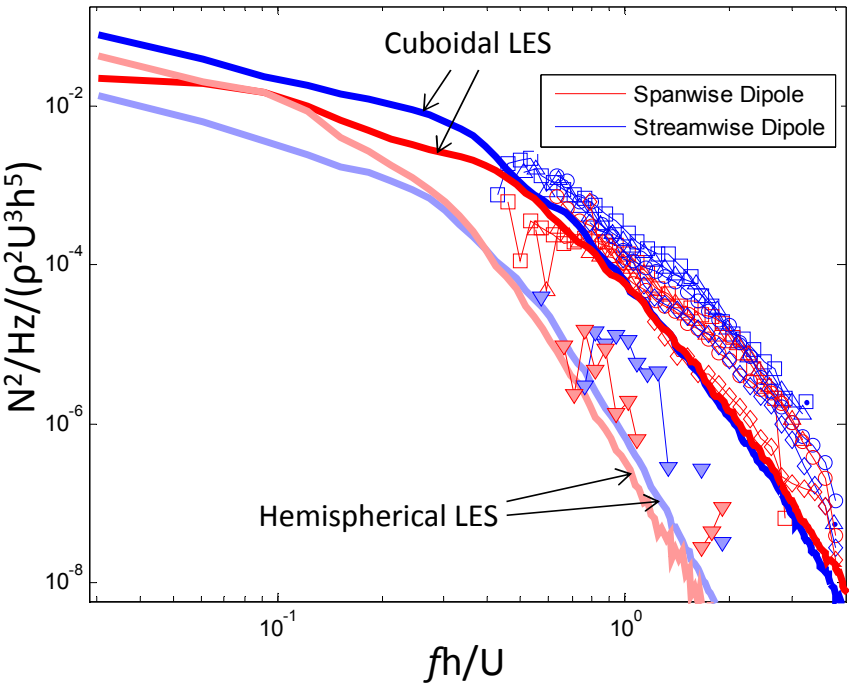

a)

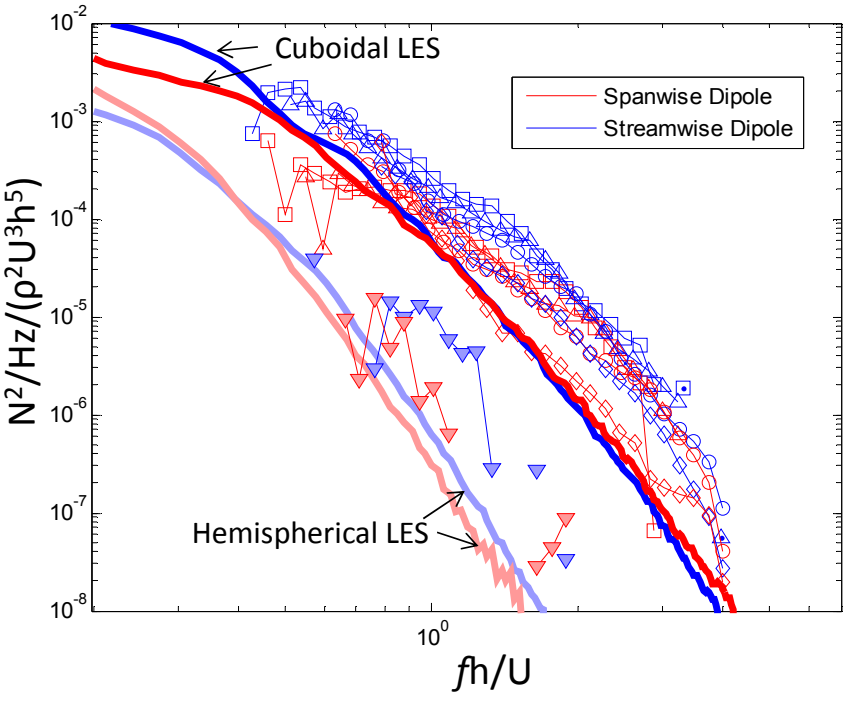

b)

Figure 6-9. Single element source strength results compared to Yang & Wang (2011) LES results

6.2 Multi-Element Cubic Fetches

6.2.1 Source Strengths of Individual Elements in Fetches

The least-squares method of source strength analysis was developed to decompose the source strength distribution further than was capable through examination of the beamformed source maps presented in Chapter 5. To show the effect of the addition of multiple elements on the least-squares analysis, the number of elements in the roughness fetch can be increased from an individual roughness element to a single spanwise row of six 3mm cubic elements. The least-squares results from this analysis are shown in Figure 6-10. The source maps in Chapter 5 show that the streamwise and spanwise dipoles at 10368Hz remain relatively constant across the span of the roughness fetch. This frequency corresponds to a non-dimensional frequency of 1.77. At this frequency in Figure 6-10, there is very little spread among the streamwise and spanwise dipole strengths agreeing with the source map results. However, at lower frequencies the results fan out more. Also, the least-squares method fails to calculate source strengths for all roughness elements at all frequencies. Source strengths of zero are assigned to some of the roughness elements occurring more often at lower frequencies. This is probably due to the acoustic wavelength growing with decreasing frequency creating a condition that makes the individual roughness elements indistinguishable from one another. This causes the source strength at one element to be identified as coming from another location. Therefore, to reduce uncertainty, the spanwise average of the source strengths in the single row of roughness elements was calculated to produce single spanwise and streamwise dipole strength spectra that represent the per-element average produced by each roughness element in a spanwise row.

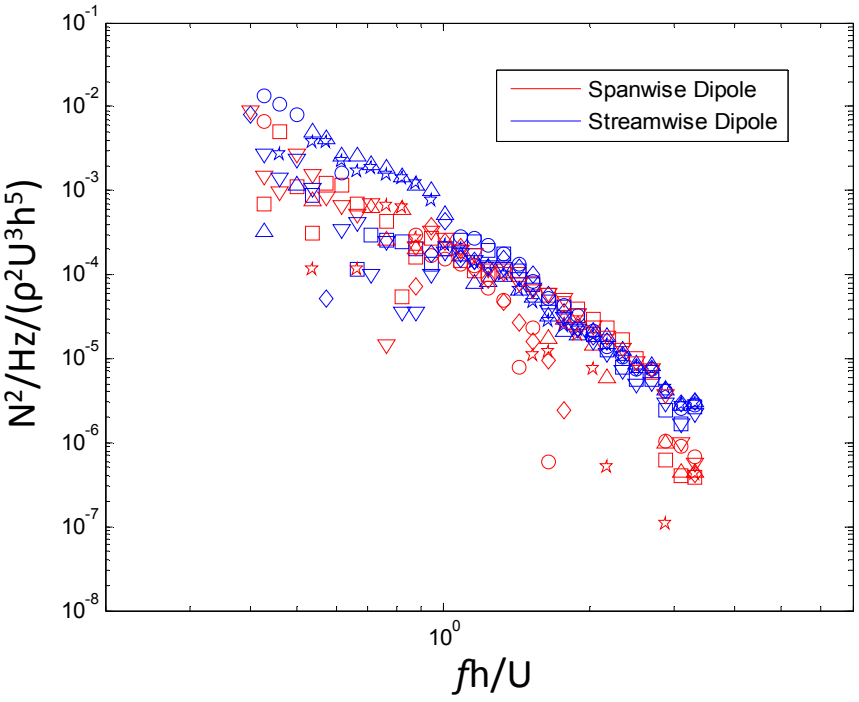

Figure 6-10. Spanwise and streamwise source strengths of individual elements in a 6x1 fetch at U_o=60m/s, elements located at (x, z) mm: square (1257, -0.0413); triangle (1257, -0.0248); circle (1257, -0.0083); diamond (1257, 0.0083); pentagram (1257, 0.0248); upside-down triangle (1257, 0.0413)

The per-element averaged streamwise and spanwise dipole strengths for the 6x1 cubic element fetch at U_o=60m/s are shown in Figure 6-11 compared to the results from a single cubic element. This average is calculated by summing the results including the values indicating zero strength and dividing by the number of spanwise elements, 6. The resulting spectra are much smoother than the curves produced by the strength spectra calculated for each roughness element. Like the results from the single cubic element, the streamwise dipole is stronger at all observed frequencies than the spanwise radiating dipole. The source maps in Chapter 5 indicated that the addition of spanwise adjacent elements may increase the spanwise dipole radiation per element, but these least-squares results confirm that the spanwise noise from the 6x1 fetch is approximately the same as that from the single element. The streamwise results from both the 6x1 and single element roughness are also approximately equal. This method of spanwise averaging the dipole source strengths will be used in the presentation of data from all of the multi-element fetches since it is reasonable to assume that there is little variation across the span of the roughness as shown in the beamformed source maps of Chapter 5.

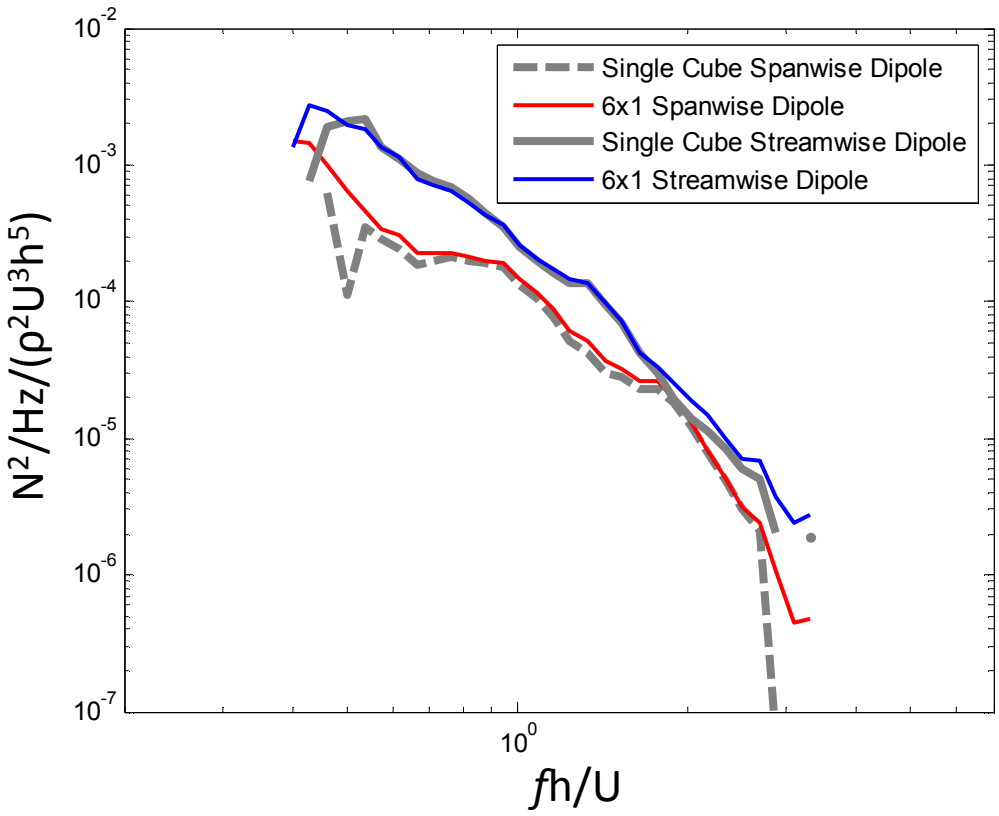

Figure 6-11. Spanwise averaged spanwise and streamwise dipole strengths of a 6x1 fetch of cubic roughness compared to single element source strengths at U_o=60m/s

6.2.2 Variation of the Lead Row's Source Strength with the Addition of Downstream Elements

The effect of adding spanwise adjacent elements was studied in Figure 6-11 by comparing the results of the single element's dipole strengths to the spanwise average strengths in a 6x1 configuration of roughness. The effect of adding trailing elements can also be examined by comparing the spanwise averaged source strengths of the initial spanwise row of cuboidal roughness for each of the roughness configurations from 6x1 to 6x7. Figure 6-12 and Figure 6-13 show the spanwise per-element averaged streamwise and spanwise dipole strengths, respectively, for the initial spanwise row of cuboidal roughness in each of the examined configurations. These results are for the condition U_o=60m/s.

Figure 6-12 shows that the calculated streamwise dipole strength of the lead row increases slightly with the addition of trailing elements. However, compared to the single cube results the single row of roughness (labeled 6x1) also shows a slight increase in the streamwise dipole above a non-dimensional frequency of 1.77. The addition of the spanwise elements from the single cube configuration causes the spectral levels to increase by a factor of 1.28. The small increase in strength spectra due to the trailing rows may be an artificial amplification caused by the large wavelength to source separation ratio so that source strengths of trailing rows or the background noise are included in the strength of individual elements. Even at 20kHz, the highest considered frequency, the acoustic wavelength is approximately 17mm while the roughness elements are only spaced 16.5mm. As the frequency is decreased, increasing the acoustic wavelength, the calculated strength of the lead row's streamwise dipole, shown in Figure 6-12, increases further with the addition of almost every trailing row. The result at high frequencies may be real, but below a non-dimensional frequency of 1.33, the frequency at which the data begins to separate by number of elements, the results may be artificial. It is unlikely that the addition of the 6^{th} or 7^{th} row of roughness influences the source strengths of the lead row. The uncertainty of this calculation over the presented frequency range will be analyzed further in Chapter 7.

The results for the average spanwise dipole strength of the lead row in Figure 6-13 show a similar behavior with frequency. The data begin to fan out at lower frequency in order of number of elements suggesting that the addition of the 7^{th} spanwise row of roughness affects the spanwise dipole strength of the lead row. Again, this is most likely an artificial effect due to the long acoustic wavelengths at these frequencies. At higher non-dimensional frequencies, there is very little difference between the estimated spanwise source strengths for the varying size fetches ranging from a single element to a full 42 element fetch. This indicates that the addition of multiple elements has no effect on the spanwise dipole strength of the lead row at these frequencies.

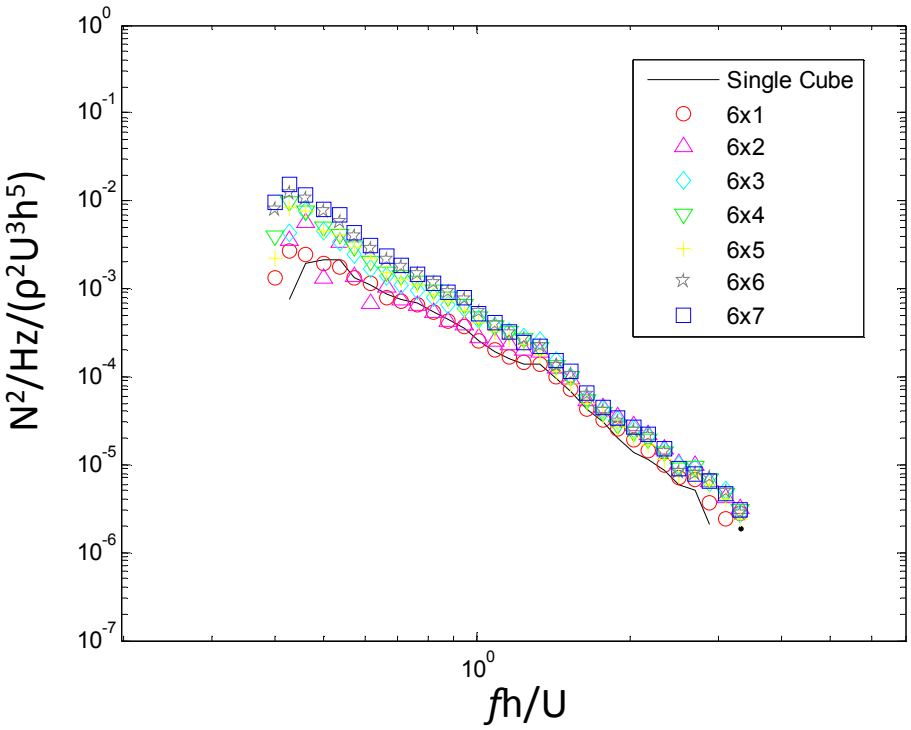

Figure 6-12. Streamwise dipole strength of the lead row for all of the examined cuboidal roughness fetches at U_o=60m/s

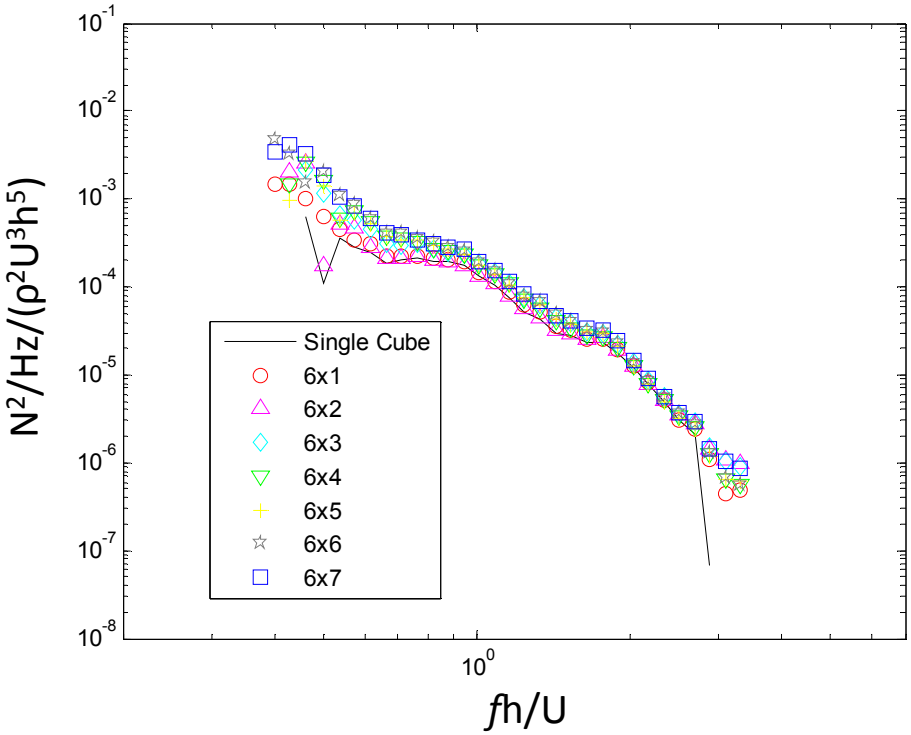

Figure 6-13. Spanwise dipole strength of the lead row for all of the examined cuboidal roughness fetches at U_o=60m/s

6.2.3 Streamwise Source Strength Distribution through a 42 Element Fetch of 3mm Cuboidal Roughness

The source strength variation through the 6x7 fetch of cuboidal roughness is shown in Figure 6-14 compared to the source strengths determined from the single cubic element presented in Figure 6-1 for a nozzle exit velocity of 60m/s. The results are spanwise averaged so that 14 total strength spectra are shown representing the streamwise and spanwise per-element averaged dipole strengths for each of the 7 spanwise rows. In general, the relative estimated strength of the streamwise dipole for each row is stronger than that of the corresponding spanwise source. The estimated streamwise strengths for the trailing rows in Figure 6-14 mostly fall below the curve created by the lead row so that the lead row is the strongest producer of noise in the spanwise and streamwise direction. As shown in Figure 6-12 and Figure 6-13, both the streamwise and spanwise dipole are slightly stronger for the lead row of the 42 element fetch as compared to the single cubic element with the difference increasing towards lower non-dimensional frequencies, but this is within the uncertainty of the estimation as will be shown in Chapter 7.

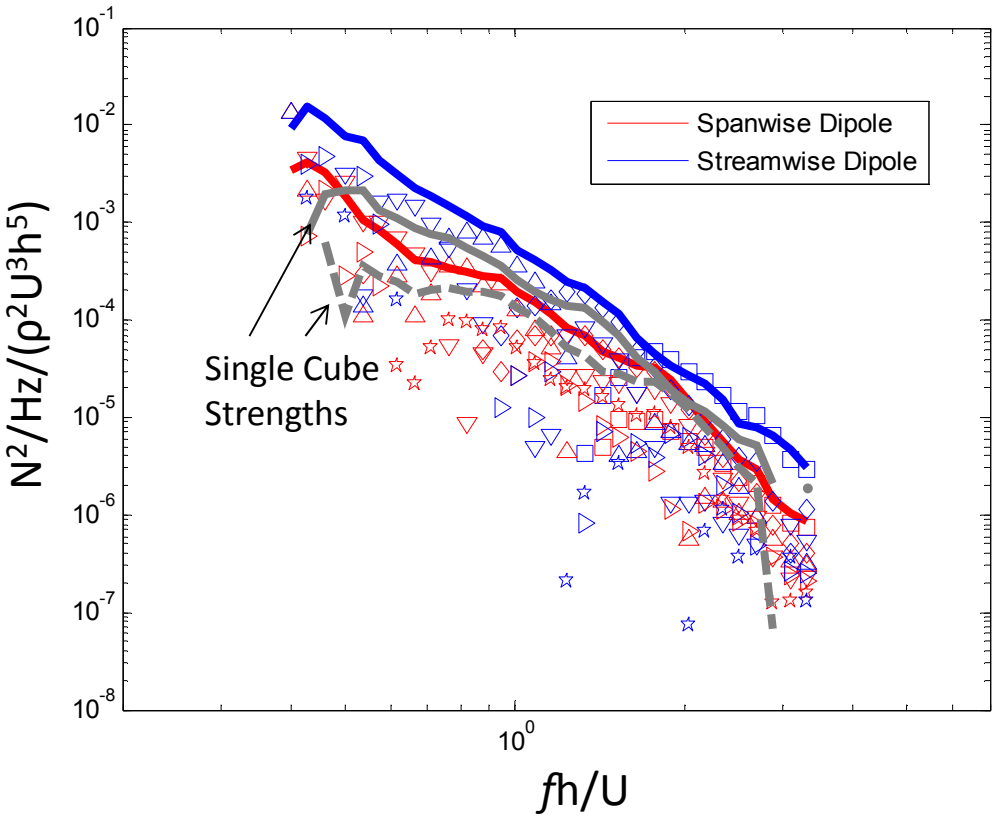

Figure 6-14. Source distribution through 42 element cubic roughness fetch at U_o=60m/s: solid lines (1st Row), square (2nd Row), diamond (3rd Row), triangle (4th Row), upside-down triangle (5th Row), right-pointing triangle (6th Row), pentagon (7th Row) compared to single cubic element strengths in grey (solid) streamwise dipole (dashed) spanwise dipole

6.2.4 Comparison with LES

Direct comparison of the estimated strengths in Figure 6-14 can be made with the LES study of Yang & Wang (2011). This comparison is shown in Figure 6-15. The LES results are the same as presented in comparison with the estimated single cubic element source strengths in Figure 6-9. The LES data are the per-element averaged streamwise and spanwise dipole strengths for the lead row of cuboidal roughness arranged in a 4x10 grid pattern. The least-squares estimated streamwise dipole strength is larger than that determined from LES at all non-dimensional frequencies. Estimation of the spanwise dipole is actually closer to the LES results, but the slopes of the estimated spectra differ slightly so that comparison of the streamwise and spanwise dipoles agree better at lower non-dimensional frequencies. The spanwise results agree within a factor of two over the entire non-dimensional frequency range. The disagreement between the streamwise dipole results increases from a factor of 2 to 17 with increasing non-dimensional frequency.

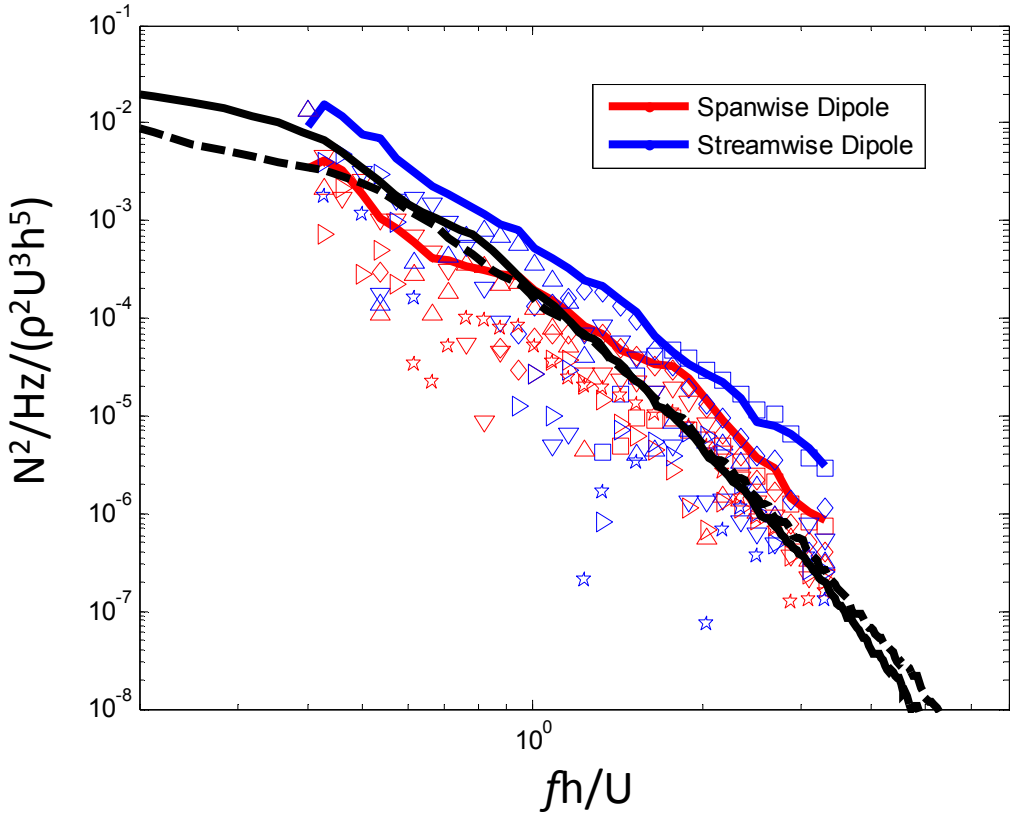

Figure 6-15. 42 cubic element roughness fetch streamwise and spanwise dipole strengths at U_o=60m/s compared to lead row results from LES of Yang & Wang (2011): symbols same as Figure 6-14

6.2.5 Confirmation of Streamwise and Spanwise Dipole

This least-squares analysis is dependent upon the assumed presence of a streamwise and spanwise dipole located at each roughness element location. To test this presumption, the analysis for the 42 element cubic fetch at U_o=60m/s was completed assuming only a streamwise dipole, only a spanwise dipole, and a complete representation including both. A diagram of the three source radiation models is shown in Figure 6-16 as applied to single cubic roughness elements. For the two models that assumed only a streamwise or spanwise radiating dipole, the least-squares method was used to calculate only 42 total sources over the roughness fetch, one for each roughness element. The full representation included the simultaneous computation of 84 independent sources.

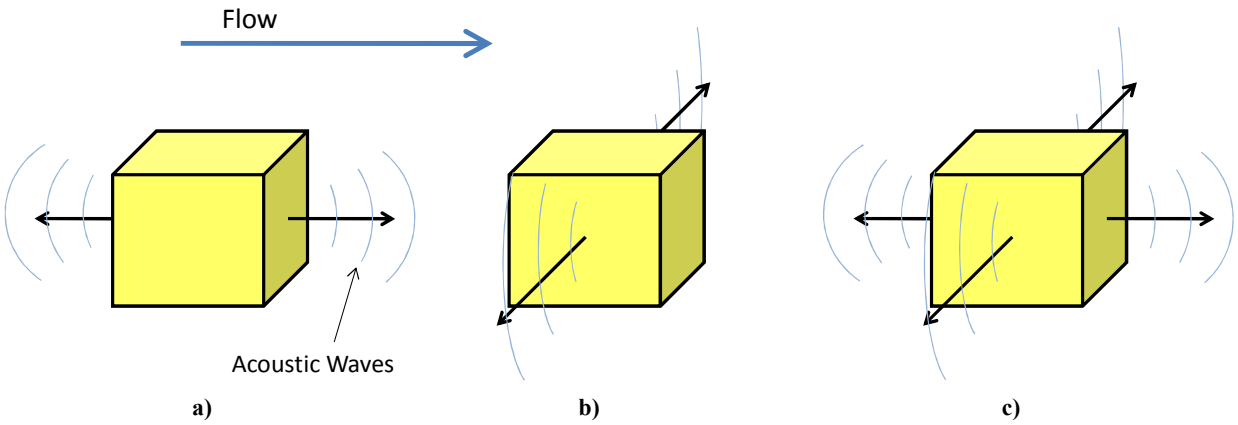

Figure 6-16. Diagram of assumed roughness noise models a) streamwise-only dipole b) spanwise-only dipole c) and the full representation including both dipole sources

The least-squares analysis was conducted three times using the three different source models. The results were compared to the corresponding single point far field measurement in Figure 4-8 for U_o=60m/s. To calculate the estimated single point far field noise using the least-squares determined source strengths and models the far field noise was attained using a similar transformation matrix of Greens functions originally used to determine the source strengths as defined in Equations 2-9, 2-10, and 2-11. The estimated source strengths are combined into vector form and are multiplied by a vector of Greens function transformations that apply the assumed radiation pattern to transfer the dipole strengths to the far field noise produced at the considered far field location. This process is shown in Equation 6-10.

$$G_j = \frac{ikcos\theta_j e^{ikr_j}\left(1+\frac{i}{kr_j}\right)}{2\pi r_j} \qquad cos\theta_j = \hat{\mathbf{x}}\cdot\left(\mathbf{x}-\mathbf{y}_j\right)/r_j$$

$$\overline{PP^*} = \overline{q_1^2}G_1G_1^* + \overline{q_2^2}G_2G_2^* + \cdots \overline{q_j^2}G_jG_j^* \qquad \text{Eq. 6-10}$$

$$\overline{PP^*} = \vec{\boldsymbol{G}}_{GG}\vec{\boldsymbol{Q}}$$

where θ_j is the receiving angle from the far field location to the axis of source j's dipole, r_j is the distance from observer position to the source, $\mathbf{x}$ is the position vector of the observer, $\mathbf{y}_j$ is the position vector of

the source, $\overline{PP^*}$ is the measured autospectrum, q_j is the strength of source j, $\vec{\boldsymbol{G}}_{GG}$ is a vector of Greens function transformations with dimensions of one by number of sources, and $\vec{\boldsymbol{Q}}$ is a vector of source strengths with dimensions of number of sources by one.

The comparison of the results using the three dipole radiation models is shown in Figure 6-17. Using only a spanwise dipole, the analysis produced estimated far field results that were far below the measured single point values since the compared position was in the streamwise direction. The individual calculated sources using the spanwise-only dipole model radiate very inefficiently in the streamwise direction producing low level far field results at the single point measured far field position which was at x=1029mm, y=469mm and z=0mm. Therefore, these results are not displayed in Figure 6-17. When assuming only a streamwise dipole, the measured far field was overpredicted. This is due to the streamwise dipole having to compensate for the large volume of sound measured in the spanwise direction by the microphone array. The least-squares calculation for this case does not have an assumed spanwise dipole source. So the only way for the calculation to resolve the large spanwise radiated noise is to increase the strength of the roughness noise model's streamwise dipoles. The complete representation produced the best results agreeing with the measured single point far field roughness noise spectrum within 1dB. This corroborates the assumption of both spanwise and streamwise aligned dipoles that emanate from each roughness element to produce the radiated far field noise.

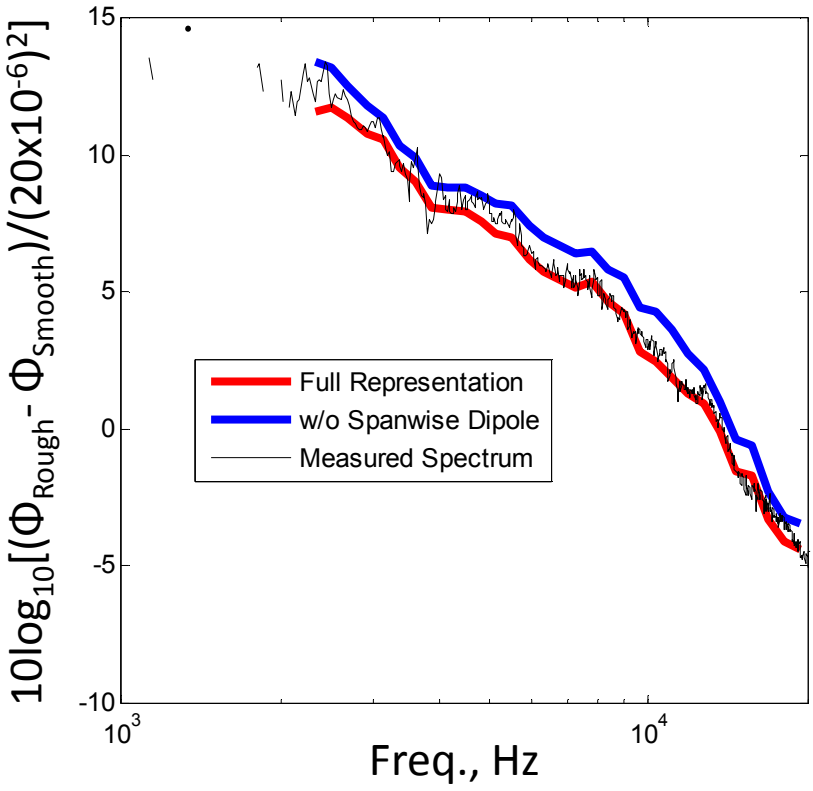

Figure 6-17. Comparison of the far field noise determined by extrapolation of the least-squares estimated results assuming both streamwise and spanwise dipole sources and only a streamwise dipole source with the measured single-point far field spectrum

6.3 Multi-Element Hemispherical Fetches

Multi-element fetches of hemispherical roughness were also analyzed using the least-squares method. Figure 6-18 displays the spanwise-averaged source strength results for the 42 element fetch of 3mm hemispheres at U_o=60m/s. The single hemispherical element results from Figure 6-1 are shown for comparison. The strengths calculated from the multi-element fetch are similar to the strengths calculated from the single roughness element. Again, the estimates show that the lead row of roughness is the largest producer of sound in the streamwise and spanwise directions, but the low signal-to-noise ratio produced by the hemispherical roughness increases the uncertainty of this measurement. Therefore, no definitive conclusion can be made about the relative strengths of the trailing rows. Also, like the results from the cuboidal roughness, the calculated streamwise dipole strengths for the hemispherical roughness are stronger than the corresponding spanwise dipole strengths for each spanwise row.

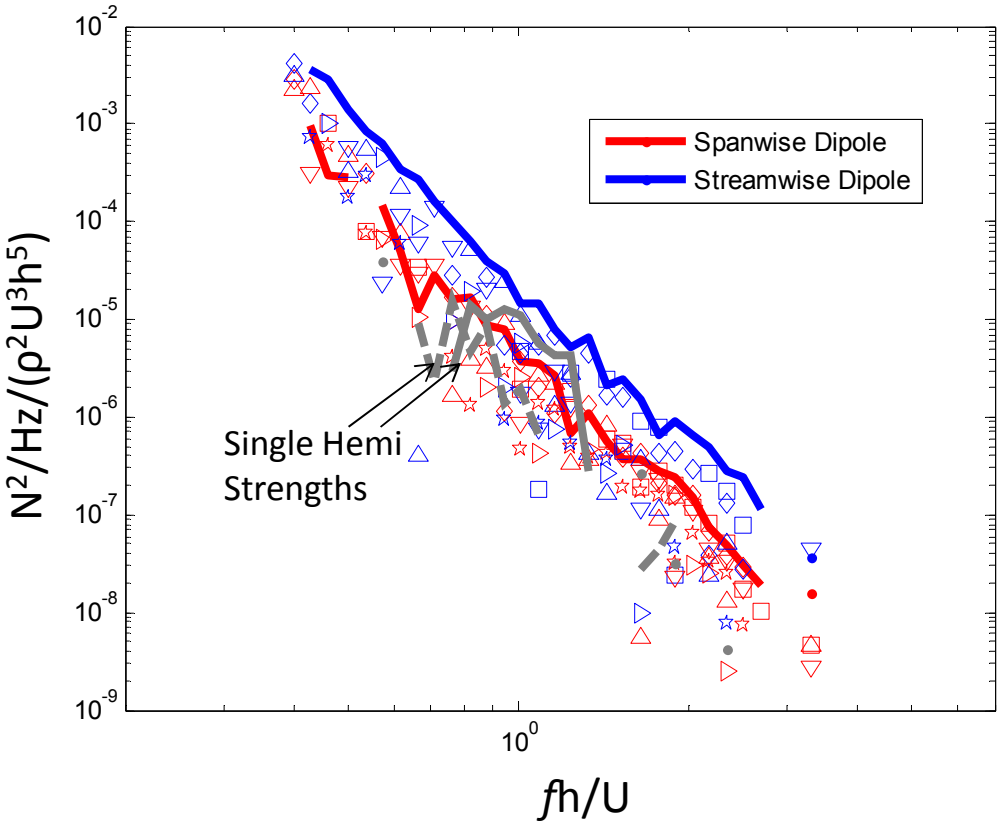

Figure 6-18. Source strengths determined by the least-squares method for a 42 element fetch of hemispherical roughness at U_o=60m/s (symbols same as Figure 6-14) compared to the results for a single hemispherical element (streamwise dipole: grey-solid, spanwise dipole: grey-dashed)

These data for the 42 element fetch of hemispheres are compared to the source strength data calculated from the LES of Yang & Wang (2011) for a 40 element fetch of hemispheres. This comparison is shown in Figure 6-19. The data differ by up to 30dB disagreeing more than the comparison of the cuboidal roughness studies shown in Figure 6-15. Like the cuboidal roughness comparison, the source strength estimations of the hemispherical roughness agree better at lower non-dimensional frequencies.

The least-squares estimated spectra have a shallower slope than the LES spectra so that the difference grows with non-dimensional frequency. The presented data is clearly in the upper frequency limits of reliability for the LES analysis. The LES estimated strengths show significant noise in the estimations at the highest presented frequencies indicating that these results may be limited by the resolution of the computational study. This may explain the difference in spectral slope over the calculated frequency range.

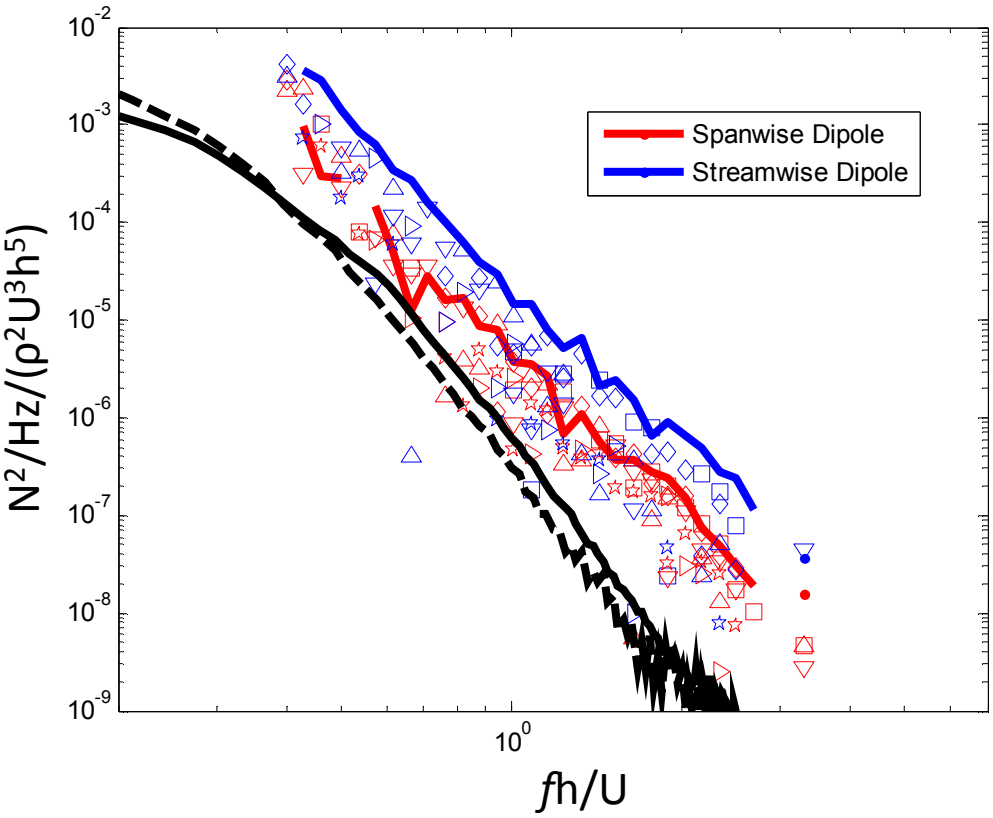

Figure 6-19. Comparison of source strengths from a hemispherical roughness fetch determined by the least-squares method (symbols same as Figure 6-14) and Yang & Wang's (2011) computational study (streamwise dipole:black-solid, spanwise dipole:black-dashed)

Chapter 7 Uncertainty of Least-Squares Analysis

The least-squares method provides estimates of the streamwise and spanwise dipole source strengths for single and multi-element roughness fetches, but the signal-to-noise ratio and number of sources in the analyses appear to have an effect on the quality of the solutions. The following section analyzes the uncertainty of the least-squares source strength estimations and the sensitivity of the solution to uncertainty in the microphone array sensors, the signal-to-noise ratio, the error in source location, and the number of sources.

7.1 Jitter Analysis

A jitter analysis was conducted for several of the least-squares source strength estimations to determine the sensitivity of the calculation to the uncertainty of the measured cross-spectra of the linear microphone array sensors. The uncertainty of the cross-spectral matrix was determined by repeat measurements during the experiment and is due to uncertainty inherent in the instrumentation. These uncertainties were found to be 1dB amplitude of the cross-spectral matrix and a 10° phase variation, at 10368Hz. Therefore, each cross-spectral matrix pair in the least-squares analysis was jittered by these amounts separately and the results summed to determine the total uncertainty as shown in Equation 7-1.

$$\delta\left(\overline{q^2}(f)\right) = \sqrt{\frac{\partial\overline{q^2}(f)}{\partial A_{i,j}}\delta\left(A_{i,j}\right) + \frac{\partial\overline{q^2}(f)}{\partial P_{i,j}(f)}\delta\left(P_{i,j}(f)\right) + \cdots} \qquad \text{Eq. 7-1}$$

where $\delta\left(\overline{q^2}(f)\right)$ is the uncertainty in the determined mean squared source strength at a given frequency, $\frac{\partial\overline{q^2}(f)}{\partial A_{i,j}}$ is the sensitivity of the calculated source strength to the amplitude of the index (i, j) and its conjugate pair (j, i), $\delta\left(A_{i,j}\right)$, of the measured cross-spectral matrix. $\frac{\partial\overline{q^2}(f)}{\partial P_{i,j}(f)}$ is the sensitivity of the calculated source strength to the phase uncertainty at a given frequency of the index (i, j) and its conjugate pair (j, i), $\delta\left(P_{i,j}(f)\right)$, in the measured cross-spectral matrix.

The results of the jitter analyses for the source strength spectra of the single roughness elements shown in Figure 6-1 are given in Figure 7-1. The results for the single cubic element are only mildly affected by the uncertainty of the measured cross-spectral matrix. The uncertainty bounds are wider on the high and low frequency extremes of the estimation. The estimated values for the single hemispherical element are much more sensitive. The results for the two dipole sources have uncertainties that are as much as a factor of 2 different from the estimated value. This shows that the sensitivity of the analysis is dependent upon the signal-to-noise ratio of the measurement itself.

A similar jitter analysis was conducted for the results of the streamwise and spanwise dipole strengths of the lead row of the 42 element fetch of cuboidal roughness. The results for the spanwise-averaged dipole strengths are shown in Figure 7-2. The addition of more roughness elements increases the sensitivity of the least-squares analysis results to the uncertainty of the cross-spectral matrix. The uncertainty is greatest over the middle of the calculated frequency range and extends up to a factor of 2 for the streamwise dipole and a factor of 1.5 for the spanwise dipole. Overall, the uncertainty determined

by the jitter analysis seems reasonable over the entire calculated frequency range for all of the studied surfaces, but this analysis does not calculate or give any indication as to the accuracy of the estimated source strengths. It only portrays the sensitive of the analysis to the uncertainty of the sensors used. The jitter analysis itself is dependent on the number of assumed sources and the signal-to-noise ratio of the measurement. Therefore, an analysis of these effects on the accuracy of the estimation is also studied.

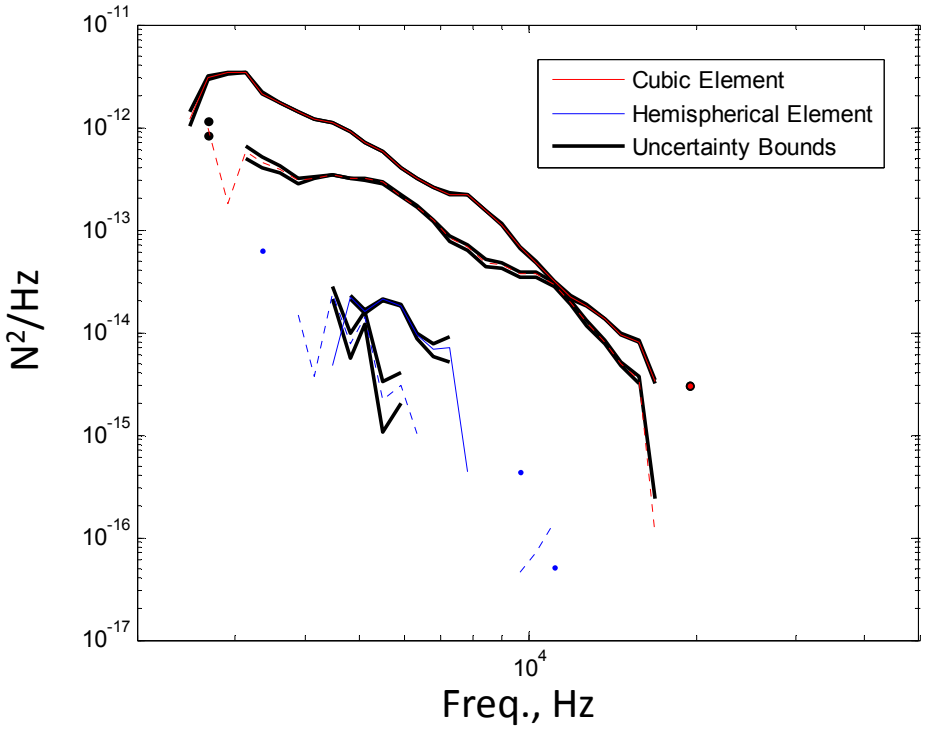

Figure 7-1. Single element jitter analysis for the cuboidal and hemispherical roughness (streamwise dipoles: solid, spanwise dipoles: dashed)

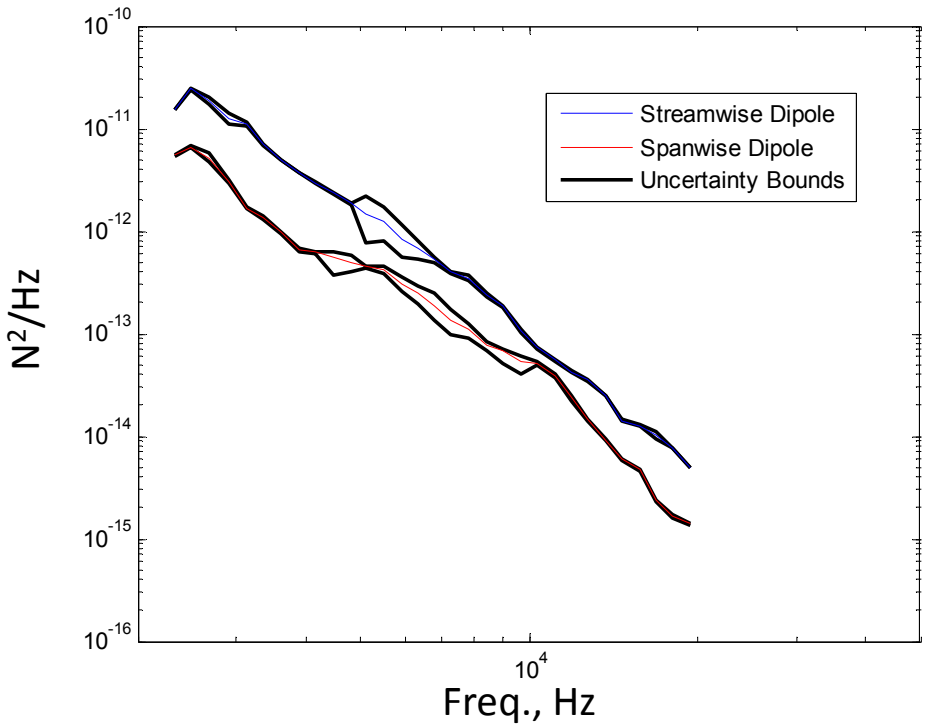

Figure 7-2. Jitter analysis for the 42 element cubic fetch's lead row spanwise-averaged dipole strengths

7.2 Uncertainty Due to Noise in Measurement

To calculate the uncertainty of the estimated source strength values due to noise in the measurement, a simulated measurement was conducted of a pair of dipoles with origins at x=1257mm, z=0 having constant source strengths of 2.244×10^{-5} N^2/Hz, 1dB with reference 4×10^{-10}Pa^2, aligned in the streamwise and spanwise directions. The cross-spectral matrices were calculated for this pair of sources over the entire least-squares estimated frequency range as would be recorded using the linear microphone array at the four positions used in this study. Varying levels of noise were added to the cross-spectral matrix of the signal. The cross-spectral matrix of the noise varied by 3dB and from 0 to 2π in phase. The level of the signal-to-noise ratio for each sensor was different due to the dipole source directivity, varying sensor to source distances, and 3dB variation of the noise, but average signal-to-noise ratios were computed for each array position and are used to denote each noise level. Five different noise levels were examined which were a constant strength below the measured signal at each array location over all frequencies. An illustration of the studied signal-to-noise ratios is shown in Figure 7-3. The far field autospectrum of the signal, and therefore noise level spectra, have a slope of ω^2 because of the dipole efficiency factor, $k_o^2 = (\omega/c_\infty)^2$.

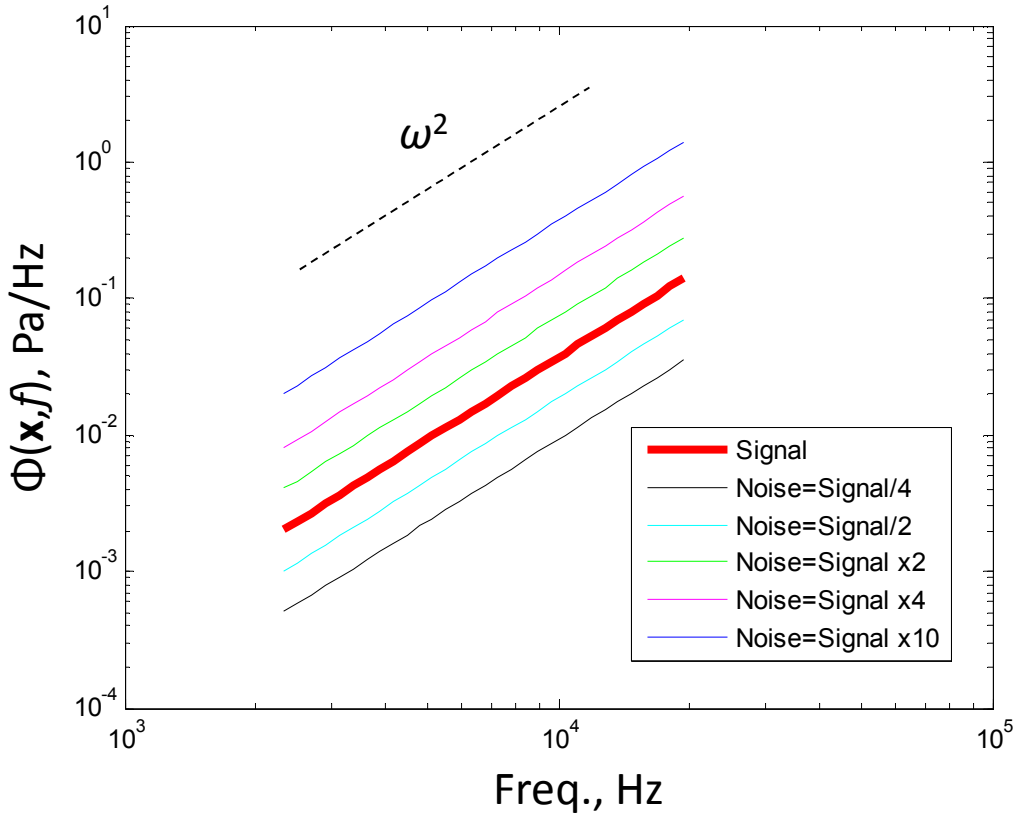

Figure 7-3. Example signal-to-noise ratio at far field position

The least-squares analysis was conducted for this pair of dipoles with the varying levels of noise added to the spectra. These results are shown in Figure 7-4. For the case with the largest signal-to-noise ratio, the exact source strength is very accurately computed at all frequencies. As the signal-to-noise ratio is diminished from a factor of 4 to 1/10, the computed source strengths become progressively more inaccurate. With a 1/10 signal-to-noise ratio, the error is as great as a factor of 2 which is still a reasonable estimation method for these very low signal-to-noise ratio sources.

The measured noise from the single cubic roughness element had a signal-to-noise ratio at U_o=60m/s as high as a factor of 0.6 as measured from microphone array Position 2. This indicates that the estimations of the source strengths at this condition are only slightly influenced by the background noise. The signal-to-noise ratio of the far field noise recorded by the single hemispherical element is extremely small. If the relative difference of noise recorded from the 42 element fetches is an indication of the single element differences, the SNR of the single cube is 63 times stronger than that of the single hemisphere.

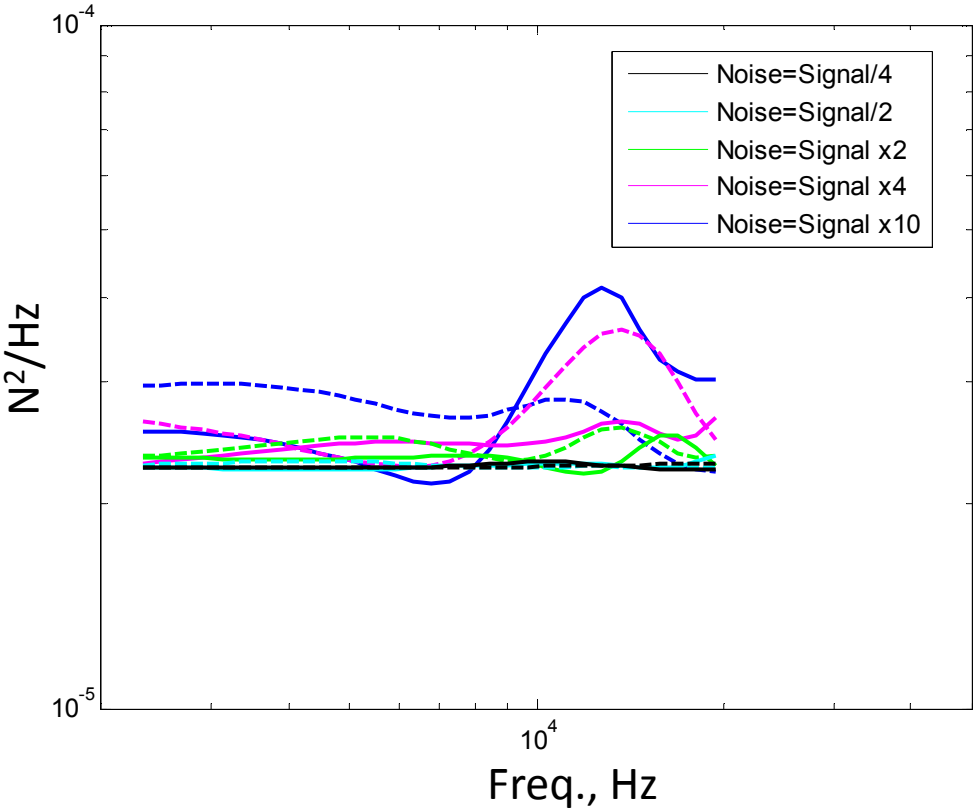

Figure 7-4. Single element source strength analysis with varying background noise levels: streamwise dipoles (solid) spanwise dipoles (dashed)

7.3 Sensitivity to Error in Source Position

The source locations for the experimental analysis of the measured roughness noise were assumed to be located at the central position of each of the roughness elements. The physical source locations were adjusted in the analysis to correct for an acoustic wave convection effect due to the local flow velocity. This resolved the difference between the observed and physical source location. The source maps in Chapter 5 indicate that this correction method works well to visually identify the source locations. The same corrections were applied in the least-squares analysis, and the sensitivity of these numerical solutions is an important aspect of this method to consider.

A simulation of a single dipole pair with a signal-to-noise ratio of ¼ was used to analyze the effect of source location error on the determined source strengths. This is the same case examined in Figure 7-4. Figure 7-5 shows the least-squares analysis of the streamwise and spanwise dipole strengths with independent 6mm source location errors in the *x* and *z* directions compared to the nominal solution and the exact solution without any noise in the measurement. Interestingly, the solution is minimally affected with source location errors equal to twice the roughness height over this frequency range. Error in the *z*-location has very little effect on the computed spanwise dipole strength. Error in the *x*-direction has an impact on both the estimated streamwise and spanwise dipole strengths. In both cases, the error remains within the maximum error produced by the analysis of the ¼ signal-to-noise ratio using the exact

known source location. The deviation from this nominal case grows with frequency showing that the error due to source location increases with the ratio of the location error to the acoustic wavelength.

Combining the results of the jitter analysis, signal-to-noise ratio analysis, and the source location error, the total estimated uncertainty of the single cubic element source strength estimations appears to be within 1dB, a factor of 1.5, at the highest calculated frequencies and within 3dB, a factor of 2, at the lowest frequencies. The source strengths determined from the single hemispherical element have a higher uncertainty. This limited frequency range of results should only be trusted within 5dB, or a factor of 3.

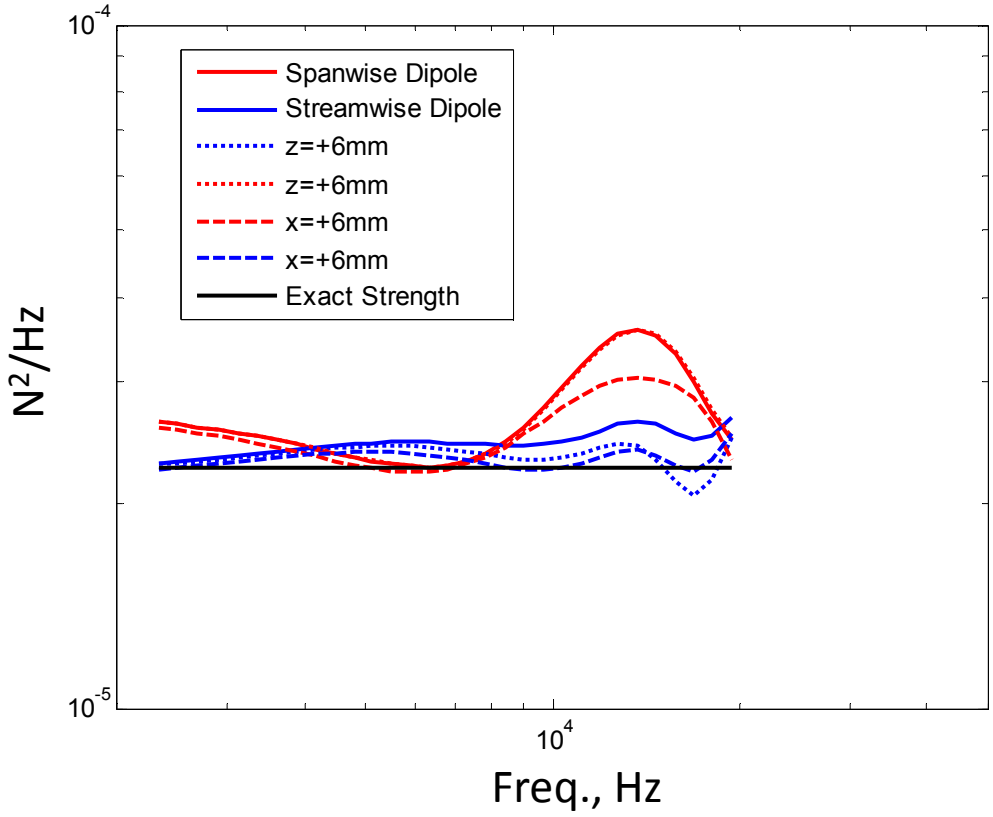

Figure 7-5. Single source least squares results with ¼ SNR with varying position error in the *x* and *z* directions

7.4 Effect of Multiple Source Locations

Using three of the signal-to-noise ratios illustrated in Figure 7-3, the addition of multiple source locations was studied. The first analysis involves two source locations with varying source spacings. At each source location the same roughness noise model was assumed having a spanwise and streamwise aligned dipole source with constant, equal source strengths of 2.244×10^{-5} N^2/Hz. Therefore, this analysis included four total sources. The location of one dipole source pair was held fixed at (0, 0) and the other was offset in the positive *z*-direction by 8.25mm, 16.5mm, and 24.75mm. The level of the signal-to-noise ratios listed in Figure 7-3 is approximately doubled by the addition of a second uncorrelated source. Figure 7-6 shows the result of the least-squares analysis for all four independent source strengths. To stay consistent with the labeling in Figure 7-3, the legend of this figure lists the signal-to-noise ratio as applicable to the signal from one source. The true average signal-to-noise ratio for the sensors at each

array position are approximately double these values. The level of noise was not increased because the increased signal-to-noise ratio is a more accurate representation of the experimental condition when the number of sources is increased as the background levels remain approximately constant.

As the source spacing increases from 8.25mm to 24.75mm, the error reduces as well. Also, the instances of zero value solutions assigned to source strengths diminishes with increased source spacing. An interesting observation from all three source spacings is that the value of the two streamwise dipoles are approximately inversely related as well as the values of the spanwise dipoles for the two source locations. Therefore, as the estimated value of one is underpredicted, the value of the other is overpredicted to compensate for the measured signal strength. As sources are assigned strengths of zero, the corresponding source from the other location is approximately double the exact source strength. This confirms the value of the spanwise-averaging method used to present the average dipole strengths in Chapter 6 from the multi-element fetches. Averaging does reduce the uncertainty of the solution by diminishing the effect of estimated source strength fluctuations by reassignment and distribution of the true strengths between roughness elements.

The grid-spacing of the studied roughness fetches was 16.5mm. At this spacing there is considerable error with decreasing signal-to-noise ratio for individually calculated source strengths, but the average values are very near the actual source strengths. To study this averaging effect to reduce uncertainty, a 6x7 arrangement of sources will be simulated recreating the measurement of the 42 element cuboidal and hemispherical fetches.

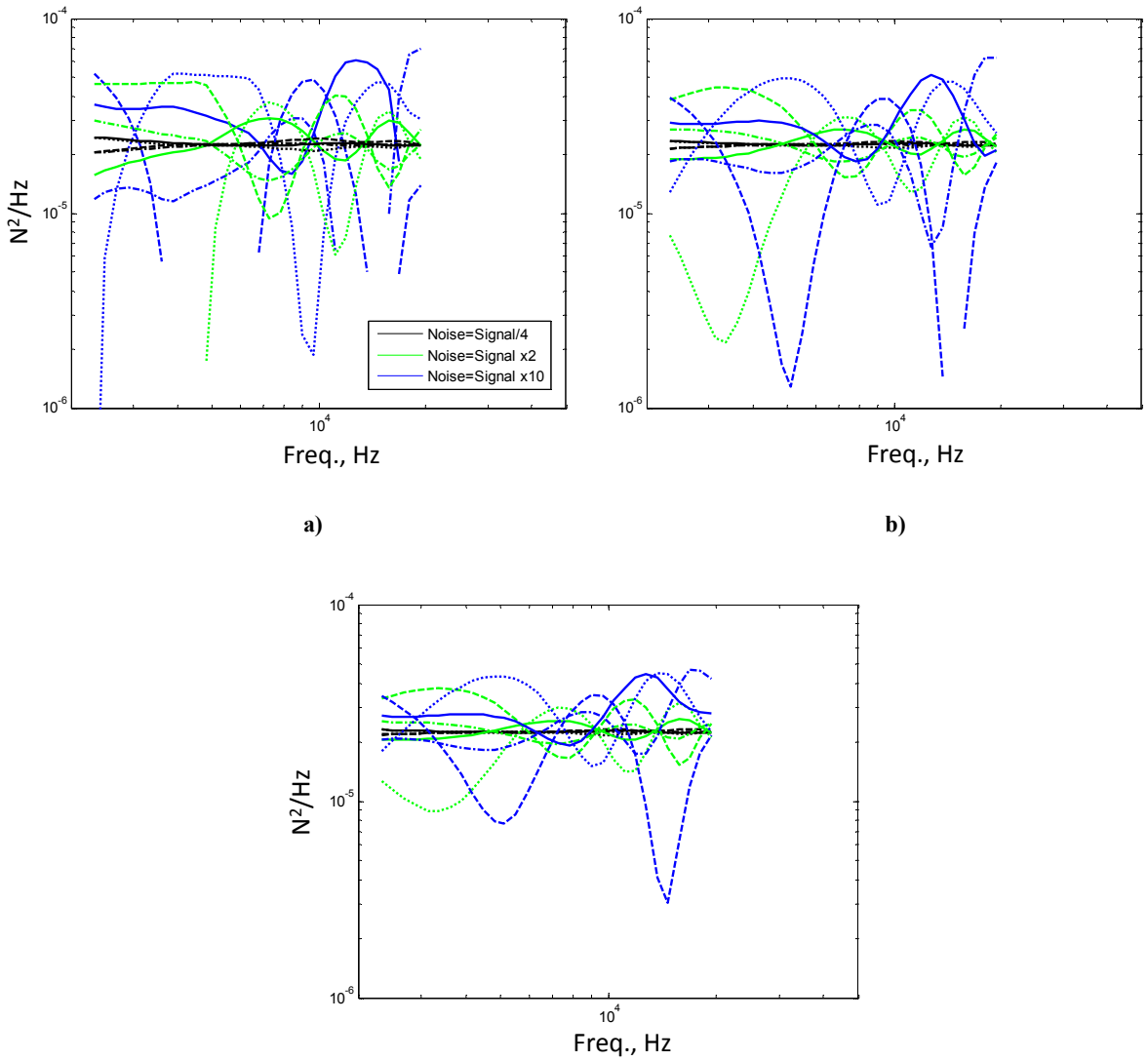

Figure 7-6. Estimated source strengths of at two source positions separated by z=8.25mm, b) 16.5mm, c) and 24.75mm with various background noise levels: source (0, 0) streamwise dipole-solid, spanwise dipole-dashed; source (0, z) streamwise dipole-dash/dot, spanwise dipole-dot

7.5 Uncertainty of the 42 Element Roughness Fetch Strength Analysis

The 42 element cuboidal roughness fetch had an 18dB signal-to-noise ratio at the highest measured frequency, 20kHz. This means the signal was a factor of 63 greater than the background noise. Using the cross-spectral matrix of noise that created the average signal-to-noise ratio of 2 as calculated for the single source location, corresponding to the cyan curve in Figure 7-3, the addition of 42 streamwise and spanwise aligned dipole sources in the 16.5mm grid arrangement with source strengths of 2.244×10^{-5} N^2/Hz results in an average signal-to-noise ratio of 75 at each array position. The signal-to-noise ratio is not increased by a factor of 42 from 2 to 84 because the directivity pattern of the dipole sources reduces the average signal recorded at each array position. Therefore, this simulation is an experimentally similar estimate of the uncertainty of the 42 element cuboidal fetch results. A least-squares analysis of the spanwise-averaged streamwise and spanwise dipole strengths was conducted under these simulated conditions to determine their deviation from the known values.

Figure 7-7 shows the estimated spanwise-averaged streamwise dipole strengths calculated for each row of the source fetch. These results are accurate within a factor of 1.2 diminishing with increased frequency. All rows have similar levels of estimated uncertainty. The least-squares analysis does not appear to favor any source location positions. This indicates that the streamwise dipole strengths estimated in Figure 6-12 and 6-14 are accurate within a factor of 2.5 over the entire frequency range and are even more accurate at higher frequencies above 9kHz within 10%. The results from the lead row of the cuboidal roughness fetch may indeed have this low level of uncertainty, but the trailing rows appear to have more uncertainty possibly due to their lower signal-to-noise ratios. At some frequencies, an entire spanwise row has an average estimated source strength value of zero and the strength reallocation effect shown in Figure 7-6 works to transfer source strengths between the spanwise rows. The total fetch-averaged streamwise and spanwise dipole strengths should be a more accurate representation of the streamwise and spanwise dipole radiation but would not provide an understanding of the source strength distribution. Therefore, the uncertainty of the spanwise-averaging analysis needs to be quantified with a justifiable approach. The uncertainty of the estimated source strengths for the trailing rows cannot be calculated as factor of the estimated value because zero values are assigned. The only way to analyze the results is by observing all of the source strengths and making a judgement on the level of accuracy at each frequency solution. A lower cut-off is needed beyond which estimated source strengths are ignored. The predicted strength of the lead row of the cuboidal roughness fetch is a repeatable measurement with varying size roughness fetches and is therefore, most likely an accurate representation of the source strength. The majority of estimated source strengths for the trailing rows are contained within two orders of magnitude of these lead row dipole strengths. Below this, there are no repeatably estimated spectral values and the estimated strengths may be carefully ignored by assuming that the source strengths through this short fetch of large discrete roughness do not vary by over a factor of 100. In Figure 6-14, if these values are ignored, the results of these trailing rows appear to have an uncertainty that is within 5dB.

The spanwise-averaged spanwise dipole results are shown in Figure 7-8. These results are far more uncertain at frequencies below 9kHz corresponding to an acoustic wavelength of 38mm which is slightly over double the source separation. The arrangement of the four microphone array positions appears to bias measurement of the streamwise dipole producing much greater uncertainty of the spanwise dipole source. Above 9kHz, the average spanwise dipole results are extremely accurate and deviate negligibly from the true value. A noticeable change in the source strength spectra as observed in Figure 7-8 below 9kHz is not seen in Figure 6-13 and 6-14. This may be due to differences in the

simulated experiment with the roughness noise measurement. The consistent estimated spectral shape of the spanwise noise from the cuboidal roughness indicate that the uncertainty may be better than the simulation suggests. Like the streamwise dipole, the trailing rows of the spanwise dipole appear to have an uncertainty within a factor 5, ignoring results more than two orders of magnitude less than the lead row's estimations, while the lead row's results, estimated as the strongest, are less uncertain within a factor of 2.5. Above 9kHz, the lead row's results are uncertain within 10%. For both the streamwise and spanwise dipoles, the uncertainty analysis indicates that the results for all rows are more accurate at higher frequencies.

This simulation was representative of the evaluation of the noise from the cuboidal roughness, but the hemispherical roughness produced a much lower total signal-to-noise ratio. The 6x7 array of hemispherical roughness was barely distinguishable in the measured autospectra with only a ¼ total SNR. Therefore, the estimated streamwise and spanwise dipole strengths from this fetch are far more uncertain. If the estimated values that fall more than two orders of magnitude below the lead row's calculated source strengths are ignored, the estimations shown in Figure 6-19 for the 42 element hemispherical roughness fetch are most likely accurate within 10dB, or an order of magnitude.

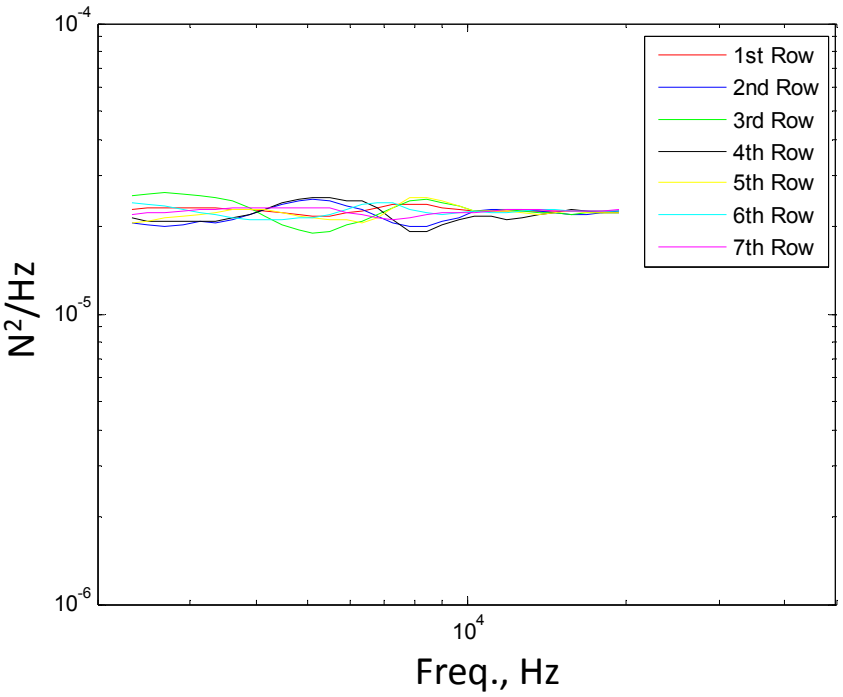

Figure 7-7. Spanwise averaged streamwise dipole strengths

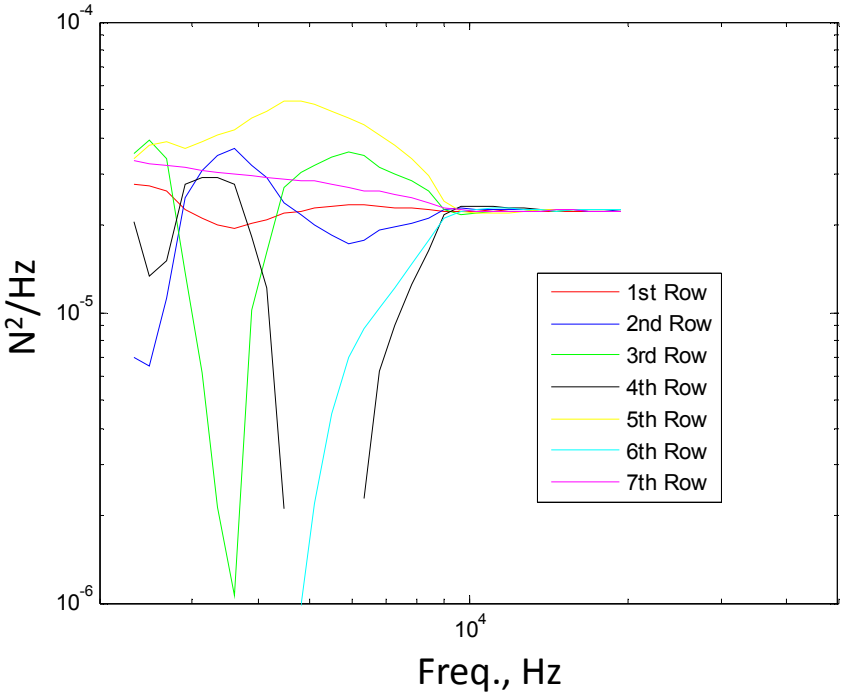

Figure 7-8. Spanwise averaged spanwise dipole strengths

Chapter 8 Conclusions

Far field noise and wall pressure spectra have been recorded from turbulent wall-jet flow over discrete hemispherical and cuboidal roughness. Also, the scattering theory of Glegg & Devenport (2009) has been investigated and used to make predictions of roughness noise for stochastic and deterministic rough surfaces at conditions with boundary layer to roughness height ratios ranging 0.06 to 0.18 and roughness Reynolds numbers 46 to 198. These predictions were also used to explore the form and accuracy needed of the model wavenumber wall pressure spectrum to make absolute predictions of the far field noise. A linear microphone array was used to record the far field noise from fetches of discrete cuboidal and hemispherical roughness. These array data were examined using standard delay and sum beamforming techniques as well as a novel least-squares source strength analysis to determine the strength and variation of source strengths through fetches of discrete roughness.

This analysis showed that the scattering theory of Glegg & Devenport (2009) can be used to accurately predict the radiated roughness noise even from surfaces with large roughness Reynolds numbers and moderately large roughness height to boundary layer thickness ratios. These predictions only entail knowledge of the surface geometry and form of the wall pressure spectrum, specifically the convection velocity. These estimations are improved with the addition of measurements of the rough wall pressure frequency spectrum, but the accuracy of this prediction is only mildly affected by the form of the wavenumber wall pressure spectrum. Therefore, further study of the wavenumber wall pressure spectrum will have little effect on the predicted results. The "break frequency" as described in Alexander (2009) and Devenport *et al*. (2011) was found to be a predictable function of the surface geometry that is related to the size of the roughness elements.

The least-squares method of source strength analysis was shown to be a viable method to decompose source strengths through a fetch of discrete roughness noise sources. Using this technique, the existence of streamwise and spanwise aligned dipoles located at each roughness element was confirmed. Also, the estimated relative strengths of the dipole sources were found to vary with frequency.

The following list details the remaining conclusions of this study:

Measurements of Roughness Noise and Wall Pressure Spectra

- Noise spectra produced by different roughness geometries varies in form and so cannot be collapsed on one another with simple inner or outer boundary layer variable scaling.
- For rough surfaces with large element height to boundary layer thickness ratios, the produced wall pressure spectra are highly inhomogeneous. The measurements show increased pressure fluctuations in the wakes of elements and a wall pressure field around elements consistent with a horseshoe vortex wrapped around the base of elements with separation zones just upstream and downstream of individual elements.
- Normalizations of the far field noise using the average measured wall pressure through fetches of discrete roughness produce similar collapses as observed in Alexander (2009) and Devenport *et al*. (2011) for stochastic and deterministic surfaces. The normalized spectral shapes differ with the roughness geometry. The normalized spectra produced by the fetch of randomly distributed 1mm hemispherical roughness resembles the ω^2 collapse and "break frequency" observed from

the stochastic roughness in Alexander (2009). After the "break frequency" the data fan out in order of velocity.

Roughness Noise Predictions

- Predictions of the far field noise normalized on the single point wall pressure spectrum accurately reproduce the spectral shapes of the measured normalized curves for all of the surfaces. Absolute predictions for the smaller roughness heights are closest to the measurements, with the normalized spectrum becoming somewhat underpredicted for the larger roughness sizes. For the smaller 1mm roughness, the normalized spectra are accurately predicted within 3dB before the "break" and 6dB after.
- The origin of the "break frequency", as observed in Alexander (2009) and Devenport *et al*. (2011), was shown to be a predictable function of the roughness geometry. The "break frequency" occurs at the frequency where the peak of the convective ridge lines up with a major lobe in the wavenumber filter function.
- Predictions of the absolute far field noise show that the radiated roughness noise for roughness that is a small fraction of the boundary layer thickness can be very accurately determined if the surface geometry and rough wall pressure spectrum are known.

Microphone Array Beamforming Analysis

- Source strengths were observed to vary only slightly across the span of the roughness, but the lead rows of the roughness produced stronger source strengths in both the streamwise and spanwise directions.

Least-Squares Source Strength Analysis

- A single hemispherical element produced weaker far field noise, and therefore, the drag and side force spectra are over an order of magnitude lower than that of the cube. For multi-element fetches, the lead row of roughness was found to be the strongest producer of sound in the streamwise and spanwise direction with weaker estimated source strengths from all of the following rows.
- The relative magnitude of the estimated streamwise and spanwise drag spectra for a single cubic element changed with frequency indicating that the directivity varies by frequency.
- The LES calculated strengths of Yang & Wang (2011) for the lead row of cuboidal and hemispherical roughness and the source strengths calculated by the least-squares method are similar at lower non-dimensional frequencies. The disagreement between the computational and experimental studies grows with non-dimensional frequency. The streamwise dipole source strength calculated by the least-squares method is greater than the LES estimated strength at all non-dimensional frequencies.

Appendix A: Random Roughness Locations

The following is a list of the roughness element locations for the roughness fetch of 6209 randomly located 1mm hemispheres. These positions are given in millimeters relative to a corner of the roughness fetch so that all values are positive. The *x*-values (left column) are in the streamwise direction and *z*-values (right column) are the spanwise orientation.

x, mm	z, mm
1.7744	8.1782
4.4593	11.604
2.4263	13.0956
3.2291	24.8829
0.7076	38.4728
3.8698	46.5077
2.4146	58.9069
3.2955	59.8024
0.5355	66.1555
4.6244	66.5863
2.2699	70.3113
2.4798	73.4209
4.3278	82.5653
0.3253	99.9817
3.1761	106.3556
4.8792	123.9834
4.0789	131.4389
2.0497	131.9367
3.608	132.4311
4.961	139.5366
1.4384	144.6372
4.6901	161.899
2.1289	164.1995
3.959	173.9764
4.2306	179.2613
0.6649	182.9747
4.9218	203.1552
3.1451	210.2435
2.2204	224.1609
4.2817	230.3143
0.9342	231.5066
3.2219	232.358
1.6163	240.3933
4.0997	241.0904
0.8063	242.8526
4.3728	250.3746
0.8814	259.6831
1.5039	262.2216
3.7659	263.5634
0.4399	276.0559
4.1235	277.0742
2.8435	277.9425
4.9641	290.6265
2.9303	298.2746
2.2261	313.0154
0.0919	323.2728
4.1343	349.1438
4.157	365.3336
1.5944	369.6248
4.0596	379.8659
3.1312	393.5142
4.6004	394.9581
1.4445	395.8687
2.7832	397.3482
1.9012	416.9629
4.5769	424.4937
4.2726	426.5591
1.0286	427.9581
2.5374	434.4302
3.6671	442.187
0.6461	452.3276
1.012	456.2324
4.629	459.5297
1.9127	469.3319
3.4273	472.3657
4.7038	483.8104
3.6226	493.6068
1.1839	497.1707
4.2573	504.5523
4.2239	505.3874
4.5856	505.5961
0.7061	512.0727
0.2701	513.9341
4.4671	514.0954
0.6545	518.1962
4.5947	531.0815
3.1193	534.2646
1.3499	536.383
3.1907	537.3027
0.8927	549.4226
4.8506	550.9835
1.7427	557.0625
4.8388	564.666
4.9364	568.224
3.0315	585.051
2.0455	590.8688
2.7736	609.7724
7.4614	606.1123
8.1144	605.8448
11.0154	604.3678
10.1446	597.622
11.8428	596.0281
5.8076	594.0913
12.6526	593.9538
8.2949	591.4881
5.5658	588.5061
9.7096	586.7229
12.5624	584.8839
11.9465	581.4468
10.0131	571.216
11.0468	566.7414
14.7761	561.171
13.3339	560.8206
6.5757	560.565
5.7527	557.259
12.7785	556.922
9.9635	553.6318
5.8184	542.7183
11.9388	539.7409
11.6723	538.1618
12.9158	536.6349
6.811	536.0215
8.7896	528.5968
14.1657	526.0978
8.5883	520.7279
5.7914	514.4071
10.3009	511.3371
10.3227	511.3053
13.9081	509.3751
9.371	508.8399
9.155	503.6252
9.8804	489.9207
6.6735	485.2657
13.0427	482.3091
5.0095	478.7812
11.4863	478.4521
6.3375	478.2494
9.3582	476.5248
5.4076	476.0821
8.8326	472.0675
8.3276	469.8939
9.1634	462.8346
6.0854	461.8512
12.7863	460.0216
8.911	456.516
10.0188	455.5169
7.8058	454.0347
9.4725	451.1342
7.4807	448.2241
14.2399	446.0087
9.2603	444.4718
5.7079	444.3325
13.0574	441.4539
6.504	439.4611
14.7803	437.6484
9.2247	436.5613
10.2935	434.4472
7.1651	429.3455
10.2873	427.4307
8.748	420.2156
5.6688	417.3367
8.3868	415.764
12.6915	413.8157
14.9781	412.7621
9.1418	409.5119
8.2079	409.052
8.5459	407.9143
8.8766	406.458
10.0746	405.3084
6.4262	404.4577
9.8849	401.3207
10.6845	396.6899
9.7333	396.0335
9.1026	394.8476
12.3963	394.768
10.089	394.609
6.7419	390.7774
12.6023	388.1198
6.234	386.8263
9.9701	382.617
7.3269	378.3887
8.4446	376.6159
7.8403	372.0357
12.198	370.8759
12.8295	370.7222
9.1365	368.0089
8.9028	359.8615
5.9354	357.1424
7.2077	347.2576
7.1769	336.5123
10.0651	336.0722
14.6963	335.6572
7.4766	331.1315
7.2903	329.37
10.5141	325.8912
13.0585	325.5895
13.0932	318.6473
14.449	316.9881
12.67	309.9554
6.1543	307.4834
11.3655	303.3179
10.1373	296.8587
10.9438	294.9905
6.2076	289.1054
5.8354	288.1598
10.9201	280.4476
14.3485	279.5112
6.3396	278.6798
5.9907	268.3875
5.6514	266.5129
12.7127	266.4534
14.9171	264.2959
9.6288	259.4622

9.9231	257.673
7.5137	255.8329
11.0707	253.2578
8.4217	253.0079
7.6328	247.6954
11.5376	246.8215
8.8881	242.4685
5.1923	242.1799
14.9516	241.9783
12.4178	233.6191
7.6516	228.956
6.8728	228.1919
7.8619	228.1535
6.7927	227.7611
9.3036	224.515
12.2716	221.9714
9.4285	219.3793
10.7462	213.695
5.4386	212.2876
9.764	210.407
8.8126	203.6622
11.3092	188.2168
5.6555	185.7885
9.4763	183.5575
11.6233	181.4199
11.0323	181.3421
6.2384	168.4882
9.7118	166.9623
10.8048	163.4187
14.4686	160.8855
14.9065	154.2962
11.2606	153.9444
14.2591	153.8732
11.2506	153.1993
7.2572	152.4676
14.3867	146.138
10.6268	145.3633
12.3767	137.1507
10.8426	130.0425
11.891	113.8465
7.8305	105.9002
5.3068	100.4875
8.4362	97.3506
12.1017	96.6052
9.0935	96.3241
13.78	89.7005
12.2152	87.1957
7.2942	74.5482
6.7545	70.4615
8.1171	69.4022
7.9242	65.5645
9.6101	64.5855
8.8232	62.1964
14.3868	61.896
8.1522	60.5009
13.9337	55.5229
10.1485	54.505
7.1182	50.5479
6.8119	42.9777
14.3688	39.8818
14.6401	38.4081
11.444	32.1623
14.4261	30.1834

8.2232	29.8827
6.619	25.8735
5.0582	25.4661
10.5855	20.6457
5.0364	16.2614
13.9261	12.8848
10.8943	6.2782
6.7904	3.4081
6.7141	2.3716
24.0041	2.2209
20.9058	10.8701
19.4729	11.6485
21.4767	19.9056
16.2149	23.2985
22.7803	25.0222
15.1587	28.1027
18.2843	28.4348
21.8412	28.5892
17.5339	28.6729
20.8369	29.4415
22.114	29.6029
17.5249	33.5333
23.984	33.8426
21.6718	35.8468
15.0943	42.6161
19.9115	45.6242
20.7843	48.6901
17.972	55.8433
23.2149	68.1272
18.0974	70.2367
15.0452	73.294
19.0807	75.2997
22.2175	75.8444
15.375	80.7743
16.6429	92.8207
22.1156	96.2764
17.6812	110.1123
17.4515	110.3853
21.7641	111.387
23.7855	117.852
18.0225	118.9825
19.1235	119.8798
19.4772	122.5245
16.799	123.8566
21.8013	124.1205
17.179	124.3878
18.5542	126.4676
20.0625	127.1504
24.2468	127.7603
15.1265	128.8366
20.9157	129.3655
18.5856	132.8392
23.3534	136.498
18.8204	144.7898
18.3614	150.5018
16.656	153.814
15.8225	154.7353
20.8968	157.0232
17.7117	157.4037
21.451	157.6308
18.8466	165.3648
21.2768	167.9457
16.3464	172.7954

22.2288	173.9144
24.3715	175.8264
24.1461	187.6716
22.4872	190.3521
18.9857	198.5184
17.0684	199.6024
16.9657	200.3117
19.1595	201.8289
16.4079	203.3944
19.545	205.653
18.7923	207.601
22.1775	208.8367
15.0579	209.5764
18.6287	218.8772
22.914	219.4246
15.7106	222.8253
18.6841	224.6436
15.2039	226.3012
19.2294	226.9246
23.7486	229.6261
20.1533	232.2731
18.3295	232.9722
20.5072	235.5765
23.1521	244.217
17.3709	249.6486
21.45	260.2299
20.3899	261.994
20.3965	269.1327
15.8102	269.2566
24.3064	270.0862
20.4322	273.8505
23.5335	277.4156
22.3003	282.2541
23.0895	285.0207
16.9399	287.7336
22.4359	295.0971
15.5113	295.8177
24.6332	296.3321
20.4606	305.0283
18.8888	305.0632
17.8135	307.0466
24.5348	307.8285
15.3405	308.4666
19.0122	309.4803
19.9053	312.4741
24.041	315.7145
16.4857	318.6186
16.6218	319.3562
15.1471	319.4527
15.2002	320.7069
16.7692	325.6291
20.5369	326.3168
16.9559	327.3103
18.422	332.9811
20.6747	334.4072
18.7342	339.2646
18.3264	347.0428
18.8767	347.8803
24.4507	352.532
24.1056	353.8832
18.0546	355.3917
20.0108	363.0395
20.1216	366.3568

21.6435	367.2318
23.7656	369.3308
23.7592	372.9738
21.6293	374.5107
15.2508	380.5632
17.4466	388.4291
22.5284	389.2011
22.6278	394.5822
19.8478	395.7342
15.2828	398.6109
16.9606	401.444
23.1553	403.0858
15.5408	405.7051
19.6796	411.9731
19.8399	412.3982
16.3184	412.5353
24.3609	415.0051
15.2983	416.1428
16.7306	417.6709
22.2234	418.0436
21.554	418.1946
17.2015	419.1916
24.7582	423.6471
15.4844	434.2532
24.7762	437.2893
19.0831	439.6697
19.5226	447.6265
16.5386	447.6632
22.1508	447.994
19.49	449.8759
18.947	455.3218
21.6998	461.9438
23.3458	462.0235
20.6955	463.4515
19.8065	470.5055
20.2736	471.739
24.0509	477.8675
22.6451	479.3394
17.3679	483.1831
23.929	490.3758
16.0609	492.236
20.528	495.2993
17.652	497.624
23.1842	501.5583
18.3751	501.6662
21.7457	505.1343
18.8206	506.9257
15.2309	508.546
17.4473	510.4773
21.8782	511.1604
24.1847	517.3945
21.1311	518.4839
16.2692	521.1073
18.5949	522.0795
18.232	522.8107
17.8473	526.2601
21.3352	529.5531
22.4598	532.503
22.9068	535.5992
21.3087	535.9779
20.6137	541.0226
22.5484	542.2388
15.4221	542.3295

18.0295	550.2218
24.884	551.6708
20.1868	555.2082
22.0273	555.8525
16.5044	561.1037
19.9191	561.5769
18.2966	561.9546
24.8633	565.8363
18.9266	569.2621
24.9952	569.6225
21.9466	570.927
15.9595	571.7018
17.9994	572.5053
15.8712	574.1911
23.3599	575.903
15.8332	576.7143
16.8804	579.5913
16.4701	580.2531
19.1209	582.7787
22.8166	584.6889
17.1272	586.3705
21.1368	587.6916
17.9655	600.1623
21.8665	601.212
24.6559	604.0251
21.3757	605.9012
19.7313	606.536
19.8636	609.6733
28.4075	609.173
31.583	607.3272
28.5318	606.3356
25.2053	604.2007
28.0998	602.8823
28.6279	600.2025
26.5105	597.0346
34.6159	595.2364
28.7462	594.4808
32.2646	590.411
27.9224	587.9884
29.6801	587.2354
34.1364	585.3985
33.0643	585.0025
34.0307	581.9028
27.4818	575.9602
25.5124	573.2536
27.3517	571.5456
34.2329	562.2294
32.9451	560.858
27.8976	560.4626
28.277	559.5083
30.1928	559.4479
28.9987	557.7813
28.3737	556.9678
28.6786	553.9136
33.3761	553.0334
34.7481	550.5438
29.4527	546.0916
29.8798	543.7614
29.6742	542.6667
32.9708	535.4327
34.0974	535.3918
25.5284	532.3365
26.9904	531.3943

31.1923	529.1185
29.2755	527.1962
34.8039	522.5636
31.7431	519.8772
33.0979	519.487
30.2782	512.0566
34.9428	511.7083
32.7162	511.0768
28.1333	507.5998
27.3291	507.306
30.0183	505.163
29.01	486.6032
31.661	482.5911
31.6487	478.5142
32.1141	477.7972
30.2205	476.0176
33.7436	470.4819
30.0117	466.8444
25.268	464.9988
26.3134	458.8155
31.1039	453.1002
28.2074	441.9067
33.595	441.3879
31.7045	429.4139
25.4471	422.0251
34.3751	421.3926
29.391	416.5729
30.6005	415.4333
28.3679	414.8235
30.3054	413.7019
33.2715	411.5253
32.8356	410.2098
28.7904	399.4923
26.9966	399.0686
33.0234	396.1351
28.307	389.5848
33.6599	383.5878
27.7333	383.2627
33.1869	380.9027
33.2503	379.7358
25.2851	379.2383
34.398	379.2292
29.9171	377.5895
25.1037	376.4268
32.9219	375.7849
28.0933	370.0669
28.1008	369.0751
28.3856	368.1713
31.8463	367.112
28.6387	366.5913
31.0889	364.8871
33.809	363.8003
32.8589	363.1493
28.7779	361.2015
25.1661	354.0962
28.272	350.0312
25.4694	348.8851
32.3436	348.1219
25.4651	346.5586
34.0698	344.1701
26.0094	340.4692
33.1197	337.879
33.278	337.8621

32.9039	337.8202
32.1734	336.3919
31.6536	334.0137
28.3577	333.1367
34.8737	329.7707
30.7366	327.3817
31.4304	327.2602
32.7731	326.9224
30.8363	325.4078
25.3508	324.9292
30.3531	322.9332
34.1946	322.7984
27.3147	318.4391
26.951	311.3107
27.2484	308.2005
28.1257	306.3945
27.2958	305.8258
28.4045	302.4586
26.9033	301.3111
26.7454	299.7805
27.4002	298.0867
33.7439	276.2461
27.8453	274.7509
25.8981	267.4274
32.2644	258.9034
31.0839	255.6075
31.7131	254.6237
34.8006	254.2123
31.4398	253.7889
31.1415	250.5923
30.7544	248.4929
31.2744	245.5553
31.2789	242.0435
27.7242	238.2842
33.9834	236.2296
33.3669	231.0082
34.1936	229.3705
33.7673	227.2484
34.2952	226.3325
27.32	223.5544
26.5774	222.1816
30.3492	220.3474
25.3917	220.1358
31.0742	219.6104
32.6817	218.1423
25.8974	213.5951
30.3216	210.6612
34.2132	205.7639
33.6106	203.931
34.3912	203.2586
30.2321	197.9818
33.3106	192.5561
31.1439	192.0728
29.6552	185.4665
33.2938	177.7425
32.2478	172.761
28.8675	170.6728
28.5696	164.6094
27.7749	164.4995
31.086	163.4477
29.1046	159.9685
31.1205	158.1124
34.7802	153.0004

31.1664	150.5847
33.4329	143.4665
25.4192	137.8236
27.4345	130.1348
29.6882	124.9192
25.8096	123.9504
31.8879	117.649
27.1495	117.6162
27.0862	117.5977
25.5732	111.9506
28.5358	109.7953
25.1969	107.0742
33.4089	105.7662
30.4236	100.3607
27.1263	98.8242
27.3773	96.5773
34.9751	89.9079
33.327	86.9447
34.1746	86.4701
31.0143	83.3686
28.4427	78.2812
34.6884	72.302
30.8233	66.5409
27.786	65.8377
29.9758	63.4512
31.6371	60.017
25.9553	57.7532
28.0005	57.5408
31.9733	48.4587
34.5183	41.9883
32.8007	37.3957
26.2517	37.0465
25.2391	33.2563
29.772	31.9788
34.8263	30.6057
30.2846	30.3259
32.5473	22.9216
32.9602	21.5443
26.4586	15.2438
27.9201	13.2216
27.8472	10.0475
33.4047	8.9636
32.3979	8.2973
34.9003	3.8182
41.5052	0.7804
43.7527	5.684
43.8448	6.7955
44.2223	11.7623
41.327	18.0089
43.8522	21.7436
36.7786	22.7725
41.121	24.2738
43.768	32.4259
42.3232	36.2237
40.0522	38.0033
41.3531	39.8302
42.8975	52.349
36.7608	55.1094
43.9018	60.3682
35.3229	65.1749
40.9201	68.3543
37.0525	72.6342
41.0018	73.3657

43.2814	77.4043
44.9704	78.7579
44.9031	86.7624
39.691	90.5012
39.9713	93.7311
40.3228	95.7021
36.2862	100.7806
44.5276	101.4312
38.7368	104.688
40.3521	108.9903
40.0351	114.5185
44.2195	116.0025
41.8218	117.4759
43.5412	119.9032
43.4741	121.3452
36.1837	122.511
38.5141	124.1827
39.0766	127.7873
35.6342	133.4159
40.3893	135.8169
35.7552	138.052
39.1791	140.6407
39.8918	141.103
36.9984	142.3234
42.8761	143.8238
39.6593	148.3156
42.9855	150.0199
40.7386	155.135
38.9481	157.7265
39.8756	159.1017
43.6554	161.5495
36.2659	165.5803
38.5802	165.8285
37.0305	171.7215
35.9933	175.085
42.8051	175.319
39.8042	177.6726
38.6453	178.7975
41.2038	182.1282
42.7796	184.1168
42.4486	185.441
43.1697	186.1822
39.1562	192.6765
41.1232	192.758
43.3107	203.8969
37.8806	211.4634
38.1441	218.9364
35.7364	220.2773
44.0065	221.436
37.2599	221.9
39.902	224.2797
44.4478	226.6515
42.4117	231.5663
36.0975	231.7136
40.2516	231.9224
41.2332	231.9979
38.8341	237.5564
41.8737	237.6188
40.9262	239.9828
40.751	245.4989
44.6318	245.7336
42.1952	249.6314
35.3258	252.8247
41.3786	253.0655
37.6724	254.1235
38.2652	257.8952
42.8133	258.5221
44.745	259.1778
40.4052	259.8986
39.3856	261.4877
38.6151	266.2849
41.7632	267.0832
40.8863	267.2423
43.0609	268.7321
41.8222	270.0058
41.1498	275.0674
35.4282	279.3455
39.116	279.531
37.9799	283.8516
39.2731	294.5485
36.6724	299.3178
40.0705	303.0745
43.6929	306.9587
41.8923	307.1517
38.2333	307.7351
41.6556	309.5205
39.2556	309.8221
43.2859	311.0064
44.8113	311.1431
40.0829	315.0942
37.879	317.7927
43.6026	319.4013
43.4362	321.0432
44.2172	326.7509
43.2554	327.2826
39.1212	327.3207
43.7599	327.8744
38.1577	332.8001
43.5957	332.9155
43.7856	334.5013
39.621	334.5271
41.4206	335.7877
43.1824	338.8086
40.268	340.3179
42.9412	341.8889
35.0524	347.0945
40.1556	348.1733
38.6943	352.1762
37.3041	354.4292
42.7654	355.5341
38.9796	358.4371
38.1975	361.2513
39.9641	362.2935
43.7979	369.791
44.5152	371.0114
38.2075	372.3282
41.9706	393.6934
36.5934	394.8105
43.9935	395.0803
40.5066	396.378
35.1334	398.7332
41.3923	399.3257
37.4633	400.2409
35.2943	402.2679
39.908	404.0552
35.3227	405.5283
42.9654	407.0115
39.4455	414.5557
44.6878	419.1953
36.4919	420.3804
43.8646	424.0781
39.3804	425.2497
43.0102	425.8455
44.3435	426.9955
38.7247	429.4503
38.1717	431.1712
40.5557	432.4826
39.9371	433.3172
41.3551	434.0893
44.5413	434.4183
42.2005	440.9039
36.4894	441.0226
43.6883	443.6885
39.6094	443.7482
37.5704	444.6268
43.556	448.5666
43.2587	450.5954
36.0715	457.6876
36.5401	470.8797
37.4314	472.3324
42.7282	472.3543
44.6559	480.0924
36.2533	487.0359
41.2706	500.1753
35.075	500.4733
35.1337	502.3228
42.1339	503.0864
43.0285	503.1538
35.5951	504.2605
42.9354	504.5574
41.1419	514.1393
44.6252	515.1554
36.5907	516.474
38.6958	517.0729
41.7494	524.5619
37.9686	525.0798
37.8361	525.3696
44.3487	530.1721
44.1309	535.4248
35.6877	535.498
41.5009	542.8427
42.639	549.8404
37.4413	552.4401
36.7537	553.1764
39.7891	559.1658
38.6065	561.8308
35.0061	564.6957
40.067	564.7785
38.3606	568.7675
42.3059	569.5905
44.9838	575.0798
39.319	575.8107
44.9532	577.8405
39.0841	580.4962
41.5469	582.1622
38.5724	583.5603
37.5148	585.451
44.794	588.3331
43.4389	595.3379
42.5204	599.8368
38.3611	600.748
42.2082	603.0757
44.7357	605.1023
51.8828	609.6341
46.4871	608.6359
54.7693	604.5696
50.3604	602.9347
52.9256	600.972
46.8357	599.2139
45.6847	598.4917
50.0573	596.7543
48.6882	596.4385
46.6863	595.6269
50.0876	590.9496
49.309	582.1351
54.0263	580.977
48.5606	580.93
54.6526	568.3388
46.2494	566.0627
52.8258	565.9311
48.4445	563.4895
46.7332	561.1581
46.1895	559.8388
51.4124	559.151
53.3024	551.5937
54.8541	549.5461
46.2812	548.8613
53.305	546.4882
47.1355	544.9727
54.5885	538.5081
51.4232	532.8563
53.3022	524.4886
50.423	522.3913
45.9659	516.132
50.7662	513.4943
54.5151	508.1475
49.8969	497.6735
53.4557	497.3295
53.6307	480.2523
50.0804	477.43
52.5845	477.2266
52.871	473.4796
45.7096	467.9808
50.1599	465.4442
52.4807	464.7269
54.3012	462.3233
54.2023	459.16
46.1016	457.8048
54.32	457.0643
46.4125	451.2537
50.5225	450.4297
50.2849	447.3267
45.4104	446.4107
48.17	446.3809
52.4921	445.3274
54.4563	444.229
45.0849	437.8981
50.89	437.3779
48.8192	436.1476
49.7749	433.0422
51.4487	430.8051
54.3508	426.312

45.8491	425.9073
52.9765	421.694
48.8067	418.4949
49.6208	417.2653
47.9875	411.7028
50.3322	409.5941
47.2722	406.2761
53.2149	405.7889
54.1564	402.6669
53.9724	402.0127
47.3165	397.4591
50.7838	396.7291
52.0083	395.6639
50.1788	393.1413
47.8945	389.814
48.9953	385.2463
54.8276	382.9186
47.1705	380.8235
51.5619	379.8925
46.8923	378.6917
52.7002	374.2363
54.1471	364.0949
49.6875	362.9676
50.7497	359.5236
45.7721	342.4062
51.3848	337.4308
46.4253	328.5521
48.9426	328.3644
49.477	324.7101
48.8544	324.5476
51.2659	323.8353
48.842	323.4122
48.617	321.9343
48.2759	319.0527
51.1159	314.4778
52.7824	314.0443
45.5274	313.4284
45.9048	311.9971
50.9753	311.791
46.6204	307.8954
49.8818	300.3313
50.4654	295.7316
53.7381	293.4232
54.1304	290.1487
47.6121	286.5476
54.7276	284.7547
53.492	276.5831
52.2784	274.385
45.003	270.2189
53.2653	259.2128
45.5738	255.1025
49.628	246.3377
48.1776	232.6074
47.844	231.4043
52.68	221.7711
45.0672	219.9853
48.5198	218.3873
48.8507	217.876
54.4403	214.2757
54.9437	211.8163
46.2331	205.6038
45.0428	204.788
46.9866	204.336

46.7769	202.8427
47.6126	201.49
47.6651	200.0376
46.1457	194.0813
53.4683	184.2507
45.2717	183.581
49.2203	183.036
48.2693	180.3093
54.4514	179.933
45.4624	179.692
49.6129	178.3311
45.9094	175.7479
48.2215	168.9695
48.921	166.8581
53.0051	166.3181
50.0559	161.7796
47.7359	160.986
51.1197	160.0263
52.8553	157.2621
54.1459	155.1671
50.6998	152.7242
47.8405	149.991
49.7771	145.1409
50.1634	143.0899
49.4438	143.0782
47.0774	143.0282
51.881	140.1244
51.4948	135.7437
46.2687	131.7496
51.3018	125.0458
50.4325	120.7567
49.5002	120.0201
53.671	119.4356
54.006	113.7294
49.9969	112.2832
49.9958	109.7525
45.9907	103.4097
48.1952	103.2647
45.845	98.6421
52.9971	97.5752
52.0252	96.5523
54.0581	90.4837
45.1801	89.0401
49.1123	81.7649
47.6138	79.59
45.2666	78.9779
48.473	76.3182
50.0878	74.7284
49.8299	73.2713
49.9744	72.4403
46.8512	66.3096
54.6271	64.2209
53.7886	59.8456
52.8908	59.3838
48.8969	57.5129
48.784	55.6374
53.3933	51.0285
45.8554	50.5804
46.8818	45.5333
47.2965	45.0024
50.8517	41.9173
49.9303	36.4556
49.8063	32.1562

52.5865	31.0318
45.304	28.6198
47.9512	25.0355
46.6142	17.9323
63.4358	2.398
59.7097	11.1223
59.4274	11.1782
61.4569	11.5122
63.2107	11.7816
56.2434	12.3748
64.0403	26.6801
56.7852	26.9579
62.7688	27.9063
62.4533	28.7751
64.0953	29.0656
55.731	29.9347
60.5613	32.0542
64.6863	34.4845
55.4122	38.2226
57.969	46.0178
58.8934	52.2379
59.2911	54.1608
64.6698	57.5871
64.9462	59.0243
58.5037	65.7612
57.9349	66.4854
57.1721	66.787
60.4534	67.3493
56.3858	73.3203
64.3807	73.7598
63.9761	80.6376
60.3642	87.0525
61.7097	91.5183
57.0966	91.6543
58.7899	93.2753
59.1544	95.8025
60.7529	99.5334
55.4411	101.2168
63.822	101.8318
61.643	103.956
62.1495	107.143
60.7086	120.1199
61.3084	122.8746
55.5562	124.5917
61.1313	128.4195
55.2683	129.0004
62.4889	132.2378
60.5409	133.3496
58.452	133.8809
58.7695	134.3736
57.9376	136.9442
57.9216	138.1891
56.5454	142.7671
59.134	147.7962
56.119	148.795
60.4336	151.1767
58.9292	151.5293
62.0603	152.8216
61.208	157.3571
58.7234	174.291
55.1274	180.6157
57.3825	182.3957
60.1979	188.3415

61.8172	191.8836
57.4251	195.1679
59.6146	201.0824
57.2474	204.1764
58.6965	207.4523
55.8153	210.785
59.8378	211.257
60.0933	211.3864
59.4831	219.4739
62.1429	220.0884
57.4052	225.2546
64.4772	226.1712
56.4354	229.965
64.8817	232.0014
60.0229	233.4159
62.9007	239.9338
60.4521	240.3441
55.7748	243.4078
55.2444	247.8386
55.7175	250.7752
55.6195	252.0602
58.5976	254.2766
61.3376	255.4031
59.3412	262.6613
64.8306	266.5347
64.6002	267.23
57.639	269.8747
62.4954	270.8149
62.2271	272.5119
58.8689	275.9258
64.7247	279.4884
55.308	279.7551
64.7504	280.3541
55.3252	281.8085
61.1353	282.6755
60.6902	284.993
60.3728	286.0097
56.9531	288.5015
58.4923	291.734
57.9816	293.534
55.5925	294.2449
63.5496	299.0374
62.9668	301.0246
62.1659	303.16
55.7394	307.4077
59.9768	315.1049
57.0182	316.055
64.2601	316.8639
61.4368	320.0675
64.7324	320.8797
55.4447	324.4465
60.324	324.7081
61.6115	326.4479
58.5126	337.1296
61.8859	342.3403
58.617	345.8689
62.3908	346.2647
56.4242	362.1687
63.6854	389.3238
64.4633	389.8598
64.4088	389.9586
56.9121	390.2942
64.0762	390.3666

56.9602	391.8677
61.6192	396.2383
56.9766	397.4392
61.8943	403.1957
62.9141	412.7505
57.8563	413.9711
59.3684	416.169
57.9608	417.5087
56.7902	422.1037
62.2985	427.3588
60.566	432.6312
59.3187	433.7104
63.2032	435.2098
59.154	435.6419
62.2833	435.7289
62.1018	440.7267
55.6802	441.6835
57.2879	444.0202
64.2332	444.5978
56.1078	449.731
64.9245	452.094
55.6697	452.1625
56.6241	453.1078
58.5987	456.0902
59.9425	456.6222
62.3626	457.3085
58.0533	458.174
61.44	459.4708
60.7419	460.7338
64.7617	464.765
55.7709	464.966
57.6983	467.1214
60.922	467.1698
63.4852	479.9376
59.6542	480.209
55.374	480.8404
56.5985	481.1152
56.7117	485.2013
61.8114	485.9337
62.7232	493.5778
56.1867	496.2281
58.1224	498.0977
57.6818	500.8361
63.4606	505.5086
63.6264	506.9681
63.7057	508.8547
59.7775	509.4491
62.7988	512.1037
59.9371	512.7589
63.9576	516.1416
64.7547	518.9818
62.4725	525.6072
61.406	531.1022
58.4225	531.8774
64.8371	535.1924
60.5476	537.9708
61.0777	554.569
62.697	554.6045
57.6378	558.3132
55.9129	559.8885
59.6887	560.3762
58.6353	561.3455
60.3216	573.8751
62.6397	574.2689
56.9105	577.7923
55.7345	578.0652
59.599	581.8681
57.9419	585.1831
62.1764	586.5835
55.2652	590.4796
60.6398	590.8587
61.2419	592.8598
55.6627	595.9273
60.2305	601.0109
56.1321	606.389
66.1858	607.7261
72.9805	607.4238
72.7479	605.5545
66.3837	603.0357
74.4377	602.4763
65.2229	594.7524
72.421	593.6188
73.1574	593.4452
65.073	593.2876
73.9654	590.9472
73.7862	589.9256
71.3009	587.5073
71.4932	585.2275
71.6938	583.4823
71.8746	582.8642
72.274	580.646
70.356	580.3684
70.2045	578.0559
72.5325	575.6404
65.8923	570.1241
71.0064	569.6209
72.5861	568.566
74.5551	565.7599
66.9936	563.7534
73.0837	555.6176
70.1661	552.9801
74.1842	545.056
72.1455	544.2301
73.6291	541.9017
66.3725	536.0527
74.6802	533.7494
71.2061	530.5041
71.8355	527.272
68.8439	525.582
74.49	518.7085
65.0242	516.8634
74.8558	516.6739
66.5505	506.8297
69.4021	506.6697
67.3034	506.1362
66.9411	503.0171
68.2927	501.5157
66.349	499.5757
74.8566	495.6531
69.0726	495.553
74.9127	495.1572
65.9894	492.9977
71.9951	491.8822
71.7362	490.8848
66.7203	487.9946
72.3988	484.6236
65.7973	482.5538
73.6093	473.2703
71.3595	473.2374
66.1888	468.5879
72.2289	467.8703
65.9438	467.4737
72.9983	460.2527
74.2441	457.8257
66.6757	454.6147
73.142	454.2055
69.3432	449.7357
73.7481	448.3266
67.7182	446.065
65.0337	444.752
69.1253	441.5055
74.2952	439.928
69.077	437.6022
74.7492	434.8533
70.0182	433.3723
70.4438	428.8705
68.0181	427.6996
71.9218	425.8196
67.8351	423.7622
74.9163	423.6342
72.7164	418.4029
74.6501	418.3341
71.7871	416.1182
73.9983	414.0331
73.0952	405.6354
68.8151	405.3715
69.2472	399.2244
74.7628	399.1264
74.6369	396.2359
67.1927	393.9561
67.2747	393.913
69.3218	393.7898
66.8842	392.1259
65.8937	385.9032
69.6645	374.5237
68.9094	373.6173
72.6384	372.7622
67.315	369.7781
67.3422	367.2424
73.1955	359.1296
72.036	353.8357
70.2905	349.7315
73.1966	349.2302
70.6395	347.9552
71.7198	341.2991
74.5828	340.0908
69.0129	337.7893
74.8159	333.6697
68.3982	331.9453
66.789	331.8675
71.754	328.4985
66.5872	323.9475
73.5326	323.4708
67.7909	316.5841
65.9973	314.8973
67.0283	313.885
73.1014	313.4888
68.79	300.1914
65.8081	284.2706
65.0597	280.7123
66.9358	273.8775
72.1174	269.3329
69.439	267.2723
69.1415	265.3155
67.1364	261.1378
73.6671	259.5891
67.877	259.4836
73.0512	259.1322
70.4063	258.1913
65.4433	255.0891
73.0844	248.1013
65.7697	247.3296
66.3735	236.4494
65.932	234.4747
72.8698	228.4791
69.6949	228.3829
66.6204	227.1677
73.8445	223.6021
65.756	222.7312
72.0112	208.9975
74.7032	208.0623
73.0016	203.3189
71.4748	202.7859
71.5491	200.3936
67.548	194.3363
71.2106	192.6886
71.7733	192.0359
65.1898	191.1951
70.1589	181.9906
69.8829	180.8082
66.3248	172.0608
68.2658	170.2263
70.8561	169.811
73.4746	167.9358
67.292	166.559
65.7709	157.4764
71.5339	153.6517
72.6945	147.0837
67.8266	138.3078
73.6098	133.6036
74.4921	131.0758
74.4679	127.9605
70.7405	126.2526
68.8639	126.1403
69.6497	124.9336
65.5702	123.7935
66.1162	116.1029
67.0952	115.9159
70.3765	111.9926
71.7533	110.5589
68.0224	110.3037
65.1514	108.6827
73.8704	105.3655
68.4944	100.8369
66.4409	97.6724
66.7659	94.5577
73.8375	94.2408
73.9584	94.0946
65.8884	92.9062
67.5673	87.8457
74.8383	86.445
71.5574	85.7673

70.7309	83.0045
73.862	74.4521
72.1912	68.1741
74.4908	60.9412
67.4087	55.868
73.3586	51.9377
66.5348	50.8325
71.3984	45.8678
74.8515	43.0474
70.8744	40.6419
72.4576	34.6658
72.0777	32.7872
67.3564	32.5218
71.0427	23.2077
72.2622	13.5522
65.0175	11.5509
73.9764	5.8531
74.8153	5.2454
66.1958	4.909
72.9587	2.6523
69.9693	2.5164
84.7273	3.3152
82.1257	3.4067
84.0703	6.8473
76.0518	10.4815
80.3956	10.7329
84.6839	11.656
75.1744	11.9111
75.8367	12.3825
76.8104	13.1768
82.8982	15.7528
76.5531	16.6434
83.8854	19.2585
79.1387	21.5959
83.4412	23.3705
84.9279	26.9172
79.2444	30.3822
77.2257	32.8212
75.8337	34.0783
78.2702	35.3175
80.5266	38.6324
79.0046	41.6672
81.2132	42.9635
75.409	43.7015
82.1164	44.6968
77.5911	50.0134
78.3861	51.1357
79.8585	52.5798
77.0638	54.0376
79.2944	55.9236
83.2001	55.9667
84.664	57.2307
80.3643	68.7995
75.7308	71.2968
79.1169	72.7008
83.1173	76.4982
82.0319	77.672
84.5061	84.724
78.0443	85.3286
80.9081	85.9929
81.1877	86.1771
77.2334	87.0198
79.9635	93.8109

78.0332	97.6573
77.1217	99.5151
83.6498	101.4687
77.0421	104.7828
81.8662	115.0009
77.6961	118.2785
77.5034	124.7602
78.903	124.8695
78.0761	125.7278
82.0559	125.9893
79.2772	129.3058
77.5929	129.339
81.7658	129.4258
84.7748	130.6301
80.7761	131.3481
75.9738	133.008
83.8066	138.7906
84.3119	139.9853
81.7598	141.4922
78.8515	153.571
75.3377	153.645
84.7309	154.4507
81.3705	157.8307
75.3911	158.9842
75.2929	161.585
76.7818	172.1891
75.9624	179.8513
82.6557	182.9386
82.5001	187.7654
84.5803	191.1848
81.6443	198.0726
77.6998	206.05
76.1947	213.4295
82.1364	215.6555
80.7335	216.9319
79.5243	217.2557
82.2428	222.5629
77.0622	225.0287
83.4133	233.4442
82.6479	234.333
80.2427	237.7668
78.7362	240.8654
84.3321	248.0942
84.7095	248.2319
76.2154	251.2606
80.3151	252.5815
80.3431	252.6506
82.7123	252.7902
83.3995	256.0572
84.1889	257.2142
77.5575	266.1751
83.972	270.0594
82.1331	270.1191
75.8409	271.7868
84.5808	275.6368
76.6038	277.4991
84.4992	281.3666
83.924	282.7824
78.444	288.71
83.2741	290.1692
76.3967	293.0689
84.3354	293.4028
78.3646	295.2001

83.5142	296.9617
79.9411	299.2303
80.6378	303.0296
78.9935	307.6199
81.5016	312.5475
79.4357	315.9662
77.4555	325.112
76.1071	325.539
77.003	326.8096
75.907	328.9998
82.0484	337.0363
82.7043	337.8704
77.9014	339.8438
82.2079	343.1515
82.4156	344.4149
84.7175	346.5043
83.6734	347.0113
81.3806	347.9414
77.5284	349.3783
84.7895	354.1603
75.2123	361.9823
83.3633	362.7876
77.9592	364.7752
83.0909	368.648
75.8985	374.0857
81.0959	377.1871
79.1953	378.6878
76.5646	379.0456
79.7661	379.5761
84.9665	380.1331
82.0597	383.9017
78.7882	386.1311
83.7994	387.7258
78.1627	387.933
81.9376	394.0525
75.4009	400.8131
81.6318	403.7432
83.8741	404.5017
84.5193	410.5967
81.6235	415.3849
82.4988	415.5238
77.6334	419.6462
80.9964	426.0094
76.9371	427.1987
80.309	430.3792
80.501	430.5912
79.4875	433.3201
81.7647	437.3837
78.2908	440.1514
84.5345	441.7042
84.4721	441.9019
80.0882	445.7246
76.4736	447.8037
80.4144	448.935
80.6978	449.4171
79.1863	456.6312
76.2943	457.0585
80.9631	459.5241
79.8028	460.9421
79.4911	463.1569
76.4372	464.6886
81.216	475.6535
81.9854	484.72

75.1345	490.1101
80.3379	491.356
80.3786	497.5817
82.1909	497.732
78.7445	498.0257
79.0523	499.1432
79.0177	499.9235
78.8625	504.1173
75.9355	506.9398
75.3092	506.9789
75.2975	509.0782
76.7533	509.9312
77.8279	510.2953
78.5405	515.1017
81.3565	516.3897
79.3248	516.4386
75.5576	516.6948
75.3455	518.2834
79.0664	527.0192
83.5603	528.51
82.1409	529.4998
76.9148	532.4437
79.6369	537.1543
76.8132	538.0986
75.6394	541.2926
80.5943	564.118
77.7133	564.2615
75.0035	564.4721
76.3382	565.1727
76.9525	579.7306
82.3727	580.3359
81.3764	581.8988
79.0916	582.5246
79.0098	584.0448
80.3431	584.6398
84.079	594.0429
81.4553	594.6347
75.8436	599.5771
77.1932	603.3721
82.9711	603.6085
80.0309	604.4767
87.1928	609.8612
85.9492	605.302
90.8759	594.6581
85.7201	593.2922
94.986	588.0331
88.1044	585.7748
92.6293	582.4664
87.8715	576.7351
92.6583	576.2841
94.5415	572.9636
90.7754	571.281
93.8577	570.6365
86.0607	568.8116
89.0778	567.3012
86.3088	566.5362
91.4051	564.8341
91.3553	563.5742
92.4061	563.0769
94.8898	562.4332
88.7823	557.0047
89.6899	556.383
94.6509	555.9957

88.5898	554.5265
89.9707	554.2774
90.8782	553.2702
94.0656	552.4906
91.6511	551.5017
92.6432	548.6944
93.2482	547.5734
93.7716	546.4229
92.6922	546.3859
92.4337	546.334
94.9969	544.4958
93.8924	531.1504
88.0388	528.1732
85.5758	527.7349
89.4052	523.4342
89.5428	519.6681
86.5634	515.1041
92.254	514.6033
92.5468	512.1162
90.975	509.7509
94.7527	506.1004
93.9591	505.7343
87.2429	499.4462
91.9828	497.9327
93.579	496.0533
94.8917	489.8027
88.6271	474.7063
94.1179	472.5556
85.764	472.457
93.8242	467.261
94.0845	466.1694
91.2078	465.9549
92.2181	462.6463
88.5719	462.5576
86.9606	457.3086
94.0939	457.0819
92.1093	457.0744
92.8236	455.0123
85.9434	447.5319
86.8424	441.6672
89.5213	440.4094
92.8304	438.0367
90.2479	437.0931
89.4398	433.7165
94.7513	432.9207
88.3278	432.4232
89.2959	430.1956
94.7584	426.5407
88.7614	409.044
89.1571	405.513
90.4382	398.5607
89.9519	395.8166
88.8875	390.0306
94.5973	388.9987
94.2288	386.5653
88.2293	385.4993
89.7574	385.0147
92.6862	380.1724
85.4556	377.9247
94.8684	375.0104
86.2283	374.6893
92.8154	367.3327
86.1259	366.6068

85.301	365.2845
92.0106	364.3706
90.1656	362.1553
87.1714	358.6844
85.9798	354.3541
86.4426	352.0978
94.3387	345.7081
90.1908	342.1955
85.0425	341.9241
86.0012	341.9041
88.3629	339.5479
90.849	336.269
86.0067	335.7224
93.6763	328.8219
87.5583	326.7381
90.4244	320.0489
92.286	319.3903
93.132	316.8516
94.4761	315.8891
89.8032	314.5292
87.1338	313.6308
92.1946	307.5336
91.8767	306.3153
89.6763	303.1788
92.854	301.2221
87.2959	296.5783
88.901	290.7379
93.8855	289.1025
92.5318	288.1339
94.3684	286.8686
93.0023	284.7881
89.6916	284.031
93.9337	281.8546
94.5363	277.1868
92.3118	271.6924
87.8828	271.2864
86.0216	270.7095
92.3597	265.3621
90.602	261.8162
91.025	257.5441
91.1834	257.3625
91.5471	252.2994
93.0106	252.1994
88.2938	250.4388
92.8509	233.1159
94.6686	232.1361
85.4933	231.8786
87.9368	231.6877
91.2125	231.5966
86.4145	224.8026
88.278	221.1612
88.7279	218.4938
93.7423	217.9928
85.6576	196.6951
90.8714	182.3081
92.5307	177.6137
92.7223	176.4147
92.416	171.6287
94.4664	169.568
86.0828	168.0929
90.2994	162.5521
94.5487	159.7515
90.0428	156.0592

89.4164	152.7343
87.2201	145.1767
89.3139	141.6906
92.1282	138.7126
94.7353	134.1878
92.2067	132.0429
92.383	129.5694
87.6416	128.1265
90.666	125.7123
93.8528	125.0333
93.2075	123.4317
93.7364	121.4756
91.2259	117.6076
94.7931	110.6188
86.1771	109.6566
87.7434	101.183
85.3335	89.0568
93.53	87.9734
90.0315	84.1834
87.4781	77.8761
87.1913	76.4296
93.6803	74.1569
94.96	72.7303
92.7135	72.3644
86.5993	69.3099
89.1412	67.6706
86.3603	67.0877
93.8839	63.9871
87.3017	62.8622
92.7283	62.6484
88.9787	61.2321
86.0885	53.5944
93.8794	53.5491
86.1333	53.1694
90.0268	52.1825
94.8743	49.3566
85.6982	48.7267
86.5183	46.8788
89.5456	41.3015
88.3114	40.4572
90.7923	34.052
86.4116	28.0468
89.666	26.8106
87.2432	24.3492
93.5609	19.4731
92.7265	18.3026
89.2642	18.0844
87.6948	10.0218
90.0907	8.9413
89.1883	5.2157
90.4617	4.9409
91.7307	0.741
87.1894	0.0741
102.7939	0.7087
100.5377	0.995
99.7233	1.8936
103.2935	2.2315
101.7974	6.8634
98.4838	10.945
97.1347	11.8209
96.0164	12.2005
102.7259	18.5415
100.9977	19.4306

95.8709	19.9607
103.1733	32.0418
102.3654	38.4669
97.1489	44.496
96.7587	49.1782
98.8607	49.5985
96.4914	50.2038
95.4506	52.0537
96.4701	53.9456
97.8246	55.1197
96.8848	57.4829
101.7432	63.8858
98.2076	65.8815
104.2302	68.7073
98.5842	68.9286
95.0117	71.7654
100.3626	75.3344
103.6553	77.7424
104.4672	80.0783
104.1414	80.8748
103.9878	83.5681
100.4048	84.8634
101.2189	88.2077
99.7032	88.6886
100.6531	90.8843
96.7361	92.3478
100.1328	93.3671
104.4982	93.9682
95.4902	95.642
100.2181	96.2808
97.4867	106.579
104.3806	107.6606
102.6046	108.6379
101.9385	109.2798
99.4243	110.2744
98.0327	111.9898
99.8458	120.5078
98.246	122.2819
95.2387	124.7318
101.5127	128.8914
96.4007	129.5767
99.8729	130.3171
98.4667	136.9985
101.0606	139.1532
99.7965	139.8747
96.0516	140.384
96.5226	156.3321
96.8494	157.3587
102.5842	162.2672
103.9317	167.9655
104.5005	171.6861
98.2106	172.7855
99.6935	174.6964
96.8424	174.8259
103.2547	177.2929
97.421	183.9547
101.5681	184.156
100.9566	188.5934
97.9189	199.154
104.3161	202.6664
97.6373	204.4295
103.2983	206.1866
102.2857	207.1567

104.0503	210.5893
103.2273	213.1903
103.3727	215.1346
103.973	217.715
103.6925	221.4473
102.7203	222.0006
96.2938	225.2694
96.1378	229.4535
95.2803	237.3899
104.0475	237.5105
95.3662	237.6604
95.0324	240.1118
99.4105	240.6869
104.5513	242.8608
103.2688	243.9048
97.2667	249.4174
96.8174	253.461
103.7334	258.5357
95.8126	260.1559
99.4524	260.9296
103.6164	262.6339
95.2839	264.0376
97.7129	270.0426
96.2523	270.7778
95.1	272.0472
96.6472	273.6643
103.1024	274.0312
95.4631	279.1176
96.645	280.3108
95.5858	281.1804
104.5046	282.218
99.8506	286.2255
96.5119	286.501
99.0243	288.3868
98.8406	290.6011
96.0985	292.3178
95.2928	293.9895
104.6565	297.3947
104.5861	302.577
97.4313	302.9321
96.7048	307.6312
104.2976	311.3924
104.7632	316.9677
102.9477	323.1018
101.1039	325.5163
104.6415	326.8724
99.0956	330.9855
101.0946	331.3329
96.3662	332.4415
97.8415	337.9129
102.6997	338.0165
96.6164	339.003
101.1177	339.1833
101.1226	341.4702
97.0549	342.0561
95.2835	343.856
100.3244	346.5512
100.6841	356.9686
103.4852	358.5591
102.1419	361.1383
103.5743	366.9112
98.0644	370.8967
95.3594	371.5283

101.2717	375.6445
101.2108	375.7087
95.7084	378.8898
104.2162	390.6523
100.4147	392.0105
101.696	394.1013
100.5488	394.8488
96.7047	406.3637
103.6054	409.3843
99.1631	411.7765
99.9411	414.0506
104.2521	423.2101
99.3168	429.0608
103.963	429.2462
103.7736	431.5104
101.6202	434.2976
104.2767	435.0533
103.3744	442.9676
100.9385	449.2392
99.0181	454.5437
104.5377	458.9236
102.5465	460.7237
95.0558	461.4091
97.7345	471.0925
103.4674	476.0697
100.8295	482.3269
104.351	484.4159
103.7526	488.1204
100.0269	489.1408
100.8825	491.4301
95.5031	491.7593
102.6299	496.4366
101.6733	500.2458
103.0683	501.3417
101.5799	501.6268
95.216	501.7877
102.4339	507.2458
95.3644	510.4413
95.3835	511.7067
104.1551	512.7174
101.2021	513.6999
96.6988	516.7931
102.6831	517.1625
103.3298	528.0483
100.7577	531.7045
103.7382	533.4432
98.001	543.1255
95.6236	543.1528
101.5915	544.6315
103.0583	546.5256
99.0497	547.7282
96.1857	549.4706
95.2602	551.7794
101.107	553.6926
101.9941	555.452
96.2989	555.7855
99.2025	558.3987
103.3039	558.7618
95.1804	576.1043
97.3684	582.3874
96.4872	586.0998
101.3838	592.5951
102.2251	598.5525

97.8835	606.3941
95.9898	607.9832
114.6641	604.6678
112.8541	597.7435
109.6891	595.703
111.5326	592.5358
107.3945	592.4573
111.6467	587.7103
106.749	582.0477
107.5943	579.3117
113.5823	578.6405
112.7823	576.4662
113.3019	576.2382
105.992	572.8488
112.8464	566.5386
111.2719	566.418
109.3235	562.9782
114.8926	560.7889
108.537	554.1967
111.7817	551.4805
111.2237	543.8893
106.4682	539.3653
113.7196	536.5611
108.2911	526.7615
109.7424	526.18
110.5416	519.4415
105.9597	518.9773
113.8844	518.6806
107.2181	516.1229
113.0508	512.4923
106.9719	512.4114
112.6562	512.201
111.6896	509.9928
112.9831	503.2694
105.1625	500.8365
108.647	500.3326
112.4228	494.9166
107.6971	492.9252
108.5907	492.4061
109.9795	492.3815
112.6533	491.0207
113.0667	486.4822
108.9296	485.9886
111.0331	484.8219
114.7631	481.3524
112.2366	481.1535
112.4535	477.0099
113.9558	467.6036
111.8166	466.5866
106.0002	458.8437
107.8337	456.885
105.8697	455.4913
112.9683	454.5689
114.4598	450.8251
105.523	449.188
106.9275	447.6566
107.7699	443.5714
112.3345	442.0856
106.1369	439.8711
113.7522	436.8164
114.088	434.9978
105.0515	433.2347
105.0841	431.2517

108.0995	429.7126
111.7438	425.1184
108.2425	420.2352
109.8738	417.4264
109.0284	414.8901
113.1354	411.3585
108.3134	405.5858
112.7127	404.2816
107.3643	392.6825
108.7659	392.2919
105.1331	387.4906
107.1361	384.0263
106.2758	375.9883
110.939	375.2567
114.5144	374.0835
114.7211	372.625
106.5682	369.6563
113.5149	367.3275
107.4264	364.195
106.8693	363.3924
110.8712	362.9298
105.7518	362.7884
109.4376	362.1633
110.6055	361.7906
112.5476	359.0315
109.5419	357.0741
114.8465	356.1511
106.5284	352.074
105.4817	351.802
113.3097	348.6875
108.0424	337.4342
114.3406	335.05
112.9639	334.4527
114.552	331.8954
114.9233	329.8826
110.399	329.7439
107.0154	329.5669
109.7053	328.7777
109.9447	326.6032
112.3737	322.7932
111.7486	321.4807
112.2736	321.3257
105.1327	320.7319
105.6683	313.6836
107.5594	311.4337
112.956	310.0689
107.8355	309.528
108.8195	307.5823
111.568	305.9591
106.3952	304.9796
111.3125	303.3963
108.1903	300.8796
109.3633	299.4519
111.2396	295.2371
105.2478	292.0208
111.074	291.1207
112.4637	288.0967
108.4273	286.4438
105.7553	278.9516
110.0891	278.4085
110.2736	273.0125
110.7504	267.3851
108.1831	264.9347

107.5543	259.4929
112.1594	258.443
108.6966	253.1517
109.437	253.0518
113.2167	251.8592
109.0108	247.9752
105.2976	241.8243
111.7044	241.0398
105.5153	228.795
109.3309	228.2933
112.6873	227.8681
112.5753	225.3692
109.7282	222.7988
107.6353	220.4644
114.9967	218.3642
106.7125	215.9081
105.7881	213.6492
107.3664	205.0395
106.2897	205.0267
113.0225	203.7796
114.4035	199.2552
114.0005	195.5526
107.1049	186.5752
111.1773	184.42
106.6096	184.0591
105.536	181.8601
108.9349	174.5349
108.54	173.7735
108.423	173.2418
111.2067	169.9074
105.7313	164.4585
107.3424	164.2428
114.6854	159.4093
105.773	158.6345
113.8263	157.1796
114.3438	149.3501
107.0898	146.7878
105.7837	145.2085
113.2039	139.5066
106.9257	136.1826
114.4479	134.065
108.5575	133.7896
111.791	133.4698
112.4505	133.04
110.7001	132.5107
110.7939	131.0287
111.0018	128.7293
113.9913	125.1968
106.0835	124.5382
109.7615	124.3636
110.6843	123.8593
113.4081	123.8267
109.7829	121.3422
112.9853	118.9826
112.1559	118.7904
106.1229	115.125
112.8881	114.1693
112.7408	113.7622
108.5621	112.6211
105.9958	111.1159
107.158	103.9626
108.1666	103.9148
112.503	101.485

107.9439	100.523
111.2864	98.7734
109.106	92.129
109.9175	84.9036
113.296	82.9014
107.1663	80.4301
105.3201	79.4432
107.021	77.0932
108.3926	75.6239
112.8885	71.4058
114.4426	70.9977
106.0035	69.7713
110.0293	68.5946
112.6854	63.8714
112.4168	59.1021
111.2684	58.5967
112.2818	49.1342
107.3898	48.4128
110.0266	41.4008
114.9647	32.2481
110.1839	32.0131
108.4275	29.7011
110.7463	23.0177
105.1908	21.3816
107.8176	18.8376
111.938	18.8326
106.0231	17.2356
107.1322	16.6687
107.5761	15.9164
107.7397	13.947
113.0239	8.8115
114.0265	0.5502
116.0622	0.2134
117.2184	1.96
122.4086	4.0565
115.657	4.9551
116.1857	5.6468
118.8854	9.3288
120.1916	12.9621
121.9625	17.9556
116.5978	22.6356
119.6626	24.11
119.4509	24.4396
121.7245	26.2212
120.4273	26.4321
123.1214	26.4722
117.5873	28.0677
119.0579	33.78
123.1362	35.099
123.8761	35.7517
118.6564	37.3051
123.9323	38.408
116.4212	40.8307
120.5213	42.2045
121.2191	42.4039
123.6856	42.7373
120.3763	44.6987
124.1695	45.4898
115.041	47.7904
121.8994	49.6774
117.0485	50.9075
123.6813	51.5392
116.2	63.2376

124.0288	63.8657
121.5465	66.1755
122.0092	67.779
124.8955	71.859
122.1633	72.3639
115.768	72.5316
124.1369	72.5385
123.6285	72.6816
123.4926	74.8345
117.5815	80.4248
119.9664	81.9756
122.7876	86.5322
116.4734	86.6122
115.9808	91.1186
123.3807	92.0991
124.4571	92.1505
123.2338	95.3458
118.2591	101.5186
121.9301	105.64
124.7712	109.1989
117.5983	112.9453
124.5	113.5224
118.6296	118.9371
115.996	120.8725
120.6956	123.5344
124.7411	124.021
115.8608	125.5144
124.1037	127.7871
117.0384	130.6022
119.488	134.0593
122.4367	136.2316
122.2132	139.9556
123.2233	141.1138
120.6399	142.4468
115.0541	151.1075
122.5838	152.8134
115.9914	153.6164
122.9955	161.9656
124.2646	164.7388
121.1002	165.7254
121.9604	169.157
119.1699	170.1439
120.9333	178.9994
117.8491	179.9549
120.6537	182.3124
120.4758	189.464
124.9886	200.2571
119.2764	202.3
122.349	202.7694
116.9378	207.7707
122.4035	208.2304
119.9076	209.4767
123.3343	209.7856
120.2026	211.3365
117.6616	214.9321
124.0591	215.6768
119.2171	221.3281
116.9511	224.1321
122.7781	224.871
123.9695	226.5312
118.4493	228.3955
121.0586	243.6491
122.2306	245.7307

124.8674	247.3662
116.991	249.4462
124.7378	249.5708
115.682	251.9493
120.8225	252.9954
124.6886	257.099
115.3007	261.4182
123.9715	262.7674
122.6744	266.7713
120.7151	268.7428
120.6409	275.8236
121.0752	278.9686
124.0342	280.8967
117.2237	285.8904
120.022	287.9244
116.2469	290.3109
123.5332	290.3559
118.2755	293.216
119.9458	297.8338
121.0652	298.4932
124.0343	299.6121
116.8204	301.2313
118.7025	302.7405
116.9464	305.7389
118.7174	305.8343
122.7441	307.0627
119.2317	307.9731
119.3329	311.4254
115.179	313.2763
121.8849	316.2545
121.3129	317.1522
116.6251	326.804
117.4194	331.5372
122.807	337.5361
118.5317	341.2665
120.31	342.3831
117.7304	347.1876
117.3913	350.959
115.715	353.1331
122.0033	355.58
119.631	356.8337
119.5576	357.5763
124.5648	361.3586
118.0387	367.997
123.828	368.0931
117.1008	369.1464
118.7213	369.479
116.664	370.6132
123.0364	374.1154
115.8518	374.5113
124.9298	377.9117
123.3379	382.8099
117.5691	385.0368
121.8071	388.7576
119.4151	388.9148
120.6069	394.2294
117.5179	395.8962
121.814	396.9574
118.1589	402.9919
118.8827	406.3052
117.0352	408.6432
124.2191	409.7918
119.4746	411.5437

115.5097	421.0829
124.533	422.2828
117.9466	424.0144
121.918	431.5914
122.7299	435.2129
117.6353	441.2016
123.8703	444.3103
122.9647	449.2781
123.2029	451.578
122.5044	451.6309
123.8167	451.8358
118.3481	457.9259
122.7357	461.6486
124.1336	465.1901
124.4891	468.9363
122.009	471.7667
119.5481	478.5183
117.4797	482.9744
118.3286	484.0199
122.973	490.9818
124.946	494.9063
122.3079	500.6115
123.8236	500.804
122.1188	505.3582
119.2825	508.8691
121.3955	513.8901
122.615	516.4792
122.9437	523.3013
121.3178	528.8486
120.9338	543.7335
119.6955	545.1401
120.5425	547.23
122.424	549.3454
117.912	550.4561
119.4726	557.7841
115.5212	559.108
119.5147	561.3234
120.7622	563.1798
116.5288	564.5567
119.6079	564.736
123.9302	564.805
116.275	567.9801
119.0886	575.2395
119.1826	586.6813
117.5134	587.1812
123.9843	588.8438
118.8906	589.6285
118.4781	590.9302
124.3667	591.8627
120.0796	592.9205
120.8025	599.1595
115.3989	604.6707
124.9951	607.2707
122.9563	607.2967
119.6744	609.404
133.337	609.3209
126.7509	605.3442
126.1571	602.3256
130.695	600.9144
127.8283	598.2095
131.4444	593.6399
125.8929	581.802
132.7524	579.7262
127.0578	579.5005
130.1239	576.7858
127.2947	576.6517
131.0108	574.7666
128.1562	570.8968
130.1816	568.1456
129.4359	564.3009
130.5888	563.2899
127.7002	560.6551
130.7777	558.8437
129.8819	556.476
130.5086	554.2506
129.9864	553.6803
133.8846	542.1031
127.8225	540.9207
127.5183	540.2379
132.4818	534.7476
127.2989	534.7136
126.5937	518.2343
130.1256	517.6348
134.4907	510.4601
131.0923	504.4165
134.0401	501.1235
133.973	494.4351
125.1953	492.7535
127.6036	490.4233
126.9643	485.73
133.8075	480.0126
133.542	478.85
132.6326	478.5657
134.2633	475.1368
132.3565	474.237
134.3742	473.2591
125.2032	470.1958
129.6241	462.0264
129.8898	459.8439
128.8201	458.7635
127.5796	457.4514
125.0008	454.076
130.771	453.9677
132.4574	450.7737
134.7711	448.1325
131.9895	446.2433
131.8827	442.5703
125.65	440.409
126.789	436.3698
134.701	436.0117
134.8908	430.8462
131.0889	425.0894
134.774	424.8134
129.319	423.4893
126.438	423.0603
131.0714	419.2434
134.6486	417.3005
132.4878	415.6257
133.0435	415.0839
126.5861	414.3675
127.9397	414.3564
132.5084	413.956
125.094	411.5299
131.4576	398.1528
129.1648	397.5856
133.298	396.3856
130.5029	395.9263
131.4925	393.4623
128.7111	390.7155
127.6554	388.3671
131.4679	387.8756
126.1234	387.8317
131.5672	386.5527
129.1554	385.9925
132.5448	382.13
127.3262	379.756
134.3525	378.5653
133.0963	375.994
133.2105	375.6323
129.6614	371.813
133.0066	371.0968
134.6374	370.1415
128.5753	369.7977
129.1547	369.0187
126.0577	368.2606
125.7879	367.4538
131.0869	363.8402
130.2048	363.2619
131.7161	361.2993
132.5808	360.1163
133.8592	358.9738
130.2709	353.8863
131.9794	345.2684
130.1959	343.7613
130.6444	339.2939
133.0251	338.1099
129.5246	334.7198
134.2198	330.4239
130.9484	328.7475
133.7723	327.6798
128.4532	313.3359
132.6547	309.2007
134.9574	305.6455
127.2925	303.3501
133.2349	302.4912
125.0718	298.154
132.7363	295.6247
132.5747	294.0014
128.0088	292.4112
133.0448	290.6522
129.0025	288.2547
125.7189	287.6751
127.7454	286.3072
130.313	278.5844
134.5413	276.5581
130.2354	273.1139
127.2656	265.7315
128.8698	264.6877
125.1112	264.28
130.394	263.478
133.5206	258.2664
133.6093	255.7515
126.504	255.7219
132.6233	254.1327
129.9277	253.3319
129.1917	246.9122
132.6505	245.8127
125.4504	241.6004
133.5947	235.2173
126.6015	235.1338
133.0085	234.33
128.6238	228.0318
127.2956	225.3089
125.3172	221.6046
130.6748	221.2569
134.7737	217.7801
134.9852	215.3158
126.285	213.7891
130.2675	208.7409
125.0177	206.8076
125.3909	205.9778
132.281	204.0116
127.4673	203.5269
130.7862	203.0196
129.9388	199.6612
128.3404	192.2704
125.6931	191.6726
133.7756	185.6343
129.9112	176.8292
125.5094	176.6523
134.5296	169.2691
132.5612	167.444
131.7715	164.3756
134.1107	164.1183
131.5567	157.1965
125.3246	151.7406
132.2412	134.6286
127.6309	126.6958
133.8256	126.041
133.0411	124.0117
127.8905	121.5007
127.3288	113.9664
133.9092	109.3245
125.9317	109.2971
128.1908	106.2542
132.1511	101.9964
132.6403	99.2318
125.7231	99.2148
128.4175	98.9191
125.0305	95.723
127.9925	94.111
125.3277	91.1066
125.6213	88.8076
125.8172	85.7029
126.6925	83.0075
127.5902	74.692
129.8527	73.3057
132.5976	70.2674
132.2109	69.704
128.9865	68.7563
126.5819	67.4682
134.1192	64.6625
130.412	63.5383
131.1237	63.1512
126.8779	60.6905
127.5197	56.5661
128.2398	53.3272
132.9635	50.5352
125.0412	49.8662
132.9976	47.0463
132.9583	45.378
129.2738	41.7444

127.1585	39.0597
126.7614	38.6691
130.2533	38.5477
125.5687	36.9812
134.7262	26.0867
125.6864	25.6634
126.095	13.6146
128.9711	13.3832
129.8331	8.2917
126.4148	7.6166
128.4896	5.985
127.9516	3.5342
129.4472	1.6966
129.5193	1.0922
144.1541	5.2317
138.1081	11.6747
137.2592	14.4724
137.5984	17.139
142.1608	22.2984
142.288	22.5535
138.5665	24.1023
138.0085	26.2152
140.1839	28.8351
144.8277	31.8628
144.8546	33.1398
135.1975	35.1641
144.5202	41.76
136.6473	44.4281
144.8282	49.04
140.6881	49.3146
136.0769	50.8454
138.9805	58.9363
142.8975	61.3615
136.0398	64.1052
141.9845	66.2357
140.1604	69.8951
135.1883	71.5833
141.2977	71.7554
139.9475	71.9195
139.2991	74.1181
136.7615	74.9353
144.336	75.5089
140.9887	76.1918
136.1518	77.3506
138.8369	82.0644
142.3837	82.5243
137.7014	82.6256
140.2519	84.4727
144.8901	84.8396
136.957	86.5983
137.3635	86.7593
137.483	89.0504
136.4979	93.2402
144.2843	96.8056
143.5027	100.0277
135.2186	103.334
141.7837	109.4349
144.8378	111.0757
136.5962	113.3493
137.5377	113.943
140.3569	114.0993
139.272	115.3623
138.1614	118.7823

139.6526	123.4007
142.1896	124.1838
143.2724	129.8316
137.2046	130.558
139.4936	133.5947
142.7706	134.5801
138.2744	136.0419
142.9747	136.0702
137.0953	136.6647
141.5545	138.618
139.657	138.7451
139.2933	140.3541
142.5094	140.9019
138.3804	141.9793
136.4018	143.8398
136.7537	145.5264
135.0837	147.5954
141.9516	149.0404
144.9953	152.6259
137.3626	158.2547
143.8923	158.5252
136.9635	162.83
139.2221	163.1491
137.8677	163.7305
141.2375	168.686
139.9677	172.744
136.1612	173.7658
144.8767	176.3523
141.7736	176.4662
144.5319	180.6691
143.6387	182.4474
141.2528	184.8472
140.5588	185.4694
136.7853	188.5036
135.9492	192.5494
144.1215	193.2424
139.0171	196.9596
143.0504	197.5221
142.8428	198.6763
135.4919	205.4736
138.1649	210.169
140.947	211.0632
139.4394	214.1425
144.0715	217.8344
138.0192	227.4716
138.8383	228.4772
138.668	236.2513
137.9023	237.408
136.1549	239.2152
142.342	239.9743
142.0768	242.3491
142.7937	242.3954
143.1961	242.7128
142.1815	243.5988
141.3733	243.8613
137.3415	248.4809
142.2161	251.9269
135.6709	254.6779
136.7856	255.0584
140.0818	255.2373
141.8563	259.7575
143.0189	266.964
136.8748	266.9826

139.1342	277.9716
144.5567	278.4821
140.585	278.9425
135.4308	279.6906
137.9022	280.7065
142.9229	281.5851
136.5047	283.1812
136.8312	283.8713
140.9699	286.511
142.1621	290.346
142.1811	295.9666
144.1414	296.3393
138.7728	299.2589
138.9632	299.864
135.1641	300.7039
137.1136	308.7189
142.3913	315.0096
143.8158	315.8757
138.7525	317.1573
138.9956	318.2319
135.5734	320.7098
139.3582	323.048
135.0945	331.5475
143.0181	339.0151
142.6755	342.6646
135.8482	342.6827
139.9574	344.1639
135.1623	353.5342
143.6923	354.2733
138.6008	356.3975
143.7871	357.4109
140.2326	362.3907
141.5561	362.7489
136.7215	368.7774
138.263	374.3118
138.2943	385.1739
144.5664	385.4196
135.4821	387.4434
140.7736	394.2018
136.7625	394.876
143.7945	395.6775
141.7145	396.1284
139.1669	398.7529
142.7791	403.2855
139.9522	408.5365
143.8476	409.3458
142.606	410.5622
138.5786	411.1225
135.9352	420.162
141.5187	426.3586
143.2634	430.4985
144.1971	431.2335
144.4057	435.01
143.9047	436.7197
136.0419	438.9189
143.7025	447.5076
144.6205	452.8729
142.0627	458.7538
137.8066	458.9639
143.3852	460.0479
142.1704	461.8874
135.5467	464.473
137.5622	476.0045

137.1488	476.311
138.8117	477.376
136.5911	480.5832
140.8353	482.2511
144.5003	484.9876
141.0041	485.319
137.1024	485.642
135.4237	491.5144
142.3488	496.1648
136.0679	496.2291
136.6019	505.5813
144.0263	511.6445
137.2187	511.777
139.7755	512.1024
144.1384	512.1156
141.6347	512.2327
138.4432	517.5543
138.797	519.1097
136.6382	521.5831
140.7234	524.464
141.6755	532.8976
142.4044	533.8591
135.2641	535.4249
142.6363	535.5042
140.7304	539.4359
141.5637	545.3636
136.7297	550.5784
144.5901	552.9718
136.782	557.757
137.4182	558.5827
138.1124	559.1705
142.6732	561.1424
138.4381	562.6092
138.4668	565.3098
137.7295	575.2229
143.9968	579.6891
143.3837	585.8678
143.7717	589.3175
137.6073	591.2187
142.9199	594.5341
138.6513	604.3039
138.405	606.4136
143.6229	607.9258
142.135	609.1026
150.7277	609.8473
149.8939	609.471
146.6333	608.4691
151.283	600.8974
151.5962	599.8298
148.0634	597.8406
152.4766	591.8194
151.2167	587.9775
149.8091	586.1937
152.3376	581.3972
145.0193	571.2311
148.8138	555.4485
153.001	554.6552
146.4434	553.2559
154.4212	539.6666
148.8073	533.2334
151.922	530.9062
154.3271	528.7534
148.9015	525.105

150.9212	519.0233
153.5321	516.5182
147.7785	514.0213
150.1986	512.8072
146.3355	508.1173
154.346	507.0594
154.7292	504.0706
150.2921	500.105
152.494	495.2303
152.0349	495.0831
149.411	491.0503
145.6491	488.9003
154.6819	487.4934
145.0727	485.8805
153.3907	483.0734
147.4892	482.6975
153.9662	477.7402
153.379	477.5632
153.6067	477.0341
150.9878	476.0853
148.0852	474.6861
149.7208	473.6399
154.9522	470.3925
153.9342	470.0997
149.3537	468.2908
151.9503	467.4696
153.8101	467.0531
154.4252	465.6967
154.3226	464.8097
154.4652	464.7793
146.2334	454.9117
145.7134	452.4032
148.0201	445.3934
153.4029	444.8566
147.5008	438.6649
150.7168	434.9692
147.1264	430.1908
149.9046	429.0928
148.2664	427.1327
149.1754	422.2739
145.9203	416.0165
149.0487	416.0093
152.0099	411.081
147.0143	404.8198
150.1447	404.7369
146.3926	404.4383
149.1009	404.1826
153.3146	400.4197
147.3892	396.3863
145.5144	396.0396
150.0402	391.9756
154.6273	390.225
152.0414	389.4418
150.3014	387.0181
148.3046	386.8491
151.2125	384.9172
151.3258	384.781
154.9891	369.6393
145.5439	366.9035
148.176	366.4103
152.5354	361.7771
153.2794	355.8987
151.8816	353.81

154.365	353.5503
151.6961	352.2797
150.4604	352.2349
145.7579	346.5902
145.3918	345.965
152.8303	343.6515
148.0871	342.2587
154.0907	342.1366
151.7256	341.2861
153.2268	339.1464
148.2788	338.4621
150.7577	338.2331
152.1205	331.3856
154.2914	329.8394
154.7871	326.0906
148.6041	318.2585
151.1625	317.3812
152.7502	314.6267
154.8181	313.2807
154.1195	311.1635
150.5195	310.2302
153.6133	304.803
151.7362	303.3233
151.8544	299.4214
148.3648	299.351
150.5529	295.911
153.9405	294.0417
152.5079	293.6033
146.6672	291.5139
151.6134	278.2021
146.371	277.3621
153.072	275.9847
152.7747	271.7137
146.6673	270.4612
154.2147	268.8292
153.3832	266.8116
148.8758	261.7618
146.968	259.4208
150.6466	256.6932
154.344	256.4628
148.6495	256.2552
146.3806	251.8839
145.1673	247.9544
154.6992	246.967
148.6882	244.4808
145.0216	242.754
147.5846	241.0415
152.6535	240.6428
146.627	236.47
152.5251	236.0775
145.2769	235.4122
146.0448	234.8595
148.7193	233.97
147.4373	232.4342
148.8602	230.0966
150.4289	229.7284
150.0819	226.109
151.3354	222.638
153.5689	214.0411
151.0377	212.817
153.8919	206.1274
148.3419	204.8208
148.0107	204.7687

146.7117	201.598
146.2455	193.1278
148.198	188.7451
154.87	183.5993
151.5082	181.5458
152.2796	179.0648
148.5791	176.5539
152.7742	176.0782
148.108	175.7912
152.6966	173.6664
145.7653	173.3041
145.5524	169.6047
149.3601	167.5708
150.7996	163.7462
149.9541	163.7117
145.6473	163.4282
152.3035	159.5486
149.2677	158.5746
151.5795	154.72
154.7826	152.1734
149.7764	149.4239
151.5374	148.6003
149.1587	147.5782
147.3094	141.6481
145.4936	137.5848
147.0753	137.0677
146.545	133.7084
148.2044	132.8985
153.7519	131.8101
150.1718	129.9154
149.0201	127.3584
153.1418	127.2812
147.8483	126.7012
152.6834	125.5863
148.8954	119.4604
154.7948	118.9785
149.3133	117.5016
150.6692	113.8628
148.5804	109.533
147.4649	108.4571
153.5612	107.5607
149.0955	106.7696
154.5725	105.6453
154.97	102.692
147.3283	101.5628
148.2428	99.044
150.9883	97.7476
145.4225	96.0821
148.7214	87.3467
147.01	85.5391
145.5803	85.0732
150.0712	70.9675
150.3687	65.5795
151.6485	64.8177
153.0597	62.714
154.0617	56.8225
150.835	56.4825
153.0145	53.6885
153.4168	49.1723
146.1181	35.1144
151.6745	32.1513
149.9198	28.2895
153.2747	23.6277

149.0424	19.1002
148.255	13.5839
147.408	11.3662
145.6106	10.085
151.3195	8.3353
148.1061	5.0602
148.4096	4.5723
146.587	1.063
162.8272	2.2495
158.7891	5.969
160.2028	11.513
159.0988	11.7657
160.901	14.9853
158.3678	16.0485
158.8802	19.9154
158.5874	20.4164
156.7107	25.6244
155.4055	25.9752
156.5592	26.4303
158.4956	29.3406
162.6524	29.8971
162.1818	33.1229
160.8111	33.2297
157.4892	35.6598
162.3017	36.9957
162.1898	43.1798
162.0629	43.7938
157.4796	45.0093
159.7622	45.1124
156.6596	46.6466
156.2246	47.5005
156.6265	52.2169
157.8109	61.7543
156.7634	63.1181
156.2394	66.8173
160.592	68.4574
157.6749	69.0881
161.6323	75.4389
160.9756	79.6307
158.931	80.562
155.5658	82.8035
162.1571	84.9519
156.8301	84.9934
164.6505	90.3882
161.9885	96.7197
156.5909	101.0547
156.9003	102.8206
159.1864	113.1546
160.6257	113.3578
163.1303	117.7618
155.4305	121.0368
159.1954	126.8739
164.7377	127.9617
155.9331	132.0882
156.3119	140.4649
158.8754	140.5927
162.3396	141.6162
160.4198	143.3776
155.3723	146.7181
164.9145	150.1763
162.2839	154.8338
162.5175	155.535
161.678	155.5747

160.0351	170.3483
161.1125	174.8941
157.6319	178.6568
163.7766	178.9959
155.5148	182.6535
161.657	184.3491
158.5551	185.4122
157.8029	191.9667
156.9659	199.8198
162.517	200.3315
157.6939	202.7582
162.7937	206.575
164.9467	208.2861
162.4735	208.73
159.2119	209.3382
163.0929	211.9207
155.2696	212.3625
156.0486	217.3845
158.9172	233.7091
155.6133	240.2657
164.3643	240.5396
157.7201	241.6546
163.9011	243.757
157.4981	244.3476
162.3851	244.6662
155.5078	247.6947
158.5349	247.9369
155.9672	248.4805
158.6901	249.1499
158.2075	254.4063
162.6519	255.0085
159.1441	255.1259
160.9072	258.5882
157.473	262.4112
164.9368	263.7106
162.2638	265.5105
160.1316	265.7595
159.6179	270.4823
155.0677	272.3167
157.0946	279.6307
158.1892	279.7534
158.0399	281.3139
164.3742	281.7647
159.3427	284.6704
161.2442	286.296
161.1781	290.7907
162.3055	306.0154
157.9232	306.2711
164.1029	308.5825
163.8256	309.6615
162.5618	311.6551
162.7134	311.701
164.0701	313.854
157.9513	317.6059
155.2287	318.6565
156.6597	319.9069
158.3844	324.9182
160.7962	328.2709
164.2053	328.3074
156.093	330.193
163.9013	331.2228
159.445	336.5305
161.7529	338.7965
163.19	344.7821
156.5765	349.5528
164.5366	350.9726
160.3638	357.4327
155.8374	357.6958
159.1023	359.3708
161.8913	362.004
160.9259	362.4747
157.1837	363.5671
158.6399	371.2864
157.4043	372.0931
162.586	373.3364
158.1801	382.4201
163.5273	384.1005
161.2561	386.7927
164.802	386.9909
161.7014	387.1183
157.3373	390.7318
157.0479	391.8012
158.6097	397.4264
161.8528	403.7939
162.5585	404.3783
158.478	404.9048
164.3074	408.4009
161.8984	416.5033
156.0084	418.7938
161.9469	420.9505
157.3967	424.4405
156.246	430.6269
158.7877	432.4449
155.5181	435.1854
157.9329	437.1466
161.681	437.9939
159.4029	440.1493
160.8021	441.4351
162.3102	442.3254
159.471	444.011
161.5468	446.9147
159.0462	449.0252
155.5979	451.0408
157.2249	451.6171
161.427	454.6779
157.1871	456.1223
158.8126	458.9607
155.4166	460.3273
155.5062	461.3005
156.7058	463.7593
157.6772	464.6721
156.8379	467.4306
156.7415	471.2366
159.6816	471.4066
162.5906	471.981
163.7628	474.9465
161.0085	478.4841
155.1729	482.6877
157.3111	483.0499
162.6653	487.5564
158.3113	492.2197
159.1965	500.0399
160.8006	500.3493
163.9069	501.8296
161.9244	518.3156
157.317	525.3441
156.6008	528.3579
158.9512	530.8566
160.5279	532.8476
155.8949	540.9057
157.6514	546.1743
160.5797	547.2081
160.4097	548.8137
156.736	554.6722
155.3817	562.7005
160.6761	568.8057
164.2186	568.9164
155.8672	570.5667
162.6829	570.7646
155.4084	571.6286
156.5038	572.0847
157.3483	572.204
156.6563	574.4704
157.9356	578.3028
159.2765	579.7089
163.7599	579.8088
162.0867	580.8806
164.2024	581.6239
160.4413	585.5836
161.5632	586.8084
163.1271	587.362
161.7454	591.3067
156.4648	599.333
160.907	604.3893
163.7224	609.3464
165.4989	608.4912
166.4332	607.479
168.122	606.9686
172.5948	602.8404
170.2719	602.6848
165.3237	602.6075
171.4696	595.5868
170.7063	592.182
168.1856	592.1811
173.8558	585.7508
172.2469	580.358
170.051	578.6405
168.3862	576.8718
167.7903	573.7717
174.1246	572.7766
173.719	572.2705
174.34	571.5713
165.0601	571.1612
165.9029	565.6797
167.9681	562.6429
173.9281	556.2187
166.6635	546.688
168.6683	542.2161
169.599	536.9755
171.4318	534.0468
172.3772	532.3441
172.4863	530.114
171.2587	526.5907
170.8093	524.5447
166.5741	522.3583
171.2985	520.9343
170.1392	517.4966
169.3605	514.123
169.1423	509.7858
167.5885	505.6021
171.0534	502.9948
165.0335	500.1672
168.4087	497.6968
174.2085	496.2738
173.3544	496.2043
173.2007	495.5444
169.6229	491.0123
170.2374	489.8348
169.712	488.7096
167.5774	485.706
166.6743	482.4723
168.2991	482.2271
170.433	473.0541
168.0334	471.7843
165.2034	469.051
170.5805	466.4267
173.5868	466.2004
174.1635	460.6305
166.425	459.7331
171.4362	456.2029
169.8873	449.2538
172.5053	445.132
174.3345	444.0323
173.8565	441.1193
171.402	429.6326
173.3827	428.8512
165.9793	424.6845
170.53	418.3146
170.9089	414.8866
166.6212	413.4925
171.3933	412.854
168.9109	412.6295
173.4453	404.3136
172.6178	386.9879
165.1146	385.0914
166.1712	384.8622
166.8749	381.153
168.4858	379.5636
167.6414	377.9771
165.9083	377.0273
174.0604	375.3581
172.0078	374.651
168.9897	368.5451
166.7029	366.3679
170.5925	364.7828
171.448	361.3507
166.5947	357.0424
172.6991	353.2751
171.8814	352.0127
167.7068	347.8046
167.5979	346.4123
165.454	342.712
168.8873	342.1832
170.7583	341.6924
168.9875	330.5684
172.7354	330.4309
173.1594	329.0022
172.6548	321.8494
165.2084	318.1902
168.7265	313.253
166.2416	305.6976
166.6574	304.9749

170.3241	302.3154
169.99	299.3425
170.7777	298.1822
172.4953	295.3627
169.5679	294.3465
173.8687	293.2339
173.552	285.4796
167.3532	283.9199
172.1584	281.718
168.0473	279.3204
168.864	277.1046
170.9659	270.3534
174.9773	269.9076
167.861	268.5398
173.9218	267.5242
172.7355	266.0497
172.4768	264.4081
172.257	258.8212
168.7279	253.355
165.1455	248.968
173.8257	245.7174
169.3995	242.7949
165.2144	238.761
172.5793	236.3803
168.9546	236.1954
165.1036	228.8616
171.1677	222.2564
170.9189	222.057
167.2122	219.8422
174.8942	219.6645
174.2693	217.2441
170.7507	217.2136
172.5961	214.0913
174.6625	213.5359
169.5875	205.6698
168.0526	204.0934
167.1244	202.4473
170.8311	201.3541
167.7005	200.8549
174.6738	187.1543
165.2088	179.2396
166.4242	176.2255
169.341	175.4147
169.8402	174.9954
173.9845	171.7631
173.1139	171.0685
169.1049	169.9906
174.604	167.0444
167.8198	161.3369
167.6699	154.7073
169.3277	152.4199
167.1286	151.7681
166.5888	151.6256
171.2635	150.9475
171.0121	149.2726
172.0797	145.6248
174.0098	143.2836
171.3153	138.0029
166.5279	137.7823
168.7352	136.2151
166.22	133.4325
171.5765	129.2507
168.1488	127.9234

167.5472	127.2085
167.3538	126.1599
166.6383	121.5288
166.637	120.7727
170.3931	119.3653
166.172	114.9803
171.8242	107.7432
167.7282	88.8446
166.7813	86.9939
166.6667	85.4078
169.7495	83.5572
170.1354	81.5524
174.8373	79.674
171.4809	75.5178
165.389	71.7015
172.3834	68.4597
173.0762	62.2198
172.8772	57.0112
170.6357	52.7483
167.8174	52.6465
174.7774	37.4653
168.2146	31.1541
171.1474	31.1322
174.6955	28.0596
173.1921	25.1966
165.6537	23.5515
170.7504	22.4845
174.9339	19.9138
169.7869	16.6421
170.3378	8.5007
169.168	7.3114
177.9039	4.1389
175.4222	6.488
175.5445	7.816
177.163	10.5837
179.083	12.7174
184.697	17.481
184.011	18.4681
184.7993	22.45
179.0545	23.699
180.6301	25.3654
181.6137	29.8443
182.8383	31.9501
181.9981	33.9032
178.6379	33.9056
177.5247	33.9109
175.5456	36.3207
182.8882	41.8727
178.9186	42.7404
182.3492	42.7843
184.0447	48.5273
181.2331	48.8938
177.5065	51.4327
183.1753	54.2575
178.4722	54.3737
179.6432	56.9853
183.5536	60.865
177.5108	61.018
182.3375	72.7824
180.7916	73.4832
181.6602	76.1936
184.3149	77.7799
183.4965	82.3993

177.3919	93.9291
176.3189	94.4017
178.6752	95.0596
175.1949	107.4329
179.105	109.3885
176.2034	119.5091
181.1882	123.1761
179.9253	123.9276
177.3975	127.9733
184.1312	134.3609
180.553	135.5928
180.078	143.2845
181.6849	146.0797
175.5572	150.0594
183.3829	152.8072
182.8667	156.2359
179.771	157.5428
180.5944	158.0582
177.6117	160.2138
183.1286	160.2593
182.6388	166.4622
181.1102	172.9651
176.5288	176.87
177.7601	180.0316
176.42	181.2248
183.9044	187.5025
175.4068	188.1004
183.5689	189.0091
176.8506	190.5916
176.0929	190.7548
178.7681	192.7085
184.3698	194.0921
183.8417	195.9527
179.5775	197.0136
176.0238	203.1526
178.7681	208.3519
181.6728	208.4312
184.0033	209.0523
176.2726	209.6889
182.2602	210.2233
181.3082	213.0779
182.5352	213.2277
184.1539	213.7723
179.2801	215.8334
177.1049	218.8025
178.92	220.0348
182.6579	235.3744
177.4718	236.5569
176.5078	239.5792
183.8718	241.5069
182.2069	248.3578
176.3547	251.4454
180.9547	252.4795
182.8853	255.2691
184.4404	256.2327
178.8001	256.2526
182.1003	257.0087
184.3318	266.8843
182.5913	267.5152
181.1334	267.5418
181.9825	268.8612
179.7554	278.2479
184.7729	278.2618

175.4436	282.1411
178.7664	282.9236
182.6376	286.3156
175.2773	286.5085
179.6531	289.7239
178.6248	295.0878
182.5758	298.3823
182.6373	301.6158
176.6555	305.8904
179.4878	308.1872
177.0374	316.0848
183.6748	318.0392
180.9185	322.1339
182.9139	323.4984
181.9606	323.8582
177.4101	326.7917
182.3156	330.7839
182.0398	334.248
175.517	339.0618
176.752	340.469
183.573	342.1487
179.1096	342.6032
183.9484	343.5065
175.5598	346.765
175.8852	351.6121
177.3592	353.1869
176.0377	354.175
177.3313	355.0941
183.0252	356.6629
179.0485	357.6091
181.7812	358.2652
183.3281	362.963
175.4529	379.0207
179.8254	380.0792
181.2663	380.7378
179.7978	384.2304
178.0951	386.2105
179.219	387.8017
182.9456	390.5168
181.0874	390.5782
181.2317	394.4637
175.5587	394.6354
179.4375	395.336
176.8072	402.5471
184.2478	405.6575
179.7621	407.069
179.1492	408.5123
180.1177	408.8529
181.1085	411.5045
183.634	411.9557
177.1421	412.6266
176.4318	414.6871
183.7589	415.6765
184.5644	416.7822
180.9826	418.8242
179.8694	419.1591
175.3394	421.0723
179.3979	423.7096
183.8064	423.8981
177.6072	428.4409
175.8834	430.1504
176.8548	431.6427
180.7528	437.5266

180.7632	437.83
177.9946	438.1112
182.8774	448.0694
184.4825	451.523
184.927	453.6514
179.7801	461.5908
182.2995	462.5418
177.5899	466.3476
177.6454	468.1235
184.5137	470.2251
175.6916	472.6944
183.1387	480.5199
180.8086	485.5066
178.8194	492.0068
181.6915	493.6803
175.331	499.3737
184.1496	501.5564
176.8498	502.4414
182.6575	513.5843
177.8914	520.7831
180.9472	521.5925
180.7638	525.9788
184.5494	526.3433
182.5693	528.0527
178.6437	528.6762
181.7333	537.9854
175.5415	538.8857
177.5285	539.8724
181.5874	541.189
181.9718	545.9115
175.0957	547.3695
181.9072	548.4726
180.9436	557.6414
184.9853	559.3628
175.3727	563.4062
176.1081	563.4157
183.5907	564.352
179.5651	567.2933
175.5443	570.893
178.532	571.5891
182.5345	576.7008
176.8113	581.0034
175.3691	586.4734
181.5895	586.5409
175.5811	588.7816
177.0216	591.9072
184.1754	599.0337
177.4957	600.335
180.6719	606.1395
193.0759	607.479
192.5557	604.1304
190.8423	602.8616
191.2311	602.4442
187.9013	600.1896
186.2641	599.1509
193.8193	598.8344
193.9964	597.59
191.8819	594.8248
193.3948	594.5885
193.9174	587.4515
192.0869	583.9866
186.2229	583.2448
193.584	582.871

186.9456	579.986
190.7247	577.8579
189.1587	575.2926
189.2174	560.0851
191.6785	554.2548
191.4216	551.4055
189.7328	549.8527
190.6021	547.4479
185.9467	547.362
186.8255	544.1149
194.6977	537.8207
188.1981	535.6797
186.0774	533.8195
188.9957	532.1716
190.8968	527.882
191.2372	526.3207
190.7738	523.9984
189.6397	523.8091
187.0144	523.0085
194.4992	522.7087
192.0226	521.6958
189.3428	520.4977
186.4088	514.9602
193.4295	514.4654
186.592	514.3858
192.4333	513.1194
189.6152	509.6798
192.7002	507.1145
186.9161	503.0303
190.0105	497.5529
191.1232	495.12
191.8957	490.92
185.447	489.0185
185.2646	483.4566
188.9812	478.4492
185.8075	477.4899
187.8096	475.4754
189.196	473.1561
189.7646	472.35
193.5406	467.7928
191.2322	467.0497
194.0477	463.5742
188.3479	463.2171
188.7925	461.2589
189.1752	460.371
189.2993	459.695
188.5691	458.9521
193.684	453.8832
185.3074	453.6355
194.9332	451.4449
194.4233	450.4257
188.2496	442.1241
185.7638	441.5521
194.6976	436.4175
191.7947	427.8132
186.7428	418.9232
190.1182	412.6382
190.2649	411.9838
189.9963	399.8254
185.278	396.3113
190.7266	395.6451
194.9503	394.2998
187.0352	392.4027

188.2288	391.5066
191.9068	383.6117
189.1871	380.5607
193.0125	378.9936
190.3019	372.818
190.9089	369.9441
185.4929	369.1834
190.5136	368.5748
187.6211	367.7014
189.2247	366.9018
190.5958	366.2096
191.1384	364.8842
194.173	363.5826
194.0606	360.0101
194.8521	358.981
193.032	358.5115
192.2139	352.1083
191.7892	351.8427
188.321	349.9389
191.3995	348.7379
192.6704	346.4498
185.9078	345.7363
192.9022	344.2554
190.0626	342.0627
191.9391	338.2301
194.0565	337.1561
188.2895	333.8199
191.842	329.1036
185.2853	328.3085
192.3739	316.3743
186.1024	312.3004
192.6649	307.7621
192.6528	305.1428
191.1923	297.0014
190.2772	296.3002
189.4098	289.0329
191.656	288.5244
187.7056	282.8657
194.6567	278.5961
191.4971	277.6206
193.6657	276.7608
192.0114	273.6929
189.0802	273.6091
189.457	273.281
190.9417	272.5047
189.2886	272.3449
186.7179	271.7989
192.8189	268.5711
188.1118	263.0825
185.8886	261.6184
187.8979	258.6011
191.3494	257.6696
194.4446	257.3275
188.9049	256.8425
188.2802	255.9244
187.1789	248.8662
193.4151	248.3684
187.6808	245.8046
194.872	242.9406
192.3182	241.7519
188.1133	240.5176
187.6504	232.194
188.0124	230.3959

187.9532	224.3466
187.459	220.9367
189.7334	219.5361
189.5862	218.8376
187.6199	218.3031
194.111	218.2356
189.5821	214.2452
188.6428	213.18
193.1955	212.6338
192.0615	212.3881
191.55	211.7803
189.8011	211.0865
188.9725	209.6277
193.4988	205.1512
193.3822	197.9516
187.6619	197.7963
194.2568	193.2136
188.9365	182.8033
187.426	181.8058
189.2442	169.9394
194.3495	168.0803
188.8598	167.5702
185.6345	163.4204
190.8078	156.9004
190.1788	156.4577
189.1843	155.411
186.2945	155.3288
187.5556	151.0427
187.0758	150.8885
187.1472	144.7225
190.4125	139.0759
190.7629	131.5336
193.4876	127.7126
190.4733	127.5392
187.2389	125.3244
194.594	121.9081
192.13	119.3201
190.4557	118.89
189.7855	116.9016
194.6682	115.9599
190.6605	115.9308
185.6118	111.3979
186.1087	110.938
186.8694	109.2854
186.0734	108.9678
192.3633	107.4651
187.8528	107.2664
190.377	107.0093
190.3198	104.6965
188.8897	104.3399
194.5674	92.8215
189.0245	90.8424
188.529	89.8597
194.817	88.399
188.4041	84.0189
186.8258	75.8649
189.8669	70.5703
192.098	69.9817
192.3037	65.796
188.25	65.4893
185.5193	56.1619
188.6472	52.0872
188.0303	48.6605

185.7422	28.6169
187.6153	27.2651
194.2533	19.2417
190.1876	13.3966
190.0616	12.8297
192.9276	9.2787
186.4515	9.1527
194.8602	4.1496
190.7711	3.7736
199.5794	2.966
204.9653	3.2872
196.8461	7.3396
198.5979	7.4503
198.3833	10.9086
199.4693	13.0134
203.0462	13.1285
196.2637	18.5396
204.4668	18.6509
202.718	20.0047
200.5768	21.4396
200.4919	22.2553
202.6418	25.6277
195.7818	32.4926
201.1018	33.2477
201.1802	34.9217
199.2322	38.0064
195.396	41.9336
201.584	42.4088
202.4179	46.7639
202.8329	49.7424
199.5099	56.5213
196.1844	57.0142
197.6838	61.354
197.6241	73.6282
201.1279	75.087
200.3131	75.5223
203.989	75.5989
196.5497	77.3338
199.6257	79.0525
201.8066	79.316
201.4086	79.5933
195.573	79.6257
198.4066	81.3567
201.8929	82.6838
196.2932	85.5236
202.1858	85.5689
201.8589	88.4189
197.2118	92.1305
203.3328	92.3212
200.3843	93.4874
203.2544	93.527
203.8297	95.5945
204.4642	97.1435
204.7955	100.3999
199.8627	102.6155
196.1276	109.5474
200.5001	110.8002
204.694	114.7247
197.1197	114.8822
203.7182	118.3075
197.3771	126.0321
196.5475	127.7992
195.0282	133.8129

201.45	136.2706
195.0127	137.4794
204.6489	138.0755
203.2344	140.8582
197.0892	142.688
195.3992	142.821
195.0426	146.6785
202.5984	151.341
197.5463	157.1057
201.5612	158.8485
197.6731	164.0361
200.5604	164.3667
197.3755	165.6684
196.7424	165.8405
204.9885	168.9556
202.7597	175.4277
197.0476	181.3139
203.9143	181.9959
198.1501	186.5821
201.615	187.9934
203.5774	190.2653
196.64	190.8977
204.7083	197.997
196.1521	207.8095
203.7221	208.398
198.014	213.7629
195.9017	215.297
195.2834	221.6044
195.9329	222.661
198.9232	224.1067
202.0169	224.4157
196.0347	225.6385
195.2197	226.0849
204.9342	238.7954
196.7272	238.8254
200.7286	245.2116
204.85	249.298
200.1895	253.5914
199.7426	254.4965
202.8271	259.3601
201.1307	261.6097
199.9793	262.712
204.0414	263.4785
198.2417	270.2179
196.4771	275.0174
201.7491	278.7964
199.0943	279.326
203.0345	285.6336
197.3474	285.8884
198.7442	287.2189
203.4828	290.6591
197.479	296.031
200.9242	297.0477
200.436	306.0004
200.9599	308.0139
204.8477	317.1958
196.568	318.9042
196.0422	322.0289
204.0037	324.4125
202.0654	325.7811
201.1022	328.6583
199.5519	334.3423
201.0116	334.5697

202.1607	343.7053
199.7838	345.8512
203.3554	348.551
197.7636	350.9985
202.1395	354.2116
202.6534	363.5758
197.5364	364.4662
203.6274	366.337
196.1366	367.3733
197.6732	369.5517
203.7311	374.3643
200.7291	375.1698
202.8431	376.1773
197.7148	377.12
198.2524	387.815
195.2287	389.7751
202.5951	390.221
196.2753	390.8135
200.5104	391.6043
200.8623	402.9489
198.0551	409.2749
201.8973	409.7199
197.3136	411.3959
199.4952	422.8064
198.5315	441.7773
199.8734	442.3449
201.4265	443.3975
198.3048	445.4324
197.2757	447.832
199.248	455.1182
198.781	455.8279
200.6146	463.4273
198.3276	474.8945
199.9945	475.0971
196.8414	475.7697
201.1329	475.9421
198.8932	477.5614
204.9421	477.5859
200.5948	481.9073
203.4662	482.0235
200.2313	492.9914
202.2287	494.814
204.6109	497.0602
199.5323	510.5961
195.8443	514.7903
198.9403	515.0994
202.9037	516.0388
197.9954	521.0607
197.1296	521.7777
196.9089	527.5244
201.4359	527.8974
203.8998	530.4967
203.5264	538.0696
204.6638	544.629
195.2949	551.3534
203.7238	556.7723
201.0154	557.4911
203.239	561.349
204.8933	562.6289
197.4142	575.523
204.9807	577.2948
201.5695	580.6008
199.525	590.3035

198.7993	598.4027
198.0535	602.3082
201.3575	603.7731
201.6856	606.9556
199.4938	607.8606
214.2937	609.1509
209.2235	607.5708
209.2902	606.2412
208.0445	605.1536
208.4925	604.0154
212.1011	598.8825
205.7709	598.03
205.666	597.6111
207.3418	594.2646
212.0225	581.5961
212.8315	579.8375
205.9577	578.4192
212.6527	578.3381
214.4857	570.5457
209.9486	570.1703
208.9886	559.4624
211.4107	554.7537
213.0593	550.6132
206.7179	543.4665
210.7801	542.1693
207.5177	540.6409
212.8085	530.3751
213.3187	529.8513
211.5242	527.6701
213.4614	527.0697
207.304	523.0463
212.7808	521.3033
209.7085	511.7543
209.2753	510.3713
214.0418	510.2784
205.0404	509.5491
209.3567	503.8255
207.9048	499.5065
208.772	496.63
210.6512	493.5748
205.9908	489.9967
208.9383	487.7488
210.9586	485.9073
212.6167	482.6979
210.0536	479.8694
209.0102	465.993
210.6735	459.8371
209.6019	459.2142
209.7557	456.6952
213.104	450.661
205.2714	450.23
206.4633	449.3901
205.4058	444.6131
207.4475	442.9423
209.8735	440.9861
211.1999	437.4673
205.3156	437.2221
213.8176	436.8645
205.2758	436.0659
205.4702	431.6491
208.4729	429.2425
205.8089	428.2322
205.3228	425.2184

212.4059	424.9945
209.3649	424.7008
205.9805	424.3853
205.1084	423.083
210.8842	419.8608
209.7359	418.8879
209.6299	418.1595
210.7613	415.341
205.6109	413.6271
209.8369	409.8317
209.4256	404.6766
212.5506	403.0666
214.1389	398.8998
206.5285	395.5452
211.2312	393.0213
212.8305	391.9117
207.5506	390.8069
206.2129	389.5397
209.5148	388.2336
210.4549	387.3194
207.7138	381.6992
213.4737	371.3156
207.8857	370.2064
213.6173	369.4911
212.2204	365.9617
206.5257	360.1635
213.1444	359.83
213.2673	354.2162
210.6502	338.0592
210.5472	334.628
213.0269	333.6569
210.9403	331.5917
206.2562	331.4505
212.7192	324.7714
212.9922	324.7279
205.755	320.8552
213.6126	320.6454
214.4062	318.044
208.574	315.5047
207.0098	309.4577
208.3686	299.3775
211.6649	299.055
205.0277	298.1218
213.3832	297.6158
213.9872	295.1408
212.0467	293.4651
210.0927	291.952
213.0957	291.335
209.7329	282.9284
211.6485	282.0198
210.4121	275.2172
205.8091	274.831
208.2617	271.3809
206.8564	267.6356
205.4153	266.5472
214.9568	264.1505
210.559	263.888
211.2299	259.8118
213.9561	247.7093
207.9609	242.8
211.141	240.9465
208.8705	240.4946
214.5128	239.7193

207.2113	238.4331
206.8166	230.0436
211.7989	229.4754
214.2444	229.4659
211.3059	227.7157
214.1497	219.9016
209.6344	218.4737
207.7356	214.7378
211.4232	211.6405
207.7697	208.2933
205.6507	206.9669
208.8421	198.6865
213.5307	178.7437
212.6184	177.7259
213.9059	176.153
214.6446	176.0698
214.8456	169.0837
206.2381	165.6332
210.0284	165.521
209.3418	164.4382
213.3791	162.0744
208.4414	159.5634
210.8006	157.0758
207.717	154.5777
206.2912	150.1002
207.1751	148.3299
210.7729	143.674
214.697	140.0866
210.8506	139.4362
214.5393	130.976
213.6794	126.6576
212.9337	122.3065
212.1846	121.0271
209.8886	119.1849
214.3029	114.8335
205.2657	111.5335
206.2537	107.2222
207.9574	102.7154
210.2067	101.0666
213.7095	100.9015
214.2316	97.4872
210.7052	96.0516
213.4789	91.2362
210.6259	90.2037
214.0695	86.0606
207.0252	84.3346
208.9251	78.5445
206.9758	76.1053
210.5583	73.7616
205.8402	72.9233
208.1771	71.827
213.3736	71.5582
211.5201	66.7952
213.2156	66.2918
206.1728	64.3142
205.5358	63.3695
208.7494	59.6998
210.4561	59.6865
206.5605	56.4798
207.6165	55.1514
205.4881	54.7113
214.7334	50.6723
207.6591	49.3206

212.5394	47.1967
211.9728	45.4101
209.165	40.6187
211.3023	39.4597
209.5923	29.5581
213.6641	25.6261
211.0642	24.2963
206.7779	21.8751
207.4612	15.7466
212.0531	14.3639
205.5257	12.5413
213.6234	11.9602
209.897	9.5608
206.0022	6.3751
210.0735	6.1287
206.3505	4.6429
207.7088	0.2061
219.8592	4.0474
217.2722	6.0968
223.0547	6.9006
224.9837	7.2604
223.3074	9.5935
218.9988	9.9371
221.3298	16.8105
215.1714	19.0797
223.7427	21.5376
219.3408	23.7165
215.7736	25.9086
224.1976	31.9656
216.174	34.4847
222.2729	36.858
220.7196	38.3672
217.5069	41.8942
221.0255	45.4115
223.478	46.7936
215.2697	47.7681
216.4527	48.3072
218.4322	49.052
217.2165	50.4727
220.1529	51.3061
220.0495	57.0507
222.0098	57.4177
217.5278	58.9485
216.5194	60.2879
219.7134	61.9874
220.15	65.6988
215.8349	66.4505
218.8083	67.3715
221.433	67.7915
216.6945	70.1103
223.9755	71.144
221.1749	71.6338
224.7138	72.2508
222.2377	77.4102
223.2204	77.7301
221.7073	78.4137
218.7552	78.744
218.53	85.171
219.905	86.9479
223.3745	87.37
218.587	89.5665
223.0983	90.5171
222.5051	92.2679

219.2349	93.6397
215.7826	94.061
223.9544	94.3326
215.2948	98.7219
223.3074	108.2011
218.2133	110.4457
219.9831	111.8521
223.8746	113.841
221.0396	114.7921
218.5727	115.2493
222.8208	119.7532
216.2254	120.8516
222.0054	121.1879
221.0374	125.4263
216.7204	129.7215
222.5615	137.7299
223.639	148.3761
219.237	153.6778
217.8793	154.4641
217.8967	156.5079
221.6982	156.6092
218.7098	157.3929
222.2083	163.1365
223.1476	176.9297
220.6924	179.6504
219.9168	182.0076
222.2308	185.3815
224.504	187.5147
222.705	189.5377
224.571	189.917
220.6084	190.6051
217.8618	190.8169
220.8199	191.4189
224.1738	192.9364
218.1764	200.373
218.7633	200.518
219.7481	203.2067
220.6449	211.6463
221.742	214.7644
223.6512	215.7115
222.8931	218.1394
216.9469	221.9851
219.8094	222.7706
217.5156	226.3144
224.6477	227.5367
223.9665	229.9371
224.5223	230.9954
221.2089	231.9879
220.2929	232.1698
220.5019	233.537
221.908	234.2386
218.0959	236.5172
217.6756	245.5783
218.8665	246.9003
219.8833	246.969
218.9138	249.6698
219.6702	250.7698
222.8869	256.5479
220.1457	258.1952
223.0761	258.8126
220.721	271.9699
222.5072	276.7349
216.0814	277.0673

217.5019	279.8587
219.6346	280.9353
221.1064	284.3265
215.3034	289.5915
217.222	293.5414
220.4659	296.1832
222.6893	298.5378
219.5707	301.4992
224.8741	304.5531
216.1063	305.9956
218.9793	307.19
219.771	309.6337
216.8161	309.7184
219.9496	313.7322
221.2843	315.0465
219.0178	317.0536
220.6191	318.4365
222.8696	318.9517
218.6105	322.3985
220.7954	322.4278
215.2532	322.9865
218.7585	327.963
223.8374	332.5166
219.7633	336.0071
215.9701	340.1369
215.0613	344.1086
219.663	345.0501
218.8905	347.3163
218.1335	348.1314
222.9786	348.2563
220.3804	350.2506
223.0125	351.7753
219.5875	352.7583
217.9207	355.3442
215.8022	357.2336
223.8143	362.6631
222.4811	362.8003
218.5543	367.0287
222.9511	376.5482
219.287	379.2259
216.6001	379.8458
223.1295	380.6197
217.6701	382.2835
219.3932	383.8937
215.2113	386.2594
215.9683	387.9118
223.8821	392.2362
218.3476	394.6355
217.142	398.8296
216.9191	402.9383
216.4935	409.3695
218.3168	412.6721
220.0403	423.2989
216.1287	425.1786
217.7449	431.587
223.2449	438.7196
221.1394	438.8801
221.8208	440.9879
223.4111	445.3524
221.5179	445.5836
219.7502	446.5167
218.3023	448.2959
222.3883	448.8019

220.462	452.2582
221.1337	458.1741
220.9804	469.2089
221.1024	470.784
224.9717	471.7105
222.3547	474.3637
215.7803	477.921
219.9074	492.8944
216.634	502.0863
221.9459	503.7975
221.9516	505.1155
222.7561	505.7393
218.6877	511.9145
219.0848	512.7206
224.8206	517.0308
216.1768	517.6823
224.7637	518.8919
216.7768	519.4655
222.3909	519.9122
220.5487	523.5054
224.1638	525.3723
220.9994	532.2451
221.3904	534.4366
223.2494	538.6228
220.8818	541.3869
223.6045	541.8612
221.3393	545.0592
215.2269	545.5702
220.6371	552.1262
221.2596	553.2734
218.5721	553.6421
216.6156	558.7497
223.8526	558.9569
219.8314	559.0131
216.1594	559.2334
216.4036	560.951
217.8525	561.2246
216.2284	564.0632
216.9857	564.1215
219.7309	565.1246
217.4685	565.5694
219.8375	567.0281
216.5979	568.4717
215.3176	569.5104
222.2615	572.2686
216.4968	577.9395
219.5305	582.3381
216.3268	584.9057
222.0565	591.7366
223.8697	592.6773
220.2651	592.9026
217.4222	597.5147
216.3273	599.3373
224.4188	602.1983
224.2739	602.8924
224.6368	605.6119
219.9086	607.5006
228.2607	601.1678
228.943	595.6837
226.6193	590.096
234.3092	590.0857
225.7572	586.749
231.5555	581.5603

232.1013	569.7086
227.5697	568.407
226.6426	565.3887
226.3476	564.3921
233.8468	562.706
234.6968	560.5938
233.3601	554.5579
231.5114	553.9731
232.5463	548.1991
233.6071	547.7981
225.8769	545.5925
227.9826	541.6685
230.0823	540.5026
228.9025	539.4248
228.5693	538.6879
227.1585	538.6315
231.6112	537.4553
225.5664	528.4757
226.818	523.5417
234.7449	520.4343
231.8966	518.3963
230.8907	517.5119
226.2166	516.9109
227.1338	514.2782
228.4479	512.4244
234.435	510.1773
232.409	509.0548
234.9793	508.3056
227.9692	506.865
230.3029	502.4408
233.6284	500.9953
228.1318	500.0161
234.547	499.9573
234.3846	497.9289
226.7195	497.9275
232.7794	497.883
228.5607	492.7148
228.2504	488.6195
226.7707	487.5748
233.8725	487.5617
225.0357	483.8891
226.8731	480.9018
234.5024	478.959
233.5052	475.586
225.0824	469.3379
226.2192	469.2941
227.7325	466.7432
226.6745	464.8945
225.0797	464.1704
234.6179	463.1879
229.9903	462.7426
226.4693	462.5322
233.2298	456.9051
233.7858	454.1474
229.3183	452.6798
232.6266	450.1682
227.3642	450.1557
233.5811	446.3316
226.126	446.2184
225.5497	439.4525
225.7691	436.7394
233.7085	432.9996
231.0197	432.5172

233.8055	432.3112
234.0817	430.776
226.5504	429.0969
228.8575	429.0686
228.9844	428.4887
230.2572	422.6718
232.0873	422.4502
232.1465	421.3168
228.8087	419.4306
234.7129	419.2996
232.581	418.7689
225.6214	414.369
233.0993	409.4871
225.7594	409.4413
232.2814	404.5876
233.4549	403.656
229.338	394.8252
234.683	389.9009
226.8373	387.8172
234.9301	385.6647
226.2942	385.1216
225.8562	380.4244
229.6192	374.2617
228.9281	370.6029
226.3384	370.1293
227.6994	368.4924
232.2083	366.1093
230.8547	364.7766
227.0289	362.5241
233.4017	357.2382
229.6792	356.8766
233.1812	354.2628
232.1553	352.2163
232.9242	349.5706
231.9095	342.6983
229.5895	331.5547
230.0285	329.1425
233.0447	326.5349
232.1659	325.1414
232.4751	322.614
228.8461	314.9313
230.7058	312.2332
232.6231	308.627
229.9245	303.863
226.9361	302.5697
233.3519	301.9369
226.5498	276.4815
228.4125	274.9984
227.5857	268.9051
230.9695	268.773
234.4846	264.1124
226.0244	264.0714
229.8587	263.9852
229.6186	261.4233
232.5587	258.7541
226.8549	256.5922
229.5932	249.4897
233.3153	249.47
231.6756	234.9776
232.4765	234.681
227.133	234.4696
229.7109	227.8699
229.984	223.9303

232.1691	219.4207
230.543	218.8969
231.0428	218.5643
226.1576	216.3246
229.7185	215.4447
233.5241	211.799
230.0652	206.9642
231.5155	205.93
229.6388	200.6168
229.6539	197.8021
226.9828	197.1281
232.3976	196.2592
230.4821	194.3252
230.8088	192.8512
228.0697	185.4031
234.5446	183.6184
230.0755	179.3757
229.8601	178.994
226.89	178.889
227.1202	172.49
226.0721	170.9733
231.2844	169.7463
229.3264	167.7625
234.7661	165.9411
226.4406	160.9658
231.4485	158.6588
233.7883	155.8112
233.1152	155.8003
231.9716	142.3094
230.2458	138.6632
227.174	135.6361
227.4737	130.6497
230.4843	130.57
228.0787	130.2786
231.733	125.5263
234.2984	123.7947
230.025	123.7186
227.6414	122.4957
232.4926	122.39
226.9073	121.3395
228.9923	111.6783
233.3077	108.8742
228.6625	106.6111
226.7909	105.3511
229.3851	103.2234
232.2001	100.8703
227.0732	95.9275
234.7126	93.3605
231.8871	81.5377
227.2868	80.7548
227.9079	79.772
232.0673	75.6836
234.8467	64.9964
232.441	62.6267
230.1942	60.6536
225.2527	60.4887
234.1124	59.9054
234.3244	56.0981
234.0908	55.3188
226.0233	49.4671
233.7768	48.4152
228.8776	46.818
226.9438	34.794
228.2246	33.913
227.9302	33.2211
231.1997	30.2403
226.9918	25.038
228.3758	24.7391
234.2168	17.9069
226.8579	17.7832
228.6777	16.053
225.9721	9.2822
229.6565	7.3933
233.2052	3.1247
230.3315	0.6976
237.042	0.5103
238.7837	2.7624
242.1636	11.5476
244.7822	13.1607
240.6779	14.2659
235.4396	14.84
237.6902	15.7469
242.4956	16.6381
244.8282	21.4849
238.1836	27.3011
243.7754	29.1918
241.8452	30.7512
240.0597	32.0786
243.5384	36.3959
243.0327	36.936
241.8393	48.9381
242.8962	51.8823
240.0084	54.118
236.2087	54.2915
239.7212	57.2738
239.6176	65.0905
238.3691	73.4464
237.4459	74.4825
235.4422	74.698
241.91	76.9537
241.8336	77.4285
235.2379	77.5907
244.1749	83.6925
240.9471	87.2514
235.5531	88.453
238.7753	95.613
240.7346	96.4064
236.4012	97.0607
242.8275	100.5745
238.5714	104.821
235.4874	108.5387
244.7583	112.9477
237.7084	117.2782
235.945	119.6489
235.744	121.4196
240.4969	123.4426
241.3801	124.7604
243.9902	126.9049
237.9387	127.7554
236.4308	132.8417
244.5588	133.474
239.2246	134.8297
237.5743	148.4164
239.8541	148.7247
236.2877	150.2586
237.7332	165.7037
244.5109	166.8795
237.7638	167.1664
237.0472	175.6024
235.0238	178.025
235.5795	179.3685
237.0069	182.8566
241.9536	185.3321
242.3186	194.5575
235.8616	197.971
237.3912	212.7018
243.4848	216.5849
244.0737	216.7523
241.7211	220.0155
243.3513	225.153
243.3413	225.1596
235.2405	234.779
236.8596	236.4034
237.6886	236.6316
243.5003	237.3211
238.3379	240.0816
237.3893	242.5705
241.0168	246.6959
239.6398	255.1067
235.7995	262.0079
240.2583	262.8436
244.3752	263.2914
236.1547	263.3928
242.0622	268.1881
240.0032	271.0311
242.3743	271.4833
235.4557	271.9182
237.975	273.1205
238.1631	277.5189
236.9597	282.3254
243.1278	282.6586
241.752	285.2377
241.5649	287.9825
240.2619	288.3443
240.2063	296.2171
238.5214	303.6248
236.337	304.2598
243.0307	316.0885
236.11	316.4908
236.0839	317.8099
237.0948	318.0846
241.2191	320.1144
237.885	321.4342
244.5665	326.1432
239.0781	326.2121
244.2618	326.7133
241.7924	327.1784
235.7495	333.6597
237.503	338.8418
236.4803	340.143
243.5196	340.2227
240.3671	342.672
241.4613	346.1998
239.8664	351.868
237.039	355.3137
238.8751	355.4896
243.1291	356.7384
236.3916	362.7376
238.4512	363.6105
236.6873	363.6497
242.5988	366.3888
235.2962	366.4624
243.2837	366.968
237.1485	367.4194
237.948	367.5052
241.5752	370.1165
243.3176	371.4943
242.1475	373.8326
242.3193	376.1379
235.6549	378.5825
236.5974	384.133
236.8343	390.6969
237.2395	395.053
241.2132	398.9415
239.0297	399.8168
235.6536	403.9244
237.6244	404.2772
236.1088	405.0826
238.3287	406.5034
240.9001	406.7449
236.619	407.7927
243.2002	411.8091
242.4142	426.4466
239.0607	433.4288
236.5037	442.9487
238.3934	451.235
241.0053	452.5033
244.8563	452.9595
235.8539	457.192
243.0852	463.89
238.8363	464.6241
241.3348	466.5345
238.4209	470.7598
236.41	470.8884
235.2434	474.7008
241.4678	475.3878
243.3607	485.2304
241.6794	495.7145
241.7275	497.7213
243.7986	497.774
235.6098	501.6725
244.2496	502.2518
239.458	503.5115
240.6475	505.4446
235.2289	510.1923
240.6553	513.3544
240.2143	513.3588
235.5089	514.4729
242.0528	517.1284
241.8934	517.5066
241.6154	519.3192
241.6513	519.5549
243.0515	524.5758
237.2293	524.6516
240.4866	529.1851
238.6082	531.071
239.2469	534.1887
244.5347	538.1419
243.9108	538.6686
244.0317	538.9304
243.6515	539.0512
239.5751	539.3647

236.0735	540.6266
238.7214	543.9232
241.5562	544.5767
236.261	545.2071
237.3377	545.8681
241.9877	547.9883
239.9275	551.1459
235.0373	554.9046
240.2151	559.2193
243.8726	560.7397
236.4784	565.1087
238.2187	565.5489
242.9154	567.2151
237.683	571.0914
236.9766	571.3311
241.5366	573.2472
241.6079	575.7625
239.9564	587.0733
237.0202	589.0939
240.3656	590.9271
237.2553	592.0919
242.8268	595.2307
242.1407	596.2076
236.9525	601.4735
244.6327	602.0161
237.4643	603.6087
240.304	605.0147
240.1024	606.4733
243.1051	607.3078
252.5773	609.7039
249.7842	608.3873
254.033	607.9711
254.4903	605.6103
247.3453	604.2383
253.1886	594.0881
248.5876	593.8828
253.6477	587.5086
249.6861	582.5272
245.3378	582.0542
246.147	581.1005
245.686	580.0885
248.9118	573.2422
247.4461	570.1361
250.8687	565.7879
254.1611	559.1897
254.7025	559.0692
248.8864	544.4197
252.532	544.1734
254.6764	534.3846
245.1962	529.4323
251.041	527.0139
248.9684	520.3906
252.9926	518.5785
249.9767	515.1181
248.121	512.1001
250.7417	511.225
251.2251	508.082
249.1302	493.2793
254.6487	489.8677
254.1798	488.9327
253.3827	488.5056
245.1591	486.0296
248.166	473.3141

245.7104	470.6658
251.1644	470.2336
248.2577	466.8323
245.9654	463.5007
252.3619	461.8651
248.459	461.7957
252.8678	456.3594
250.6213	455.8741
252.8597	454.862
246.6842	452.2386
254.8524	450.0258
248.793	449.463
246.7495	445.8641
246.8072	444.5566
251.7305	442.1161
248.2422	440.8389
245.6245	439.0756
248.343	437.4218
245.7295	423.2358
254.6322	422.6598
249.0552	420.5616
250.3778	419.2593
245.6409	418.5255
251.796	406.8484
246.9798	406.0022
249.5075	402.8189
250.4135	401.869
245.4738	400.4144
248.29	393.7541
250.2415	389.7367
250.9729	385.9948
247.5784	384.7935
253.5112	384.1263
253.4041	380.1577
247.8737	379.456
248.9523	379.0898
250.4105	377.9331
249.6438	373.162
248.7456	369.8381
249.9875	369.6349
249.9075	366.5026
249.445	358.7276
250.7802	358.6901
250.3598	356.4354
246.5329	354.6594
254.2201	349.8184
248.1616	348.1144
245.2925	346.9666
251.9037	342.3793
249.8633	338.3371
252.227	333.8089
253.6201	324.9976
247.6065	321.7643
254.6659	320.2832
253.9913	315.1054
251.4711	314.7012
249.8532	310.9513
254.5411	307.3216
245.6171	305.1343
249.493	304.2948
250.1601	303.5767
250.3219	300.5971
245.4731	292.9467

250.2889	291.3141
252.852	289.087
251.011	287.7729
254.5196	279.9218
254.5994	279.8088
253.9641	279.2225
254.1172	276.3954
253.3037	274.0984
252.5512	269.1687
246.7861	265.8103
245.3113	256.1021
249.1985	255.0265
249.4833	253.0898
247.6868	251.646
246.0793	246.5814
248.1196	246.0091
251.8227	243.7051
246.4969	239.8437
248.1605	234.8133
253.7016	233.6071
248.8278	230.2897
254.2497	229.61
246.1624	215.1571
251.622	214.5961
246.8845	211.9985
254.8657	208.5573
251.1327	199.2717
254.1257	190.4248
252.9927	190.1985
251.5771	190.1164
245.7462	187.3827
246.4144	183.3746
245.6272	176.071
251.7869	175.1061
248.3981	174.5935
245.7757	173.1293
248.6376	169.014
249.4249	165.085
245.5949	164.3431
246.8966	162.122
249.5814	157.2068
253.169	154.5528
249.3119	152.9405
254.007	150.4848
250.1262	143.3522
251.6948	137.2608
246.674	134.8258
248.4817	126.691
253.2158	124.4196
251.2312	123.81
252.3326	117.5887
252.1922	109.6419
253.1392	107.7498
245.0518	107.6936
249.0462	105.487
251.359	103.6742
246.6017	98.8504
249.9238	87.0575
248.5977	84.4183
246.571	82.345
252.4944	77.2144
246.6901	75.3362
249.4748	73.1263

247.3396	69.7519
253.6857	68.6823
245.806	64.566
251.1484	58.2328
251.2802	58.1793
252.5132	57.9549
245.0111	57.9377
247.8188	57.904
247.5194	52.0394
254.9468	50.8719
245.1202	44.4593
254.0852	42.3883
245.1569	41.0898
252.3509	39.4172
245.6033	35.8859
250.7449	32.7051
252.3949	27.9718
245.5038	19.1027
253.5605	14.9214
250.8868	14.5163
251.5816	6.9717
249.1451	2.4408
254.1307	1.5901
260.8891	3.581
260.8939	14.6554
262.6401	14.6833
260.484	14.9858
257.7508	15.0124
255.0986	15.8585
262.0149	15.9236
260.7867	23.8942
259.2695	35.8922
262.3352	35.9203
257.9863	38.0605
259.3521	42.5445
257.6794	44.3497
259.9854	44.5666
264.0065	44.6593
259.0665	51.4773
258.801	67.6346
255.8029	67.8193
260.2297	70.3584
264.8507	72.4788
264.6615	77.6195
257.0771	77.9298
258.5608	79.7684
257.9662	81.0939
257.8486	83.5721
260.2745	93.9086
256.7449	99.1358
262.259	99.2518
261.4601	103.2112
262.3115	104.0442
263.225	105.3568
257.8652	105.9175
255.7426	113.5081
255.2421	114.2446
259.5716	114.4622
264.9257	115.6735
256.1639	123.3634
256.9964	124.7711
260.8526	129.3857
261.8863	132.0654

258.7267	139.7264
264.0853	144.5944
264.1379	145.4356
258.2964	147.4445
260.0975	152.4407
259.472	152.9714
261.0622	157.0351
255.4611	162.5194
257.7024	163.042
261.7837	166.0565
261.8477	168.717
259.0941	171.3773
259.0168	171.875
256.7635	173.4882
258.2281	174.1972
255.7734	179.7521
263.1533	181.8899
264.1766	182.3288
259.6846	182.6081
255.7944	185.3043
262.6366	186.8589
258.3454	187.2127
264.9203	190.9528
255.7661	191.2813
264.5563	197.1089
256.6999	197.3303
259.6571	198.734
255.2067	200.699
264.2001	202.4515
264.1736	206.9675
256.4041	213.592
264.7312	215.0863
261.2211	216.1371
262.1742	216.5816
262.9086	220.6149
257.3169	221.9228
263.7056	223.165
263.2022	226.1093
257.0389	226.2179
257.9173	239.5129
258.0497	241.3612
264.1415	241.613
259.1151	248.3956
264.214	251.8654
264.457	252.3343
257.6345	253.0504
263.3294	258.5892
257.1895	258.7294
255.5887	261.0021
260.659	262.2522
258.429	263.3777
258.7793	264.1892
255.7321	273.3074
259.4562	273.4622
264.1174	274.1517
257.8232	279.6115
259.0358	280.6298
260.2099	281.2308
263.0199	281.4972
259.2107	281.5673
262.703	285.6697
260.4895	286.6625
255.5292	287.7182

264.6156	299.7114
256.5821	299.7434
262.5955	301.7686
263.9066	304.679
259.8121	307.8568
261.0524	309.6951
258.0388	317.8332
255.3369	318.5478
259.6301	319.054
259.4688	319.0737
257.6022	320.9343
260.9933	322.0392
263.7966	328.7486
263.7208	328.836
257.2975	332.4961
262.0891	334.9708
261.7193	336.3335
259.4054	336.7233
257.8078	339.4881
259.8665	344.9804
255.7331	345.8553
263.7926	347.3553
262.9238	350.6964
260.049	353.43
262.8134	355.7101
263.8431	355.9029
255.4893	357.251
257.6061	357.6773
260.694	360.0815
257.8818	360.1194
256.5922	361.1856
261.233	366.5677
255.1377	368.7426
256.6253	372.8561
261.8544	374.9323
263.8673	376.5259
262.9908	378.4846
264.4941	380.7762
256.1644	383.7124
257.7699	388.5805
260.5669	391.4446
257.1212	397.0421
256.7818	403.2691
258.2348	414.2448
264.341	416.9054
261.5546	420.1388
257.1467	421.4573
262.8885	426.7496
261.0251	426.9475
262.5529	429.3122
262.6016	432.8494
256.4839	433.8372
262.1981	437.9402
258.1212	438.0917
259.0906	438.8663
260.2685	441.2734
262.8373	444.1206
259.8873	451.6381
255.2426	453.4726
260.0152	461.4116
258.9784	462.3579
262.0507	464.8602
260.3632	466.0945

258.8451	470.5856
259.8191	470.9289
257.4676	473.5389
256.3967	475.6807
261.3172	476.6334
259.2619	478.3534
258.7795	481.807
259.929	483.1522
258.6224	485.5507
259.4996	489.9946
255.0509	490.8708
264.1273	500.2715
263.9131	506.9843
262.6785	509.7147
259.6079	511.539
258.8608	518.5828
259.1384	519.9013
260.1786	524.8951
255.5881	525.3231
257.3009	525.8563
260.9684	527.9269
260.2199	528.1656
257.8486	529.944
263.7421	531.9459
262.8871	533.815
258.0405	534.6579
260.4306	535.8562
255.2408	538.4832
258.7228	539.3796
256.9206	544.284
261.9408	546.1772
263.9034	552.5729
257.5628	556.7245
260.3651	558.1945
255.4291	561.9454
257.2831	563.0529
263.1643	565.0473
255.2793	568.7796
263.9939	568.9988
264.8504	579.6798
257.417	582.3794
255.6422	585.4766
260.581	585.8516
259.5819	586.1872
256.3848	586.5895
259.8386	593.3451
263.3866	600.5784
257.5422	603.7962
256.9513	607.1876
262.7058	609.3455
263.0974	609.7469
268.6318	605.1948
268.3496	604.2646
273.6224	600.7121
266.2963	596.4946
274.4462	595.2097
274.9095	595.1353
273.6009	594.507
266.4123	593.9602
274.6377	589.637
273.9928	588.5854
266.725	585.2275
271.8021	582.8299

273.4531	579.9855
266.4498	579.0704
269.691	577.4441
274.3419	575.8708
267.8777	573.6839
269.2175	571.1778
265.5558	568.856
270.172	565.6767
270.0245	564.909
271.1075	562.5489
267.3969	558.9156
265.1259	558.8371
272.0579	555.7806
268.535	550.7462
270.109	550.2446
266.7945	549.1336
269.4563	548.7027
270.2275	546.7327
274.3932	546.02
272.4889	543.271
270.0848	542.7112
269.1035	542.1618
267.7356	540.607
266.6299	537.5404
265.9801	528.2507
273.441	523.1912
272.0486	521.5645
266.661	521.1139
270.6224	520.2997
270.6402	503.4412
272.6029	503.4092
266.2061	501.2196
272.337	499.2248
273.3854	498.7605
266.9606	497.5513
274.7498	491.1977
273.8464	485.6523
270.672	485.4093
271.6442	481.0575
272.9455	476.6171
271.7562	461.5711
267.4274	461.5073
274.9096	456.7187
271.4454	454.0142
266.8349	450.0193
273.4127	447.0362
274.9266	446.7618
267.8732	440.9863
274.5057	439.3035
273.148	428.9477
267.9724	426.605
272.7608	423.0958
271.848	402.8555
266.9038	399.8265
273.3644	398.3865
272.9092	392.6823
269.0193	390.9538
266.6031	390.5892
268.3959	389.333
268.4769	388.7229
274.775	388.6426
269.9412	384.1095
270.164	380.1645

271.2344	379.5687
271.0637	379.4173
274.0736	376.975
272.8813	372.5838
273.9935	364.1953
270.2735	362.8425
266.5602	362.3615
267.0598	362.2504
273.931	361.4458
266.687	358.5968
267.8707	345.377
274.0129	341.7087
268.1584	340.0072
272.4171	339.9482
273.9492	337.7759
271.8274	337.0638
272.9418	334.735
268.7685	332.5134
271.0311	330.166
269.5529	329.6834
271.7852	329.4965
265.1294	328.5443
270.3167	326.1115
274.7932	322.7612
266.9612	322.2462
268.3945	318.4145
272.4585	317.0352
273.3937	311.8324
268.5106	309.1411
274.2334	308.939
266.5311	306.3664
267.2611	305.3837
268.296	296.2595
270.4208	295.9565
265.622	294.5952
265.3096	291.7896
271.9796	291.3563
266.7735	289.1248
266.4405	288.5171
268.2848	288.495
267.4256	286.6348
269.6571	278.6436
266.1412	276.7565
267.3674	272.5632
267.4188	271.1268
270.1127	269.0822
269.2408	268.6072
268.1197	268.2564
269.9535	265.2805
267.2564	260.2619
270.137	259.5202
273.3662	259.0159
265.6014	257.8101
268.3795	240.9209
270.555	238.7878
267.8987	236.031
269.0615	235.5876
272.2045	233.6106
267.7187	233.1211
266.2732	230.8264
273.2835	227.7961
266.4013	224.78
267.3043	221.5354

268.1698	210.2348
266.2634	209.4679
268.3883	205.7365
273.672	203.391
266.5143	201.3439
269.0931	197.6261
272.6067	194.4182
267.9525	194.2338
265.4777	190.3395
269.1833	189.2082
274.6124	187.8121
267.2584	187.5622
269.5676	187.2816
272.1801	184.7801
266.4215	180.9453
268.7459	171.1634
266.9329	165.098
266.9351	164.366
265.9174	162.7663
270.0204	161.8929
272.9398	161.4497
270.1184	159.1837
267.3553	157.7697
270.4464	155.4136
265.7494	153.1925
273.8866	153.0735
270.634	149.0119
274.7099	148.4356
272.5679	139.5639
271.6932	133.585
273.3462	133.5618
266.6255	129.4922
269.7261	128.9703
267.098	128.5346
272.1375	125.1136
274.3062	124.3165
266.7194	121.8051
272.2989	119.9909
272.22	118.7938
269.6111	117.9953
270.1325	115.9564
269.9235	113.2257
265.2586	107.8279
274.8927	106.3246
266.7241	105.5648
272.1088	103.0621
269.4123	102.7927
265.1838	92.9448
269.0527	92.467
267.0471	90.3106
266.3261	88.4482
271.6401	86.5715
267.0574	81.0067
272.6539	79.8224
268.039	78.0902
268.3557	72.8477
269.2831	71.0318
268.7701	70.0134
266.8543	69.9193
269.5176	63.4609
266.2957	61.7943
268.7454	61.4018
270.4413	60.4127

268.2732	58.3834
272.4155	55.8028
270.6922	54.0116
269.8139	48.4472
268.1706	47.8901
273.7438	47.5721
265.6415	42.8052
266.848	41.9766
267.5214	40.3704
270.6828	39.7223
271.064	36.9595
268.2121	36.8568
272.6439	34.9941
270.9083	34.7761
274.5916	24.1348
273.1633	20.8092
265.4044	20.7534
271.86	18.136
274.2169	11.3981
269.7316	7.9178
276.8085	1.6567
279.7563	2.2229
282.8511	7.0243
282.9554	10.9155
282.6384	11.3751
279.4649	12.6443
278.7409	19.8941
279.5713	27.8918
278.1021	28.1658
280.4049	29.7613
280.8937	35.0838
278.0528	35.3891
278.2887	37.2321
275.4163	41.0842
278.6785	43.0142
277.5032	46.8343
275.7033	49.0997
280.0015	53.2349
281.1134	58.4708
276.9946	59.6036
277.4519	61.7292
282.5696	63.9397
280.5743	66.3494
282.7632	66.7665
283.2577	67.2328
281.5584	70.637
280.5686	71.5084
283.2917	87.2384
282.3713	88.5326
281.915	92.4873
275.5021	96.0546
284.3191	99.935
281.5405	105.7201
280.729	110.9215
275.8238	122.3359
280.6741	123.524
284.4635	124.4518
277.4566	124.6081
278.5204	128.0375
277.6916	130.414
278.9537	133.2037
283.0781	138.7621
276.819	138.8975

280.059	139.1167
280.5112	143.0877
275.8991	143.8224
281.8826	147.5051
275.5196	148.0032
275.3619	154.74
279.0547	157.8075
282.1511	159.6265
280.1583	161.1795
281.8422	161.7787
280.5693	164.2298
278.2912	181.6152
279.0051	185.9303
278.966	186.2497
282.0578	188.6934
283.2579	190.7964
280.7676	192.2751
276.3995	194.5094
278.3361	208.94
284.5692	209.817
277.4683	211.1061
278.2296	211.4403
275.3808	214.8277
276.4955	221.7835
277.6518	225.7494
281.1803	226.5703
278.7006	227.094
283.1524	228.7048
283.2248	230.3092
279.1751	232.8806
279.7298	234.5745
280.2252	239.1033
284.6956	242.0071
282.2467	247.0556
275.92	248.0191
276.4095	249.336
280.1279	250.0414
278.1152	254.8629
275.7761	256.9358
284.1644	263.532
275.8078	266.7205
281.6972	267.4783
276.2274	270.2288
284.5856	271.1646
281.0175	274.3585
279.3187	281.0218
283.6273	282.7156
277.7854	285.8292
283.042	287.3298
282.0032	292.0766
281.5219	295.8923
277.865	299.5448
284.6845	301.994
276.1337	306.1777
284.1064	318.3217
283.5147	320.2554
280.7674	321.1516
278.5803	328.4051
278.4633	334.193
276.5679	335.3677
280.1754	341.8362
278.9919	343.1981
281.7904	343.7771

276.3024	345.0293
284.6683	346.7906
284.163	353.1178
277.0711	354.1693
282.6834	356.1524
284.413	357.7309
281.1924	359.174
283.9659	361.8857
280.4837	362.3591
283.5104	362.439
279.3842	366.3117
281.2276	369.0448
278.9401	371.9091
276.2469	373.0449
279.2158	377.9886
281.7809	380.9182
277.8771	380.9353
283.2517	382.0811
277.5019	383.1412
276.963	385.8745
276.329	388.2655
281.8675	388.668
278.7311	390.2158
275.3148	391.0929
282.4406	401.0052
276.4269	402.0649
277.8665	408.6681
277.3638	409.6306
278.3378	410.5975
284.4679	412.5353
280.3522	413.3592
275.1782	415.9004
277.3384	416.5333
283.0287	420.4297
278.9497	425.6666
281.4003	430.09
282.615	433.9575
280.9207	434.5031
276.1633	435.4802
279.6926	437.766
275.432	452.5408
282.3564	458.3081
277.1373	462.8118
275.9748	465.3648
280.171	466.366
284.0196	468.5776
279.9393	472.4001
283.895	472.545
276.8361	475.7304
284.419	475.8161
280.2365	478.8157
278.3895	482.3965
283.6016	487.0134
283.4874	487.2521
279.0603	494.6796
275.9905	496.2244
281.4337	496.3965
281.8474	497.5656
277.6698	503.1204
279.0995	511.4923
281.1046	513.1646
281.4828	520.8301
279.1193	521.6573

276.7327	525.0008
284.9265	533.6183
283.0253	534.1379
282.9294	534.1942
275.8901	541.7625
282.6162	547.3363
283.0695	549.5441
282.5804	550.8256
275.7542	557.4712
279.8819	559.5688
284.7682	582.3
278.1161	582.7745
277.2115	584.3092
284.114	585.0687
279.6439	585.6008
284.9419	590.382
284.7058	591.4986
279.1098	593.6766
277.7207	597.1628
282.4178	602.2909
283.6417	605.179
279.2429	608.6996
276.1185	608.8492
289.7456	598.8331
287.1418	595.1542
294.4968	595.1062
290.1004	592.5527
289.3003	589.2172
293.3359	580.7718
289.3736	578.847
294.0738	577.6667
287.5056	571.0522
292.5666	567.4285
288.6393	561.4426
288.015	558.6993
286.0638	557.836
294.7917	557.1868
286.1471	557.0032
293.832	553.3739
288.9025	552.7773
285.9078	552.5553
290.052	548.4191
288.7955	545.2252
291.0456	540.8483
289.0464	535.9197
285.2782	533.1985
285.4929	533.1123
294.568	533.0827
289.7324	529.1181
289.136	522.4848
292.2277	514.6741
291.1762	511.6303
294.6153	511.5164
286.9314	509.622
292.5621	509.136
293.7408	507.1766
291.4055	490.0578
291.739	488.7667
285.965	488.4827
285.7283	488.2597
291.666	487.5114
286.8198	481.9866
291.1406	481.5308

287.0769	473.311
290.133	472.0712
290.481	470.0256
289.0733	466.0231
294.3983	462.6003
292.6686	459.7183
289.7248	456.6938
290.4424	451.3516
285.0388	449.6472
285.784	448.3276
294.9355	448.2846
293.1369	441.6362
286.5573	436.6492
287.9967	434.6101
286.4605	429.8141
293.913	424.5694
287.5793	422.6704
292.2841	418.6076
291.9634	416.4433
289.4376	411.778
294.1086	410.4736
294.1668	407.7911
285.8012	403.7239
290.2567	398.2647
291.5304	395.9001
286.5631	389.8163
287.9401	383.7438
288.0512	379.9047
285.4008	379.7088
291.8736	377.7993
293.9729	371.2906
294.9174	369.9961
293.4114	369.136
288.6099	365.8395
294.3638	365.2476
286.0538	360.8775
292.4047	360.5052
289.6502	349.6838
290.5453	342.723
289.3085	340.9402
294.3972	339.9126
286.2855	338.8571
292.711	337.9491
288.2647	337.5473
289.9691	335.5987
289.6163	331.5196
290.5567	329.1375
288.0304	325.3623
289.9181	323.108
293.2861	315.7487
292.052	311.4566
294.2619	303.361
288.6108	302.5218
293.1618	291.8065
288.9545	289.8196
286.6001	285.1913
290.0133	284.168
293.9006	282.6122
293.5562	281.7275
290.0936	280.7683
292.1604	280.5739
293.6253	280.4662
294.9503	277.3123

286.3467	277.0351
286.7997	275.6496
288.7149	275.1713
291.1956	274.9164
289.2444	269.2331
294.5699	266.8683
291.1245	260.8076
288.076	253.6762
287.7885	247.239
286.2285	245.237
289.2512	244.5507
289.5726	244.2705
286.1123	238.0287
285.2321	223.436
289.6113	221.2964
290.3593	218.4915
293.3969	216.5616
290.5982	215.1993
286.9076	214.3643
292.3477	202.3413
289.449	196.5907
289.0537	194.7762
285.0081	191.3715
287.5274	189.9577
294.303	188.1732
294.9171	186.4084
287.095	175.9836
288.1452	175.2204
289.2433	172.855
292.4668	167.188
294.1581	163.8541
292.1202	159.7399
288.9021	156.734
293.007	156.5893
290.2591	151.1572
289.7446	149.7475
285.9551	148.2054
289.7712	147.2149
289.2856	146.9131
287.3948	145.2676
285.6489	133.9861
292.3665	133.9354
290.0573	132.2554
291.9369	128.7224
290.6739	125.9491
287.5898	123.7596
293.1856	123.6943
293.3112	119.5577
291.6838	119.308
290.1227	117.3833
287.9842	117.0453
286.4847	115.7909
286.7572	114.8568
294.6224	114.1461
286.7073	104.7509
292.9367	102.4754
290.9233	100.2131
285.5321	97.214
288.6255	96.6245
286.424	94.8617
292.0706	90.5722
293.1426	88.9871
289.4953	87.3209

292.2175	86.4869
288.3876	84.7938
293.1701	81.7945
286.7052	80.4772
288.1017	78.2619
290.7891	76.1005
294.4749	71.9146
285.9171	62.5187
293.876	61.4543
289.5846	53.7255
289.4378	47.9578
289.6556	45.5558
287.3047	43.0339
287.6028	40.3619
293.8286	32.7154
293.7997	26.2056
285.9344	25.4063
286.7892	19.8694
286.3007	18.3387
289.9868	11.7349
291.5696	11.0606
293.4521	9.8665
285.5185	9.5637
295.5176	0.5061
303.4548	3.4449
296.774	4.6739
303.5818	5.9431
297.4809	9.1381
302.3748	13.127
303.6843	18.4362
302.4273	20.0096
300.9591	21.9272
301.8945	30.1737
303.3793	33.9034
300.8491	36.9381
296.389	36.9489
301.3474	43.3384
304.2254	44.7098
304.368	45.1294
301.5874	48.4076
295.8396	51.928
304.7647	52.1351
298.6458	54.0376
301.5255	59.6923
304.2878	59.8
295.4423	66.2361
298.5142	68.7188
296.0584	73.2203
299.9107	78.5055
303.6752	80.2372
297.8967	85.8164
303.33	86.0266
301.7641	88.2149
297.3192	91.2671
302.3648	92.1327

295.6762	95.8112
295.2347	95.879
299.0734	96.8507
302.0445	101.2814
301.5099	101.7831
299.6168	102.7691
302.4599	105.532
304.4401	114.2071
299.9975	114.8323
298.1752	114.9864
302.3223	117.8622
299.4881	121.4665
302.2818	122.104
300.8719	126.7753
297.7563	137.6693
295.3963	140.1151
297.2853	140.5273
303.2341	144.3263
297.3222	147.662
303.9142	147.9402
295.6648	149.6143
296.9262	151.5736
304.2279	152.6981
296.5046	162.2166
303.2612	177.1687
297.3925	178.4967
301.1362	182.7025
296.6443	184.8713
300.8558	187.3661
301.0875	194.696
303.5753	204.5945
297.9813	206.5986
304.8967	207.2038
303.6276	211.3324
300.9203	213.4969
303.0447	216.1918
296.3504	219.2101
298.5373	221.4111
297.2697	222.6566
300.8722	223.703
299.9891	226.6644
295.6827	230.1609
295.4786	231.5563
299.2464	233.0725
302.9273	233.823
297.1466	234.3125
301.7714	238.808
303.3619	245.5089
301.579	253.9102
304.3956	254.6304
296.9932	257.1012
304.1331	264.5923
296.1846	269.8201
302.4327	269.9767
303.7914	272.9873

301.4528	276.6839
298.2998	279.0579
304.6169	284.3121
299.5199	285.2803
303.068	289.75
301.0044	296.6598
295.162	302.7664
298.1475	303.1786
298.3044	308.5389
304.281	309.65
300.8484	313.9106
300.1385	318.7002
297.8947	322.8859
299.4435	328.0033
296.9887	328.7544
296.0142	328.9172
302.1865	331.3475
301.2827	334.0871
300.7227	335.9354
304.3983	337.2758
300.9929	337.6958
299.8002	339.0448
304.7524	347.1992
298.0096	348.4648
298.002	350.7639
300.8648	355.0265
298.5397	363.7738
301.6494	366.998
297.1545	368.0493
302.2055	368.9536
299.7562	375.7337
297.6649	377.4627
303.0112	384.7635
298.8352	390.644
304.8514	392.2815
300.199	394.8427
297.4959	399.8423
297.4548	409.0444
295.4943	415.155
297.1136	417.8837
304.4132	429.3212
295.486	430.6931
304.524	430.7348
304.498	432.7492
302.0484	435.4168
300.2835	438.3198
297.2896	442.5792
301.831	444.7487
301.835	446.826
297.9158	447.1552
302.4977	451.0727
302.5648	451.7621
303.4246	457.1882
295.486	457.6242
301.432	457.8395

297.4999	458.4516
299.1352	459.3025
298.8627	460.4873
300.553	461.1274
297.7551	462.9739
300.4599	466.381
301.9872	466.5158
302.7119	469.3405
296.0341	473.8527
303.582	477.2665
302.3972	478.5524
299.2194	478.7413
298.0498	484.9842
300.1737	486.2524
300.7002	491.8029
297.6159	491.9937
300.7465	492.5463
298.9807	496.9805
301.676	503.1226
296.216	508.8408
300.7121	511.6325
296.0646	514.3484
303.4897	515.2723
301.215	523.4679
301.6586	536.4938
304.8573	538.4836
301.6784	552.9069
298.4456	554.8631
299.7252	556.6516
300.607	558.4906
299.8398	558.9891
297.5787	571.8747
297.8436	574.613
304.9548	580.0165
297.6704	580.632
295.9462	584.9615
296.529	586.6727
297.6229	592.8298
300.7201	593.7748
298.0323	598.4027
303.1104	598.4632
300.9348	600.4803
299.3463	602.4749
304.6025	605.6975
297.0759	609.0075

References

Alexander W N, 2009, "Normalization of Roughness Noise on the Near-Field Wall Pressure Spectrum", Master's Thesis, AOE Department, Virginia Tech. Avail: http://scholar.lib.vt.edu/theses/ available /etd-06182009-104314/.

Anderson J, Stewart D, Goody M, and Zoccola P, 2007, "Sound from Flow Over a Rough Surface", Proceedings of the 2007 International Mechanical Engineering Congress and Exposition, Seattle WA, Nov. 11-15, IMECE2007-41847.

Antonia R A, and Luxton R E, 1972, "The Response of a Turbulent Boundary Layer to a Step Change in Surface Roughness. Part 2. Rough-to-Smooth", Journal of Fluid Mechanics, vol. 53(4), pp. 737-757.

Billingsley J, and Kinns R, 1976, "The Acoustic Telescope", Journal of Sound and Vibration, vol. 48(4), pp. 485-510.

Blake W K, 1986, *Mechanics of Flow Induced Sound and Vibration*, Academic Press, New York.

Bradshaw P, and Gee M T, 1960, "Turbulent Wall Jets With and Without an External Stream", Aeronautical Research Council Reports and Memoranda, no. 3252.

Brooks T F, 2006, "Extension of DAMAS Phased Array Processing for Spatial Coherence Determination (DAMAS-C)", 12th AIAA/CEAS Aeroacoustics Conference, Cambridge, MA, May 8-10, AIAA-2006-2654.

Brooks T F, and Humphreys W M, 2006, "A Deconvolution Approach for Mapping of Acoustic Sources (DAMAS) Determined from Phased Microphone Arrays", vol. 294, pp. 856-879.

Chanaud R C, 1969, "Experimental study of aerodynamic sound from a rotating disk", Journal of the Acoustical Society of America, vol. 45, pp. 392-397.

Chase D M, 1980, "Modeling the Wavevector-Frequency Spectrum of Turbulent Boundary Layer Wall Pressure", Journal of Sound and Vibration, vol. 70(1), pp. 29–67.

Chase D M, 1987, "The Character of the Turbulent Wall Pressure Spectrum at Subconvective Wavenumbers and a Suggested Comprehensive Model", Journal of Sound and Vibration, vol. 112, pp. 125-147.

Cole L D, 1980, "Measurements of Sound Generated by Boundary Layer Turbulence over Smooth and Rough Surfaces", DTNSRDC Report SAD-288E-1942.

Corcos G M, 1964, "The Structure of the Turbulent Pressure Field in Boundary-Layer Flows", Journal of Fluid Mechanics, vol. 18(3), pp. 353–378.

Curle N, 1955, “The Influence of Solid Boundaries Upon Aerodynamic Sound”, Proceedings of the Royal Society. A, London, vol. 231, pp. 505-514.

Devenport W J, Wahl E A, Glegg S A L, Alexander W N, and Grissom D L, 2010, “Measuring Surface Pressure with Far Field Acoustics”, Journal of Sound and Vibration, vol. 329, pp. 3958-3971.

Devenport W J, Grissom D L, Alexander W N, Smith B S, and Glegg S A L, 2011, “Measurements of Roughness Noise”, Journal of Sound and Vibration, doi: 10.1016/j.jsv.2011.03.017.

Efimtsov B M, 1982, “Characteristics of the Field of Turbulent Wall Pressure Fluctuations at Large Reynolds Numbers”, Soviet Physics Acoustics, vol. 28(4), pp. 289–292.

Fang F M, Chen J C, and Hong Y T, 2001, “Experimental and Analytical Evaluation of Flow in a Square-to-Square Wind Tunnel Contraction”, Journal of Wind Engineering and Industrial Aerodynamics, vol. 89, pp. 247-262.

Farabee TM, and Cassarella M J, 1986, “Measurements of Fluctuating Wall Pressure for Separated/Reattached Boundary Layer Flows”, Journal of Vibration, Acoustics, Stress, and Reliability in Design, vol. 108, pp. 301-307.

Farabee T M, and Geib F E, 1991, “Measurements of Boundary Layer Pressure Fluctuations at Low Wavenumbers on Smooth and Rough Walls”, Flow Noise Modeling Measurements and Control. ASME NCA, vol. 11, pp. 55-68.

Ffowcs Williams J E, 1982, “Boundary-Layer Pressures and the Corcos Model: A Development to Incorporate Low-Wavenumber Constraints”, Journal of Fluid Mechanics, vol. 125, pp. 9-25.

Glegg S, Devenport W, Grissom D, and Smith B, 2007, “Rough Wall Boundary Layer Noise: Theoretical Predictions”, 13th AIAA/CEAS Aeroacoustics Conference, Rome, Italy, May 20-23, AIAA-2007-3417.

Glegg S, and Devenport W, 2009, “Far-Field Sound from Rough-Wall Boundary Layers”, Proceedings of the Royal Society. A, London, vol. 465, pp. 1717-1734.

Goody M, 2004, “Empirical Spectral Model of Surface Pressure Fluctuations”, AIAA Journal, vol. 42(9), pp. 1788-1794.

Graham W R, 1997, “A Comparison of Models for the Wavenumber-Frequency Spectrum of Turbulent Boundary Layers”, Journal of Sound and Vibration, vol. 206(4), pp. 541-565.

Grissom D, 2007, “A Study of Sound Generated by a Turbulent Wall Jet Flow Over Rough Surfaces”, Ph.D. Dissertation, AOE Department, Virginia Tech. Avail: http://scholar.lib.vt.edu/theses/available/etd-07192007-123339/.

Hersh A S, 1983, “Surface Roughness Generated Flow Noise”, AIAA 8th Aeroacoustics Conference, Atlanta GA, April 11-13, AIAA-83-0786.

Howe M, 1984, “On the Generation of Sound by Turbulent Boundary Layer Flow Over a Rough Wall”, Proceedings of the Royal Society. A, London, vol. 395, pp. 247-263.

Howe M, 1986, “The Influence of Viscous Surface Stress on the Production of Sound by Turbulent Boundary Layer Flow over a Rough Wall”, Journal of Sound and Vibration, vol. 104, pp. 29-39.

Howe M, 1988, “The Turbulent Boundary Layer Rough Wall Pressure Spectrum at Acoustic and Subconvective Wavenumbers”, Proceedings of the Royal Society. A, London, vol. 415, pp. 141-161.

Howe M, 1998, *Acoustics of Fluid-Structure Interactions*, Cambridge Univ. Press, Cambridge, England.

Hwang Y F, and Geib F E, 1984, “Estimation of the Wavevector-Frequency Spectrum of Turbulent Boundary Layer Wall Pressure by Multiple Linear Regression”, ASME, Transactions, Journal of Vibration, Acoustics, Stress and Reliability in Design, vol. 106, pp. 334-342.

Jordan P, Fitzpatrick J A, and Valiere J-C, 2002, “Measurement of an Aeroacoustic Dipole Using a Linear Microphone Array”, Journal of the Acoustical Society of America, vol. 111(3), pp. 1267-1273.

Lighthill M J, 1952, “On Sound Generated Aerodynamically. Part 1. General Theory”, Proceedings of the Royal Society. A, vol. 211, pp. 564-587.

Liu Y, and Dowling A, 2007, “Assessment of the Contribution of Surface Roughness to Airframe Noise”, AIAA Journal, vol. 45(4), pp. 855-869.

Liu Y, Dowling A, and Shin H C, 2008, “Measurement and Simulation of Surface Roughness Noise Using Phased Microphone Arrays”, Journal of Sound and Vibration, vol. 314, pp. 95-112.

Mish P F, 2003, “An Experimental Investigation of Unsteady Surface Pressure on Single and Multiple Airfoils”, Ph.D. Dissertation, AOE Department, Virginia Tech. Avail: http://scholar.lib.vt.edu/theses/available/etd-03312003-173021/

Morton M A, personal communication, July, 2011

Narasimha R, Narayan K Y, and Parthasarathy S P, 1973, “Parametric Analysis of Turbulent Wall Jets in Still Air”, Aeronautical Journal, vol. 77, pp. 355-359.

Nelson P A, and Yoon S H, 2000, “Estimation of Acoustic Source Strength by Inverse Methods: Part I, Conditioning of the Inverse Problem”, Journal of Sound and Vibration, vol. 233(4), pp. 643-668.

Powell A, 1960, “Aerodynamic Noise and the Plane Boundary”, Journal of the Acoustical Society of America, vol. 32(8), pp. 982-990.

Rasnick M B, 2010, “The Noise of a Boundary Layer Flowing Over Discrete Roughness Elements”, Master’s Thesis, AOE Department, Virginia Tech. Avail: http://scholar.lib.vt.edu/theses/available/etd-05242010-161659/.

Rusche M T, 2011, “Structure of Turbulent Boundary Layers and Surface Pressure Fluctuations on a Patch of Roughness Elements”, Master’s Thesis, AOE Department, Virginia Tech.

Skudrzyk E, and Haddle G, 1960, “Noise Production in a Turbulent Boundary Layer by Smooth and Rough Surfaces”, Journal of the Acoustical Society of America, vol. 32, pp. 19-34.

Smol’yakov A V, and Tkachenko V M, 1991, “Model of a Field of Pseudosonic Turbulent Wall Pressures and Experimental Data”, Soviet Physics Acoustics, vol. 37(6), pp. 627-631.

Smith B S, 2008, “Wall Jet Boundary Layer Flows Over Smooth and Rough Surfaces”, Ph.D. Dissertation, AOE Department, Virginia Tech. Avail: http://scholar.lib.vt.edu/theses/available/etd-05082008-144350/

Tester B J, and Glegg S A L, 2008, “A Review of Engine Noise Source Diagnostic Methods for Static Engine Tests, with Phased Array and Polar Correlation Techniques”, 14th AIAA/CEAS Aeroacoustics Conference, 5-7 May 2008, Vancouver, BC, AIAA-2008-2854.

Wygnanski I, Katz Y, and Horev E, 1992, “On the Applicability of Various Scaling Laws to the Turbulent Wall Jet”, Journal of Fluid Mechanics, vol. 234, pp. 669-690.

Yang Q, and Wang M, 2009, “Computational Study of Roughness-Induced Boundary-Layer Noise”, AIAA Journal, vol. 47(10), pp. 2417-2429.

Yang Q, and Wang M, 2010, “Boundary-Layer Noise Induced by a Roughness Patch”, 16th AIAA/CEAS Aeroacoustics Conference, 7 - 9 June 2010, Stockholm, SE, AIAA-2010-3772.

Yang Q, and Wang M, 2011, “Statistical Analysis of Acoustic-Source Field in Rough-Wall Boundary Layers” 17th AIAA/CEAS Aeroacoustics Conference, 5-8 June 2011, Portland, OR, AIAA-2011-2738.

Yoon S H, and Nelson P A, 2000, “Estimation of Acoustic Source Strength By Inverse Methods: Part II, Experimental Investigation of Methods for Choosing Regularization Parameters”, Journal of Sound and Vibration, vol. 233(4), pp. 669-705.